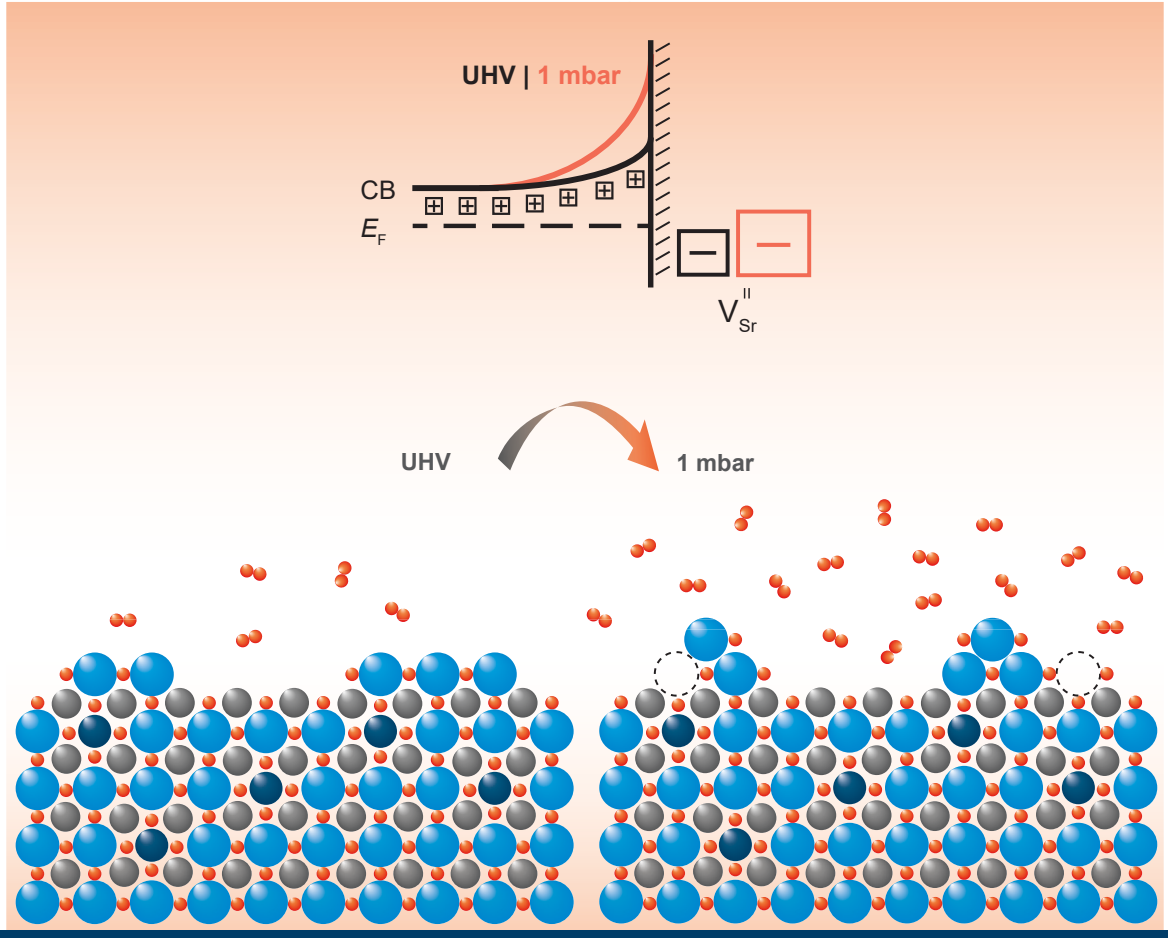

Chemical control of the electrical surface properties of *n*-doped transition metal oxides

Michael Tobias Andrä

Information
Band / Volume 60
ISBN 978-3-95806-448-5

Mitglied der Helmholtz-Gemeinschaft

JÜLICH
Forschungszentrum

Schriften des Forschungszentrums Jülich
Reihe Information / Information Band / Volume 60

Forschungszentrum Jülich GmbH
Peter Grünberg Institut (PGI)
Elektronische Materialien (PGI-7)

Chemical control of the electrical surface properties of *n*-doped transition metal oxides

Michael Tobias Andrä

Schriften des Forschungszentrums Jülich
Reihe Information / Information Band / Volume 60

ISSN 1866-1777 ISBN 978-3-95806-448-5

Bibliografische Information der Deutschen Nationalbibliothek.
Die Deutsche Nationalbibliothek verzeichnet diese Publikation in der
Deutschen Nationalbibliografie; detaillierte Bibliografische Daten
sind im Internet über http://dnb.d-nb.de abrufbar.

Herausgeber und Vertrieb:	Forschungszentrum Jülich GmbH Zentralbibliothek, Verlag 52425 Jülich Tel.: +49 2461 61-5368 Fax: +49 2461 61-6103 zb-publikation@fz-juelich.de www.fz-juelich.de/zb
Umschlaggestaltung:	Grafische Medien, Forschungszentrum Jülich GmbH
Druck:	Grafische Medien, Forschungszentrum Jülich GmbH
Copyright:	Forschungszentrum Jülich 2019

Schriften des Forschungszentrums Jülich
Reihe Information / Information, Band / Volume 60

D 82 (Diss. RWTH Aachen University, 2019)

ISSN 1866-1777
ISBN 978-3-95806-448-5

Vollständig frei verfügbar über das Publikationsportal des Forschungszentrums Jülich (JuSER)
unter www.fz-juelich.de/zb/openaccess.

Abstract

Novel classes of materials are required to meet the technological challenges in modern electronics. By ultimately merging surface physics and band engineering approaches with the chemistry of complex oxides, oxide electronics are believed to meet the rapidly growing demands stemming from the decreasing structure size of electronic applications. A lot is known about the behavior of complex oxides in the bulk. Surfaces and interfaces, however, may show fundamentally varying properties due to the reduced dimension and short diffusion lengths involved. Thus, the surfaces of complex oxide semiconductors and especially their interfaces formed with other complex oxides and metals are expected to play an even more important role in the technological progress of the upcoming decades. In order to pave the way to novel tailored applications, understanding the redox processes at the complex oxide surfaces is essential.

Within this thesis, state-of-the-art spectroscopic tools are used that allow for *in-situ* surface investigations in varying atmospheres thereby demonstrating the differences between surface and bulk chemistry and determine how space charge formation couples the surface chemistry and the electronic properties. By the utilization of ambient pressure photoelectron spectroscopy the previous experimental limitations of an undefined surface state and contamination that occurred due to the *ex-situ* transport of samples. The spectroscopic results determined on n-$SrTiO_3$ single crystals and thin films clearly demonstrate the pO_2-dependent activation of the strontium sublattice at intermediate temperatures that is accompanied by a shift of the Fermi level from the conduction band edge into the band gap. This shift illustrates an electron depletion layer being present at the n-$SrTiO_3$ surface and thus the formation of a surface space charge layer.
These findings are substantiated by electrical characterization of the surface contact and the *in-plane* sheet properties in Pt/n-$SrTiO_3$ heterostructures and n-$SrTiO_3$ thin films, respectively. The surface contact of the heterojunction exhibit an increased transport barrier after annealing in oxidizing conditions while the thin films demonstrate a reduced carrier concentration directly after growth in oxidizing conditions and a pO_2-dependent *in-plane* sheet resistance.

As the underlying surface redox process, the precipitation of strontium oxide cluster in oxidizing conditions at the n-$SrTiO_3$ surface, leaving behind negatively charged strontium vacancies confined to the surface, is identified. Subtle changes of the

strontium sublattice result in a substantial electronic response of the n-$SrTiO_3$ surface, consistently explained based on *in-situ* spectroscopy, electrical characterization and density functional theory. Such a redox process is remarkable since up to now the bulk defect chemistry of n-$SrTiO_3$ proposed the strontium sublattice, to be active only at much higher temperatures above 1250 K. At lower temperatures, however, the rearrangement of the strontium sublattice is found to be restricted to the n-$SrTiO_3$ surface due to the inhibited cation diffusion into the sample. In fact, this restriction is fundamental for the electrical charge separation leading to a surface space charge layer in which electrons are depleted. In this way, classical rules of bulk defect chemistry are expanded to the surface allowing for accelerated ionic dynamics and thus chemical control of the electrical surface properties of complex oxides by their redox chemistry at fairly low temperatures.

The results of this thesis give fundamentally new insights on the electrical surface properties of complex oxides and their dependence on different thermodynamical biases. Controlling the electrical properties of thin films by their surface chemistry might result in innovative applications such as novel gas sensors.

Kurzfassung

Um den technologischen Herausforderungen moderner Elektronik gerecht zu werden, ist die Verwendung neuer Materialklassen unumgägnlich. Durch die Verschmelzung von Oberflächenphysik und Bandstruktur mit der Chemie komplexer Oxide soll die wachsende Forderung nach einer Verringerung der aktiven Strukturgröße elektronischer Bauelemente erfüllt werden kann. Die Bulk-Eigenschaften von komplexen Oxiden sind gut untersucht. Die Ober- und Grenzflächen hingegen können aufgrund der verringerten Abmessungen und der damit verbundenen verkürzten Diffusionslänge grundlegend veränderte Eigenschaften aufweisen. Daher wird erwartet, dass die Oberflächen komplexer Oxidhalbleiter sowie besonders ihre Grenzflächen, die sie mit anderen komplexen Oxiden und Metallen bilden, in den nächsten Jahrzehnten eine starke Rolle für den technologischen Fortschritt spielen werden. Für die Entwicklung neuer Bauteile mit maßgeschneiderten Eigenschaften is es daher unumgänglich, die Redoxprozesse an den Oberflächen komplexer Oxide zu verstehen.

Im Rahmen dieser Arbeit werden modernste spektroskopische Instrumente eingesetzt, die es ermöglichen, die Oberflächeneigenschaften *in-situ* in verschiedenen Atmosphären zu untersuchen. Dadurch können die Unterschiede zwischen Oberflächen- und Bulkchemie aufgezeigt sowie die Verbindung der Oberflächenchemie und der elektronischen Eigenschaften durch die Bildung einer Raumladung an der Oberfläche aufgeklärt werden. Durch den Einsatz dieser modernen Techniken ist es möglich die bisherigen experimentellen Probleme eines undefinierten Oberflächenzustandes, die durch den *ex-situ* Probentransport entstanden sind, zu überwinden. Die spektroskopischen Ergebnisse, die an n-$SrTiO_3$ Einkristallen und Dünnfilmen gemessen wurden, belegen deutlich die pO_2 -abhängige Aktivierung des Strontiumuntergitters bei mittleren Temperaturen. Diese Aktivierung geht mit einer Verschiebung des Fermi-Niveaus, von der Leitungsbandkante tiefer in die Bandlücke, einher. Diese Verschiebung zeigt eine Elektronenverarmung an der n-$SrTiO_3$ Oberfläche und damit die Bildung einer Oberflächenraumladungszone.
Diese Resultate werden durch die Charakterisierung des elektrischen Oberflächenkontaktes von Pt/n-$SrTiO_3$ Heteroübergängen und der elektrischen *in-plane* Eigenschaften von n-$SrTiO_3$ Dünnfilmen bestätigt. Der Oberflächenkontakt der Heterostrukturen zeigt eine deutliche Erhöhung der Transportbarriere nach dem Ausheizen in oxidierenden Bedingungen, während die Dünnfilme eine verringerte Ladungsträgerkonzentration direkt nach dem Wachstum in oxidierenden Bedingungen und einen pO_2-abhängigen Schichtwiderstand aufweisen.

Als zugrunde liegender Oberflächenredoxprozess wird die Ausfällung von Strontiumoxidclustern unter oxidierenden Bedingungen identifiziert. Dabei bleiben doppelt negativ geladene Strontiumleerstellen an der n-$SrTiO_3$ Oberfläche zurück. Geringe Änderungen des Strontiumuntergitters führen zu einer enormen Veränderung der elektronischen Oberflächeneigenschaften die mit Hilfe von *in-situ* Spektroskopie, elektrischer Charakterisierung und der Dichte-Funtkional Theorie, konsistent erklärt wird. Ein solcher Redoxprozess ist bemerkenswert, da die Bulk-Defektchemie von n-$SrTiO_3$ vorhersagt, dass das Strontiumuntergiter erst bei viel höheren Temperaturen oberhalb von 1250 K aktiviert wird. Bei niedirgeren Temperaturen wird hingegen aufgezeigt, dass die Umordnung des Strontiumuntergitters, aufgrund der gehemmten Kationendiffusion in die Porbe, auf die n-$SrTiO_3$ Oberfläche beschränkt ist. Tatsächlich ist diese Beschränkung grundlegende Vorraussetzung der beobachteten Trennung von elektrischen Ladung, die zur Bildung einer Oberflächenraumladungszone mittels Elektronenverarmung führt. Auf diese Weise werden die Regeln der klassischen Bulk-Defektchemie mit beschleunigter Ionendynamik auf die Oberfläche ausgedehnt. Dadurch wird die chemische Kontrolle der elektrischen Oberflächeneigenschaften von komplexen Oxiden bei moderaten Temperaturen, mit Hilfe der Redoxchemie, ermöglicht.

Die Ergebnisse dieser Arbeit geben grundlegend neue Einblicke in die elektrischen Oberflächeneigenschaften von komplexen Oxiden und deren Abhängigkeit von verschiedenen thermodynamischen Einflüssen. Die Steuerung der elektrischen Eigenschaften dünner Filme durch ihre Oberflächenchemie kann zu neuen innovativen Anwendungen, wie zum Beispiel neuen Gassensoren, führen.

Contents

1. Introduction 1

2. Fundamentals 5
- 2.1. Fundamentals of donor-doped $SrTiO_3$ . . . 5
- 2.2. Electronic transport . . . 7
- 2.3. State of knowledge on donor-doped $SrTiO_3$ surfaces . . . 9
- 2.4. Defect chemistry of n-$SrTiO_3$ . . . 11
- 2.5. One-dimensional diffusion in solids . . . 13

3. Methods 17
- 3.1. Annealing treatment . . . 17
- 3.2. Deposition techniques . . . 18
- 3.3. Characterization of crystal structure and topography . . . 23
- 3.4. Electrical characterization . . . 24
- 3.5. X-ray photoelectron spectroscopy . . . 29

4. Donor-doped $SrTiO_3$ thin film growth 33
- 4.1. Annealing procedures . . . 33
- 4.2. Donor-doped $SrTiO_3$ thin films . . . 34
  - 4.2.1. Thin film growth process . . . 35
  - 4.2.2. Single crystalline quality . . . 37

5. Electronic surface characteristics 43
- 5.1. *Through-plane* contact properties of n-$SrTiO_3$ single crystals . . . 43
- 5.2. *In-plane* properties of n-$SrTiO_3$ thin films . . . 52

6. pO_2-dependence of surface space charge layer 57
- 6.1. Binding energy shift at different pO_2 . . . 57
- 6.2. Binding energy shift at different probing depths . . . 73

7. Thermodynamic control of the surface charge 85
- 7.1. Surface space charge layer at different doping concentrations . . . 86
- 7.2. Surface space charge layer at different temperatures . . . 93
- 7.3. Comparison of the doping concentration and temperature-dependence 100

8. Control of electronic properties in n-$SrTiO_3$ thin films 105
- 8.1. Electrochemical conductivity relaxation at different pO_2 . . . 106

8.2. Temperature-dependent sheet resistance 114
8.3. Numerical fitting of the transient sheet resistance 117
8.4. Comparison of AP-XPS and ECR results 120

9. Discussion 125
9.1. Surface redox processes at the n-$SrTiO_3$ surface 125
9.2. SrO precipitation vs. oxygen adsorption 132
9.3. Clarification of the chemical surface redox process 137

10. Conclusion and Outlook 147

A. Pressure instabilities during ECR experiments XI

B. Description of the supercell applied for DFT calculations XIII

Bibliography XXI

1. Introduction

Technological challenges in modern electronics call for the utilization of novel classes of materials in electronics. Oxide electronics have already shown their versatility in a wide variety of state-of-the-art applications and constitute an increasingly fast growing area of research.[1–3] By ultimately merging surface physics and band engineering approaches with the chemistry of complex oxides, oxide electronics are believed to meet the rapidly increasing demands stemming from the decreasing structure size of electronic applications. Thus, the surfaces of complex oxide semiconductors and their interfaces formed with other complex oxides and metals are expected to play an important role in the technological progress of the upcoming decades.[4]

In recent years, perovskite-type ternary transition metal oxides (TTMOs) have received exceptional attention due to their variety of electrical and magnetic properties.[5–9]. In particular, their surface and interface properties and the strong coupling of lattice disorder and electronic structure give rise to a wide range of interesting effects and applications, such as resistive switching,[10–13] the formation of a two dimensional electron gas at the $LaAlO_3/SrTiO_3$ interface,[14–16] and their use as highly effiecient solar cells[17] and as an electrode material for solid oxide fuel cells.[18, 19] In all of these cases, the surfaces and interfaces impact or even determine device properties, e.g. by defining interface dipoles,[20] band alignments[21, 22] or space charge layers.[23] Thus, understanding and actively tuning the electrical surface properties in TTMOs is highly desirable.

As a typical model material, donor-doped strontium titanate (n-$SrTiO_3$), and as a specific example niobium-doped $SrTiO_3$ (Nb:$SrTiO_3$), was investigated extensively and with a view to a wide variety of processes in TTMOs. It is used for direct applications, such as superconductivity,[24] resistive switching,[12, 25, 26] or gas sensing.[27] In particular, state of the art Taguchi-type gas sensors show an undesirable non-linear dependence on the gas concentration that might be overcome by the employment of n-$SrTiO_3$.[28–30] Moreover, n-$SrTiO_3$ is used indirectly as a quasi-metallic substrate material for a wide variety of applications such as superconducting thin films,[31] ferroelectric tunnel junctions,[32–34] oxidic water splitting catalysts,[20, 35],, and resistive switching devices.[11, 12, 36]

The bulk of n-$SrTiO_3$ is referred to as a degenerate n-type semiconductor. Classical defect chemistry of donor-doped bulk $SrTiO_3$ is generally accepted for elevated temperatures above 1200 K. At lower temperatures, however, ionic defect equilibria relevant to the lattice disorder of n-$SrTiO_3$ are often neglected due to their sluggish response times,[37, 38] rendering the bulk of n-$SrTiO_3$ a simple material sufficiently

characterized by its extrinsic dopant concentration and the corresponding electron concentration. Approaching nanoscale structures and devices such as thin films, heterostructures, and interfaces,[14, 39–43] however, electronic and ionic properties may differ from the known bulk behavior.[23, 38, 44–47] This is due to the reduced dimensions and the impact of the surface and hence the small relevant diffusion lengths, as well as due to the presence of space charges, built-in electric fields, and band bending.

For the particular case of n-$SrTiO_3$, there are multiple indications for the existence of a surface space charge layer and corresponding eased electronic transport and charge-trapping in the vicinity of the surface implying a more complex behavior of the surface of n-$SrTiO_3$ as compared to the bulk.[25, 39] The origin of this surface space charge layer, however, has not yet been clarified. Possible scenarios considered are intrinsic surface states,[39] surface contamination,[25] electron gases formed at the $SrTiO_3$ interfaces,[23, 48, 49] ionic charges formed at the surface by adsorption of gas molecules,[50, 51] and ionic charges originating from cation vacancy defects, namely strontium vacancies, formed in the course of oxidation.[38, 52]

So far, the majority of studies investigating the surface properties of n-$SrTiO_3$ have used *ex-situ* experiments and simulations. The electrical surface properties in *ex-situ* experiments, however, may be strongly influenced by adsorbates resulting from the atmosphere in which the samples are transported and finally measured. Thus, the results of these studies are biased by the experimental procedure. In turn, simulations mostly rely on the assumption of ideal and clean surfaces and hence do not take all possible variations of the surface into account. Therefore,

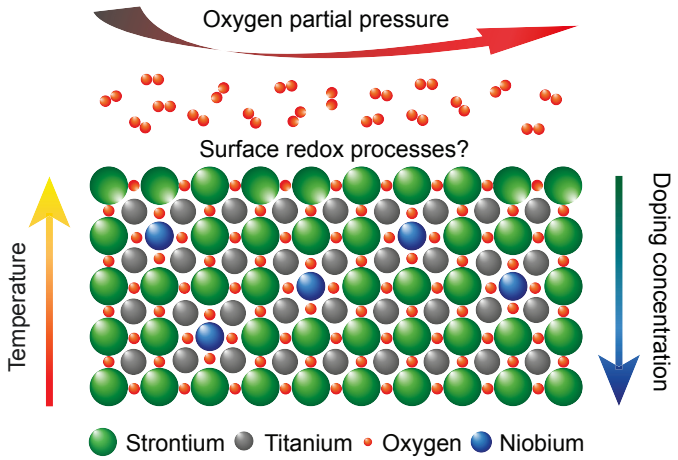

Figure 1.1.: Schematic illustration of the thermodynamic biases applied to n-$SrTiO_3$ surfaces with varying doping concentrations within this thesis.

existent research has found various different processes supposedly present at the n-$SrTiO_3$ surface, yet does not allow for drawing a conclusive picture of the impact of the defect chemistry on the electrical surface properties. Such a consistent understanding of the redox processes at the n-$SrTiO_3$ surface, however, would pave the way to novel tailored applications; hence, it constitutes a desideratum.

The scope of this thesis is to investigate the capability of defect-chemistry-based redox processes to control the chemical and electrical properties of donor-doped transition metal oxides. Therefore, *in-situ* electrical and spectroscopic characterization of donor-doped $SrTiO_3$ is employed in varying thermodynamic conditions. This thesis seeks to address and overcome the limitations of existing research by utilizing *in-situ* characterization methods, that allow for the application of specific thermodynamic biases (pO_2, T) to *in-situ* cleaned $SrTiO_3$ surfaces with varying doping concentrations, cf. fig. 1.1. The thesis's findings give direct access to the surface redox processes and thereby contribute to the development of innovative applications with tailored electrical surface properties.

Outline

The first chapter of this thesis discusses, the fundamentals of n-$SrTiO_3$, including the crystal structure, its electronic properties, its defect chemistry as well as present state of knowledge. Chapter 3 introduces the experimental methods utilized within this thesis ranging from annealing setups and over thin film deposition techniques to their growth and electrical characterization. Special attention will be paid to X-ray photoelectron spectroscopy (XPS) and their state-of-the-art utilization in *in-situ* ambient pressure measurement setups.

Chapter 4 presents the preparation of the different n-$SrTiO_3$ samples, including the description of different annealing treatments in oxidizing and reducing atmospheres and the developed $SrTiO_3$ thin film deposition process. The chapter shows that the n-$SrTiO_3$ thin films exhibit single crystalline quality, allowing for a direct comparison to single crystals and for the possibility to draw consistent conclusions.

Chapter 5 examines the impact of typical experimental procedures on the surface properties of n-$SrTiO_3$ samples. The chapter shows how both the *through-plane* contact properties of bare $SrTiO_3$ surfaces and heterojunctions formed with platinum top electrodes and the *in-plane* properties of n-$SrTiO_3$ thin films, i.e. the carrier concentration (n) are affected by the varying thermodynamic biases.

In chapter 6, *in-situ* ambient pressure XPS with varying pO_2 is used to link the varying electrical properties of Nb-$SrTiO_3$ surfaces directly to the surface chemistry. The probing depth dependence reveals remarkable dynamics of the cation sublattice, indicating cation chemistry to respond at much lower temperature as compared to the bulk. Subsequently, chapter 7 discusses the impact of varying doping concentrations and temperature on the surface space charge layer.

Chapter 8 illustrates the impact of varying pO_2 on the electrical surface and transport properties in n-$SrTiO_3$ thin films is illustrated. In particular, it shows,

how the applied pO_2 allows for a tailoring of the *in-plane* sheet resistance.

Chapter 9 reveals the precipitation of strontium oxide accompanied by the formation of double negatively charged strontium vacancies to be the underlying redox process at the n-$SrTiO_3$ surface. As this chapter discusses in detail, this process consistently explains all experimental findings as substantiated by DFT calculations.

Finally, the conclusion reconsiders the scope of this thesis and points to possible emerging ways towards innovative applications with tailored electrical properties.

2. Fundamentals

In this chapter the fundamental properties of donor-doped $SrTiO_3$ including its crystal structure, its electronic properties and its defect chemistry are explained in detail. Moreover, the one-dimensional diffusion in solids and the present state of knowledge on the surface properties of donor-doped $SrTiO_3$ will be introduced.

2.1. Fundamentals of donor-doped $SrTiO_3$

Crystal structure

$SrTiO_3$ is a typical ternary transition metal oxide. Unlike other ternary transition metal oxides $SrTiO_3$ is cubic at room temperature with a lattice constant of 3.905 Å.[38] It crystallizes in the so called perovskite structure (ABO_3). Figure 2.1 (a) schematically shows the unit cell of undoped $SrTiO_3$.

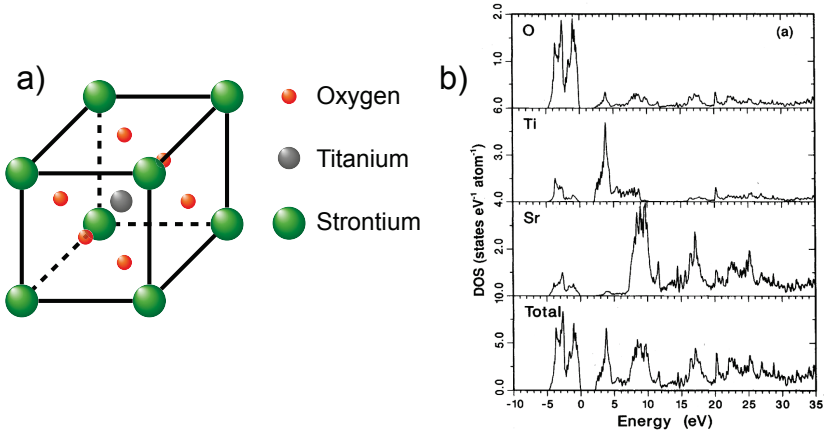

Figure 2.1.: Schematic illustration of an undoped $SrTiO_3$ unit cell (a) and the density of states calculated by density functional theory (b).[53]

The A-site cation (Sr^{2+}) is placed at the corners, the B-site cation (Ti^{4+}) is placed in the center and the anions (O^{2-}) are placed at the face-centered positions of the cubic unit cell. Considering the general ionic picture for the bonds in $SrTiO_3$ the valence electrons of strontium and titanium are transferred to the oxygen side of the bond. Therefore, the valence band should be made up by the O 2p-states and the conduction band should be made up by the Ti 3d-states and the Sr 5s-states. Figure 2.1 (b) shows the density of states of $SrTiO_3$ calculated by density functional theory.[53] The strict separation of the states responsible for the valence and conduction band is not confirmed. The conduction band is made up by empty Ti3d and Sr5s states. The valence band is formed mainly by O2p and occupied Ti3d states. This is due to not strictly ionic bonds, especially in the valence band the Ti-O bond shows a strong hybridized bonding component.

Within this thesis Kröger-Vink notation scheme will be utilized under the assumption of purely ionic bonds.[54] It describes the atoms in a unit cell with respect to the undistorted lattice position and the electronic charge. In the Kröger Vink notation, every compound lattice site is described by its chemical abbreviation, a missing atom is described by the letter V, electrons are described by the letter e and holes are described the letter h. In addition a positive charge is described by $^{\bullet}$ and a negative charge is described by $'$. As an example, a double negatively charged strontium vacancy is therefore notated as V''_{Sr}.

Electronic structure

Undoped $SrTiO_3$ is a wide band gap insulator. The band gap of $SrTiO_3$ is experimentally determined to 3.2 eV.[55] Considering the undoped case without an impact of charged defects, the Fermi energy is placed in the middle between the valence band edge and the conduction band edge. Different doping concentrations shift the Fermi energy.

Donor-doping is introduced in two different ways. One widely used doping material is niobium. By replacing a titanium atom with a niobium atom an additional electron is introduced to the system. This electron changes the valence state of a single titanium atom from Ti^{4+} to Ti^{3+} by filling up one of the empty Ti3d states of the conduction band. With increasing concentration of filled Ti3d states concentration, the electrons in the conduction band become mobile and induce metallic conductivity. Another commonly utilized doping material is lanthanum. By replacing a strontium atom with a lanthanum atom again an additional electron is introduced to the unit cell which changes the valance state of a single titanium atom from Ti^{4+} to Ti^{3+}. As an advantage by introducing lanthanum to the system higher doping concentrations can be realized without phase separation of the single crystal in comparison to Nb-dopants.

Both niobium and lanthanum are so-called shallow donors.[56, 57] Thus, they are energetically located close to the conduction band and are fully ionized at room temperature. When exceeding doping-concentrations above 10^{18} cm^{-3}, metallic

conductivity is achieved.[58] Therefore, donor-doped strontium titanate is widely used as a substrate material.

Another crucial factor affecting the electronic properties of $SrTiO_3$ is the dielectric constant. It depends directly on the temperature according to the Curie-Weiss-Law:[38]

$$\epsilon_r(T) = \frac{78400\text{K}}{T - T_\text{C}} \tag{2.1}$$

where ϵ_r is the dielectric constant and T_C the Curie temperature (28 K). At room temperature the dielectric constant of $SrTiO_3$ is calculated to $\epsilon_r \sim 300$.

In addition to the Curie-Weiss-Law, ϵ_r also depends on in-build electric fields.[59] With increasing electric fields the dielectric constant is reduced from about 300 at fields up to $\sim$300 kV/cm down to values of $\sim$25 at electric fields of 10 MV/cm. This dependence is especially evident in donor-doped $SrTiO_3$, where the field-dependent dielectric constant significantly reduces the decay length of build-in charges and thus of possible space charge layers. In the course of a possible space charge layer, ϵ_r depends directly on the local electric field. Therefore, with decreasing space charge the dielectric constant increases.[59] Within this thesis, this dependence will be important when calculating the width of surface space charge layers in chapters 6, 7 and 8.

2.2. Electronic transport

In contrast to undoped $SrTiO_3$, highly donor-doped $SrTiO_3$ is a ternary transition metal oxide that exhibits metallic conductivity at room temperature. As expected for metallic behavior with increasing/decreasing temperature the conductivity decreases/increases. In metallic samples, the temperature dependence of the conductivity results mainly from the temperature dependence of the electron mobility (μ_n). This dependence primarily arises from the scattering of electrons with phonons of the lattice, or from electron-electron scattering at very high carrier concentrations.[60, 61] The temperature dependence of μ_n was experimentally determined to[37]

$$\mu_n(T) \approx \; 3.95 \times 10^4 \cdot (T/\text{K})^{-1.62} \qquad \left[\frac{\text{cm}^2}{\text{Vs}}\right], \tag{2.2}$$

where T denotes the temperature. This is true for the in-plane properties of undistorted bulk n-$SrTiO_3$. In order to analyze the electrical surface properties, however, typical experimental geometries require metallic top electrodes which in general result in heterostructures.

Another important aspect regarding the electronic transport in n-$SrTiO_3$ is the presence of possible defects in the single crystal which can either reduce or increase

the local charge carrier concentration. This aspect will be discussed in detail in section 2.4.

Transport through a Schottky barrier

The electronic contact properties of heterostructures fabricated from a metal top electrode and $SrTiO_3$ are described by the transport across so-called Schottky barriers. These barriers result from band alignment that compensates the different work functions of the utilized metal and $SrTiO_3$. Within this thesis, platinum top electrodes with a work function of 5.1 eV to 5.9 eV are used. The work function of $SrTiO_3$ is determined to 4.1 eV.[52, 62–64] The transport across a Schottky barrier is described in detail in ref. [65] and ref. [66]. Here only a brief description of the most essential transport mechanisms will be discussed.

Figure 2.2 schematically describes the electric transport over a Schottky barrier height.[65] The three most relevant transport mechanism across a Schottky barrier are thermionic emission (TE), thermionic-field emission and field emission (FE) (a). Which of the three mechanisms is dominating the electronic transport depends on the doping concentration (charge carrier concentration) and the temperature (b). If the thermionic energy of electrons is high enough, they overcome the Schottky barrier Φ_{TBH} in a so-called thermionic emission. This process is dominating

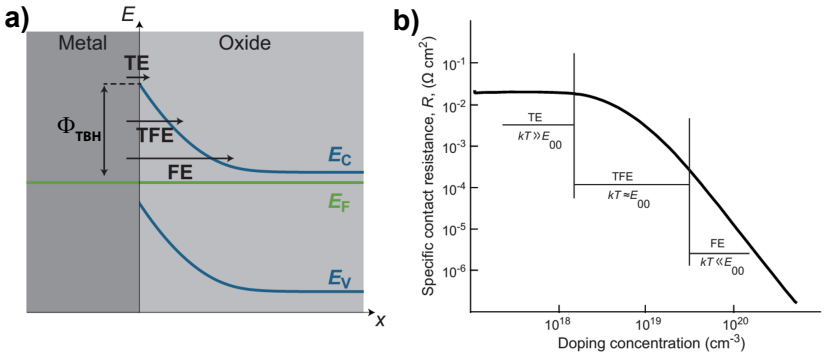

Figure 2.2.: Schematic illustration of the electric transport across a Schottky barrier with a height Φ_{TBH}. Due to the work function difference the edges of the conduction band (E_C) and the valence band (E_V) are bend upwards while the Fermi energy (E_F) is constant. The three most relevant transport mechanisms across the Schottky barrier are thermionic emission (TE), thermionic-field emission and field emission (FE) (a). The specific contact resistance of an exemplary semiconductor is depicted in (b) as a function of the donor-doping concentration. The figure was taken and modified from [65].

the electronic transport at very low doping concentrations and high temperatures. In contrast, if the thermionic energy of electrons is not high enough to overcome Φ_{TBH}, they have a certain probability to tunnel through the barrier. At very high doping concentrations and low temperatures this process is assisted by the presence of a strong electric field and thus referred to as field emission. Besides these two extreme cases at intermediate doping concentrations and temperatures a combination of both introduced processes dominates the electrical transport properties. In the so-called thermionic field emission, the electrons can not overcome Φ_{TBH} by their thermionic emission, but their energetic level is raised high enough to increase the tunneling probability due to a decrease of the Schottky barrier width, cf. fig. 2.2 (b).

Wang et al. previously showed that regardless of the transport mechanism the contact resistance (R_{SC}) depends exponentially on the apparent Schottky barrier.[67]

$$R_{\mathrm{SC}} \propto \exp\left(\frac{e\Phi_{\mathrm{TBH}}}{\mathrm{k_B}T}\right) \quad , \tag{2.3}$$

where e denotes the electric charge, $\mathrm{k_B}$ the Boltzmann constant and T the temperature. Consequently, an increase/decrease of the Schottky barrier results in an exponentially increased/decreased contact resistance R_{SC}.

The contact capacitance (C_{SC}) can be estimated assuming a classical square-root approach of the band bending at the surface. It is inversely proportional to the Schottky barrier width (d_{B}) and thus proportional to the square-root of Φ_{TBH} [65]

$$C_{\mathrm{SC}} = \epsilon_0 \epsilon_{\mathrm{r}} \frac{A}{d_{\mathrm{B}}} \propto \frac{1}{\sqrt{\Phi_{\mathrm{TBH}}}} \quad , \tag{2.4}$$

where ϵ_0 denotes the vacuum permittivity, ϵ_{r} the relative permittivity, A the contact area and d_{B} the Schottky barrier width. Therefore, a varying Φ_{TBH} changes the C_{SC} only slightly.

2.3. State of knowledge on donor-doped $SrTiO_3$ surfaces

Donor-doped $SrTiO_3$ is investigated extensively as a model material for transition metal oxides. The bulk n-$SrTiO_3$ is commonly treated as a degenerate n-type semiconductor. Ionic defect equilibria relevant to the lattice disorder of n-$SrTiO_3$ are often neglected with respect to the defect chemistry of $SrTiO_3$. This is due to their sluggish bulk response times at lower temperatures, cf. sec. 2.4.[37, 38] As a consequence, the electrical properties of bulk n-$SrTiO_3$ are considered sufficiently characterized by its extrinsic dopant concentration. Under the assumption of full ionization the free electron concentration is identical to the donor-dopant

concentration.

By the utilization of n-$SrTiO_3$ as quasi-metallic substrate material constant electrical properties right up to the surface are assumed. As shown by recent research and in more detail within this thesis, however, indicated the existence of a surface space charge layer in varying oxidizing atmospheres rendering its surface properties more complex. In the following, the most important aspects considered within this thesis are introduced briefly.

Impact of contamination on metal/n-$SrTiO_3$ heterostructures

Mikheev et al. investigated the resistive switching properties of Pt/Nb:$SrTiO_3$ heterostructures by $I(V)$-characteristics, $C(V)$-curves and SIMS measurements.[68] They proposed a model that attributed the magnitude of the resistive switching properties of a Pt/Nb:$SrTiO_3$ junction to charges trapped in an unintentional carbon contamination layer. By controlling the contamination layer a higher reproducibility of resistive switching devices might be achieved. Moreover, the proposed model might lead a way to intentionally tailor the metal/oxide interfaces and defect densities.

Bare n-$SrTiO_3$ surfaces

In addition to the electrical properties of metal/n-$SrTiO_3$ heterostructures and possible distortions, multiple studies examine the chemical and electrical properties of bare n-$SrTiO_3$ surfaces. So far, the majority of studies used simulations and ex-situ experiments and propose different models of processes present at the n-$SrTiO_3$ surface. *Ohtomo et al.* observed a surface electron depletion in La-doped $SrTiO_3$ thin films at temperatures below 300 K based on low temperature Hall measurements and X-ray photoelectron spectroscopy (XPS) spectra. The results were related to an intrinsic surface pinning potential of about 0.7 eV.[39] *Wang et al.* used scanning tunneling microscopy, XPS and density functional theory (DFT) calculations to connect a surface band bending to anti-domain boundaries in different reconstructions of the $SrTiO_3$ (110) surface after annealing treatments in different pO_2.[69]

In contrast, *Marchewka et al.* revealed the existence of an electron depletion layer in Pt/Fe:$SrTiO_3$/Nb:$SrTiO_3$ structures extending into the Nb-doped bottom electrode by electron holography.[52] They associated the determined electron depletion with acceptor-type interface defects by potential profile simulations and suggested the presence of strontium vacancies (V''_{Sr}) at the Fe:$SrTiO_3$/Nb:$SrTiO_3$ interface. These findings are complemented by *Meyer et al.* who recently proposed a high temperature surface oxidation model that associates electron depletion in

the near surface region of n-$SrTiO_3$ in oxidizing conditions with the incorporation of a negative surface charge. They suggested this negative surface charge to be generated by V''_{Sr} incorporated into the n-$SrTiO_3$ surface. This process is accompanied by the precipitation of strontium oxide (SrO) at the surface.[38, 70–72] A comparable scenario has been proposed also for electron gases formed at interfaces of $SrTiO_3$.[23, 48, 49]

In addition, *Setvin et al.* investigated bare TiO_2 surfaces by scanning tunneling microscopy. They showed the existence of oxygen molecules (O_2) forming superoxides at TiO_2 surfaces below 300 K.[50, 51] Due to the high electronegativity of oxygen the adsorbed molecules attract free electrons from the n-$SrTiO_3$ surface, generating a local negative surface charge. In accordance to the results related to V''_{Sr} incorporation, the negative surface charge forms a local electron depletion right at the surface.

Within this thesis it will be examined, which of the reported impacts is dominating the electrical surface properties of n-$SrTiO_3$ and thus are crucial for the formation of a surface space charge layer in oxidizing conditions.

2.4. Defect chemistry of n-$SrTiO_3$

One essential aspect in terms of linking electrical and chemical properties of ternary transition metal oxides is the impact of varying defect concentrations. The specific defect concentrations and structure present in a TTMO is able to switch its conductivity between metallic, semiconducting and insulating behavior.[37, 38] Hereby, the crucial defect concentrations are not only defined by extrinsic dopants, but also by intrinsic lattice defects such as charged vacancies on anion and cation sites. A well-known model to describe the impact of defects on the electrical properties of TTMOs is the defect chemistry. It requires the conservation of charge and mass and considers the interaction of pO_2, temperature and extrinsic dopants by the examination of the thermodynamic equilibrium. Thereby, the defect chemistry model is able to determine the chemical reactions describing the formation and annihilation of charged lattice defects, namely oxygen vacancies ($V^{\bullet\bullet}_{O}$), strontium vacancies (V''_{Sr}) and titanium vacancies (V''''_{Ti}). In this thesis only a brief description of the impact of intrinsic defects on the charge carrier concentration, and thus the conductivity, will be given. Further information on the general defect chemistry model of TTMOs and a detailed description of the defect chemistry of n-$SrTiO_3$ can be found in ref. [73] and ref. [37, 38, 74], respectively.

Classical defect chemistry of donor-doped bulk $SrTiO_3$ generally involves the activation of all sublattices at elevated temperatures above 1250 K.[37] Figure 2.3 illustrates the pO_2 dependence of the different defect concentrations in donor-doped $SrTiO_3$ with an active (a) and frozen (b) Schottky equilibrium, which describes the charge neutral removal and incorporation of a complete $SrTiO_3$ unit cell.[74] Here n and p denote the electron and hole concentration, respectively.

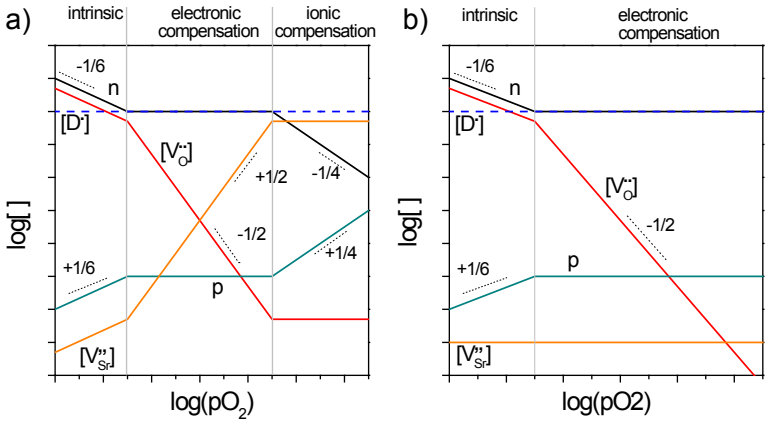

Figure 2.3.: Schematic illustration of the pO_2-dependent defect concentrations in donor-doped $SrTiO_3$ with an active (a) and frozen (b) Schottky equilibrium. Here n and p denote the electron and hole concentration, respectively. The figure was adapted from [74].

In the very low pO_2 regime, the charge carrier concentration is dominated by the concentration of oxygen vacancies $V_O^{\bullet\bullet}$ in the so-called intrinsic regime. Note that this regime is typically absent at sufficiently high donor doping concentrations. With increasing pO_2, the $V_O^{\bullet\bullet}$ concentration decreases constantly. At intermediate pO_2, the charge carrier concentration is given by the donor-dopant concentration ($D^{\bullet}$) in the electronic compensation regime. With increasing pO_2, the strontium vacancy $V_{Sr}^{''}$ concentration increases monotonously. Due to the double negatively charging, a $V_{Sr}^{''}$ concentration half the doping concentration compensate the donor electrons completely. Thus, in this so-called ionic compensation regime the conductivity is dominated by $V_{Sr}^{''}$ concentration. As a consequence, with increasing pO_2 n-$SrTiO_3$ tends to incorporate $V_{Sr}^{''}$ at high temperatures and the electron concentration drops below the donor level.[38] Therefore, depending on thermodynamic treatment at high temperatures, different concentrations of defects are incorporated that compensate electronic charges. Particularly, annealing treatments in oxidizing and reducing atmospheres are expected to yield varying defect concentrations.

At lower temperatures, it might not be possible to equilibrate either of the ionic sublattices (O, Ti, Sr) in the entire sample due to sluggish ionic movement freezing out some of the concentrations in the Schottky equilibrium (fig. 2.3 (b)). Thus, varying local defect concentrations by external stimuli might lead to an effective charge separation at the surface.[23, 38] The lower temperature limit at which the surface defect chemistry of the oxygen and strontium sublattices needs to be considered is already well investigated for acceptor-doped $SrTiO_3$. However, it is

much more complex for donor-doped $SrTiO_3$, due to long equilibration times, secondary phase formation[75] and the stronger influence of cations as electronic charge compensating species.[38] Complementing defect chemical considerations, at lower temperatures, the presence of charged adsorbates might influence n-$SrTiO_3$ surfaces in oxidizing conditions.

Strontium oxide precipitation

Based on the defect chemistry of n-$SrTiO_3$ *Meyer et al.* used dynamical numerical simulations to propose a surface process that models the precipitation of SrO at the n-$SrTiO_3$ surface at temperatures of 1500 K and oxidizing conditions. The resulting secondary phase is formed by oxygen from the gas phase and strontium from the n-$SrTiO_3$ lattice. The precipitation is accompanied by the formation of negatively charged V''_{Sr}.[37, 38] Using Kroger-Vink notations [76], the surface reaction is described by

$$\frac{1}{2}O_2(g) + Sr^x_{Sr} + 2e^- \rightleftharpoons V''_{Sr} + (SrO)_{s.p.} \tag{2.5}$$

where $O_2(g)$ denotes oxygen molecules in the gas phase, Sr^x_{Sr} an uncharged strontium atom at a strontium lattice position, e^- a negatively charged electron, V''_{Sr} a double negatively charged strontium vacancy and SrO a strontium oxide compound in the secondary phase.

The proposed surface process can dominate the surface concentrations of various ionic defects and might differ from what is expected in the Schottky equilibrium from classical defect chemistry. Unbalanced differences in charged defect concentrations between the surface and the bulk might generate a space charge layer at the n-$SrTiO_3$ surface at high temperature and oxidizing conditions. This surface space charge layer can also control the electrical surface properties and hence be of crucial importance for n-$SrTiO_3$ single crystals, thin films and interfaces.

2.5. One-dimensional diffusion in solids

The possible diffusion of charged defects is crucial for achieving thermodynamic equilibrium over the entire system. As explained above, the pO_2-dependent charged defect concentration might dominate the electrical properties of donor doped transition metal oxides at high temperatures, cf. sec. 2.4.[37, 38] Thus an improved understanding of the diffusion of charged defects in a non-equilibrium state is mandatory to describe the pO_2-dependent surface redox process.

Within this thesis, electrochemical conductivity relaxation (ECR) experiments

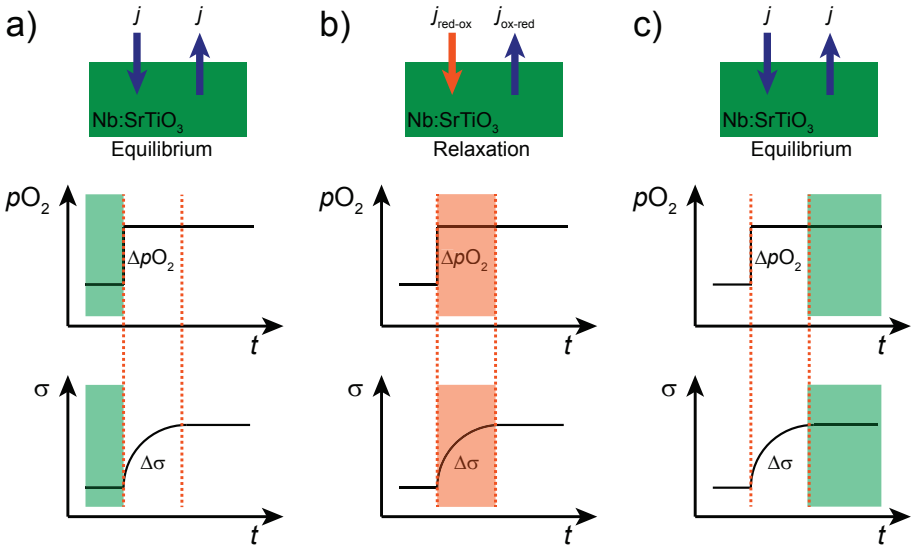

Figure 2.4.: Schematic illustration of the pO_2-dependent conductivity in ECR experiments. Here j describes the particle flux density. The figure was modified from [77].

are utilized to investigate the impact of an abrupt change in pO_2 on the electrical properties of n-$SrTiO_3$ thin films, cf. sec. 3.4. Figure 2.4 illustrates the schematic pO_2-dependent course of the conductivity in a ECR experiment. Here j describes the particle flux density.

At a defined atmosphere, the pO_2 and the corresponding conductivity σ are in an equilibrium state. The particle flux densities j into the sample and out of the sample compensate each other, cf. fig. 2.4 (a). After a sudden change of the pO_2 the system needs to adjust the defect concentrations to the new thermodynamic biases. The adjustment can be seen in the relaxation of the electrical conductivity σ. It depends directly on the surface exchange process and subsequently the diffusion process in the solid. In this regime the particle flux densities into the sample and out of the sample do not compensate each other, cf. fig. 2.4 (b). After the relaxation process the system adapts a new equilibrium state and the particle flux densities compensate each other, cf. fig. 2.4 (c).

The dependence of the particle flux on the local concentration is described by Fick´s first law.[78] Due to the utilization of thin films within this thesis, the dimension of the diffusion process is reduced to one,[79]

$$j = -D\frac{\delta c}{\delta x} \quad , \tag{2.6}$$

where j denotes the particle flux density, D the chemical diffusion coefficient, c the concentration of diffusion species and x the distance. Under the assumption of the diffusion coefficient being independent from the concentration, Fick′s second law for one-dimensional diffusion is derived utilizing the continuity equation,[78, 79]

$$\frac{\delta c}{\delta t} = D\frac{\delta^2 c}{\delta x^2} \quad , \tag{2.7}$$

where t denotes the time. The solution of equation 2.7 depends on the boundary conditions. The flux density in a one-dimensional diffusion process of a sample with the thickness $2a$ (boundaries $x = \pm a$) can be written as[79]

$$j(a) = -D\frac{\delta c}{\delta x}\bigg|_{x=a} = K_{\mathrm{tr}}\left[c(a) - c_\infty\right] \tag{2.8}$$

$$j(-a) = -D\frac{\delta c}{\delta x}\bigg|_{x=-a} = K_{\mathrm{tr}}\left[c(-a) - c_\infty\right] \quad , \tag{2.9}$$

where K_{tr} denotes the surface transfer coefficient and c_∞ the equilibrium concentration of the diffusion species at infinite time after the change in $p\mathrm{O}_2$. Note that the change of the $p\mathrm{O}_2$ in the experimental reactor is taken as instantaneous. It is thus described by a Heavisde step function.

The time-dependent concentration profile $c_{\mathrm{step}}(x,t)$ is determined by solving equation 2.7 using the Fourier method to [77, 79, 80]

$$\bar{c}_{\mathrm{step}}(x,t) = \frac{c_{\mathrm{step}}(x,t) - c_0}{c_\infty - c_0} = 1 - \sum_{n=1}^{\infty} \frac{2L_\alpha \cos(\alpha_n x/a)}{(\alpha_n^2 + L_\alpha^2 + L_\alpha)\cos(\alpha_n)} \exp\left(-\frac{t}{\tau_n}\right) \quad , \tag{2.10}$$

where $\bar{c}$ denotes a dimensionless quantity, and L_α and α_n calculation parameters. The time constants τ_n are described by [79]

$$\tau_n = \frac{a^2}{D \cdot \alpha_n^2} \quad . \tag{2.11}$$

The calculation parameters L_α and α_n are determined by the surface exchange coefficient K_{tr} and the diffusion coefficient D to [79]

$$L_\alpha = \frac{aK_{\mathrm{tr}}}{D} = \alpha_n \tan(\alpha_n) \quad . \tag{2.12}$$

Equation 2.12, and thus α_n, need to be solved numerically.[81]

Equation 2.10 describes the time-dependent evolution of the concentration. Hence, its integration results in a relative mass change during the relaxation process. The mass, however, depends linearly on the particle number and thus the

conductivity.[77, 82]

$$\overline{\mathrm{M}}(t) = \overline{\mathrm{N}}(t) = \overline{\sigma}(t) = \frac{\sigma(t) - \sigma_0}{\sigma_\infty - \sigma_0} \quad , \tag{2.13}$$

where $\overline{\mathrm{M}}(t)$ denotes the normalized time-dependent mass change, $\overline{\mathrm{N}}(t)$ the normalized time-dependent particle change, σ_0 the initial equilibrium conductivity and σ_∞ the final equilibrium conductivity after the $p\mathrm{O}_2$ jump. Consequently, the normalized conductivity $\overline{\sigma}$ is determined by the integration of the concentration over the sample volume [79]

$$\overline{\sigma}(t) = 1 - \sum_{n=1}^{\infty} \frac{2L_\alpha^2}{\alpha_n^2(\alpha_n^2 + L_\alpha^2 + L_\alpha)} \exp\left(-\frac{t}{\tau_n}\right) \tag{2.14}$$

Using this equation it is possible to determine the defining parameters of a diffusion process K_{tr}, D and L_α if the process is not limited by one of the parameters. From equation 2.12 it is possible to determine a characteristic length L_c to [79]

$$L_\mathrm{c} = \frac{D}{K_{\mathrm{tr}}} \quad . \tag{2.15}$$

L_c defines the ratio of the impact of the diffusion and the surface exchange process. For values of $L_\mathrm{c} \ll$ a the diffusion process is limited by surface exchange reaction while for values of $L_\mathrm{c} \gg$ a it is limited by the diffusion in the solid. Thus, in order to be able to determine both the surface exchange coefficient K_{tr} and the diffusion coefficient D the ratio of both coefficients needs to be in the range of the film thickness.[77, 79]

3. Methods

In this thesis, donor-doped $SrTiO_3$ samples are used to investigate the impact of varying thermodynamic biases on the electrical surface and interface properties. As sample preparation, Nb:$SrTiO_3$ single crystals were annealed in different oxidizing and reducing atmospheres and subsequently used to fabricate heterostructures with platinum top electrodes. The heterostructures were analyzed by electrical characterization, namely impedance spectroscopy and $I(V)$-curves. In addition, Nb:$SrTiO_3$ thin films were grown by pulsed laser deposition (PLD) onto undoped $SrTiO_3$ substrates. The thin films allowed to expand the electrical characterization to *in-plane* electrical properties directly at the surface by Hall measurements and electrochemical conductivity relaxation (ECR) experiments. For further *ex-situ* growth characterization atomic force microscopy (AFM) and X-ray diffraction experiments were used. For *in-situ* characterization of the electrical and chemical surface properties, conductive atomic force microscopy (C-AFM) and ambient pressure X-ray photoelectron spectroscopy (AP-XPS) both lab- and synchrotron based were performed. In the following chapter, the furnace setups of the annealing pretreatments as well as the experimental measurement techniques utilized within this thesis are discussed in detail.

3.1. Annealing treatment

Based on the defect chemistry of donor-doped $SrTiO_3$, annealing treatments in highly oxidizing and reducing atmospheres are expected to result in different electrical surface properties by varying charged defect concentrations which compensate the charge carriers induced by the donor-doping concentration, cf. sec. 2.4. To investigate the impact of varying pretreatments, Nb:$SrTiO_3$ single crystals were annealed at high temperature in oxidizing and reducing gas atmospheres. The annealing procedures were performed in an aluminum oxide furnace that could reach temperatures as high as 1673 K. A schematic illustration of the measurement setup (a) and a picture of the sample basket (b) are illustrated in figure 3.1.

The sample is placed in a basket made from a platinum net and located in the middle of the furnace at the height of the temperature control sensor. The atmosphere insight the furnace can be switched between ambient atmosphere (open furnace, oxidizing conditions) and a 4% hydrogen in argon premix (gas flow, reducing conditions) gas which is attached to a gas inlet at the top. The top and

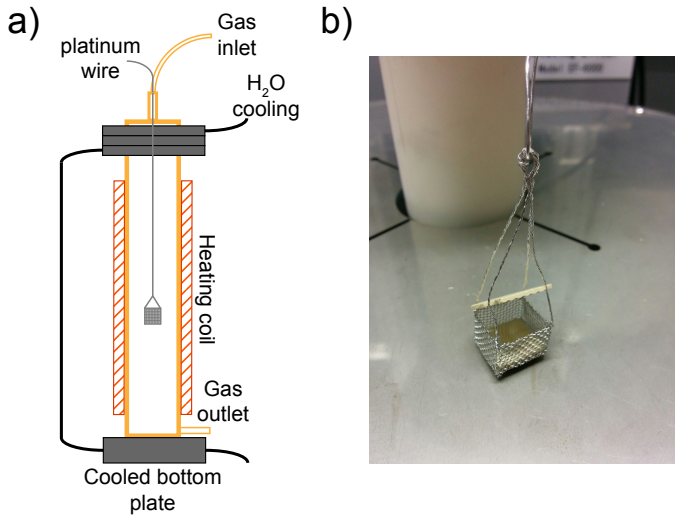

Figure 3.1.: Schematic illustration of the experimental annealing furnace setup (a) and a depiction of the platinum sample basket (b). The platinum basket was handmade by Jochen Friedrich, PGI-7, Forschungszentrum Jülich.

bottom plates of the furnace are water-cooled. The cooling is necessary to realize a quenching of the sample by lowering the basket down to the bottom plate after the annealing procedure.

Within this thesis, temperatures as high as 1423 K were utilized. Higher temperatures resulted in a malfunction of the sample basket and a loss of the sample at the bottom of the furnace. This effect was present regardless of the applied gas atmosphere.

3.2. Deposition techniques

Within this thesis, different deposition techniques are utilized to fabricate both donor-doped $SrTiO_3$ thin films with single crystalline quality as well as metallic top contacts for electrical characterization experiments. In the following the different deposition techniques will be introduced.

Pulsed laser deposition

Pulsed Laser Deposition (PLD) is an ultra high vacuum deposition technique widely used for ternary oxide thin films.[83, 84] Figure 3.2 schematically shows the construction of a PLD chamber equipped with a Reflection High-Energy Electron Diffraction (RHEED) system to monitor the layer growth.

A pulsed laser spot is focused onto a target material which is supposed to be deposited. The high energy of the laser beam evaporates the target material, creating a plasma plume. The properties of the generated plasma plume are of crucial importance for the stoichiometric growth process and are discussed in detail in refs. [86–89]. In a defined distance to the target, a substrate is placed facing towards the generated plume. The target-to-substrate distance significantly affects the ionic ratios of the grown thin film due to atmosphere-dependent propagation of the different atomic species in the plume. This so-called time-of-flight effect is especially important in high oxygen partial pressures in which n-$SrTiO_3$ thin films are grown within this thesis. Further information on this effect are given in refs. [88, 89]. The plume propagates towards the heated substrate resulting in the deposition of the evaporated ionic species. Due to the high temperature of the substrate the deposited material is able to diffuse on the substrate surface. The ionic movement

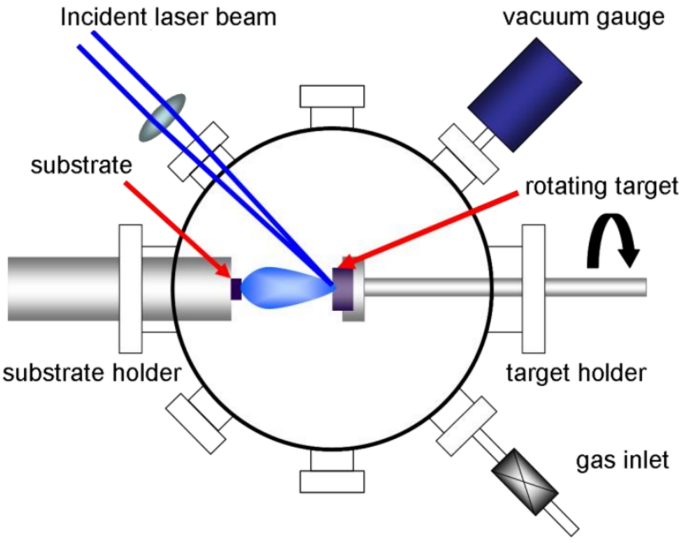

Figure 3.2.: Schematic illustration of the construction of a PLD chamber equipped with a RHEED system, modified from ref. [85].

enables the assemble of the intended atomic structure and is thus crucially required for the growth of epitaxial thin films.

Another important parameter in a PLD process is the laser fluence. It can impact the ionic ratio in the generated plasma plume due to an incongruent ablation of the target material. Moreover, the laser fluence affects the amount of ablated material in a way that with increasing laser fluence the ablation rate increases.[89] Thus, it is of crucial importance for the growth rate of the thin film.

In order to achieve high quality stoichiometric growth of Nb-doped $SrTiO_3$ thin films, all parameters were optimized carefully as described in detail in refs. [90–93], cf. sec 4.2. Further information on the mode of action and the field of operation of PLD is provided in refs. [83, 94].

Reflection high energy electron diffraction

In order to control the epitaxial layer-by-layer growth *in-situ* reflection high electron energy diffraction (RHEED) is used. A schematic illustration of the mode of operation of a RHEED setup is shown in figure 3.3.

A beam of high energy electrons is focused on the substrate surface with a very small angle of incidence. The electrons are diffracted at the surface. Due to the small incidence angle and the short wavelength of the electrons the interaction is restricted to the very surface. The diffracted electrons are monitored on a fluorescence screen. Depending on the coverage of the grown monolayer the measured RHEED intensity of the diffracted electrons oscillates and thereby demonstrates the layer-by-layer growth mode. Starting with a flat surface without any growth nuclei, the observed RHEED intensity is at a maximum. With ongoing monolayer growth, the intensity decreases due to the increased scattering of the electrons at the ionic species attached to the surface reaching a minimum at a surface coverage of $\sim$50 %. At higher monolayer coverages the intensity increases again up to a maximum when a full monolayer is grown. This evolution is due to a reduction of scatter centers resulting from an increasingly unified monolayer. Due to this oscillations of the measured intensity it is possible to monitor the thin film growth directly and determine the number of monolayers deposited precisely. By examining the growth rate it is possible to control the grown film thickness with high accuracy. Consequently, RHEED provides the opportunity to investigate the thin film growth *in-situ*.

For the monitoring of the thin film growth within this thesis, a *ksa 400 RHEED system* (*k-space*) is utilized. The kinetic energy of the electrons is 30 keV corresponding to a wavelength of 7 pm. Further information on the mode of action and the field of operation of RHEED is provided in ref. [95].

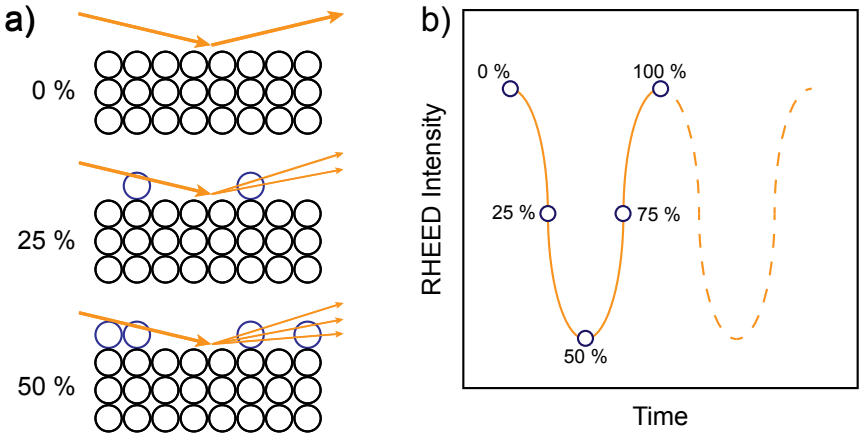

Figure 3.3.: Schematic illustration of the mode of operation of of a Reflection High Energy Electron Diffraction setup, reproduced from ref. [74]. With increasing surface covering of the growing thin film, the RHEED intensity at first decreases due to higher scattering of the electrons, reaching a minimum at ∼50 %. At thin film coverages above 50 % the RHEED intensity increases again reaching its maximum when a full monolayer is grown. This evolution results in characteristic RHEED intensity oscillations.

Electron-beam evaporation

One widely used ultra high vacuum deposition technique for metallic top electrodes is electron-beam evaporation. Hereby, a target material is heated homogeneously up to its evaporation temperature by an electron beam pattern. A substrate material is placed in front of the target material at a defined distance. Upon reaching the evaporation temperature, atoms of the target material are released into the UHV deposition setup and move towards the substrate. When reaching the unheated substrate surface the released atoms condense and form a thin layer. An advantage of the electron beam evaporation technique is the low kinetic energy of the atoms reaching the substrate surface which results in an unchanged surface underneath the metal electrode.

In order to control the growth rate of the thin film typically a quartz crystal

oscillator is used. The quartz crystal is placed in the deposition chamber next to the substrate, so that an identical film thickness will form on its surface. The grown thin film thickness is determined from a shift of the oscillation frequency of the quartz crystal. In order to precisely monitor the thin film thickness a specific calibration is required for each target material.

Within this thesis, a *Carrera* system (*FerroTec*) was used to deposit ultra thin metallic top electrodes (platinum, gold and titanium) onto Nb:$SrTiO_3$ single crystals and thin films. In order to structure the metallic top electrodes a shadow mask was placed between the evaporated target material and the substrate. Further information on the mode of operation of an electron-beam evaporation setup can be found in ref. [96].

DC magnetron sputtering

Another frequently used deposition technique for metal top electrodes is magnetron sputtering. A schematic illustration of a typical magnetron sputtering setup is illustrated in figure 3.4.

A metallic target material as well as a substrate are placed in an ultra high vacuum chamber facing each other in a specific distance. To start the deposition process an inert gas, typically argon, is pumped into the UHV chamber while a

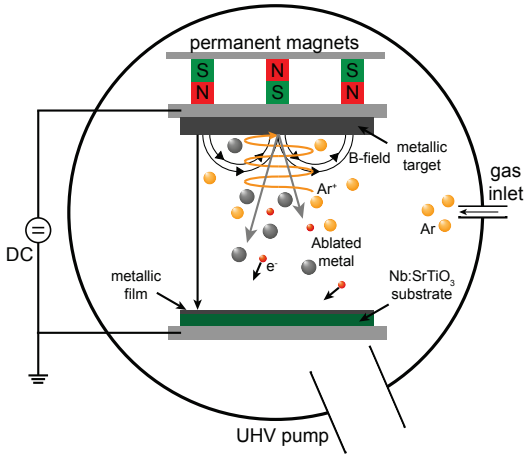

Figure 3.4.: Schematic illustration of the mode of operation of a magnetron sputtering process, reproduced from ref. [77].

high voltage is applied between the target and the substrate. Due to the electric field a plasma is ignited. The ionized argon particles are accelerated towards the target. Permanent magnets placed behind the target confine the charged argon ions to the target surface and thereby increase the sputter rate. Due to their high kinetic energy the argon ions remove atoms from the metallic target which subsequently migrate towards the substrate. When reaching the substrate the metal atoms adsorb on the surface and grow metallic layers.

One drawback of the growth of metallic top contacts by magnetron sputtering is the high kinetic energy of the incoming metal atoms. It is transferred completely to the sample surface which might cause changes at the substrate surface. Further information on the mode of operation of magnetron sputtering is found in refs. [97, 98].

3.3. Characterization of crystal structure and topography

In the following, the experimental methods utilized to examine the structure and topography of the grown Nb:$SrTiO_3$ thin films are discussed.

Atomic force microscopy

In order to image the surface topography of both single crystals and thin films within this thesis, Atomic Force Microscopy (AFM) was used. A typical measurement setup of an AFM consists of a cantilever with a tip radius in the nanometer regime, a laser beam focused onto the backside of the cantilever and a four quadrant photo diode to measure the laser beam$'$s reflection. Two main modes of operation of an AFM setup are distinguished, the contact and the non-contact mode.

In the contact mode, the cantilever is brought into direct contact with the sample surface. During the surface scan the cantilever bends due to the surface morphology varying the reflection angle of the focused laser beam and thus slightly shifting the reflected laser point on the four quadrant photo diode. The measurement electronics reset the initial bending of the cantilever. Based on the movement in x, y and z-direction necessary to rebalance the cantilever bending, an image of the sample surface is obtained. Utilizing a conductive tip, the contact mode also allows to measure a current through the measured surface by applying a voltage to the cantilever and grounding the sample. This additional measurement mode gives insight on the surface contact resistance (C-AFM). As a disadvantage of the contact mode, both the cantilever tip and the surface might be damaged or can pick up contamination during the scanning process.

In the non-contact mode, the cantilever tip is brought close to the sample surface

while oscillating close to its resonance frequency. While scanning over the sample surface, the topographical changes of the surface vary the cantilevers' resonance frequency. A topographical image is generated by the measurement electronics adjusting the cantilever position to restore the initial amplitude. Typically, the resolution of an AFM in non-contact mode is higher than in contact mode. As an additional advantage, the non-contact mode avoids possible damaging of the sample and the cantilever tip. A further description of both modes of operation is given in ref. [99].

Within this thesis, an *Omicron VT-SPM system* (*Omicron Nano Technology GmbH*) in contact mode was utilized to measure the topography and the current through the surface. In addition, the topography of annealed single crystals and grown thin films was characterized using a *SIS Pico Station* (*UltraObjective*) and a *Cypher Atomic Force Microscope* (*Asylum Research*).

X-ray diffraction

In order to investigate the crystal structure of grown Nb:$SrTiO_3$ thin films within this thesis, X-ray diffraction performed on a *PW3020 diffractometer* (*Philips*) is utilized. This method allows for the non-destructive determination of the lattice constant of the grown thin films, their thickness and their crystallinity by utilizing the elastic scattering of X-rays on the systematic crystal structure. The incoming X-ray photons are scattered at different atomic planes in increasing probing depths and show constructive interference if the periodicity of the investigated crystal structure follows the Bragg equation,[100]

$$n\lambda = 2d_{\mathrm{hkl}}\sin\Theta \quad , \tag{3.1}$$

where n denotes the order of diffraction, λ the X-ray wavelength, d_{hkl} the distance between the lattice planes characterized by the Miller indices hkl,[101] and Θ the X-ray incident angle under the assumption of a symmetric Bragg-Brentano geometry. The constructive interference results in clear intensity peaks at specific doubled incident angles 2Θ. Utilizing the angular position of the peak allows for the calculation of the distance between the atomic layers and hence of the vertical lattice constant. Further information on the mode of operation of a X-ray diffractometer is given in ref. [102].

3.4. Electrical characterization

In the following, the electrical characterization methods utilized within this thesis are explained in detail.

Hall measurements

In order to investigate the sheet resistance (R_s), the sheet carrier concentration (n_s) and charge carrier mobility (μ_n) of grown Nb:$SrTiO_3$ thin films room temperature and high temperature Hall measurements in van der Pauw configuration were performed using a *Lake Shore 8400 Series* (*Lake Shore Cryotronics Inc.*). The samples were attached to a non-conducting sample holder by scotch tape and bonded at four positions using aluminum wires generating four electrical contacts (1-4).

The sheet resistance R_s is derived directly from measurements of the ratio of the voltage between the electrical contacts 1 and 2 as $V_{1,2}$ (2,3; $V_{2,3}$) and the current between the electrical contacts 3 and 4 as $I_{3,4}$ (1,4; $I_{1,4}$),

$$R_{1,2;3,4} = \frac{V_{1,2}}{I_{3,4}} \; ; \; R_{2,3;1,4} = \frac{V_{2,3}}{I_{1,4}} \quad . \tag{3.2}$$

R_s is then calculated as

$$R_s = \frac{1}{\sigma t} = \frac{\pi}{ln(2)} \cdot \frac{R_{1,2;3,4} + R_{2,3;1,4}}{2} \cdot f\left(\frac{R_{1,2;3,4}}{R_{2,3;1,4}}\right) \quad , \tag{3.3}$$

where σ denotes the conductivity, t the thickness of the sample and f a correction factor defined numerically by the ratio of the two obtained resistances $R_{1,2;3,4}$ and $R_{2,3;1,4}$.[103] Utilizing the van der Pauw geometry the size and geometry of the sample is excluded as a crucial impact factor.

n_s is determined by applying a magnetic field B perpendicular to the conducting sample and measuring the so-called Hall coefficient

$$R_H = \frac{1}{en_s} = \frac{\Delta R_{1,3;2,4}}{B} \quad , \tag{3.4}$$

where e denotes the elementary charge and $\Delta R_{1,3;2,4}$ is determined by,

$$\Delta R_{1,3;2,4} = \frac{V_{1,3}(-B) - V_{1,3}(+B)}{2I_{2,4}} \quad . \tag{3.5}$$

By combining the sheet resistance and the Hall coefficient the charge carrier mobility μ_n is determined to

$$\mu_n = \frac{R_H}{R_s} \quad . \tag{3.6}$$

A more detailed description of room temperature Hall measurements is given in ref. [104]. In addition to room temperature measurements the setup is also capable of measuring in high temperatures up to 1273 K. Further information on the specific lake shore setup is found in ref. [105].

Additional low temperature Hall measurements were performed to examine the

temperature-dependent electrical properties. All measurements were performed in a Hall bar geometry by Felix Gunkel (IWE 2, RWTH Aachen; PGI-7, FZ Jülich) on a *Quantum design PPMS* cryostat. Further information of the temperature-dependent electrical properties are given in ref. [106].

Impedance spectroscopy

In order to investigate the contact resistance (R_{sc}) and capacitance (C_{sc}) of manufactured Pt/Nb:$SrTiO_3$ heterostructures, impedance spectroscopy was utilized. The impedance (Z) is the resistance of a system to an applied alternating current. In dependence of the frequency it is determined to

$$Z(\omega) = Z^{'} + iZ^{''} \quad , \tag{3.7}$$

where $Z(\omega)$ denotes the frequency-dependent impedance, $Z^{'}$ the real part or ohmic resistance and $Z^{''}$ the imaginary part or so-called reactance. The results of impedance spectroscopy are typically illustrated in a Nyquist plot where the imaginary part $Z^{''}$ is plotted over the real part $Z^{'}$, cf. fig. 3.5. A resulting semicircle is attributed to an RC-element as part of the measured system. A series resistance R_{se} that

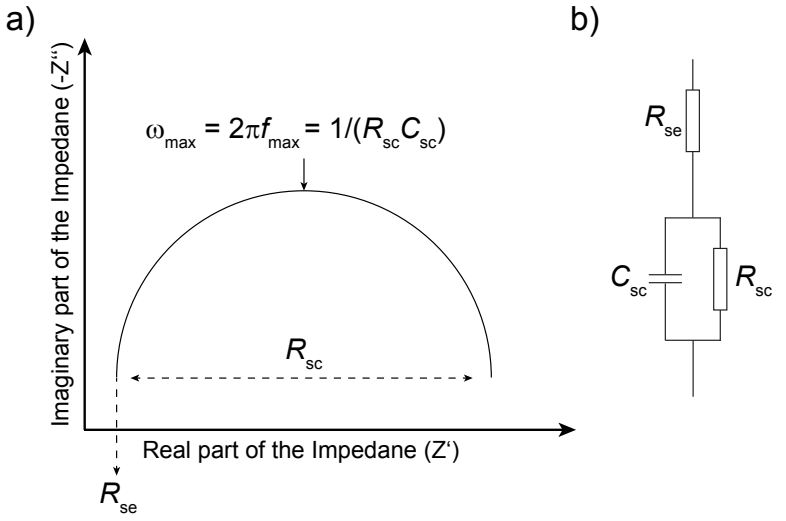

Figure 3.5.: Schematic illustration of a typical impedance spectroscopy result (a) and the corresponding equivalent circuit (b).

corresponds to the measurement setup shifts the entire semi circle towards higher resistances. R_{sc} is derived from the diameter of the semi circle. C_{sc} is determined from the maximum of the semicircle. Here, the frequency of maximum reactance ω is calculated to

$$\omega_{max} = \frac{1}{R_{sc}C_{sc}} \quad . \tag{3.8}$$

Within this thesis a *Solartron Si 1260, Solartron 1296*, with frequencies between 1 Hz $< f <$ 1 MHz was employed. The results were analyzed using *Zview 2* (*Ametek scientifc instruments*). A single semi-circle was modeled by a parallel *RC*-element associated to the Schottky-type interface contact between Pt and Nb:$SrTiO_3$ and a series resistance (R_{se}) associated to the lead resistance and Nb:$SrTiO_3$ bulk contributions, cf. fig 3.5 (b)). Further information on impedance spectroscopy can be found in refs. [107, 108]

$I(V)$-characteristics

One widely used technique to investigate the electrical properties and especially the rectifying behavior of thin films and heterostructures is the measurement of characteristic $I(V)$-curves. Within this thesis, using a *Keithley 2611A Source Meter* $I(V)$-characteristics of Pt/Nb:$SrTiO_3$ heterostructures were measured and tungsten probes. The Nb:$SrTiO_3$ single crystals acted as bottom electrode and was grounded. The voltage was sweeped between +1 V and -1 V in order to neglect resistive switching effects. The sweep rate was 1V/s. Further information are given in ref. [109].

Electrochemical conductivity relaxation

In order to investigate the impact of varying oxygen partial pressures and temperatures on the electrical properties of donor-doped $SrTiO_3$ thin films *in-situ*, electrochemical conductivity relaxation measurements (ECR) were utilized within this thesis. These measurements can also allow to draw conclusions on a redox process present at the investigated surface. Figure 3.6 shows a schematic illustration of the utilized measurement setup.[77]

The sample is placed inside an aluminum tube that is heated by a surrounding furnace which can reach temperatures up to 1473 K. The sample temperature is determined by a thermocouple located in the direct vicinity of the sample. The electrical conductivity measurement is performed in a four contact geometry setup by applying a current to the outer electrodes and measuring the voltage occurring between the inner electrodes. The gas atmosphere inside the small measurement

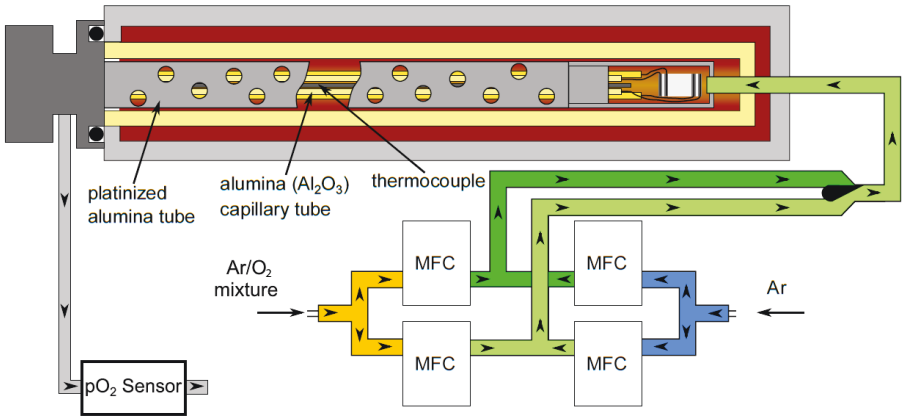

Figure 3.6.: Schematic illustration of the electrochemical conductivity relaxation measurement setup, modified from ref. [77].

reactor is controlled by an adjustable gas flow. The gas flow is regulated by four mass flow controllers (MFC) that are attached to an 0.1 % oxygen in argon premix and pure argon gas, respectively. The MFC are organized in two groups each combining both gases. Both groups are connected to a four way valve. Two different gas mixtures with specific pO_2 can be premixed and hold in the pipes between the MFCs and the four way valve. By switching the valve, the gas atmosphere in the measurement reactor is controlled.

The pO_2 in the reactor is determined by the gas inserted and veryfied by a λ-sensor located in the exhaust line.[110] It is calculated to

$$pO_2(T_{\lambda\text{sensor}}) = 0.2064 \cdot \exp\left(-46.42 \frac{V\,[\text{mV}]}{T_{\lambda\text{sensor}}\,[\text{K}]}\right)\,[\text{bar}] \quad , \tag{3.9}$$

where V denotes the measured Nernst voltage, $T_{\lambda\text{sensor}}$ the temperature of the λ-sensor. Typically the λ-sensor works at a fixed temperature of 1073 K.

In order to examine a surface redox process by ECR experiments, an instantaneous jump between two gas atmospheres needs to be realized. By applying an appropriate model, the relaxation of the electrical conductivity can be attributed directly to a surface exchange reaction, bulk diffusion or a combination of both. Figure 3.7 shows a schematic illustration of the response of the electrical conductivity on a spontaneous change in the pO_2.

The electrical conductivity needs to be coupled to the pO_2 in the measurement reactor. Thus, after an instantaneous jump of the pO_2 the electrical properties of a thin film are measured over time. This change of the conductivity corresponds to a transition from one equilibrium state to another one.

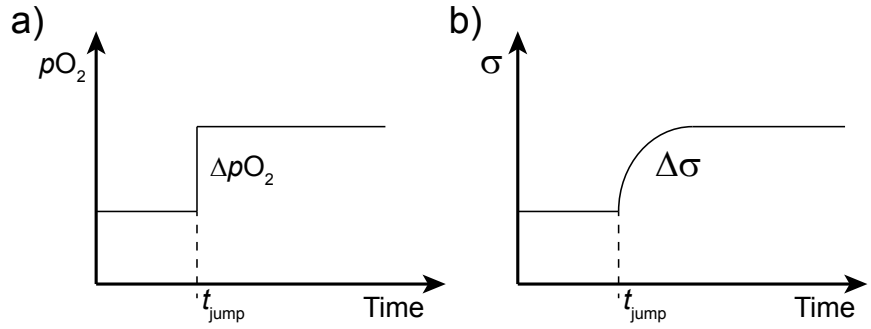

Figure 3.7.: Schematic illustration of the relaxation process of the electrical conductivity after a spontaneous jump of the surrounding pO_2. This figure was reproduced from [77].

3.5. X-ray photoelectron spectroscopy

In order to examine the chemical properties and the electronic structure of n-$SrTiO_3$ single crystals and thin films, within this thesis X-ray photoelectron spectroscopy (XPS) is utilized.[111, 112] A schematic illustration of the mode of operation is shown in figure 3.8.

A sample is irradiated by an X-ray beam with a specfic photon energy. Based on the photoelectric effect,[113, 114] the X-ray photons are absorbed by electrons which are emitted from the sample if the energy of the incoming photons is higher than their binding energy. The released electrons leave the sample surface if their kinetic energy is high enough not to be compensated by inelastic scattering at the sample´s lattice electrons. The number of scattering events increases with increasing probing depth. Thus, the contribution of emitted electrons to the measurement signal decreases exponentially with increasing sample depth yielding a surface sensitive measurement.

The electrons leaving the sample surface are attracted by an analyzer which measures their kinetic energy (E_{kin}). The binding energy of the electrons is subsequently calculated to

$$E_{\mathrm{B}} = h\nu - E_{\mathrm{kin}} - \Phi \quad , \tag{3.10}$$

where E_{B} denotes the binding energy, $h\nu$ the energy of the incoming X-ray photons, E_{kin} the kinetic energy of emitted electrons and Φ the work function of the sample.

The binding energy is characteristic for a specific core level of a certain material. The absolute binding energy of a core level also depends on the specific chemical environment and especially the bonding states.[116] Thus, XPS is a tool that can resolve the chemical composition.

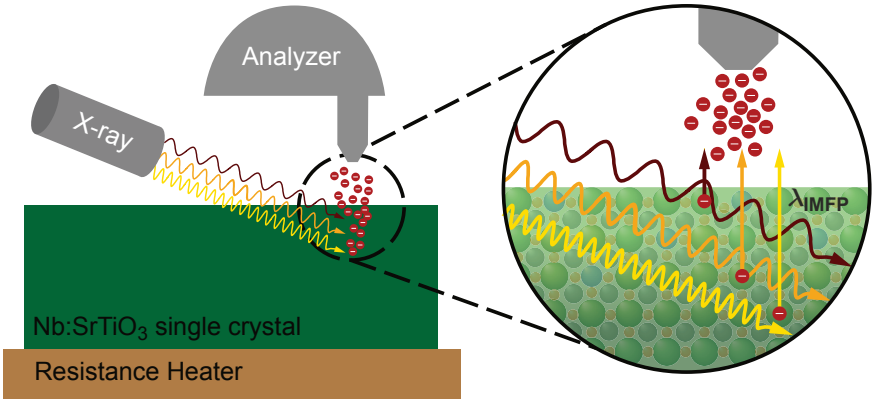

Figure 3.8.: Schematic illustration of the mode of operation of an X-ray photoelectron spectroscopy setup. By utilizing different incident photon energies the kinetic energy of excited electrons can be tuned, resulting in specific inelastic mean-free paths for a given core level. In this way, depth-resolved measurements can be obtained. This figure is partly published in ref. [115].

Moreover, XPS is a surface sensitive method due to the scattering of the released electrons at the lattice electrons. It is described by the inelastic mean free path (IMFP) of the released electrons. The IMFP is calculated from the kinetic energy of the incoming X-ray photons in combination with the properties of the sample. It is defined as the distance over which the number of non-scattered electrons is reduced to 1/e.[117] In XPS experiments, the IMFP and the information depth is typically in the nanometer regime.

The depth resolution can be tuned by varying the kinetic energy of the incoming photons. Typically, lab-based XPS experimental setups have a monochromatic X-ray source of either Aluminum K_α or Magnesium K_α with kinetic energies of $h\nu = 1486.6$ eV and $h\nu = 1253.6$ eV, respectively. In order to realize tunable depth profiling, XPS experiments are performed at a synchrotron with photon energies ranging from 207 eV to 1080 eV.

One major disadvantage of the XPS experimental technique is its requirement of highly conductive samples. In non-conductive samples, the release of electrons from the surface can not be compensated by electrons deep in the sample. As a consequence an increasing positive surface charge can be generated on insulating samples. This positive surface charge affects the measurements by effectively reducing the kinetic energy of the emitted electrons, thus rigidly shifting the entire XPS spectra towards higher binding energies.[118]

In contrast, a rigid shift of the entire XPS spectra can also be utilized to examine the electrical properties of an investigated sample. Figure 3.9 shows a superposition of Ti3s/Ti3p XPS spectra of $SrTiO_3$ single crystals with n-type and p-type (scan-

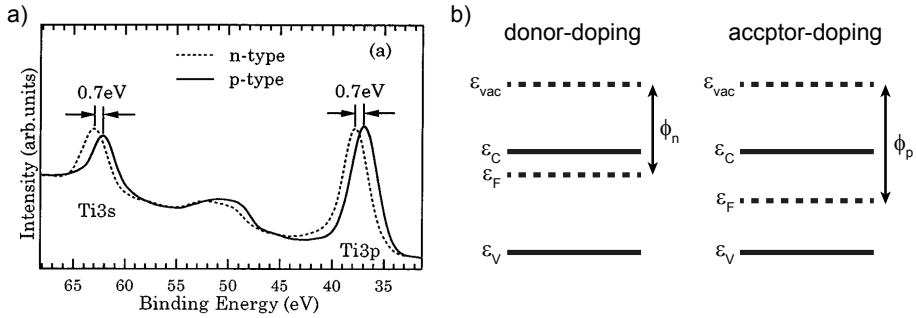

Figure 3.9.: XPS spectra of $SrTiO_3$ single crystals with n-type and p-type doping (a) reproduced from ref. [119], and a schematic illustration of the resulting Fermi energy shift (b).

dium) doping (a),[119] and a schematic illustration of the resulting Fermi energy (ϵ_F) shift (b). The XPS spectra of donor-doped and acceptor-doped $SrTiO_3$ single crystals are shifted rigidly by $\sim$0.7 eV. This is due to the shift of the Fermi energy actively tuning the work function of the samples. For donor-doping, the Fermi energy is placed right underneath the conduction band edge, leading to a low work function. For acceptor-doping the Fermi energy is located deeper in the band gap leading to an increased work function. Thus, in highly conducting samples a rigid shift of the entire XPS spectra points towards a shift of the Fermi energy and hence allows to draw conclusions on the electrical surface properties.

Ambient pressure XPS

Due to the need of electrons to travel towards the analyzer, XPS experiments are typically conducted in ultra high vacuum conditions. Thus, so far the impact of gas phases such as oxygen on the chemical and electrical surface properties could only be measured by *ex-situ* experiments. New state-of-the-art experimental setups also allow to measure XPS directly *in-situ* in different gas phases by so-called ambient-pressure X-ray photoelectron spectroscopy (AP-XPS).[120] A schematic illustration of an AP-XPS measurement setup is shown in figure 3.10.

In contrast to typical XPS performed in UHV, in AP-XPS the sample is placed in a closed cell that can be flooded with gas. Due to the reduced mean free path of the emitted electrons at high pressures inside the sample space, a differentially pumped detector nozzle is placed close to the sample surface (0.3 mm) and kept at an absolute pressure below 10^{-8} mbar. By this experimental setup, the inelastic mean free path of the emitted electrons is high enough to reach the analyzer even under applied gas phases.

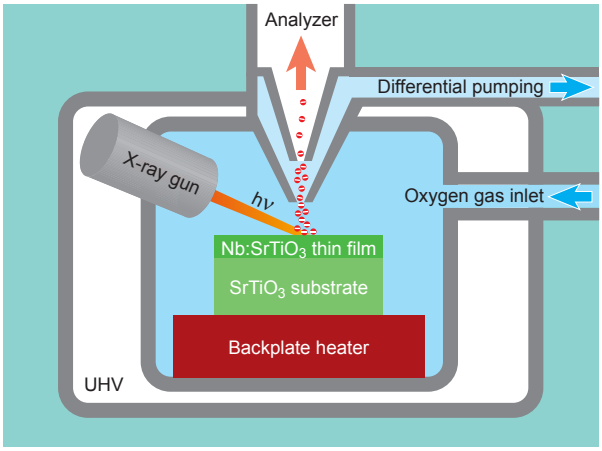

Figure 3.10.: Schematic illustration of the ambient-pressure X-ray photoelectron spectroscopy measurement setup. The figure is published in ref. [121].

Within this thesis both lab-based and synchrotron-based AP-XPS was performed. The lab-based AP-XPS experiments were performed using an Al K_α source and an emission angle of 90° on the $SPECS^{TM}$ of the CERIC-ERIC consortium located at the Department of Surface and Plasma Science, MFF UK, Charles University, in Prague. The synchrotron-based AP-XPS measurements were performed on Beamline 11.0.2 of the Advanced Light Source, Berkeley, USA. All XPS spectra were analyzed using *KolXPD* software.

4. Donor-doped $SrTiO_3$ thin film growth

Within this thesis different kind of samples have been used. Nb:$SrTiO_3$ single crystals were annealed and subsequently processed into heterostructures by depositing platinum top electrodes. Moreover, a new deposition routine has been developed that allowed for the deposition of n-$SrTiO_3$ thin films with single crystalline structure. In this chapter, the single crystal annealing routine as well as the thin film growth and its resulting quality will be discussed in detail.

4.1. Annealing procedures

In order to investigate the electrical surface contact properties Pt/Nb:$SrTiO_3$ heterostructures of different sizes were produced from single crystalline $n$$SrTiO_3$. The as-received 0.5 wt.% Nb:$SrTiO_3$ single crystals produced by *CrysTec GmbH, Berlin, Germany* regularly exhibit a rough surface structure and contamination leftover from the polishing procedure. In order to increase the surface quality and the comparability of substrates for thin film growth, all Nb:$SrTiO_3$ single crystals are cleaned by acetone and isopropanol and subsequently annealed for one hour at 1225 K in ambient atmosphere, cf. fig. 4.1 (a).

Afterwards the Nb:$SrTiO_3$ single crystals were annealed for 24 hours at 1325 K in reducing conditions (4 % H_2/Ar) or oxidizing conditions (ambient atmosphere). Representative topography images of the Nb:$SrTiO_3$ single crystal surfaces after the longtime reducing and oxidizing annealing procedures are shown in figure 4.1 (b) and (c), respectively. Note that the topography image after the oxidizing annealing procedure exhibit typical error resulting from a twin tip cantilever. Nevertheless, the step terrace structure is still distinguishable.

The Nb:$SrTiO_3$ surfaces demonstrate equal step terrace structures after both annealing procedures. Thus, an impact of microscopical contamination or possible microscopical outgrowth of secondary phases on the surface properties will be neglected. Afterwards platinum top electrodes were deposited by magnetron sputtering and electron-beam evaporation, cf. sec. 3.2. The sizes of the top electrodes were adjusted by a shadow mask process and ranged from 10 μm$\times$10 μm up to 200 μm$\times$200 μm. The manufactured Pt/Nb:$SrTiO_3$ heterostructures were investigated by impedance spectroscopy and $I(V)$-curves, cf. sec. 5.1.

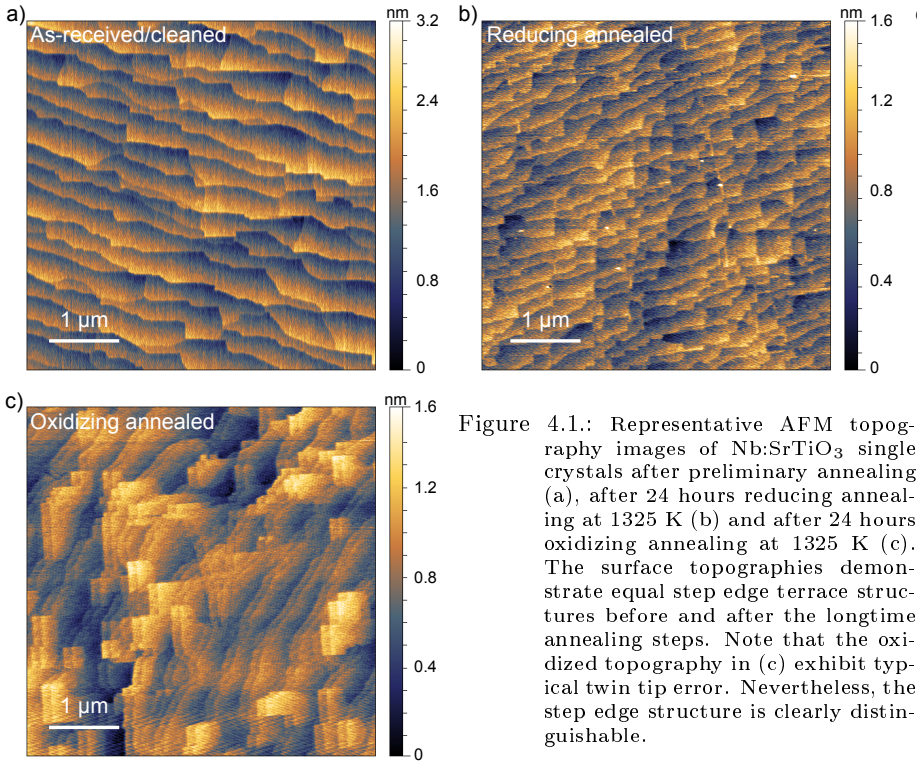

Figure 4.1.: Representative AFM topography images of Nb:$SrTiO_3$ single crystals after preliminary annealing (a), after 24 hours reducing annealing at 1325 K (b) and after 24 hours oxidizing annealing at 1325 K (c). The surface topographies demonstrate equal step edge terrace structures before and after the longtime annealing steps. Note that the oxidized topography in (c) exhibit typical twin tip error. Nevertheless, the step edge structure is clearly distinguishable.

4.2. Donor-doped $SrTiO_3$ thin films

In chapter 8, the electrical *in-plane* properties of *n*-$SrTiO_3$ surfaces will be characterized *in-situ* at different temperatures and oxygen partial pressures. Donor-doped $SrTiO_3$ single crystals, however, are not suitable for such investigations due to the highly conductive bulk covering the changes of the electrical properties arising directly at the surface, cf. fig. 4.2 (a). In order to overcome this limitation thin *n*-$SrTiO_3$ films with single crystalline quality grown on undoped $SrTiO_3$ substrates will be used, cf. fig. 4.2 (b). In the following, the growth process of thin *n*-$SrTiO_3$ thin films will be discussed in detail and their single crystal quality will be examined.

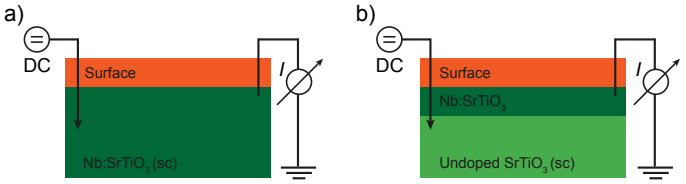

Figure 4.2.: Schematic illustration of the limitation of donor-doped $SrTiO_3$ single crystals in terms of the characterization of the electrical surface properties. The bulk of the highly conductive single crystals cover the changes arising in the near surface region (a). Thin n-$SrTiO_3$ films, however, allow to draw direct conclusion on the electrical surface properties (b).

4.2.1. Thin film growth process

The development of every thin film growth process requires the choice of an appropriate substrate material. In this thesis, undoped $SrTiO_3$ in (001) orientation (*CrysTec GmbH, Berlin, Germany*) were used due to two main reasons. First, a homoepitaxial growth process with almost identical lattice constants of doped and undoped $SrTiO_3$ produces a negligible concentration of defects resulting from lattice relaxation such as dislocations.[89] Second, due to the substantial conductivity difference, the undoped $SrTiO_3$ substrate does not impact the *in-plane* electrical characterization of the thin films significantly, cf. chp. 8.

The as-received substrates regularly show a rough terrace structure with eroded step edges. In order to ensure comparable high surface quality of the Nb:$SrTiO_3$ thin film growth, all single crystalline substrates were annealed for one hour at 1225 K in ambient atmosphere. The temperature was equilibrated in two hours resulting in a heating rate of 475 K/h. After the annealing procedure the substrate were cooled down with a rate of ∼60 K/h. Figure 4.3 shows the representative AFM topographies of an undoped $SrTiO_3$ single crystalline substrates as-received (a) and after the annealing procedure (b).

As mentioned above, the as-received single crystalline substrates exhibit a rough terrace structure with eroded step edges. Moreover, a high contamination level is revealed, that may arise from the supplier′s polishing process. After the annealing procedure at 1225 K, a smooth step terrace structure without contamination is detected. Thus, the annealed undoped $SrTiO_3$ single crystals provide a reproducible surface quality ensuring high comparability of the thin film growth.

After the annealing procedure, the undoped $SrTiO_3$ substrates were attached to stainless steel sample carriers by *Omicron GmbH, Germany* by highly conductive silver paste to ensure both thermal and electrical contact between the carrier and the substrate. To avoid a degassing of solvents from the silver paste in the growth chamber, the sample carriers were annealed for 30 minutes at 425 K at ambient atmosphere.

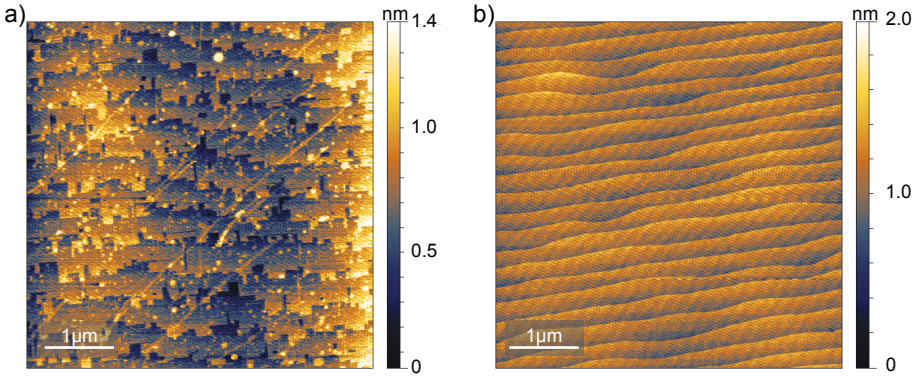

Figure 4.3.: Representative AFM topography of undoped $SrTiO_3$ single crystal substrates as-received (a) and after (b) the initial annealing procedure.

In order to achieve single crystalline quality of the grown Nb-doped $SrTiO_3$ thin films, a stoichiometric growth process is mandatory. All films presented within this thesis were deposited by pulsed laser deposition using a KrF excimer laser (λ =248 nm) with a laser fluence of 1.2 J/cm^2, a repetition rate of 5 Hz, a spot size of 2 mm^2, cf. sec. 3.2. The distance between the substrate and the 0.5 wt.% Nb:$SrTiO_3$ single crystalline target was kept constant at 44 mm. The thin films were grown in an oxygen atmosphere of 0.1 mbar O_2. A substrate temperature of 1073 K ensured a high mobility of the incoming species at the substrate surface. After the growth process, the samples were quenched down to room temperature and no further treatment was performed prior to the different experimental measurements. The described parameters, and especially the laser fluence, were derived from a carefully performed optimization process described in detail in literature.[90–93]

The growth process was monitored *in-situ* by reflection high energy electron diffraction (RHEED), cf. sec. 3.2. Figure 4.4 shows representative RHEED oscillations of a 20 nm thick 0.5 wt.% Nb:$SrTiO_3$ thin film grown quasi-homoepitaxially on an undoped $SrTiO_3$ substrate. The inset on the top right illustrates the RHEED pattern from the surface directly after the growth process. The representative RHEED signal shows distinguishable oscillations throughout the entire growth process. This findings points towards a periodic two-dimensional growth process.[87, 95] This conclusion is further substantiated by the RHEED pattern from the top surface after growth which also illustrates a two-dimensional pattern and hence a smooth Nb:$SrTiO_3$ surface directly after growth, cf. sec. 3.2. In addition to the RHEED monitoring already indicating a high quality two-dimensional growth process, the single crystalline quality of the grown Nb-doped $SrTiO_3$ thin films will be discussed in detail in the following.

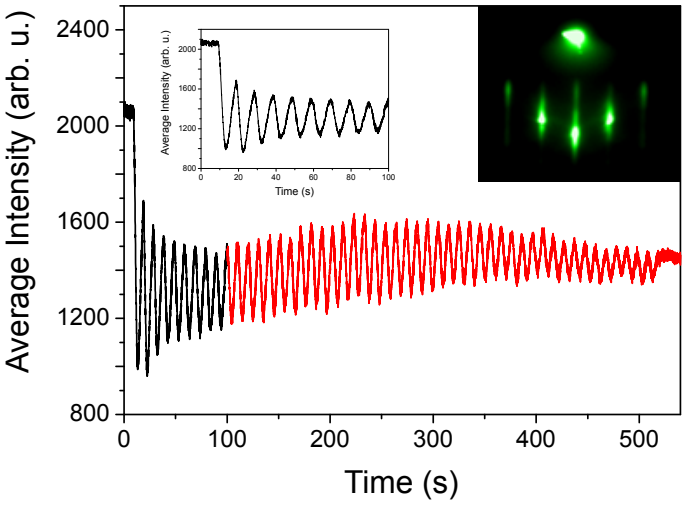

Figure 4.4.: Representative RHEED oscillations of a 20 nm thick 0.5 wt.% Nb:$SrTiO_3$ thin film grown stoichiometrically on an undoped $SrTiO_3$ substrate. The inset shows the first 100 seconds of the growth process. The RHEED pattern from the top surface after growth is shown in the inset on the top right. This figure is published in the supplement of [121].

4.2.2. Single crystalline quality

In order to analyze whether or not the Nb:$SrTiO_3$ thin films grown supposedly stoichiometric on undoped $SrTiO_3$ substrates have single crystalline quality several properties need to be discussed in detail. Firstly, the surface topography and its roughness will be investigated by atomic force microscopy. Secondly, the unit cell structure will be analyzed by X-ray diffraction. Thirdly, the homogeneity of the donor-dopant distribution will be examined by secondary ion mass spectrometry. Fourthly, the electrical properties will be determined by low temperature and room temperature Hall measurements.

Topological characterization

One major parameter that is crucial for the investigation of surface properties of ultra thin films and its comparability to single crystals is the topography. Figure 4.5 shows representative topography images of an undoped $SrTiO_3$ substrate (a) and of a 32 nm Nb:$SrTiO_3$ thin film grown on the undoped substrate (b).
Prior to the growth process the substrate demonstrates the typical step terrace structure with clean step edges and a low roughness. After the growth process, the

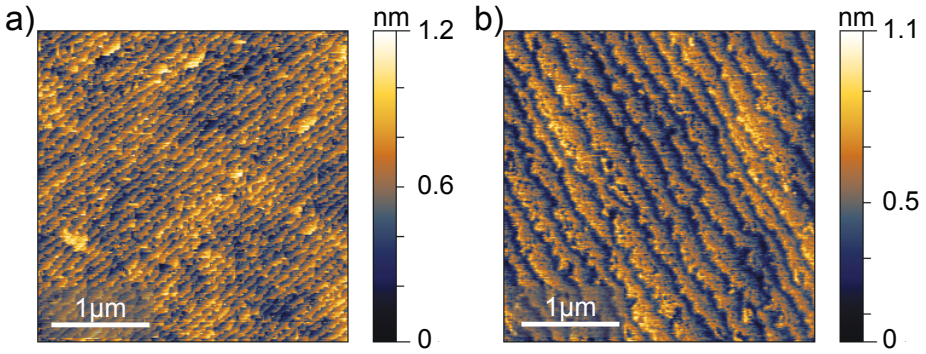

Figure 4.5.: Representative topography images of an annealed $SrTiO_3$ substrate (a) and a 32 nm Nb:$SrTiO_3$ thin film after growth (b).

step terrace structure is still unambiguously visible with a low roughness and only slightly eroded step edges which may arise from the growth of an unfinished layer. Thus, in addition to the RHEED monitoring, the surface topography also clearly substantiates the indication of a two-dimensional high quality thin film growth resulting in single crystalline quality.

Structural characterization

Another major parameter that needs to be examined carefully is the unit cell structure and especially its lattice constant. In order to analyze the out-of-plane lattice constant of the grown Nb:$SrTiO_3$ thin films, X-ray diffraction is utilized. Figure 4.6 shows a representative (002) Bragg peak of a 200 nm stoichiometric 0.5 wt.% Nb:$SrTiO_3$ thin film quasi-homoepitaxially grown on an undoped $SrTiO_3$ substrate. The vertical lines indicate the literature lattice constant of undoped and niobium-doped $SrTiO_3$, respectively.

The results allow for a clear distinction between the thin film and the substrate. The thin film peak appears as a shoulder at lower diffraction angles as compared to the undoped STO substrate peak. This finding indicates a slightly increased out-of-plane lattice constant, consistent with a lattice expansion caused by the Nb dopant concentration. *Rodenbücher et al.* reported a lattice constant of 3.907 Å for 0.5 wt.% donor-doped $SrTiO_3$, compared to 3.905 Å for undoped $SrTiO_3$.[122] The shift of the 2Θ angle observed in representative X-ray diffraction is in good agreement with this out-of-place lattice constant from literature as indicated by the solid lines added to the plot. Consequently, the out-of-plane lattice constant is consistently substantiating the conclusion of the single crystalline quality of the grown thin film.

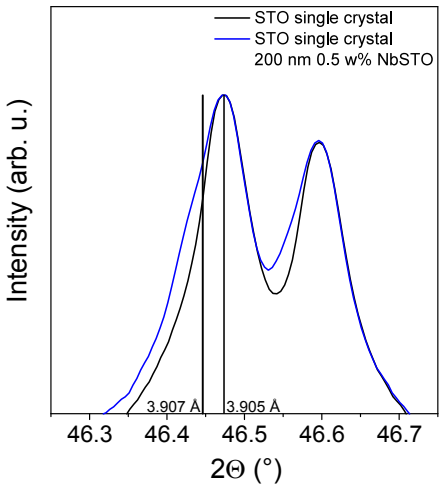

Figure 4.6.: Representative (002) Bragg peak of a 200 nm stoichiometric 0.5 wt.% Nb:$SrTiO_3$ thin film homoepitaxially grown on an undoped $SrTiO_3$ substrate. This figure is published in the supplemental information to ref. [121].

Growth conformity characterization

Another crucial parameter is the homogeneity of the growth process. By utilizing secondary ion mass spectrometry the ion ratio is analyzed over the entire film thickness. Inconstant ionic ratios in different thin film depths point towards an agglomeration of defects and hence an imperfect growth process. Figure 4.7 shows the representative intensities of titanium, strontium, oxygen and niobium of a 200 nm Nb:$SrTiO_3$ thin film grown homoepitaxially on an undoped $SrTiO_3$ substrate. Note that the conversion of the x-axis from sputter time to probing depth was performed with respect to the Nb:$SrTiO_3$ thin film thickness.

The different intensities of all investigated ions (TiO^-, SrO^-, $18O^-$), and especially the intensity of niobium (NbO^-), are almost constant over the entire thin film thickness. When reaching the undoped $SrTiO_3$ substrate, the NbO^- concentration is reduced significantly while the intensities of the other investigated ions stay constant. This finding indicates homogeneous ion ratios and doping concentration over the entire thin film. As a consequence, these results also point towards a low defect concentration in the thin film. Therefore, the observed growth conformity also corroborates the conclusion of a single crystalline thin film quality.

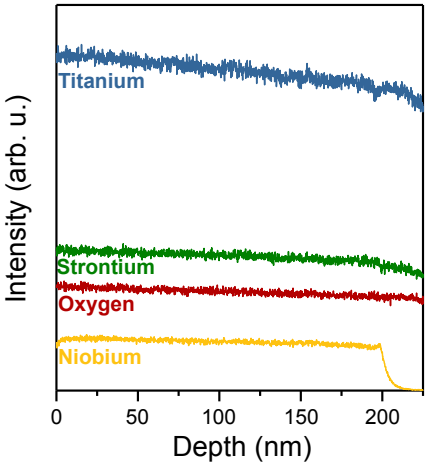

Figure 4.7.: Representative SIMS intensities of a 200 nm thick Nb:$SrTiO_3$ thin film grown on an undoped $SrTiO_3$ substrate. The almost constant niobium intensity illustrates a homogeneous doping concentration right down to the substrate. The SIMS experiments were performed by Dr. Uwe Breuer, ZEA-3, Forschungszentrum Jülich.

Electrical characterization

Another crucial parameter in terms of thin film quality are the electrical properties. In the following the electrical properties of Nb:$SrTiO_3$ thin films directly after growth will be examined by Hall measurements, both at room temperature and low temperature.

At room temperature, the 200 nm thick n-$SrTiO_3$ thin film showed a Hall electron mobility of $\mu \sim 6.6$ cm^2/Vs, which is in good agreement with the literature.[37, 38] Moreover, a carrier concentration of $n \sim 1.5\times10^{20}$ cm^{-3} was determined. Under the assumption of full dopant ionization a specific donor-doping concentration N_D results in a specific carrier concentration n calculated as the total concentration of niobium donor atoms. 0.5 wt.% niobium doping corresponds to a doping concentration of $\sim$1 at.% . Utilizing a lattice constant of 3.907 Å a total unit cell concentration of $\sim 1.5\times10^{22}$ unit cells/cm^3 is calculated. Multiplying the doping concentration in at% with the unit cell concentration results in the concentration of niobium dopants and hence the charge carrier concentration. It is calculated to 1.505×10^{20} cm^{-3}. This value matches the one measured at room temperature for the 200 nm thick Nb:$SrTiO_3$ thin film. This finding points towards a considerable low concentration of defects that would reduce the number of free charge carriers in the thin film.

In order to compare the electronic properties of the thin films to literature Hall measurements were also performed at low temperatures.[42, 106] Figure 4.8 shows

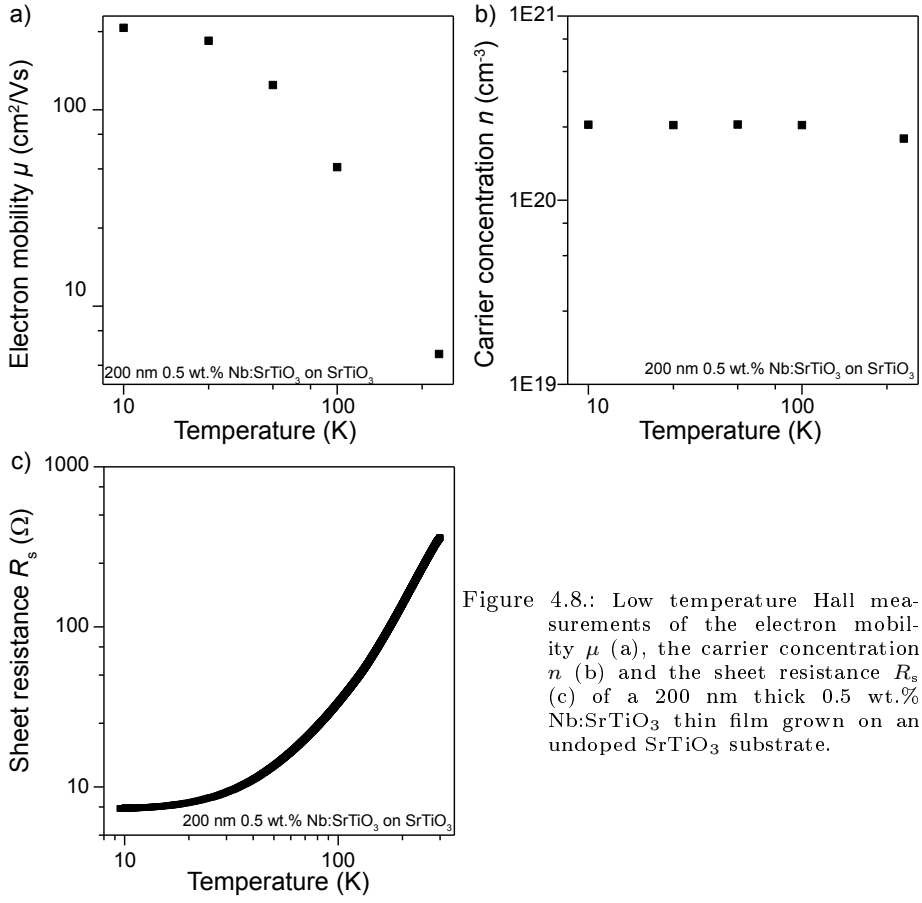

Figure 4.8.: Low temperature Hall measurements of the electron mobility μ (a), the carrier concentration n (b) and the sheet resistance R_s (c) of a 200 nm thick 0.5 wt.% Nb:$SrTiO_3$ thin film grown on an undoped $SrTiO_3$ substrate.

the low temperature Hall mobility μ (a), the carrier concentration n and the sheet resistance R_s of a 200 nm 0.5 wt.% Nb:$SrTiO_3$ thin film grown on a $SrTiO_3$ single crystal substrate.

With decreasing temperature the Hall mobility increases up to $\sim$200 cm^2/Vs at 10 K clearly demonstrating a reduction of phonon scattering and thus metallic behavior. The measured electron mobility values are in good agreement with recent literature by *Kozuka et al.*, *Moos et al.* and *Spinelli et al.* who investigated donor-doped $SrTiO_3$ at similar dopant concentration.[37, 40, 58] Moreover, *Son et al.* found an electron Hall mobility of $\sim$30000 cm^2/Vs illustrating high quality donor-doped $SrTiO_3$ thin films. The difference in electron mobility by a factor of 150 results directly from the donor-doping concentrations resulting in carrier concen-

trations of $\sim 1.5 \times 10^{20}$ cm^{-3} in comparison to $\sim 1 \times 10^{18}$ cm^{-3} utilized in this thesis and in literature, respectively. In addition, with decreasing temperature the carrier concentration is constant indicating that Nb is a shallow donor, cf. fig. 4.8 (b). Furthermore, the sheet resistance R_s is also decreasing with decreasing temperature. This is due to the observed increase in the charge carrier mobility substantiating the conclusion of metallic behavior of the grown thin film. Consequently, the measured low temperature electron mobilities, carrier concentrations and the sheet resistance substantiate the conclusion of a low defect concentration and thus thin films in single crystalline quality.

Summary

In this chapter the preparation of the samples used within this thesis was discussed in detail. In the first section, the topological changes of Nb:$SrTiO_3$ single crystals annealed in highly oxidizing and highly reducing conditions were investigated. It was shown that the single crystal surface exhibit equal step terrace structures as as-received single crystals after a short relaxation annealing. Therefore, an impact of microscopical contamination and secondary phase precipitates on the contact properties of the subsequently manufactured Pt/Nb:$SrTiO_3$ heterostructures will be neglected.

In the second section, the developed deposition process of n-$SrTiO_3$ thin films was introduced. It was demonstrated that the topography, the lattice structure, the growth conformity and the electrical properties of the grown thin films match the ones of high quality single crystals. Consequently, the comparability of the different samples is verified.

In the following chapters, the changes of the electrical and chemical properties of the prepared samples under applied thermodynamic biases are discussed.

5. Electronic surface characteristics

Typical experimental procedures and pretreatments used while investigating the physical and chemical properties of semiconducting single crystals and thin films involve varying temperatures and oxygen partial pressures corresponding to different thermodynamic conditions. In order to prepare n-$SrTiO_3$ single crystals to be examined directly or to be used as underlying substrates for varying thin film applications, annealing pretreatments at temperatures above 1200 K and ambient atmosphere are utilized to equilibrate the sample surface and to ensure comparability over several samples.[89] Moreover, for thin film growth a specific set of thermodynamic conditions is required. In terms of n-$SrTiO_3$ thin film growth, typical temperatures of 1050 K and a pO_2 of 0.1 mbar are applied, cf. sec. 4.2. This atmosphere is suggested to change the defect clustering and hence the electrical and surface properties of n-$SrTiO_3$ significantly.[37, 38]
In this chapter, it will be examined how varying thermodynamical biases applied during typical annealing procedures may affect the surface properties of n-$SrTiO_3$. The first section focuses on the *through-plane* contact properties of n-$SrTiO_3$ after different annealing treatments described by *in-situ* local-conductivity atomic force microscopy (C-AFM), impedance spectroscopy and *I(V)*-characteristics of Pt/Nb:$SrTiO_3$ heterojunctions. The second section concentrates on the *in-plane* properties, namely the carrier concentration, of n-$SrTiO_3$ thin films and the influence of the growth conditions on the sheet carrier concentration directly after growth observed by Hall measurements at varying temperatures.

5.1. *Through-plane* contact properties of n-$SrTiO_3$ single crystals

In order to investigate the possible impact of typical annealing procedures on the *through-plane* contact properties, 1.0 at% n-$SrTiO_3$ single crystals were annealed in different oxidizing and reducing conditions by applying ambient atmosphere and 4 % H_2/Ar, respectively (sec. 4.1). In the following, the surface resistance is described by C-AFM. In addition, the surface contact resistance and the transport barrier between the annealed n-$SrTiO_3$ surface and platinum top contact pads of different sizes and a thickness of 30 nm is characterized by impedance spectroscopy and *I(V)*-characteristics. Figure 5.1 shows schematic illustrations of the sample stacks used during the C-AFM experiments (a) and electrical interface contact (impedance

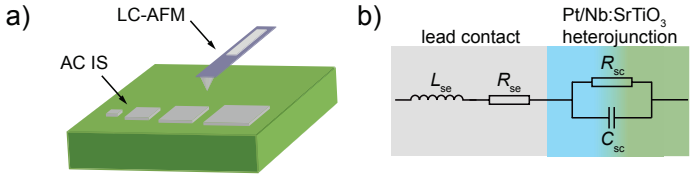

Figure 5.1.: Schematic illustration of the single crystal sampled stack used during C-AFM experiments (a) and the *through-plane* electrical measurements (b). The equivalent circuit model utilized for the fitting procedure of the impedance spectroscopy experiments (c).

spectroscopy and *I(V)*-characteristic) measurements (b) as well as the equivalent circuit model utilized in the fitting procedures of the impedance spectroscopy data.

For the C-AFM measurements, bare *n*-$SrTiO_3$ surfaces were analyzed after *in-situ* annealing in a vacuum chamber at 800 °C in reducing and oxidizing conditions with controlled pressures of 0.1 mbar of oxygen and a base pressure of 10^{-8} mbar, respectively. The measurements were performed using an *Omicron VT-SPM system* by *Omicron Nanotechnology GmbH* with an applied read voltage of -0.5 V. The low voltage ensured the surface properties to be unaffected by the applied electric field.[123, 124] During impedance spectroscopy and *I(V)*-characteristic measurements platinum pads of varying sizes were used. These pads were applied by magnetron-sputtering or electron-beam evaporation, cf. sec. 3.2. The impact of the different deposition techniques will be discussed below. In addition, the shown equivalent circuit model attributes a series resistance (R_{se}) and an induction contribution (L_{se}) to the experimental setup and the formed Pt/*n*-$SrTiO_3$ heterojunction to a single *RC* element (R_{SC} and C_{SC}).[107, 125, 126]

Local conductivity atomic force microscopy

An intuitive way to investigate the surface of single crystals after varying annealing treatments is *in-situ* local-conductivity atomic force microscopy. It allows observing changes in the surface morphology. At the same time, by applying a voltage to the AFM tip and measuring a current through the sample surface, additional information on the surface contact resistance of the single crystal can be collected assuming a high bulk conductivity. Figure 5.2 shows the morphology and the current through a *n*-$SrTiO_3$ surface after an *in-situ* reducing (a,c) and an oxidizing (b,d) annealing procedure measured by C-AFM. In order to compare the conductivity of the two surfaces directly, the color scale of the current images is identical. All experiments were conducted by Nicolas Raab (PGI-7, FZ Jülich).

The morphology does not vary significantly after the different annealing treatments. The step edges are smoother after the oxidizing annealing treatment though,

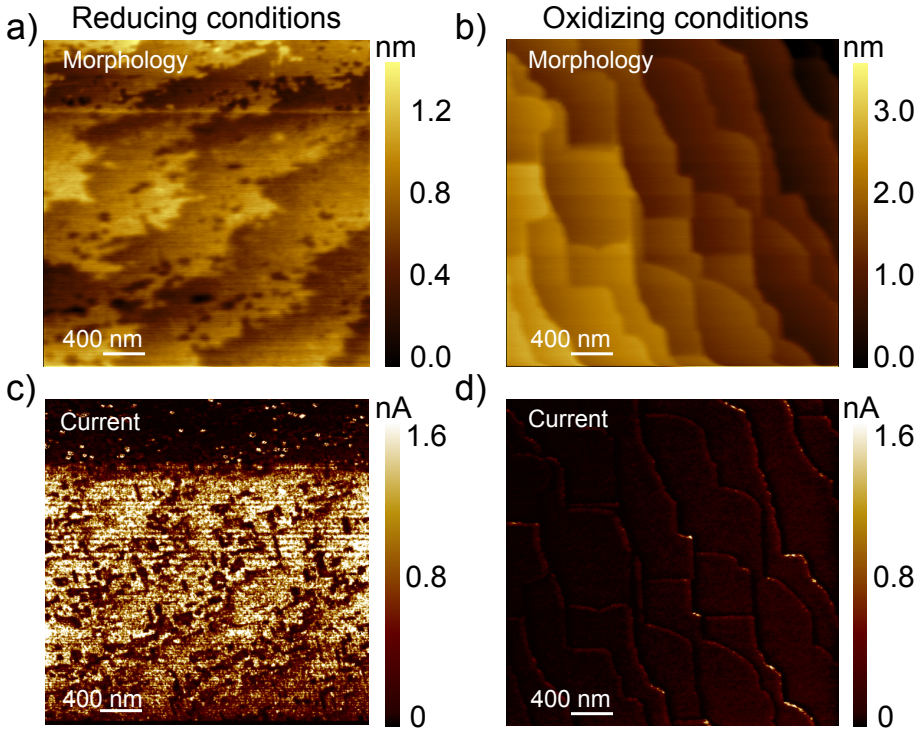

Figure 5.2.: Local conductivity atomic force microscopy measurements after *in-situ* reducing (a) and oxidizing conditions (b) of a n-$SrTiO_3$ single crystal. In both measurements a read out voltage of -0.5 V was used. The experiments were conducted by Nicolas Raab (PGI-7, FZ Jülich). The current measurements are published in ref. [127].

but neither in reducing nor in oxidizing conditions any additional surface features are developed.[72, 128] In contrast, the current through the n-$SrTiO_3$ surface varies substantially after different annealing treatments. The measured current after both annealing treatments reproduces features of the morphology. The observed current at the step edges is reduced due to the feedback loop of the measurement setup not being sensitive enough to ensure a stable contact between the cantilever and the surface. The step levels however show a stable current and are hence considered representative for the different annealing treatments. Intuitively, the current through the n-$SrTiO_3$ surface should be considerably high due to the high donor-doping concentration. As expected for donor-doped semiconductors, after the annealing treatment in reducing conditions the overall current through the n-$SrTiO_3$ surface is high (avg. $\sim$1 nA). After an oxidizing annealing treatment, however, the current

is reduced significantly to ∼100 pA, which is in the range of the detection limit. The reduced conductivity of the n-$SrTiO_3$ surface after the oxidizing annealing treatment already points towards a significant dependence of the n-$SrTiO_3$ surface properties on the annealing treatment. The C-AFM results, however, do not allow to draw a conclusion on the type of process that is present at the n-$SrTiO_3$ surface. Nevertheless, if the surface resistance is varied through annealing procedures, the contact resistance of heterojunctions to differently treated single crystals may also be affected significantly. Thus, in the following electrical characterization of Pt/n-$SrTiO_3$ heterojunctions will be analyzed to provide further inside on possible surface reactions.

Impedance spectroscopy

In order to investigate the contact resistance (R_{sc}) and capacitance (C_{sc}) of a Pt/n-$SrTiO_3$ heterojunction in more detail, impedance spectroscopy (*Solartron Si 1260, Solartron 1296*, frequency range: 1 Hz to 1 MHz) is employed and analyzed using *Zview 2* (*Ametek scientifc instruments*). A single semi-circle was modeled by one *RC* element associated to the Schottky-type interface contact, a series resistance (R_{se}) and an induction contribution of the measurement setup (L_{se}), cf. Fig. 5.1 (c). In order to examine the impact of the deposition technique of the platinum top electrodes, in the following the impedance spectroscopy results of heterojunctions produced by magnetron-sputtering and electron-beam evaporation are compared.

Sputtered top electrodes

Figure 5.3 shows the representative impedance spectroscopy results of Pt/n-$SrTiO_3$ heterojunctions after reducing (green, a) and oxidizing (blue, b) annealing procedures and sputtered platinum top electrodes, covering the entire n-$SrTiO_3$ single crystal surface (pad size of 5 mm× 5 mm), with a thickness of 30 nm plotted in a Cole-Cole diagram.

Both measurements after reducing and oxidizing annealing procedures show the typical semi-circle corresponding to a single *RC* element attributed to the formed Pt/n-$SrTiO_3$ heterojunction's Schottky-type transport barrier, cf. fig. 5.1 (c). The barrier results in an electron depletion layer associated with a finite capacitance (C_{SC}) and resistance (R_{SC}), cf. fig. 5.3. The shift of the semi-circles towards higher values on the real axis Z' corresponds to a small series resistance of the measurement setup (R_{se}). The contact capacitance of the two heterojunctions is considerably high and does not change significantly with the pretreatment from 946 nF to 669 nF after the reducing and oxidizing annealing procedure, respectively. The determined considerable high contact capacitance, in comparison to the capacitance of e-beam evaporated heterojunctions (cf. sec. 5.1), are reasonable due

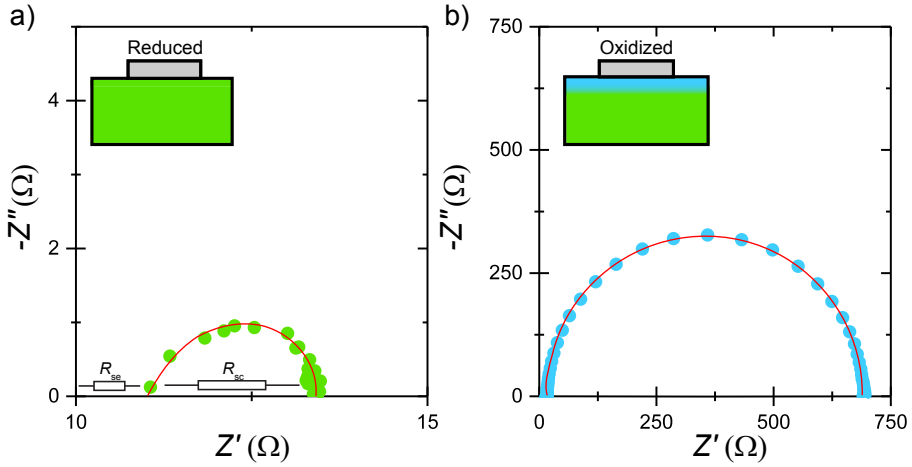

Figure 5.3.: Representative impedance spectroscopy after reducing (4 % H_2/Ar, green, a) and oxidizing (ambient atmosphere, blue, b) annealing of an n-$SrTiO_3$ single crystal with 30 nm sputtered platinum top electrodes with a size of 5 mm×5 mm. The contact resistance does not vary as significantly as expected from C-AFM results.

to the large area of the Pt top electrodes. Moreover, the series resistance is in the Ω-regime (∼12 Ω). As can be seen from the width of the characteristic semi-circle, the contact resistance R_{SC} varies with different annealing procedures and is determined to 5 Ω and 676 Ω after reducing and oxidzing annealing procedures, respectively. Both these values are considerably low for a Pt/n-$SrTiO_3$ heterojunction (cf. e-beam evaporated heterojunctions) regardless of the prior annealing pretreatment but this might also be due to the large pad size.

The observed trend of the contact resistances with the different annealing procedures of the n-$SrTiO_3$ single crystals is consistent with what has been observed above by C-AFM, which already suggested higher resistances after an oxidizing annealing treatment. The magnitude of the R_{SC} changes, however, is not high enough to match what was expected from prior C-AFM experiments. This effect might be due to morphological and chemical changes of the topmost atomic layer of the n-$SrTiO_3$ single crystal underneath the platinum top electrodes caused by the high energy introduced to the n-$SrTiO_3$ surface during the sputtering process, cf. sec. 3.2. Consequently, in the following, Pt/n-$SrTiO_3$ heterojunctions formed with sputtered platinum top electrodes will be compared to e-beam evaporated Pt/n-$SrTiO_3$ heterojunctions which avoid any significant impact of possible particle bombardment.

Evaporated top electrodes

Figure 5.4 shows representative impedance spectroscopy results of Pt/n-$SrTiO_3$ heterojunctions after reducing (green, a) and oxidizing (blue, b) annealing procedures at 1320 K using evaporated platinum top electrodes with a thickness of 30 nm covering an area of 200 μm×200 μm plotted in a Cole-Cole diagram.

The experiments reveal a single semi-circle after both reducing and oxidizing pre-annealing procedures, indicating a single parallel RC element attributed to the Pt/n-$SrTiO_3$ heterojunction's Schottky-type transport barrier.[107, 125, 126] Both semi-circles are found to be offset by $20-30\ \Omega$ along the Z' real axis, corresponding to a finite series resistance (R_{se}, fig. 5.1 (c)) owing to the contact leads of the measurement setup. After the annealing procedure in 4 % H_2/Ar (reducing conditions) the impedance spectroscopy measurements show a small series resistance of 26 Ω, a substantial contact resistance $R_{SC} \approx 23$ kΩ and contact capacitance $C_{SC} \approx 2.9$ nF (fig. 5.4 (a)), characterizing the Schottky contact formed at the interface. After annealing in oxidizing conditions, however, R_{SC} is increased by three orders of magnitude to $R_{sc} \approx 39000$ kΩ, while R_{se} and $C_{SC} \approx 2.2$ nF remained almost unchanged (fig. 5.4 (b)). Thus, the electronic properties of the Pt/n-$SrTiO_3$ het-

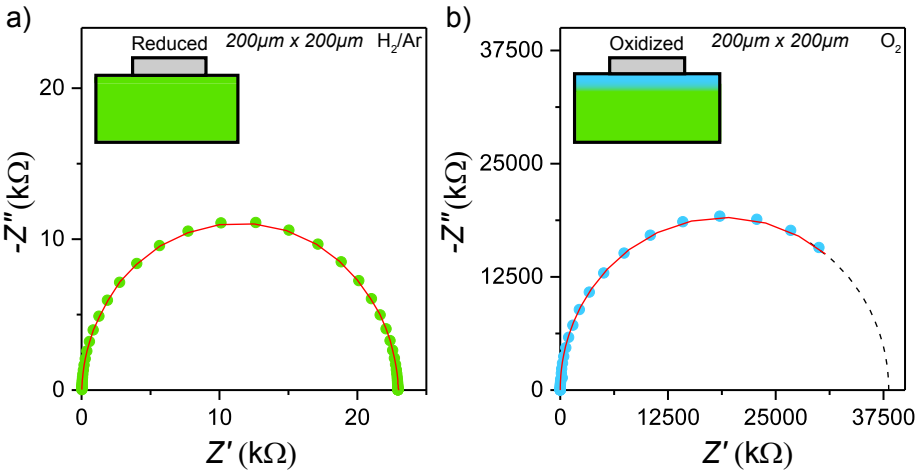

Figure 5.4.: Representative impedance spectroscopy after reducing (4 % H_2/Ar, green, a) and oxidizing (ambient atmosphere, blue, b) annealing of an n-$SrTiO_3$ single crystal for 4 hours at 1320 K using 30 nm evaporated platinum top electrodes with an example size of 200 μm×200μm. The interruption of the typical semicircle in (b) is due to the high contact resistance. The dashed black line indicates a simulation using the fitted values for the contact capacitance and the contact resistance. The surface contact resistance varies by more than three orders of magnitude depending on the prior annealing treatment. This figure is published in ref. [127].

erojunctions changed dramatically upon annealing. This finding is consistent with the changes after different annealing procedures found by C-AFM measurements on the bare n-$SrTiO_3$ single crystal surfaces as shown in fig. 5.2.

In order to further analyze the observed impact of the different annealing pretreatments, impedance spectroscopy measurements were conducted on heterojunctions formed by n-$SrTiO_3$ single crystals (as received, reducing and oxidizing annealing at different temperatures) and evaporated platinum top electrodes of smaller sizes (100 μm×100 μm, 50 μm×50 μm).

Fig. 5.5 shows the electrode area-dependence of C_{SC} (a) and R_{SC} (b) determined from the impedance spectra after annealing treatments at different temperatures. On double logarithmic scales both C_{sc} ($\propto$ A) and R_{sc} ($\propto$ 1/A) show a linear dependence on the top electrode area, indicating homogeneous interface properties on the micrometer length scale. As shown in Fig. 5.5 (a), C_{sc} did not change as significantly as R_{sc} depending on the prior annealing treatment (within a factor of 2) and stayed in the nanofarad-regime. Note that differences in the magnitude of the contact capacitance between sputtered and evaporated top electrodes results from the different pad sizes utilized within the experiments.

Using classical plate capacitor physics, these C_{SC} values correspond to an almost constant barrier width in the tens of nanometer regime, that neither changes substantially upon annealing at varied temperature nor at varied oxygen atmosphere. In contrast, as already indicated by the representative impedance spec-

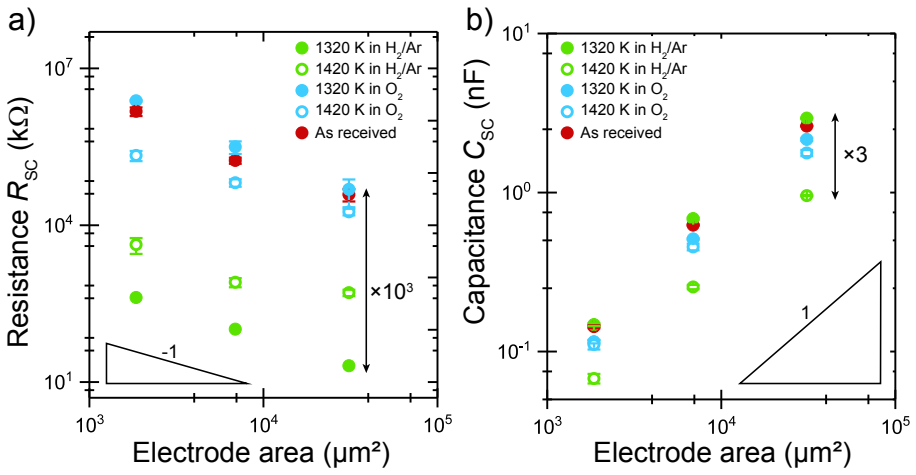

Figure 5.5.: Electrode area-dependent surface contact resistance (a) and contact capacitance (b) determined from impedance spectroscopy measurements on n-$SrTiO_3$ single crystals as received and after reducing and oxidizing annealing treatments at temperatures of 1320 K and 1420 K. This figure is published in ref. [127].

troscopy measurements discussed in Fig. 5.4, R_{sc} depends substantially on the oxygen pressure during annealing, while temperature is less important. Consistently for all electrode areas, R_{sc} is found approximately three orders of magnitude lower after annealing in Ar/4 % H_2 gas mixture (reducing) than after annealing in oxidizing conditions or without any annealing treatment at all. Consequently, these findings point towards changes in the transport barrier height at similar barrier widths.

I(V)-characteristics

In order to characterize the rectifying behavior of the Pt/n-$SrTiO_3$ heterojunctions, $I(V)$-characteristics were measured using a *Keithley 2611* source meter. The applied voltage ranged from -1 V to +1 V to avoid resistive switching.[10–12] The bottom electrode (n-$SrTiO_3$) was grounded while the potential was applied to the platinum top electrodes. Fig. 5.6 shows $I(V)$-curves measured for different electrode areas after annealing in Ar/4 % H_2 gas mixture (a) and in oxidzing conditions (b).

The $I(V)$-curves show strongly non-linear behavior consistent with a non-Ohmic contact resistance. While heterojunctions obtained after reducing annealing show considerably high currents in reverse direction, heterojunctions obtained after an oxidizing annealing procedure of the n-$SrTiO_3$ single crystals show strongly asymmetric and rectifying behavior with negligible currents in reverse direction. Similarly, in forward direction, the currents of the heterojunctions obtained after annealing in Ar/4 % H_2 are higher as compared to the ones obtained after oxidation. These findings are consistent with the C-AFM measurements shown in figure 5.2. In addition, the threshold voltage for forward currents is reduced for single crystal samples treated in Ar/4 % H_2.

At an applied voltage of 450 mV, the currents are still largely suppressed by the diode characteristics and the transport barrier of the heterojunction has not been overcome. Therefore, the measured current density is a measure of the actual transport barrier height and hence the resistance. Fig. 5.7 reveals almost 2-3 orders of magnitude lower current density for samples obtained on oxidized single crystals, indicating an increased barrier height formed at heterojunctions to n-$SrTiO_3$ after oxidizing annealing procedure.

Note that as revealed by DFT-calculations in the theory group of the IWE II (RWTH University) a direct determination of the Schottky barrier height from $I(V)$-characteristics is only valid for a strict transport mechanism for electrons *over* the barrier. As a detailed analysis of $I(V)$-curves across similar heterojunctions have revealed considerable tunneling contributions *through* the barrier,[66] an analysis of the Schottky barrier height is refrained here and limited to the comparison of absolute current densities.

All results obtained by impedance spectroscopy and $I(V)$-characteristics showed a dependence of the interfacial transport barrier in Pt/n-$SrTiO_3$ heterojunctions

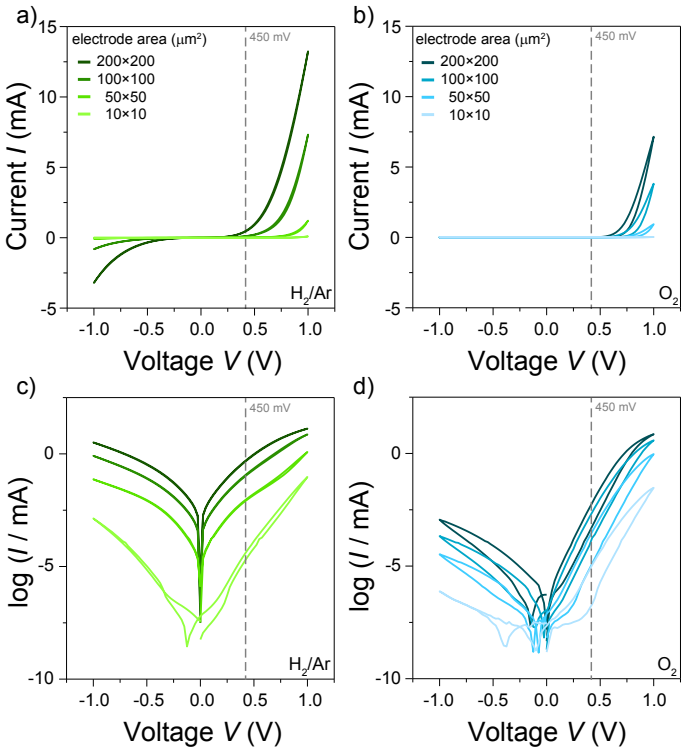

Figure 5.6.: Electrode area-dependent $I(V)$-curves measured on n-$SrTiO_3$/platinum contact after reducing (a,c) and oxidizing (b,d) annealing treatments. This figure is published in ref. [127].

on the pretreatment procedure applied to n-$SrTiO_3$ before the heterojunction fabrication. After oxidation, impedance spectroscopy and the $I(V)$-curves consistently showed a significantly increased R_{SC} due to enhanced carrier depletion at the interface, while the width of barrier as indicated by C_{SC} did not change substantially. As will be shown in more detail in section 9.3 these findings are consistent with the presence of strontium vacancies in the near surface region due to an oxidation process.

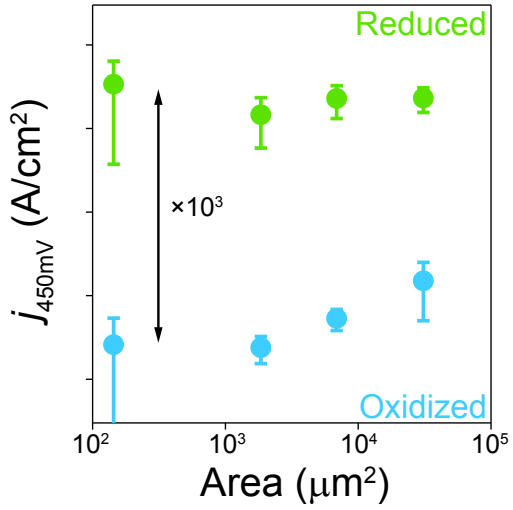

Figure 5.7.: Electrode area-dependent current densities through a n-$SrTiO_3$/platinum contact after reducing (green) and oxidizing annealing treatments determined at 450 mV. This figure is published in ref. [127].

5.2. *In-plane* properties of n-$SrTiO_3$ thin films

So far, all results from C-AFM, impedance spectroscopy and *I(V)*-characteristic measurements on Pt/n-$SrTiO_3$ heterojunctions after varying annealing procedures of the n-$SrTiO_3$ single crystals consistently showed a dependence of the electrical contact properties on the specific pretreatment. In order to expand the analysis of surface properties to electrical *in-plane* characterization, thin films will be examined directly after growth. Figure 5.8 shows a schematic illustration of the n-$SrTiO_3$ thin film stack used during Hall measurements at room temperature and at elevated temperatures. For room temperature experiments the as-grown n-$SrTiO_3$ thin films have been bonded with aluminum wires in a Van der Pauw configuration directly after growth and measured using a *Lakeshore 8000* Hall measurement setup. For high temperature experiments the as-grown samples were contacted using platinum clamps and electrodes and measured using a *Lakeshore 8000* high temperature Hall measurement setup. In AC mode, a 1.2 T B-field was varied at a frequency of 100 mHz. The Hall voltage was measured using lock-in technique, thereby decreasing noise during elevated temperature measurements.

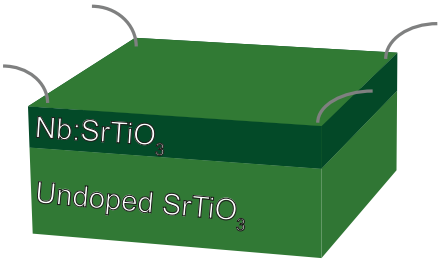

Figure 5.8: Schematic illustration of the n-$SrTiO_3$ thin film sample stack used during Hall measurements at room temperature and elevated temperatures. The figure is published in ref. [115].

Hall measurements at room temperature

Fig. 5.9 shows the carrier concentration n obtained for n-$SrTiO_3$ thin films with different layer thickness as determined from room temperature Hall measurements immediately after deposition. In an ideal semiconductor picture, one would expect a thickness-independent carrier density that matches the Nb-dopant concentration all the way up to the surface (1.5×10^{20} cm^{-3}, red dashed line in (b)). In contrast, a systematic thickness dependence of the electron density is observed. Only at a layer thickness approaching 200 nm the carrier concentration coincides with the donor concentration. At lower film thickness, however, the carrier concentration decreases significantly by almost one order of magnitude below the donor concentration to $2.9{\times}10^{19}$ cm^{-3} at a film thickness of 32 nm. At a thickness of 30 nm, the conductivity of the thin films was even below the detection limit and no carrier concentration could be determined.

The systematic decrease of the carrier concentration at small layer thicknesses below about 100 nm is indicative of a constant electron depletion layer right at the n-$SrTiO_3$ surface becoming the dominant factor for electron transport, cf. fig. 5.9 (b). To determine the volume carrier concentration n, typically a homogeneous carrier concentration over the entire sample thickness is assumed. Consequently, the integral number n_s measured is divided by the film thickness to arrive at a carrier concentration $n{=}\frac{n_s}{d}$.

A lower average carrier concentration may be understood in terms of an electron depletion layer at the surface, which would yield a thickness-dependence of n. An electron depletion layer, however, would be associated to a surface charge, Q/A, equivalent to the loss of electrons in the depletion layer. Given that all thin films show a comparable surface charge, this would yield in a thickness dependence of the measured carrier concentration of

$$n = \frac{n_s}{d} = [\mathrm{Nb}^{\bullet}] - \frac{|Q|}{A}/d \qquad \rightarrow n \propto 1/d \qquad , \tag{5.1}$$

where $\frac{|Q|}{A}$ denotes a surface charge. As will be shown in detail in chapters 6, 7 and 8 this surface charge depends on the pO_2, the temperature T and the donor-doping concentration N_D and defines the electrical surface properties.

At large thicknesses, a constant electron depletion layer does not cover a significant amount of the total thin film. Hence, the Hall measurements at large thicknesses result in an average carrier concentration n that is in the range of the doping concentration. With decreasing thin film thickness, a constant electron depletion layer at the surface more and more covers a substantial part of the entire film, thus decreasing the measured average carrier concentration. Consequently, the results of the room temperature Hall measurements clearly indicate that the as-grown layers readily form an inherent space charge layer at the n-$SrTiO_3$ surface directly after growth in which electrons are depleted. This is consistent with earlier reports.[39]

Another and more trivial explanation for the observed thickness-dependent electron density would be a non-ideal growth processes leading to the incorporation of defects and electron traps during synthesis.[37, 129–131] However, growth-induced defects would be expected to become increasingly effective as the layer thickness increases. In figure 5.9, opposite behavior is observed: the carrier density approaches the Nb-concentration with increasing layer thickness, indicating a stoichiometric synthesis process, and thus supporting the interpretation of an electron depletion layer present at the surface of the thin films, cf. sec. 4.2.

In analogy to semiconductors, the physical origin of this may be intrinsic surface states or unsaturated dangling bonds.[39] However, also ionic defect states or

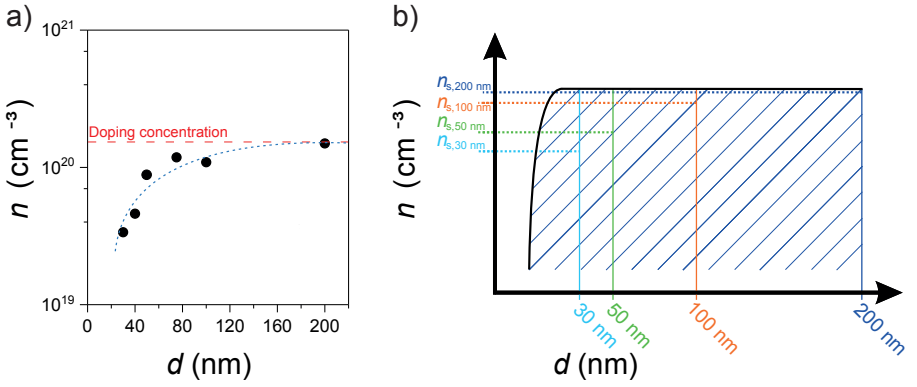

Figure 5.9.: Carrier concentration obtained for 1.0 wt% n-$SrTiO_3$ thin films with different layer thickness (a). The red dashed line indicates the nominal donor concentration. The blue dashed line is a guide to the eye emphasizing the effect of electron depletion at low layer thicknesses. Schematic illustration of the impact of a surface space charge layer on *in-plane* Hall measurements with varying film thicknesses (b). This figure is partly published in ref. [115].

charged adsorbates can form localized negative charges, which would drive electron depletion.[38, 50, 51, 121] A physical fingerprint of such a redox-chemistry-triggered effect is the characteristic dependence on the activity of the oxidizing agent. The key question arising from this is if the observed electron depletion layer shows a characteristic dependence on pO_2 that can be identified as physical fingerprint of a surface redox process which allows for a controlled manipulation. This issue one of the main focusses of this thesis and will be addressed in chapter 6 by lab- and synchrotron-based AP-XPS.

Hall measurements at elevated temperatures

In the following chapters, the evaluation of electrical transport properties at elevated temperatures require a temperature-dependent Hall mobility in the high temperature regime. In addition to the literature value extrapolated from high temperature measurements,[37] an experimental value is determined in own experiments. Figure 5.10 shows the temperature dependent Hall mobility (μ_{HT} (T)) of a 200 nm thick 0.5 wt% n-$SrTiO_3$ film (red) in comparison to literature values reported for ceramic samples (blue).
At this thickness the carrier density coincides with the expected bulk value (cf.

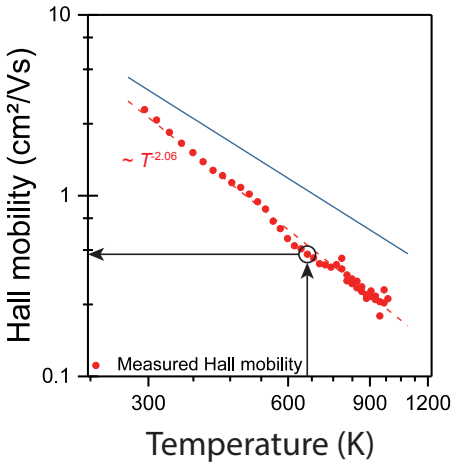

Figure 5.10.: Temperature-dependent Hall mobility measured by high temperature Hall measurements of a 200 nm thick 1.0 wt% n-$SrTiO_3$ film as well as the calculated literature values from [37] (blue line). This figure is published in ref. [115].

fig. 5.9) serving as a reference for electron transport in the n-$SrTiO_3$ thin films, in absence of space charge effects. For both the measured thin film and literature single crystal values the Hall mobility decreases with an increasing temperature following a power law behavior. This is consistent with a phonon scattering dominated transport mechanism as expected for highly donor-doped semiconductors. The experimental results are fitted by

$$\mu_{\mathrm{tf}} = 3.48 \cdot 10^5 \times (T/\mathrm{K})^{-2.06} \quad \left[\frac{\mathrm{cm}^2}{\mathrm{Vs}}\right] \quad , \tag{5.2}$$

where T denotes the temperature of the thin film. The measured thin film values are lower than the literature values determined in donor-doped $SrTiO_3$ single crystals by approximately a factor of 2. Throughout this work the thin film value measured at 670 K of 0.45 $\mathrm{cm}^2/\mathrm{Vs}$ is used (as marked by the arrows in Fig. 5.10) for calculations were applicable.

Summary

In this chapter, electron depletion at the n-$SrTiO_3$ surface was investigated. In the first section, it was demonstrated that different annealing procedures at oxidizing and reducing conditions change the surface resistance of n-$SrTiO_3$ single crystals significantly. C-AFM measurements after *in-situ* annealing pretreatments reveal an increased contact resistance after annealing in oxidizing conditions in contrast to after annealing in reducing conditions. This finding was substantiated by contact resistances determined by impedance spectroscopy, which increased by three orders of magnitude after annealing in oxidizing conditions. The contact capacitance, however, is not changed essentially. Additional *I(V)*-characteristics unveiled that these findings are due to an increased transport barrier after oxidizing annealing procedures.

In the second section, Hall measurements on n-$SrTiO_3$ thin films directly after growth demonstrated a film thickness-dependent carrier concentration. The decreasing average carrier concentration with decreasing film thickness points towards a surface electron depletion and hence a surface space charge layer at the n-$SrTiO_3$ surface at room temperature directly after growth.

All these findings illustrate a dependence of the electronic surface properties on different thermodynamic pretreatments. To further investigate the specific impact as well as the origin of the observed effect in the following chapters lab- and synchrotron-based ambient pressure X-ray photoelectron spectroscopy and electrochemical conductivity relaxation experiments will be utilized.

6. pO_2-dependence of surface space charge layer

As Nb:$SrTiO_3$ is well-known for the strong coupling of electronic and ionic structure, that may trigger significant changes in electronic response of the surface by subtle chemical changes as observed in chapter 5. By analyzing the spectroscopic signatures of n-$SrTiO_3$ it is possible to investigate both these properties directly. In lab-based ultra high vacuum spectroscopy experiments it was possible to detect the electronic response of the Nb:$SrTiO_3$ surface after *in-situ* oxidizing annealing treatment. Subtle chemical changes, however, could not be detected. This might be due to the volatility of the induced surface space charger layer while transferring the sample in ultra high vacuum conditions and the fact that a probing depth of a few nanometers might not be sensitive enough to detect the small changes presumably located directly at the n-$SrTiO_3$ surface. Consequently, analyzing the chemical and electronic structure *in-situ* in different oxygen partial pressures (pO_2) is only possible by state-of-the art ambient pressure X-ray photoelectron spectroscopy (AP-XPS). In this chapter, lab-based as well as synchrotron-based AP-XPS experiments at different oxygen partial pressures will be analyzed. In this way, the analysis can focus on both the pO_2-dependence and the probing depth-dependence of the indicated surface space charge layer. In the first section of this chapter, the pO_2-dependent binding energy shift is illustrated, the effects on single crystals and thin films is compared and the resulting calculation of the generated negative surface charge is explained. The second section of this chapter focuses on probing depth-dependent evolution of the surface potential.

6.1. Binding energy shift at different pO_2

For a spectroscopic analysis *in-situ* at different oxygen partial pressures, the sample was investigated using the $SPECS^{TM}$ ambient pressure XPS instrument of the CERIC-ERIC consortium located at the Department of Surface and Plasma Science MFF UK of the Charles University in Prague using an Al K_α source ($h\nu = 1486.6$ eV) and an emission angle of 90°. In this lab-based AP-XPS measurements, an as prepared 1 at% n-$SrTiO_3$ thin film with a thickness of 32 nm grown on an undoped $SrTiO_3$ substrate, cf. chapter 4, was contacted from the top using a thin titanium strip, providing electrical and hence grounding contact between the

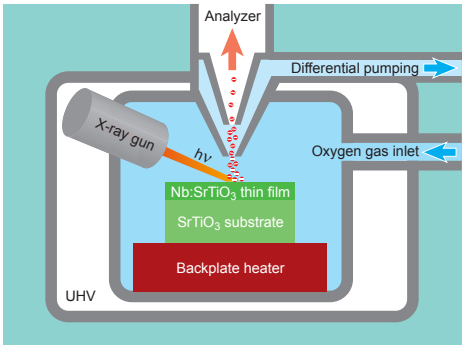

Figure 6.1: Schematic illustration of the sample stack as well as the near ambient pressure X-ray photoelectron spectroscopy measurement setup. The figure was published in ref. [121].

sample and the analyzer. Figure 6.1 shows a schematic illustration of the sample stack and the AP-XPS measurement setup.

Characteristic core level spectra at different pO_2

All constituents' core levels as well as the valence band region and typical contamination core level spectra were measured *in-situ* at a temperature of 770 K and at different pO_2 ranging from low base pressure conditions ($\sim 10^{-8}$ mbar) up to 5 mbar O_2. The lowest accurately adjustable pO_2 in the used measurement setup was 0.05 mbar O_2. Figure 6.2 shows the core level spectra[132] of oxygen 1s (O1s) and carbon 1s (C1s) (a), titanium 2p (Ti2p) (b), and strontium 3d (Sr3d) (c), as well as the valence band region (d) obtained at room temperature (dashed spectra) and at an elevated temperature of 770 K (solid spectra) at different pO_2. Initial spectra were taken at room temperature and a base pressure of 10^{-8} mbar (dashed top spectra, UHV) on an as-prepared thin film.

As can be seen by a shoulder in the O1s and a clear peak in the C1s spectra (a), a significant amount of carbon adsorbates and contaminants is present at the thin film surface resulting from exposure to air after the PLD growth process and *ex-situ* transfer to the AP-XPS setup. Upon heating to 770 K in a base pressure of 10^{-8} mbar, a reduction of the carbon adsorbates and contaminants is clearly visible in the O1s and the C1s spectra. Subsequently, the pO_2 was increased stepwise from 0.05 mbar to 5 mbar while the temperature of 770 K was maintained. All carbon adsorbates and contaminants are removed from the surface at a pO_2 above 0.05 mbar. Consequently, for all subsequent experiments the sample surfaces were cleaned at elevated temperatures and pO_2 prior to the measurements to ensure a characterization of the intrinsic surface properties. With increasing pO_2, a significant shift towards lower binding energies is detected for all the characteristic core level spectra and the valence band maximum. To emphasize the binding energy

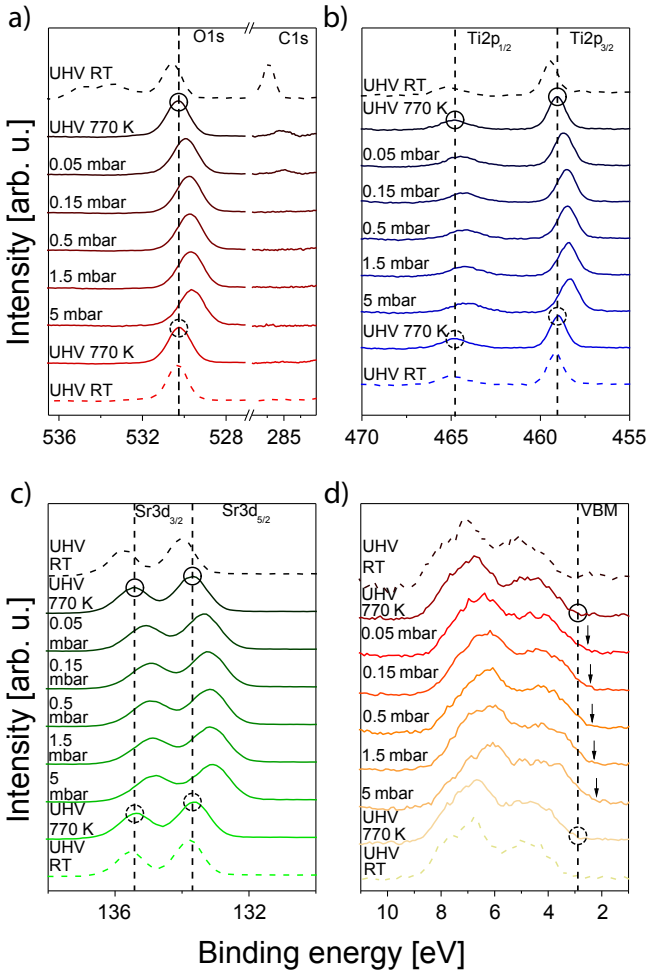

Figure 6.2.: Core level spectra of O1s and C1s, Ti2p and Sr3d, as well as the valence band region of a 32 nm thick n-$SrTiO_3$ film at room temperature (dashed spectra) and 770 K (solid spectra). The dashed vertical lines indicate the position of the characteristic binding energies at the first measurement at 770 K and a base pressure of 10^{-8} mbar (solid circles). The dashed circles indicate the characteristic binding energies at the second measurement at 770 K and low base pressure. The figure was published in ref. [121].

shifts, the vertical dashed lines indicate the characteristic binding energy of O1s, Ti2p, Sr3d and the valence band maximum at the initial measurement at a low base pressure at 770 K (solid circles). Full reversibility of the binding energy shifts was confirmed by a following set of spectra taken again in UHV conditions at 770 K (dashed circles), pointing towards a reversible underlying surface process, solely governed by the ambient pO_2. Finally, the thin film was cooled down to room temperature while the low base pressure was maintained (dashed bottom spectra).

As can be seen from the lack of spectral intensities in the C1s core level spectra, the surface was cleaned permanently at an increased temperature. Furthermore, the core level spectra measured at room temperature in low base pressure conditions show that upon cooling the characteristic binding energies shift just slightly towards higher values as compared to the ones that had been measured in the initial measurement at room temperature and the same pressure regime. The shift between the top and bottom dashed spectra respectively at room temperature and in low base pressure conditions might be due to the absence of carbon adsorbates and contaminants in the second measurement. Hence, there is an apparent effect

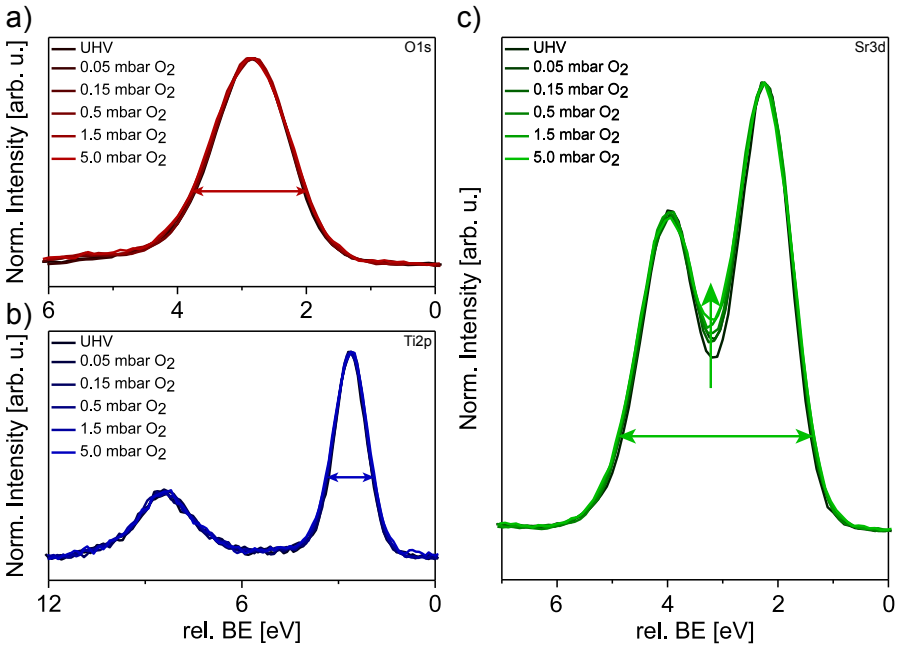

Figure 6.3.: Superposition of the O1s (a), Ti2p (b) and the Sr3d (c) core level spectra measured at different adjusted pO_2 and a temperature of 770 K. For the superposition, the spectra were shifted along the binding energy axis.

of carbon-type surface adsorbates on the electronic surface configuration. However, due to reversibility of the binding energy shift in UHV conditions without the reappearance of the C1s peak, the pO_2-dependent shifts observed at 770 K cannot be explained by surface carbon contaminants solely. Consequently, the shown core level spectra represent the characterization of the intrinsic surface properties of the n-$SrTiO_3$ thin film.

With varying pO_2, the core level spectra generally show slight changes, comparably observed in all core levels. Figure 6.3 shows the superposition of the O1s (a), Ti2p (b) and Sr3d (c) core level spectra for different adjusted pO_2. For the superposition, the spectra were shifted along the binding energy axis. All measured core levels inhibit a slight broadening with increasing pO_2 as indicated by the horizontal arrows. The O1s as well as the Ti2p core level do not show changes that can be unambiguously interpreted as chemical changes. In contrast, the Sr3d core level spectra measured at different pO_2 show significant changes. The intensity valley between the $3d_{3/2}$ and $3d_{5/2}$ peaks is increasingly shallower with increasing pO_2 as indicated by the vertical arrow. As further explained in section 9.2, these changes in spectral shape may directly result from a changed potential profile in the surface space charge layer.[21, 133] Similar intensity variations in the Sr core level, however, have also been assigned to SrO[72, 128] or hydroxide ($Sr(OH)_2$)[21] surface phase formation. Here, neither the spectral differences in the O1s,[134] the Sr3d,[72, 135] in the Ti2p,[88] nor any spectral changes in the valence band spectra[136] allow for an unambiguous interpretation as chemical changes.

Comparison of n-$SrTiO_3$ single crystals and thin films

As shown above, the thin films used during the measurements show bulk like electrical properties, cf. section 4. In order to determine, whether or not thin films and single crystals also show the same behavior in the AP-XPS, experiments in equal conditions were performed. Figure 6.4 shows the comparison of the O1s (a,b) and the Sr3d (c,d) core level of a 32 nm thick 1 at% n-$SrTiO_3$ thin film grown on an undoped $SrTiO_3$ substrate and an 1 at% n-$SrTiO_3$ single crystal measured at 770 K at low base pressure conditions of 10^{-8} mbar and high a oxygen partial pressure of 5 mbar. As indicated by the dashed black lines, the measured binding energies of both characteristic core levels in a low base pressure and high pO_2 conditions of the single crystal and the thin film are equivalent within the experimental accuracy, resulting in the same binding energy shift. In addition, as already seen above the valley between the $Sr3d_{3/2}$ and the $Sr3d_{5/2}$ peak showed a similar flattening with increasing pO_2. Thus, thin films and single crystals reacted identically to changes in pO_2 at elevated temperatures, again substantiating the quality of the grown thin films and pointing towards the same underlying surface process. Consequently, in the following experiments and discussions, thin films and single crystals are treated equally and will be compared directly.

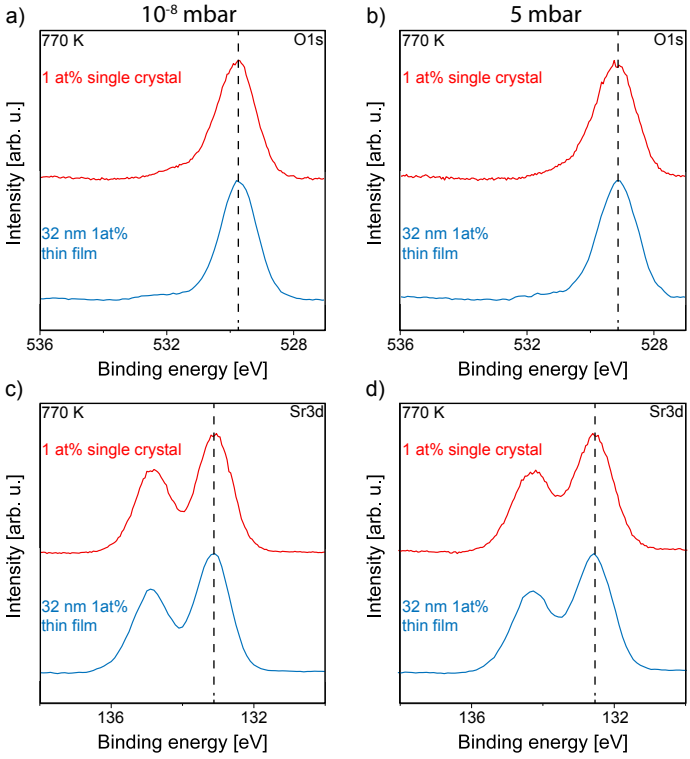

Figure 6.4.: Comparison of the O1s (a,b) and Sr3d (c,d) core level of a 32 nm 1 at% n-$SrTiO_3$ thin film and a 1 at% n-$SrTiO_3$ single crystal measured at 770 K in a base pressure of 10^{-8} bar and a pO_2 of 5 mbar O_2. Within measurement accuracy, the thin film and the single crystal show identical results.

Fitting procedures and apparent binding energy values

In order to investigate the observed shift in more detail the binding energy values of all core levels were fitted by *KolXPD* software using a Shirley background subtraction and an appropriate combination of Voigt peaks and doublets. Figure 6.5 shows typical examples of the fits of the O1s (a), the Ti2p (b) and the Sr3d (c) core level spectra and the valence band maximum (d) for measurements at 770 K and in a pO_2 of 1.5 mbar O_2 after a Shirley background subtraction. Two Voigt functions were fitted for the O1s peak, reflecting an unsaturated surface lattice oxygen and a

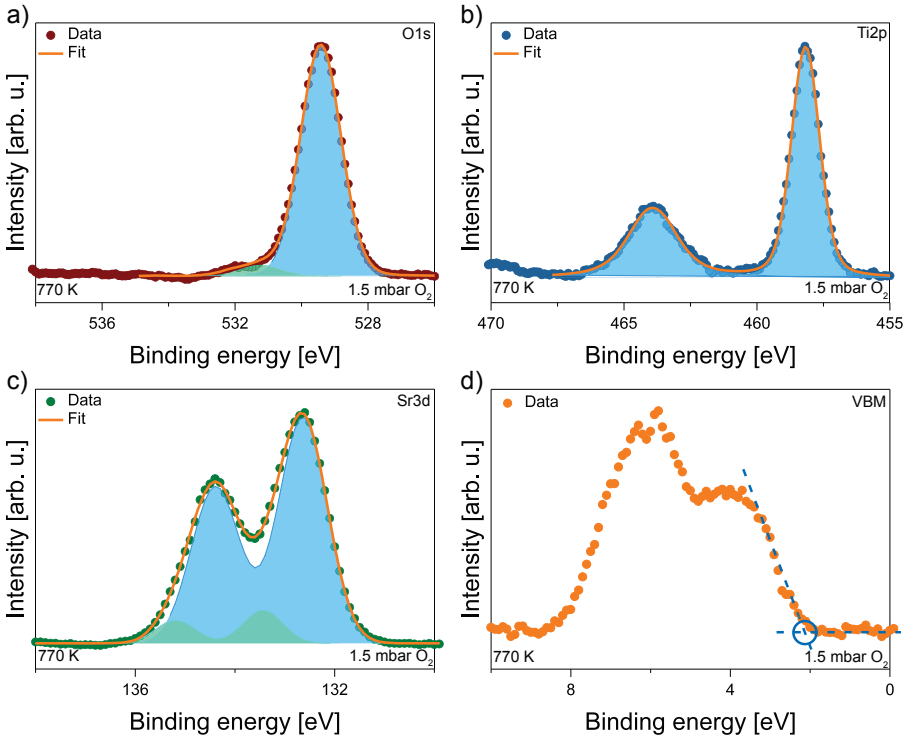

Figure 6.5.: Typical examples of the fitting procedures for the O1s (a), Ti2p (b) and the Sr3d (c) core level and the valence band maximum (d) determined at 770 K and in 1.5 mbar O_2 after a Shirley background subtraction.

saturated lattice oxygen with the similar binding energy shift,[137] one Voigt function was fitted for the C1s peak (not shown here), two separate Voigt functions with different full width half maxima[138] and a fixed distance were fitted for the Ti2p peak, two Voigt doublets with fixed peak separations and area ratios matching the spin orbit splitting and corresponding to a $SrTiO_3$ lattice component (low binding energy) and a SrO surface component shift by 0.8 eV (high binding energy) were fitted for the Sr3d peaks. To determine the valence band maximum the intersection of a linear approximation of the leading edge of the valence band spectra and background was determined (indicated by vertical arrows in figure 6.5 (d)).[139]

The different fitting procedures reproduce all the measured core level data. Utilizing these fits the apparent binding energy values at different pO_2 are extracted to represent the observed binding energy shift. Figure 6.6 shows the apparent binding energy values of the core levels (a), the difference between the Fermi energy, refer-

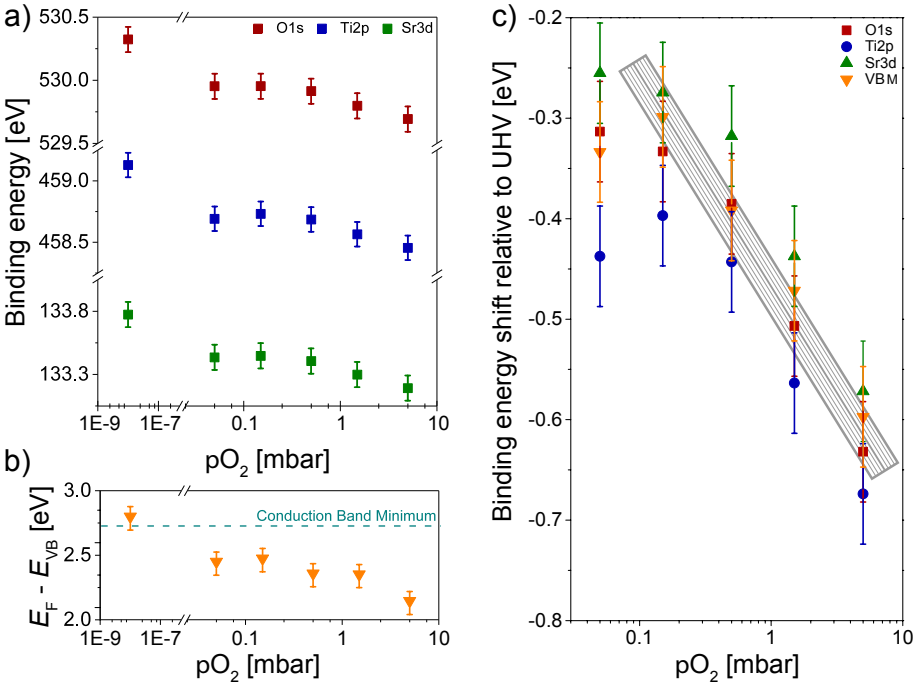

Figure 6.6.: Position of the characteristic binding energy of n-$SrTiO_3$ core levels (a), the energy difference between the Fermi energy and the valence band maximum as well as the conduction band minimum (b) at 770 K. Binding energy shift relative to measurements in low base pressure conditions (c). For a better comparability, the x-axis in (a) is interrupted from 3×10^{-7} mbar to 3×10^{-2} mbar. The figure was published in ref. [121].

enced by a gold standard measurement,[140, 141] and the valence band maximum as well as the estimated position of the conduction band minimum at 770 K[37] (b), and the relative binding energy shift of the different core level spectra and the valence band maximum with respect to the initial low base pressure measurements (c) at 770 K. The grey rectangle acts as a guide to the eye. The deviations in the apparent binding energy shift relative to UHV conditions of the different core levels and the valence band maximum correspond to the different kinetic energies of the electrons extracted from different core levels and are within the accuracy of the experimental setup.

As discussed above, all characteristic binding energies shift towards lower values while increasing the pO_2. Likewise, the measured position of the difference between Fermi energy and the valence band maximum at a low base pressure of

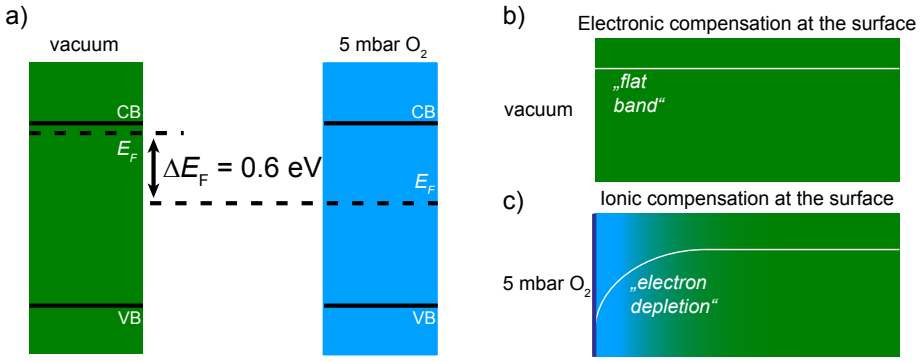

Figure 6.7.: Schematic illustration of the relative positions of the Fermi energy at a low base pressure and 5 mbar pO_2 at 770 K (a). The surface carrier concentration in the electronic compensation (b) and in the ionic compensation regime (c) resulting in a flat band and an electron depletion, respectively. The figure was published in ref. [121].

10^{-8} mbar is slightly above the conduction band minimum extrapolated at 770 K (figure 6.6 (b), dashed line)[37]. The more the pO_2 is increased the more the valence band maximum is shifted towards lower binding energies, indicating a continuous shift of the Fermi energy deeper into the band gap. Note that the extrapolation of the band gap down to temperatures considerable lower than the ones used during the empirical determination of the band gap temperature dependence, might be affected by small errors, as will be disucssed in sec. 8.4 and ch. 9.[37] For classical semiconductors with a full ionization of shallow donor dopants a Fermi energy slightly below the conduction band edge is expected considering the experimental accuracy of the measurement setup.[56, 142] Consequently, the shown position of the Fermi energy in UHV is consistent with classical donor-doped semiconductors and indicates that most donors are fully ionized.

Figure 6.6 c) summarizes the shift of the binding energy relative to the measured value at an base pressure of 10^{-8} mbar. It is clearly visible that all core level spectra and the valence band maximum shift with an increasing pO_2. The relative shifts of the different core levels nearly overlap on a single line with the one of the valence band maximum, indicating that all peaks shift rigidly with pO_2 within the experimental accuracy. The maximum shift at 770 K and a pO_2 of 5 mbar for the different measured binding energy values is about -0.6 eV. In the rigid band model the apparent binding energy of the core levels is governed solely by the Fermi energy of the thin film, cf. sec. 3.5. It is therefore a direct measure of the concentration of electrons.[119, 142, 143] Consequently, the measured rigid shift of all core level spectra of $SrTiO_3$ and the valence band maximum can be explained by a mere shift of the Fermi energy at the surface, i.e. an effective change of the conduction band filling.

Figure 6.7 illustrates schematically the relative positions of the Fermi energy in the low base pressure regime and 5 mbar pO_2 at 770 K (a) as indicated by the AP-XPS results. At a base pressure of 10^{-8} mbar, the position of the Fermi energy close to the conduction band suggests a bulk-like behavior of the n-$SrTiO_3$ surface, with a constant carrier concentration over the entire thickness of the thin film (flat band). In contrast, at increased pO_2, the observed relative shift of the Fermi energy into the band gap indicates a reduction of the electron concentration and hence an electron depletion at the surface of the n-$SrTiO_3$ thin film. In fact, these results suggests that the surface of n-$SrTiO_3$ rather acts like acceptor-doped or undoped $SrTiO_3$ under oxidizing conditions, implying a significant pO_2-dependent change in the electronic surface properties. The electron depletion is formed as a compensation of a negative charge that is generated at the n-$SrTiO_3$ surface in dependence on the oxidizing conditions. With increasing pO_2 the negative surface charge increases, hence resulting in a more pronounced electron depletion. Assuming a process limited to the surface it can be inferred that the electron concentration deep in the thin film is given by the niobium dopant concentration. The resulting electron concentration difference between the bulk and the surface of the thin film needs to be compensated and thus implies the formation of a surface space charge layer and with that, a band bending that can be controlled in a reversible manner by varying the pO_2. As will be shown in section 6.2, however, the assumption of a flatband case in UHV conditions does not hold entirely. Nevertheless, it allows the estimation of a lower limit of the generated surface charge.

Influence of adsorbates, defects and charging on XPS spectra

In terms of the chemical and electrical properties of doped and undoped $SrTiO_3$ that are influenced by a negative surface charge, there is a wide variety of possible impacts on AP-XPS measurements that needs to be considered. Firstly, typical contamination need to be excluded. In addition to the previously shown evolution of the C1s core level spectra (fig. 6.2 (a)), figure 6.8 shows the core level spectra of typical n-$SrTiO_3$ surface contamination like molybde num (Mo3d, (a)), sulfur (S2s, (a)) and silicon (Si2s, (b)) measured by lab-based AP-XPS at elevated temperatures and different pO_2. Regardless of applied pO_2 neither molybdenum nor sulfur nor silicon contamination can be detected at elevated temperatures. Consequently, the systematic and reversible character of the surface space charge formation as well as the disappearance of any observable carbon peak intensity makes a merely contaminants-based scenario unlikely.

Secondly, one major aspect that comes to mind in terms of $SrTiO_3$, especially in variable oxygen partial pressures, is the pO_2-dependent formation and annihilation of oxygen vacancies. Similar to variations in the donor doping concentration, this effect is detectable by spectroscopic experiments by a changing concentration of Ti^{3+} ions which can be identified as a shoulder on the right hand side of the Ti2p spectra.[124] The presence of oxygen vacancies at the surface of $SrTiO_3$ is

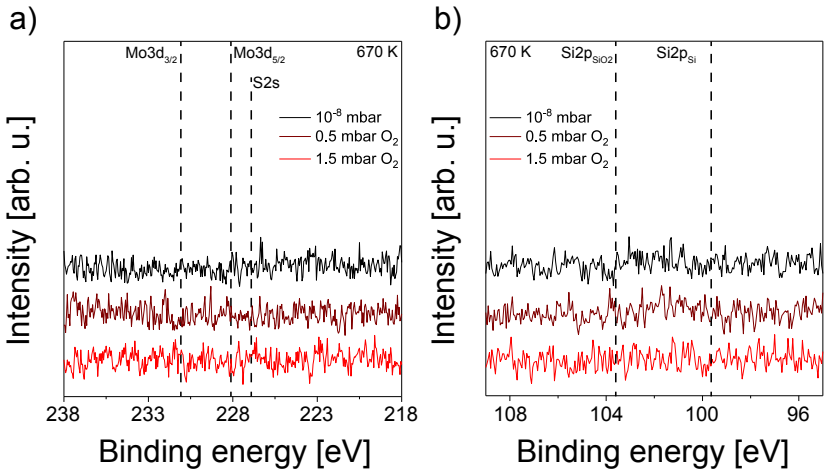

Figure 6.8.: Core level spectra of typical surface contamination of n-$SrTiO_3$ surfaces. The absence of the Mo3d, the S2s core level and the Si2p core level is shown in (b) and (c), respectively. The figure was published in the supplement of [121].

known to influence experimental methods that at first do not seem sensitive to variable oxygen vacancy concentration.[123] In donor-doped $SrTiO_3$, however, the impact of oxygen vacancies is reduced dramatically. The expected concentration of donor-type oxygen vacancies at the temperatures and oxygen partial pressures used within this work (470 K to 770 K, 10^{-8} mbar to 5.0 mbar O_2) is 10^{18} cm^{-3} and below.[37, 58] This value is significantly lower than all used donor doping concentrations. Hence, a varying oxygen vacancy concentration alone is not expected to provide sufficient charge for substantial changes of the surface space charge region in highly-doped $SrTiO_3$.

These logical considerations are corroborated by the results of the lab-based AP-XPS measurements. Figure 6.9 shows the $Ti2p_{3/2}$ spectra of a 1.0 at% n-$SrTiO_3$ sample measured by lab-based AP-XPS at 770 K in UHV conditions (b) and at 5.0 mbar O_2 (c). Neither in UHV nor in high pO_2 conditions, a significant peak or shoulder related to Ti^{3+} is detectable, indicating a Ti^{3+} concentration below the detection limit and a negligible contribution of oxygen vacancies on the thin film′s electronic properties even in UHV conditions. This finding is substantiated by the superposition of the Ti2p peaks measured at different conditions where only a slight broadening of the peak is detectable which is not related to Ti^{3+} states. As was already shown in section 6.1 and will be taken upon below, this broadening is due to the space charge layer at the surface of n-$SrTiO_3$. Consequently, both modeled calculations as well as experimental findings lead to the conclusion that the pO_2-dependent formation and annihilation of oxygen vacancies does not play a

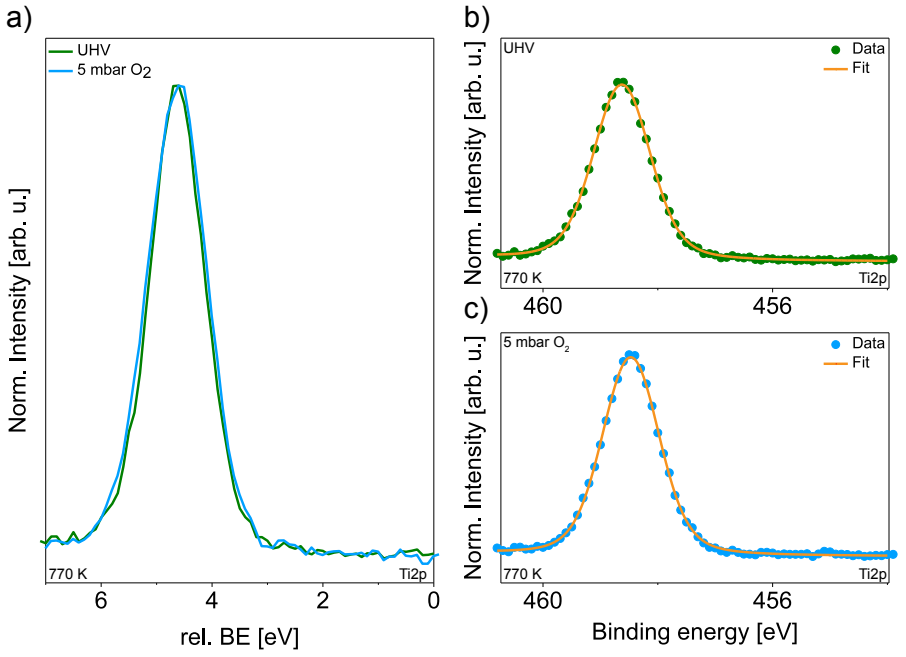

Figure 6.9.: Superposition of the Ti2p peaks is shown in (a). Magnified $Ti2p_{3/2}$ spectra measured by lab-based AP-XPS at 770 K at a pressure of 10^{-8} (b) and a pO_2 of 5.0 mbar (c). No additional peak that might be related to Ti^{3+} and thereby oxygen vacancies is detectable neither in the low base pressure nor in the high pO_2 conditions. The figure was published in the supplement of ref. [121].

significant role for the observed negative surface charge.

Thirdly, in spectroscopic experiments X-ray beam-related effects can cause a charging of the sample, falsely indicating a non existing surface charge. This typically results in a shift of the apparent binding energy towards higher values.[118] Considering that intuitively, and unambiguously shown in electronic transport experiments in sec. 8.1, $SrTiO_3$ should be more conducting in UHV than in oxidizing atmospheres, the n-$SrTiO_3$ thin film shows the opposite behavior, making charging effects on the apparent binding energy unlikely. To more safely exclude charging effects, additional reference measurements were performed on an Au electrode were deposited on the sample with an additional Ti interlayer to ensure an ohmic contact to the thin film. Figure 6.10 shows a schematic illustration of the sample stack (a) and the superposition of the Au4f peak of a 1.0 at% n-$SrTiO_3$ sample measured at 670 K and pO_2 ranging from 10^{-8} mbar up to 1.5 mbar O_2 (b).

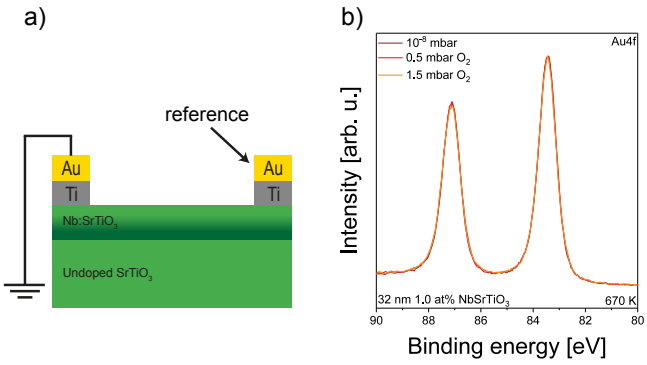

Figure 6.10.: Representative sample stack (a) and Au4f core level spectra taken on Ti/Au reference electrodes deposited on a 1.0 at% n-$SrTiO_3$ sample at a temperature of 670 K and different pO_2 (b). There is no shift detectable regardless of the apparent pO_2. The figure was published in the supplement of [121].

In contrast to the measurements of the characteristic core levels of $SrTiO_3$, there is absolutely no shift visible in the Au4f spectra regardless of the adjusted pO_2. Consequently, X-ray beam-related charging effects are excluded for all AP-XPS measurements.

Surface charge calculation

The binding energy shift shown above implies a surface potential that is reversibly controlled by varying the ambient oxygen atmosphere. This surface potential is generated by a corresponding negative surface charge that can be estimated considering classical semiconductor theory. Figure 6.11 shows the decay of the determined surface potential into the sample (a), a schematic illustration of the negative surface charge and a compensating electron depletion layer on the n-$SrTiO_3$ side (b) and the corresponding surface charge (c).

The negative surface charge is compensated by electron depletion in the near surface region. For electron depletion (reflecting the majority carriers), uncompensated niobium-dopants dominate the field screening, rendering a constant charge density within the surface space charge layer and thus a parabolic potential profile given by [65]

$$\phi(\mathrm{x}) = -\frac{N_\mathrm{D} e}{2\epsilon_0 \epsilon_\mathrm{r}} \left(\Delta x_\mathrm{SCL} - x\right)^2 \quad , \tag{6.1}$$

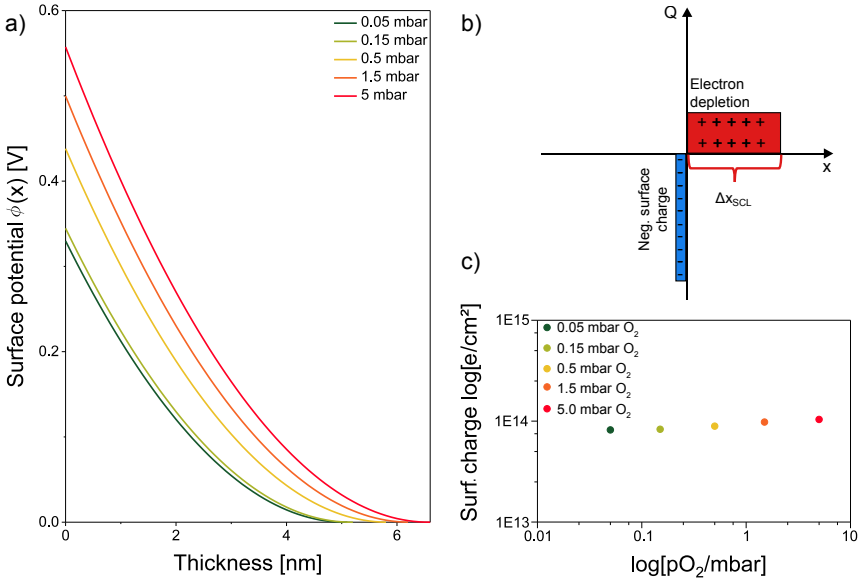

Figure 6.11.: The decay of the surface potential into n-$SrTiO_3$ sample in different pO_2 is shown in (a). Schematic illustration of the negative surface charge compensation by electron depletion underneath the surface (b). The corresponding surface charge is presented in (c).

where ϕ(x) denotes the potential at a given depth x, N_D the donor-doping concentration, e the electron charge, ϵ_0 the vacuum permittivity, ϵ_r the temperature-dependent relative permittivity and Δx_{SCL} the space charge layer width. The temperature dependence of the relative permittivity is empirically given by [37, 38]

$$\epsilon_r(T) = \frac{78400\ \text{K}}{T - 28\ \text{K}} \quad , \tag{6.2}$$

where T denotes the temperature. The relative permittivity at 770 K is determined from literature to $\epsilon_r(770\ \text{K}) \sim 105$. The resulting space charge layer width is calculated by [65]

$$\Delta x_{SCL} = \sqrt{\frac{2\epsilon_0\epsilon_r\phi_0}{eN_D}} \quad , \tag{6.3}$$

where ϕ_0 denotes the potential right at the surface (x=0). Note that the surface space charge layer width shows a slight temperature dependence due to the tem-

perature dependence of the relative permittivity ϵ_r. Combining eqs. 6.1, 6.2 and 6.3 the potential profile is determined by

$$\phi(\mathrm{x,T},\phi_0) = -\frac{N_D e}{2\epsilon_0 \left(\frac{78400\ \mathrm{K}}{T-28\ \mathrm{K}}\right)} \left(\sqrt{\frac{2\epsilon_0 \left(\frac{78400\ \mathrm{K}}{T-28\ \mathrm{K}}\right) \phi_0}{eN_D}} - x \right)^2 \quad . \tag{6.4}$$

Figure 6.11 (a) shows the calculated potential decay into the sample at 770 K for different pO_2. Here the binding energy shift between a low base pressure and the given pO_2 is used as the surface potential ϕ_0. A higher pO_2 leads to a higher surface potential and thereby to a change in the potential decay into the sample.
From the measured surface potential the negative surface charge necessary to induce the surface space charge layer is calculated by [65]

$$Q/A = \sqrt{2\epsilon_0 \epsilon_r \phi_0 N_D e} \quad , \tag{6.5}$$

where Q/A denotes the surface charge in e/cm^2. The estimated surface charge is depicted in figure 6.11 (c). It ranges from 7.95×10^{13} e/cm^2 up to 1.02×10^{14} e/cm^2 at 0.05 mbar O_2 and 5 mbar O_2, respectively. The corresponding space charge layer width ranged from 5 nm to 7 nm. As seen from the Fermi energy position relative to the conduction band edge, the impact of even comparably low changes in the surface charge Q/A on the electrical surface properties is significant. An alteration of the surface charge by less than a factor of two leads to substantial changes in the surface band bending.
It needs to be noted that this calculation is only valid for the assumption of the flatband case in the low base pressure regime. In addition, it is also assumed that the measured binding energy position is the binding energy position right at the surface. As will be shown below, both these assumptions do not hold entirely, due to band bending present already in UHV conditions and a possible fluctuation of the relative permittivity ϵ_r due to its field dependence. The potential errors, however, both underestimate the present surface potential. Therefore, all surface charges calculated from AP-XPS spectroscopy measurements are regarded as a lower limit.

Apparent binding energy

It is important to note that what is referred to here as binding energy is only the apparent binding energy value extracted from the fit of the peak profiles. Figure 6.12 shows the impact of the pO_2-dependent surface space charge layer over the entire probing depth (a) and a schematic illustration of the effect of the potential profile on the results of typical XPS measurements (b).
As the depth probed by the spectroscopy is in the same order of magnitude as the extent of the space charge layer, the measured signal is a superposition of the

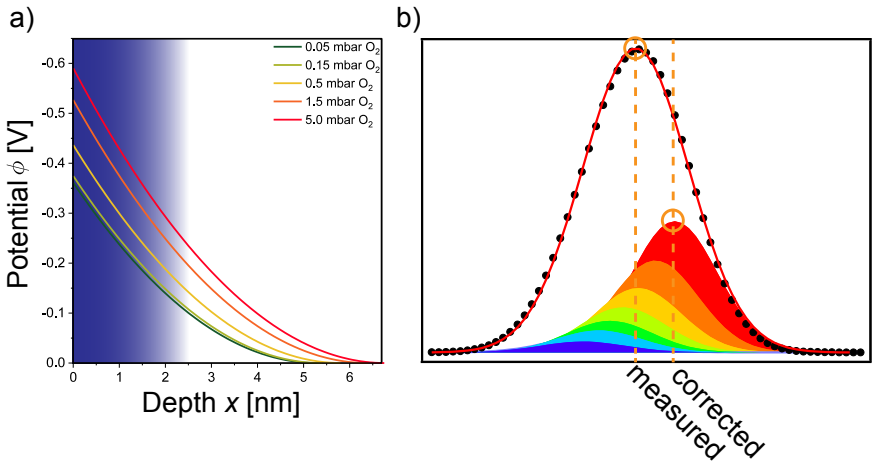

Figure 6.12.: The impact of the pO_2-dependent surface space charge layer over the entire probing depth is shown in (a). A schematic illustration of the consequences of the potential profile on the XPS measurements is displayed in (b). The full circle gives the measured binding energy position while the dashed circle determines the real binding energy of the top most surface layer. The simulation of the spectra was conducted by D. N. Mueller (PGI-6, FZJ).

peaks of varying binding energy according to the profile of the space charge layer, weighted by the attenuation.[139, 144] Within the surface space charge layer, the binding energy is given by

$$BE(x) = BE_{\text{bulk}} - \phi(x) \quad , \tag{6.6}$$

where $BE(x)$ denotes the binding energy at a specific depth x and BE_{bulk} the unaffected binding energy deep inside the thin film. The specific binding energy of all core levels in different probing depths are slightly shifted against each other, which results in two effects. First, every measured core level peak with a specific incident photon energy is broadened asymmetrically. This asymmetry could neither be observed nor unambiguously fitted in the experiments, probably due to the insufficient measurement accuracy. Second, the measured binding energy position is not the *real* binding energy of the top most sample layer, see figure 6.12 (b), but just an apparent binding energy which stems from the weighted superposition of all measured core level regions at different depths. Consequently, the apparent binding energy as obtained from the spectroscopy underestimates the surface potential. A quantitative correction to the true binding energy at the surface and thus the surface potential is only possible if the shape of the space charge layer is undoubtedly known, and the value of the relative permittivity (ϵ_r) is constant over the entire

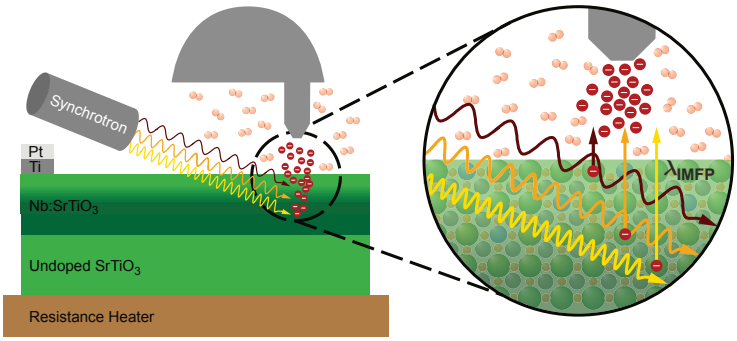

Figure 6.13.: Schematic illustration of the layer stack used for *in-situ* AP-XPS experiments enabling the application of thermodynamic biases during the measurements. Due to different photon energies and resulting inelastic mean free paths for a given core level, electrons leave the sample from different depths.

space charge layer. The relative permittivity of n-$SrTiO_3$ single crystals utilized here, however, might be influenced by the electric field in the generated space charge layer.[59] In addition, the relative permittivity of n-$SrTiO_3$ thin films might also vary from the ones determined for single crystals due to the reduced length scales. Both these requirements are not fulfilled and a quantitative correction is not possible here. Nevertheless, despite the underestimation of the pO_2-dependent binding energy shift, the apparent values can be used to calculate a lower limit of both the surface potential and the corresponding generated negative surface charge.

6.2. Binding energy shift at different probing depths

So far, the pO_2-dependent surface space charge layer has been described only indirectly by its impact on the electronic properties of the n-$SrTiO_3$ surface, namely the sheet carrier concentration at different film thicknesses (section 5.2) and the pO_2-dependent shift of the Fermi energy. In order to characterize the surface space charge layer directly and clarify its origin synchrotron-based (Beamline 11.0.2, Advanced Light Source, Berkeley, CA, USA[145]) AP-XPS measurements[120] at different pO_2 and varying incident photon energies with a pass energy of 50 eV were used. By varying the X-ray photon energy for a given core level different inelastic mean free paths (IMFP) and hence measurements at specific probing depths are achieved. Again the characteristic core levels of n-$SrTiO_3$, Sr3d, O1s, Ti2p and in addition strontium 3p (Sr3p) as well as the valence band region were investigated at a temperature of 670 K and different pO_2. Figure 6.13 shows a schematic illustration of the sample stack allowing direct access to the surface properties while

applying *in-situ* thermodynamic biases (T, pO_2). The as-prepared sample was contacted from the top using thin metal contact strips consisting of 50 nm platinum on top of 5 nm titanium deposited by e-beam evaporation. This way, an ohmic contact between the n-$SrTiO_3$ thin film and the analyzer ground contact and hence Fermi coupling is ensured. The photon energy was varied from 1080 eV to 270 eV corresponding to IMFPs ranging from 1.2 nm down to 0.4 nm for the Sr3d core level which allowed for an increased surface sensitivity and depth profiling. The IMFP was calculated by TPP2M formula [146] and corrected by the electron take off angle of 40° to arrive at the probing depth. The atmosphere applied *in-situ* during the measurements ranged from 10^{-8} mbar base pressure up to 1.3 mbar controlled oxygen atmosphere, which defined the total pressure during the AP-XPS measurements. All AP-XPS data shown here are energy corrected using the Au4f core level measured of a thin gold foil attached to the sample at every photon energy and atmospheres adjusted.[140, 141] Note that this corrects possible variations in the incident photon energy. A typical measurement took about 30 minutes to 1 hour to adjust and stabilize temperature and gas pressure, followed by about 24 hours to execute the spectroscopic experiments. During the entire time, the sample was kept under constant conditions. No transient changes in spectral shape or binding energy position were observed on a longer time scale, indicating spectroscopic equilibrium after the adjustments.

Figure 6.14 shows the O1s, Ti2p, Sr3p and Sr3d core levels and the valence band region of a 32 nm thick 1 at% n $SrTiO_3$ thin film measured with different photon energies implying different IMFPs and thereby probing depths ranging from 1.3 nm down to 0.4 nm at a low base pressure of 10^{-8} mbar (a, green) and a pressure of 1.3 mbar O_2 (b, blue). The dashed black lines indicate the apparent binding energy position at the highest measured probing depth. The different probing depths for the different core levels result from the combination of the specific binding energy position and the used incident photon energy, cf. section 3.5. As indicated by the black dashed lines, the specific apparent binding energy positions of every core level and the valence band region shift towards lower values for increasing pO_2. This is consistent with the lab-based AP-XPS results at varying pO_2 shown above.

In addition, all core levels as well as the valence band region shift towards lower binding energies with higher probing depths for both the measurements in a low base pressure and a pO_2 of 1.3 mbar. As explained above in section 6.1 such a shift is caused by a surface potential which decays into the sample. Consequently, these findings prove the existence of a surface space charge layer at the n-$SrTiO_3$ surface directly. Due to the fact that the rigid shift with varying probing depths occurs not only at high pO_2 but also in the low base pressure regime shows that the surface space charge layer is already present at ultra high vacuum conditions. This is contrary to what has been assumed in the lab-based experiments with varying pO_2. It is also contradictory to the assumption of a flat band case in UHV which is used to determine the generated negative surface charge but as explained above this only leads to an underestimation of the actual surface potential and the corresponding negative surface charge.

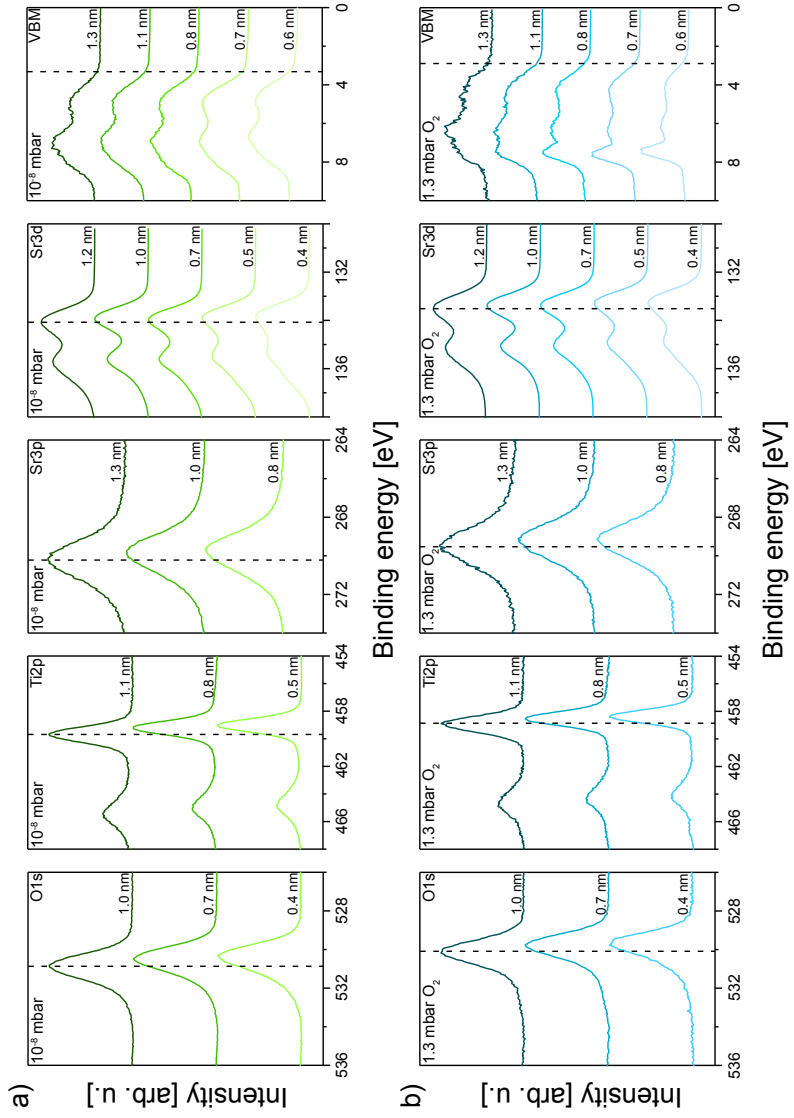

Figure 6.14.: Synchrotron-based AP-XPS measurements of the O1s, Ti2p, Sr3p, Sr3d core levels and the valance band region using different photon energies implying different inelastic mean free paths and thereby probing depths ranging from 1.3 nm down to 0.4 nm in low base pressure of 10^{-8} mbar (a) and 1.3 mbar O_2 (b) at 670 K. The black dashed lines indicate the position of the apparent characteristic binding energy at the highest measured inelastic mean free path.

Utilizing the more surface sensitive measurement accuracy of the synchrotron-based AP-XPS it is possible to investigate possible chemical changes at the n-$SrTiO_3$ surface more precisely. Apart from the binding energy shift with varying probing depth for both UHV conditions and high pO_2 the Sr3p spectra does not show any spectral changes due to its low intensity. Therefore, it will not be examined any further. Figure 6.15 shows the Ti2p core level spectra for different probing depths and their superposition (shift of the binding energy axis) measured at a low base pressure of 10^{-8} mbar (a, c, green) and at a high pO_2 of 1.3 mbar (b, d, blue) at 670 K.

As described above, the shift of the measured core levels towards lower binding energies with decreasing probing depths in both UHV conditions and high pO_2 directly illustrate the presence of a surface space charge layer. In addition, the superposition of the normalized Ti2p core level reveal a slight broadening with increasing probing depth. As explained in section 6.1 this broadening is a direct result of the surface space charge layer's potential decay since it leads to slightly different binding energy positions in different information depths which are superimposed by the AP-XPS measurement setup. As already seen in the lab-based AP-XPS measurements at different pO_2 neither in low base pressures nor in high pO_2 any changes of the peak shape could be detected that might be interpreted as chemical changes. Especially, no Ti^{3+} peak arises as a shoulder on the right side of the Ti2p spectra.

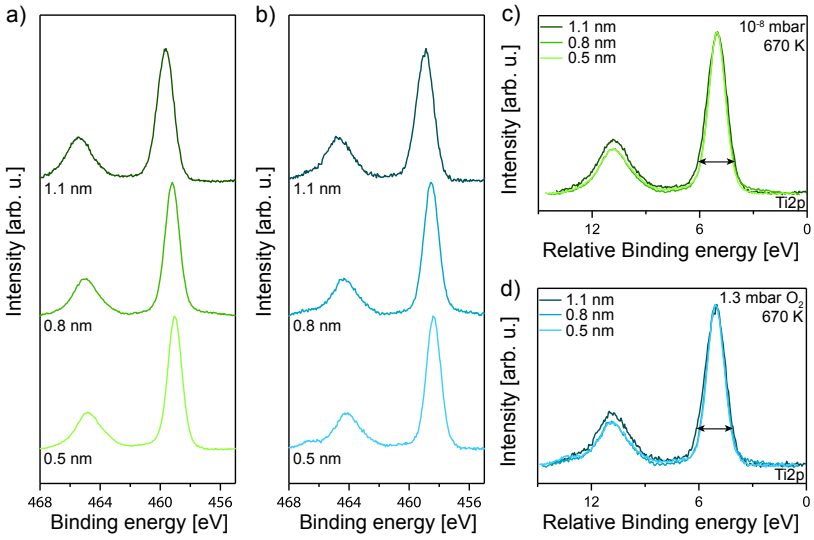

Figure 6.15.: Ti2p core level spectra and their normalized superposition (shift of the binding energy axis) measured in a low base pressure of 10^{-8} mbar (a, c, green) and at a high pO_2 of 1.3 mbar (b, d, blue) at 670 K and different probing depths ranging from 1.1 nm down to 0.5 nm.

Consequently, a surface redox process that might involve a significant amount of oxygen vacancies is excluded again, cf. section 9.1.[88]

Figure 6.16 illustrates the measurements of the O1s core level at different probing depths and their superposition observed at a low base pressure (a, c, green) and at high pO_2 (b, d, blue) at 670 K. Again, both measurements in UHV conditions and high pO_2 both show a shift towards lower binding energies with decreasing probing depth which is corresponding to the presence of the surface space charge layer. In neither of the experiments an altering peak shape could be detected that can unambiguously interpreted as chemical changes. The superposition of the measured O1s core level, however, shows a characteristic probing depth-dependent evolution of the full width half maximum (FWHM). The highest FWHM was detected at the lowest probing depth. This is true for both UHV conditions and high pO_2. The results of the remaining two probing depths is identical in terms of data accuracy. This effect might be due to the contrary impact of two effects. Firstly, as mentioned above, the presence of the surface space charge layer increases the FWHM with increasing probing depth. Secondly, a suspected additional component at the n-$SrTiO_3$ surface on the left side of the O1s peak increases the FWHM with decreasing probing depth. Hence, at higher probing depths the two effects might cancel out each other while at the lowest probing depth the impact of the additional oxygen

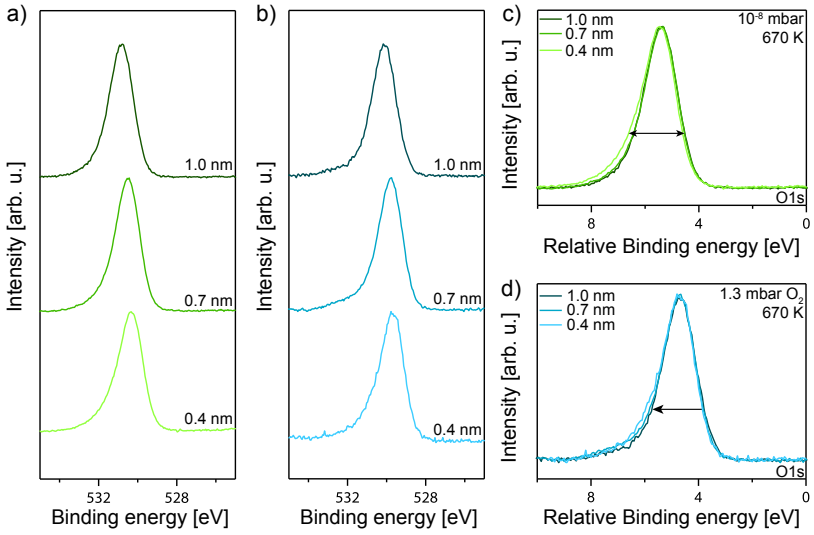

Figure 6.16.: O1s core level spectra and their normalized superposition measured in a low base pressure of 10^{-8} mbar (a, c, green) and at a high pO_2 of 1.3 mbar (b, d, blue) at 670 K and different probing depths ranging from 1.0 nm down to 0.4 nm.

component becomes dominant. Note that due to the measurement accuracy, the unknown binding energy position of the additional surface component, a resulting superposition of different components as well as the low number of possible data points did not allow for a unambiguous fitting of the suggested surface component.

Figure 6.17 shows the Sr3d core level spectra as well as their superposition measured in a low base pressure (a, c, green) and a high pO_2 of 1.3 mbar (b, d, blue) at 670 K and different probing depths. The Sr3d core level spectra also show the shift towards lower binding energies with decreasing probing depth indicating the presence of the surface space charge layer. In addition, the superposition of the Sr3d core level spectra reveals two probing depth-dependent effects. Firstly, as already explained in the case of the O1s spectra, the spectra show an non-monotonous broadening with decreasing probing depth. From the highest to the second highest probing depth the FWHM slightly decreases. For all lower probing depths, however, the FWHM increases monotonously. In accordance to the results of the O1s core level spectra, this might be due to the interplay of two contrary effects caused by the presence of the surface space charge layer and an additional surface component. As will be shown below it was possible to concisely fit the SrO surface second component at varying probing depths. Secondly, the intensity valley between the $Sr3d_{3/2}$ peak and the $Sr3d_{5/2}$ peak is continuously flattened with decreasing probing depth with the exception of the highest probing depth. As

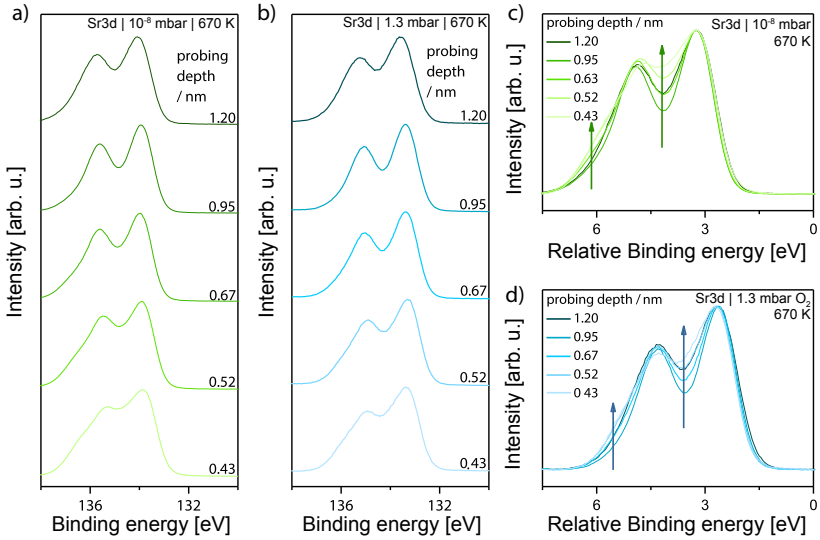

Figure 6.17.: Sr3d core level spectra and their normalized superposition measured in a low base pressure of 10^{-8} mbar (a, c, green) and at a high pO_2 of 1.3 mbar (b, d, blue) at 670 K and different probing depths.

explained in section 9.1 a solely negative surface charge that does not involve chemical changes in the strontium sublattice would lead to a consistent broadening of all characteristic core levels and a resulting flattening of the intensity valley between the $Sr3d_{3/2}$ peak and the $Sr3d_{5/2}$ with increasing probing depth due to the presence of the surface space charge layer. In contrast, the precipitation of SrO a the n-$SrTiO_3$ surface leads to a flattening of the intensity valley between the $Sr3d_{3/2}$ peak and the $Sr3d_{5/2}$ peak with decreasing probing depth due to the presence of a second high binding energy component at the n-$SrTiO_3$ surface. Consequently, the determined probing depth-dependent evolution of the intensity valley between the $Sr3d_{3/2}$ and $Sr3d_{5/2}$ peaks proves a surface redox process responsible for the space charge formation that does involve the strontium sublattice, already suggesting the precipitation of SrO at the n-$SrTiO_3$ surface.

Figure 6.18 shows the valence band at different probing depths and their normalized superposition measured at a low base pressure (a, c, green) and a high pO_2 of 1.3 mbar (b, d, blue) at 670 K. As all characteristic core levels, the valence band maximum also inhibits a shift of the binding energy towards lower values with decreasing probing depth. Additional spectral changes are also present in the valence band region. In the high pO_2 regime an additional feature rises at higher binding energies. The feature is more pronounced the more the probing depth is reduced. In good agreement with literature, this evolution is identified as a part

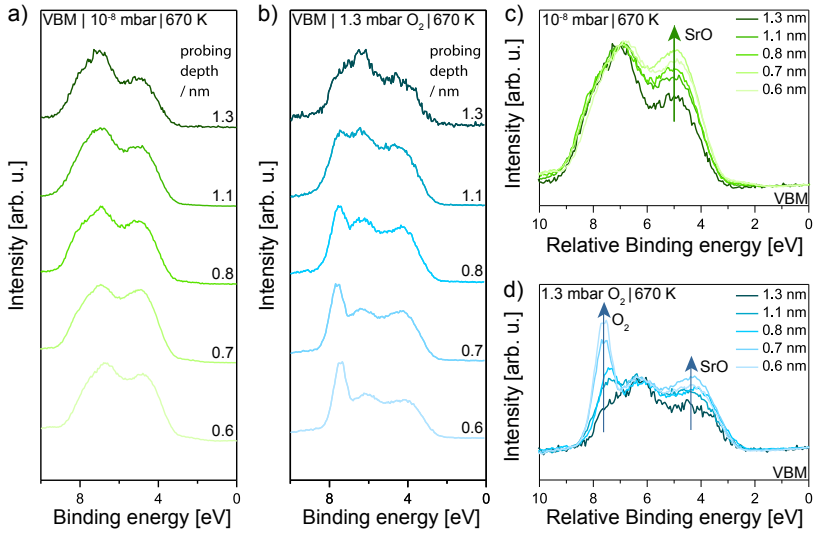

Figure 6.18.: Valence band spectra and their normalized superposition measured in a low base pressure of 10^{-8} mbar (a, c, green) and at a high pO_2 of 1.3 mbar (b, d, blue) at 670 K and different probing depths.

of the highest occupied molecular orbit (HOMO) of the oxygen gas present in the measurement chamber.[147] Furthermore, in both the low base pressure regime as well as in high pO_2 conditions the right side of the valence band rises with decreasing probing depth. This might be due to the already mentioned changes in the strontium sublattice. As will be shown in section 9.2 strontium oxide precipitates at the surface. The valence band of this additional layer is in the same binding energy regime as the valence band of the n-$SrTiO_3$ thin films investigated here.[139] Hence, the additional rising feature may be identified as part of the SrO surface layer valence band. The superposition of the two valence bands, however, affected the determination procedure of the valence band maximum as described for the measurements with solely varying pO_2 by indeterminable difficulties. Hence, in the following the position of the valence band maximum is not considered for the measurements at different probing depths.

To further investigate the properties of the present surface space charge layer and the underlying surface redox process, the measured core level were fitted. Figure 6.19 shows the apparent binding energy positions of the O1s, the Ti2p, the Sr3p and the Sr3d core level resulting from the different fits. Note that as the depth probed by spectroscopy is in the same order of magnitude as the extend of the surface space charge layer, the signal is a superposition of peaks of varying binding energies according to the profile of the space charge layer and weighted by the attenuation.[144] The O1s, Ti2p and Sr3d core level were fitted as described in section 6.1. The Sr3p core level was fitted using Shirley background subtraction in combination with a single Voigt function.

As already indicated above, the binding energy positions of all core levels are by $\sim$0.6 eV higher in the low base pressure regime, which is in good agreement with the lab-based AP-XPS measurements, cf. sec. 6.1. In both the low pressure regime and in high pO_2 conditions all core level shift rigidly with the probing depth by $\sim$-0.3 eV when varying the probing depth. Note that the probing depth-dependent apparent binding energies of the Sr3d core level showed slight deviations in their evolution due to changes in the chemical surface composition. The evolution of all the apparent binding energy positions with probing depth indicated a course of the potential decay into the sample that corresponds to a negative surface charge, cf. section 6.1. The lower the used probing depth becomes the stronger the apparent binding energy shifts towards lower values representing a higher potential present at the surface, cf. equ. 6.1. This increase of the local potential corresponds to a further reduction of the electron concentration close to the surface. Consequently, these results directly prove the existence of a surface space charge layer in the n-$SrTiO_3$ thin film not only at a high pO_2 of 1.3 mbar but also at a low base pressure of 10^{-8} mbar. Even in the low pressure regime the surface space charge layer is not fully removed. Due to the surface space charge layer being present already at a low base pressure, the actual shift of the binding energy position in high pO_2 in comparison to the bulk value deep in the sample is underestimated. Accordingly, the calculated negative surface charge still holds as a lower limit.

Special attention is paid to the Sr3d core level since the evolution of the intensity valley between the $Sr3d_{3/2}$ and the $Sr3d_{5/2}$ peak demonstrates the strontium

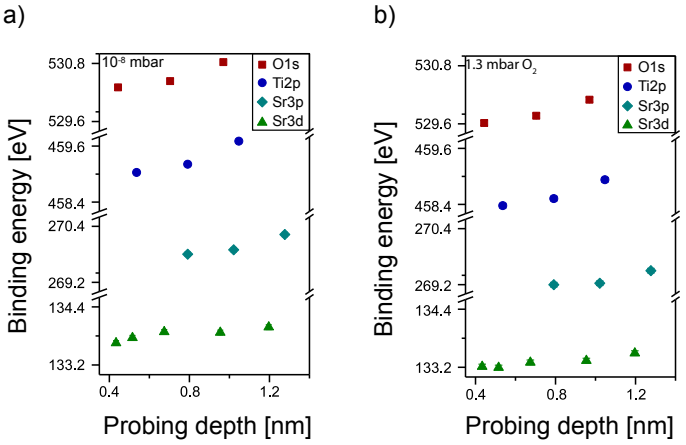

Figure 6.19.: Probing depth dependent apparent binding energy positions of the O1s, Ti2p, Sr3p and Sr3d core levels are shown in (a) for low base pressures and (b) at 1.3 mbar O_2, respectively. The probing depth dependent rigid shift of all core levels in both a low base pressure and 1.3 mbar O_2 demonstrates the presence of a surface space charge layer in both conditions.

sublattice to be involved in the surface redox process. Figure 6.20 shows the evolution of the Sr3d spectra for different probing depths ranging from 1.2 nm down to 0.4 nm measured at a temperature of 670 K, at a low base pressure of 10^{-8} mbar (a) and an adjusted high pO_2 of 1.3 mbar (b). Embedded into the data are individual fits after a Shirley background subtraction consisting of two Voigt doublets representing the saturated $SrTiO_3$ lattice (low binding energy component, light blue) and a SrO surface secondary phase (high binding energy component, turquoise) separated by 0.8 eV. The red circles and triangles indicate the binding energy position of the $Sr3d_{5/2}$ low binding energy component peak at the different probing depths measured at a low base pressure and high pO_2, respectively. The fitted binding energy position of the $Sr3d_{5/2}$ low binding energy component peaks for the different probing depths are shown in (c). The relative contribution of the SrO surface component estimated by its peak area is shown in (d).

As a result of the varied oxygen atmosphere, the peak positions obtained in a low base pressure and at high pO_2 are offset by ∼-0.55 eV. In addition, a probing depth-dependent evolution of the SrO surface component is observed at a low base pressure and in high pO_2. With decreasing probing depth the SrO surface component increases strongly, indicating a distinct surface termination of SrO coverage at the surface of the n-$SrTiO_3$ sample. It is thereby responsible for the flattening of intensity valley between the $Sr3d_{3/2}$ and the $Sr3d_{5/2}$ peaks in both UHV conditions and at a pO_2 of 1.3 mbar. The overall contribution of the SrO second

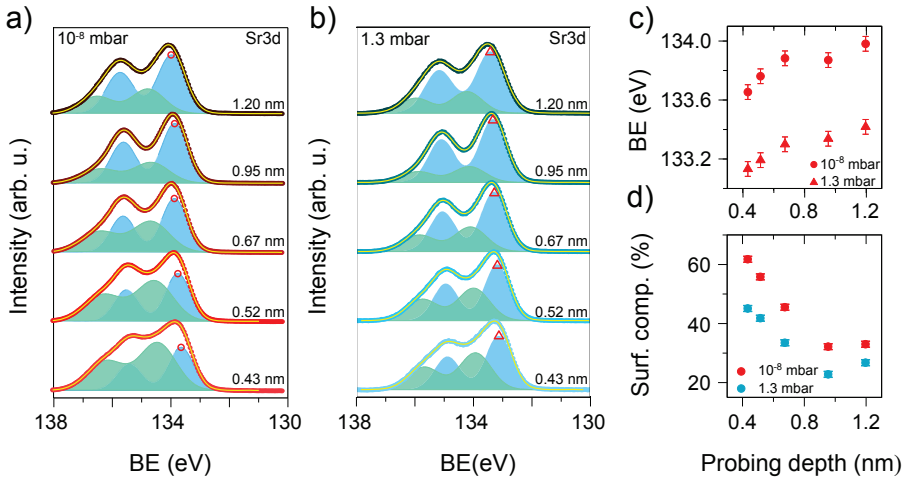

Figure 6.20.: Evolution of the Sr3d spectra at different X-ray photon energies resulting in different probing depths measured at 670 K and a low base pressures of 10^{-8} mbar (a) and 1.3 mbar O_2 (b). The dashed lines indicate the position of the $Sr3d_{5/2}$ low binding energy component peak (light blue) measured at the highest probing depth. The probing depth-dependent binding energy positions of the $Sr3d_{5/2}$ low binding energy component peaks (circles) are shown in (c). The relative contribution of the surface component (turquoise) estimated by the area of the high binding energy doublet in comparison to the peak area is shown in (d). With a decreasing probing depth, the binding energy shifts towards lower values while the share of the high binding energy component phase is increased for both measurements at low base pressures and high pO_2. This figure is published in ref. [115].

component to the Sr3d core level measurements is determined by the areal ratio of the high binding energy doublet. At a low base pressure the contribution increases from 33 % to 62 % with decreasing probing while it increases from 27 % to 45 % at 1.3 mbar O_2, cf figure 6.20 (d). In agreement with literature, this finding at first sight indicates a higher contribution of the surface component in lower base pressure, which would contradict a higher SrO concentration at higher pO_2.[38, 44, 52, 72] Nevertheless, the observations here can be understood by a chemical response limited to the very surface region of the n-$SrTiO_3$ sample which is assumed to be accompanied by nanoscopic morphology changes as will be discussed in section 9.2.

Summary

In this chapter the pO_2-dependent formation of a space charge layer at the surface of n-$SrTiO_3$ was investigated. In the first section, it was demonstrated by lab-based AP-XPS measurements that with increasing pO_2 the apparent binding energy positions of all characteristic core levels and the valance band maximum shift rigidly towards lower values. This is due to a shift of the Fermi energy deeper into the band gap that is accompanied by an electron depletion layer underneath the surface. This depletion is compensated by the generation of a negative surface charge, which dominates the properties of the surface space charge layer. The surface charge as well as the course of the potential decay into the surface has been calculated. These calculations will be used throughout the next chapters. In addition, it has been shown that what is referred to here as binding energy is an apparent binding energy which evolves from the superposition of different core level spectra in different probing depths. Consequently, the shown calculations describe the lower limit of the generated surface charge.

In the second section, synchrotron-based AP-XPS experiments at different probing depths directly track the course of the potential profile into the sample. With increasing probing depth the shift relative to low base pressure conditions is reduced. This effect is due to the decay of the surface potential into the sample. It directly proves the former indirectly described space charge layer at the surface of n-$SrTiO_3$ in both UHV conditions and at a high pO_2 of 1.3 mbar. In addition, the Sr3d core level showed spectral changes that were identified as a strontium oxide second component proving the strontium sublattice to be involved in the surface redox reaction which will be further examined in section 9.1.

To further investigate the properties of the emerging surface space charge layer the next chapter focuses on the impact of the surface charge as its dominating parameter and its dependency on pO_2, donor-doping concentration and temperature.

7. Thermodynamic control of the surface charge

The negative surface charge is the dominating parameter of the pO_2-dependent space charge layer at the surface of n-$SrTiO_3$. As can be seen in eqs. 6.2 and 6.5 the generated surface charge depends directly on the surface potential ϕ_0, the temperature-dependent relative permittivity ϵ_r and the donor-doping concentration N_D. In addition, using a classical parabolic approximation the shape of the potential decay of the surface space charge layer and especially its width also depend directly on all three parameters, cf. equation 6.1 and 6.3. As described above, the surface potential is the parameter that is in good approximation observed by AP-XPS. Hence, this chapter focuses on the impact of the N_D (section 1) and the temperature (section 2) on both the emerging negative surface charge as well as on the shape of the space charge layer. In the third section, the findings on the N_D and the temperature dependence are compared.

Figure 7.1 shows a schematic illustration of the sample stacks for the n-$SrTiO_3$ thin films (a) and single crystals (b). The samples were contacted from the top using thin metal contact strips consisting of 30 nm gold on top of 5 nm titanium deposited by e-beam evaporation. This way, an ohmic contact between the n-$SrTiO_3$ surface and the analyzer ground contact and hence Fermi coupling was ensured. All measurements were performed at the same lab-based AP-XPS measurement setup described in sec. 6. The *in-situ* pO_2 ranged from a low base pressure of 10^{-8} mbar

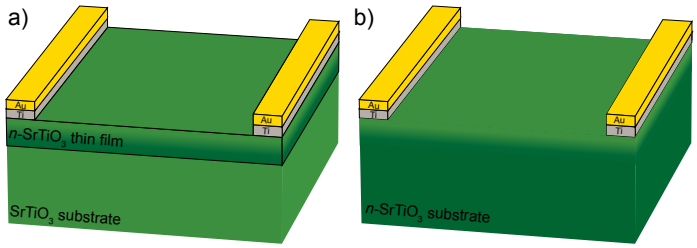

Figure 7.1.: Schematic illustration of the sample stacks for the n-$SrTiO_3$ thin films (a) and single crystals (b).

(UHV) up to 5 mbar O_2. Thereby, the oxygen partial pressures of 0.00015 mbar O_2 up to 0.015 mbar O_2 were adjusted by using a premixed gas consisting of 0.3 % O_2 in Argon and a total pressure ranging from 0.05 mbar 0.3 % O_2/Ar and 1.5 mbar 0.3 % O_2/Ar. The pO_2 between 0.1 mbar and 5 mbar were adjusted using pure oxygen gas. In order to clean the surfaces from carbon contamination, all samples were heated up to 670 K and exposed to 1.5 mbar O_2 prior to the presented measurements, cf. section 6.1. All AP-XPS data shown in this chapter was energy corrected using the Au4f core level measured at the sample top contact for all adjusted pO_2, doping concentrations and temperatures between 370 K and 670 K.[140, 141] For the measurements at room temperature and at 770 K the corrections at 370 K and 670 K were used, respectively.

7.1. Surface space charge layer at different doping concentrations

Figure 7.2 shows the O1s, Ti2p and the Sr3d core level spectra of n-$SrTiO_3$ samples measured by AP-XPS at 670 K in different pO_2 and with different doping concentrations ranging from 0.1 at% (a) and 1.0 at% (b) niobium doping up to 5.0 at% (c) lanthanum-doping. Both niobium and lanthanum act as donor-dopants in $SrTiO_3$.[37, 38, 72] The dashed circles and vertical lines indicate the apparent binding energy position of all characteristic core levels in low base pressure conditions of 10^{-8} mbar.

For all doping concentrations N_D the apparent binding energies of all characteristic core level shift towards lower values with increasing pO_2. This is consistent with the findings in sec. 6. In addition, at first sight no obvious spectral change is visible in the O1s and the Ti2p core level spectra. The Sr3d core level spectra again exhibits a slight flattening of intensity valley between the $Sr3d_{3/2}$ and the $Sr3d_{5/2}$ peak for all doping concentrations. In order to determine whether or not the experiments at different doping concentrations allows an unambiguous conclusion on the underlying surface redox process the core level peak shape is further examined.

Figure 7.3 shows the superposition of the O1s core level (a,d,g), the Ti2p core level (b,e,h) and the Sr3d core level (c,f,i) of n-$SrTiO_3$ samples measured in low base pressure conditions and a high pO_2 of 1.5 mbar O_2 with doping concentrations ranging from 0.1 at% up to 5 at% measured at 620 K. As already described above, with increasing pO_2 there are two different effects on the measured core levels. Firstly, the full width half maximum increases. Secondly, the intensity valley between the $Sr3d_{3/2}$ and the $Sr3d_{5/2}$ is flattened. Both effects are enhanced with increasing doping concentration. The spectral differences, however, do not allow for an unambiguous interpretation as chemical changes neither in the O1s core level[134] nor in the Ti2p core level[88], cf. see section 9.2. The altered intensity valley between the $Sr3d_{3/2}$ and $Sr3d_{5/2}$ peaks might be caused by both, the evolution of a SrO component at the n-$SrTiO_3$ surface resulting in an increased SrO

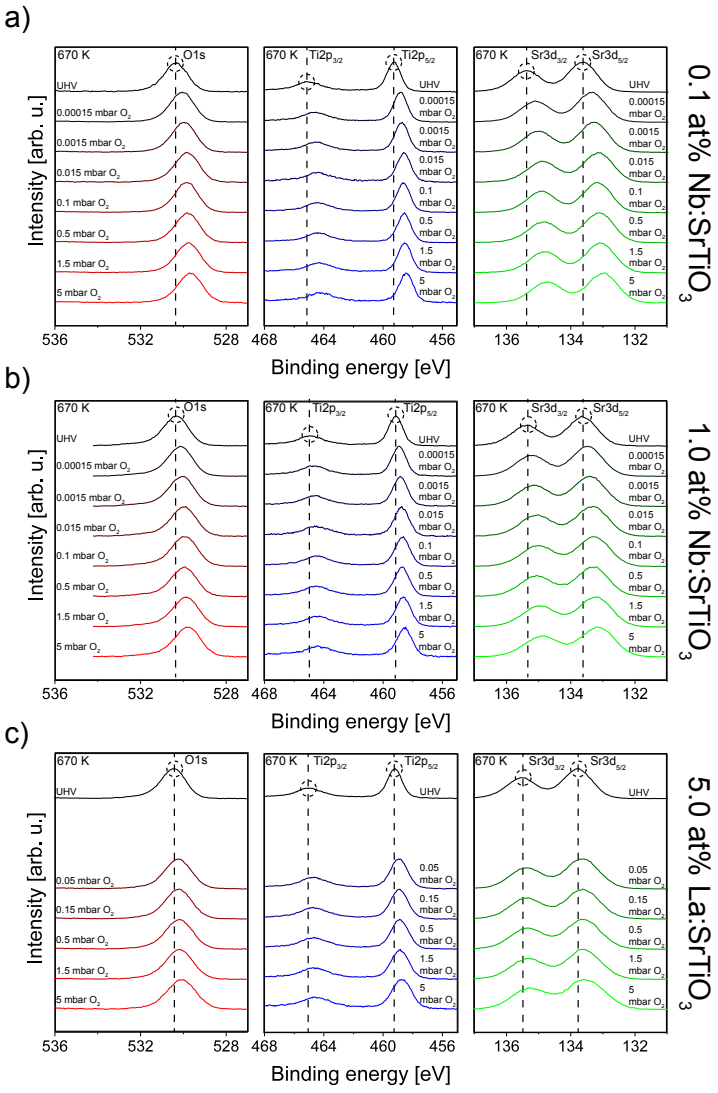

Figure 7.2.: Core level spectra of O1s, Ti2p and Sr3d of n-$SrTiO_3$ samples with 0.1 at% (a), 1.0 at% (b) and 5.0 at% (c) donor-doping at 670 K and different pO_2. The dashed circles and vertical lines indicate the position of the apparent characteristic binding energies at the measurement in a low base pressure of 10^{-8} mbar.

secondary component peak in the Sr3d core level, or the pure electronic surface effect which would be revealed as a plain Gaussian broadening due to the decay of

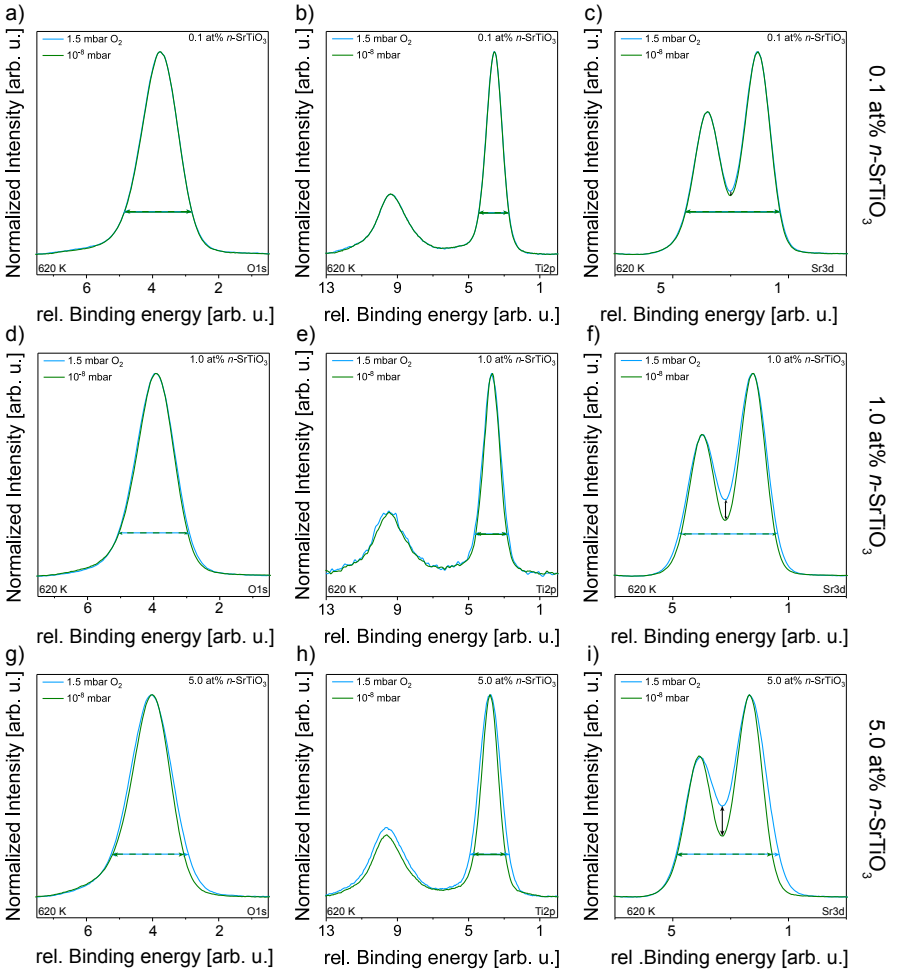

Figure 7.3.: The O1s core level (a,d,g), the Ti2p core level (b,e,h) and the Sr3d core level (c,f,i) of n-$SrTiO_3$ samples measured in a low base pressure and a high pO_2 of 1.5 mbar O_2 superimposed for different doping concentrations measured at 620 K. With an increased pO_2 the shape of both core levels is broadened significantly. In addition, the intensity valley between the $Sr3d_{3/2}$ and the $Sr3d_{5/2}$ peak is flattened. Both effects are enhanced by a higher doping concentration.

a surface potential into the sample, cf. sec. 6.1.

In order to investigate the observed binding energy shift in more detail figure 7.4 shows the apparent binding energy positions of the O1s, the Ti2p and the Sr3d core levels. Similar to the more detailed discussion in sec. 6, the measured spectra were fitted by *KolXPD* software using a Shirley background subtraction and an appropriate combination of Voigt peaks and doublets as described in detail in sec. 6.2. As already indicated by the vertical dashed black lines in figure 7.2, the apparent binding energy positions of all characteristic core levels shift rigidly towards lower values with increasing pO_2. The course of the apparent binding energy positions is parallel for the different N_D. This result points towards a similar underlying process for all doping concentrations. In addition, increasing N_D led to overall higher apparent binding energy values for all investigated core levels at oxidizing conditions. The apparent binding energy value in low base pressure conditions differs only slightly. Consequently, the binding energy shift decreases with increasing N_D, as will be shown below.

Figure 7.5 shows the pO_2-dependent binding energy shifts relative to the measurements at a low base pressure of 10^{-8} mbar of the O1s (a), the Ti2p (b) and the Sr3d (c) core level for the different N_D. The grey dashed lines act as a guide to the eye. All core levels shift rigidly with increasing pO_2 and parallel for the different

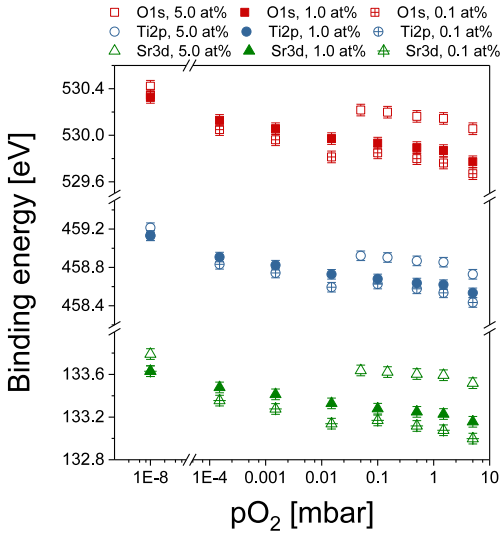

Figure 7.4.: pO_2-dependent apparent binding energy position of the characteristic core levels of n-$SrTiO_3$ with different doping concentrations. All apparent binding energies shift rigidly with pO_2. The higher the N_D is the higher is the apparent binding energy of every measured core level.

doping concentrations. For the n-$SrTiO_3$ sample with a doping concentration of 0.1 at% the binding energy shift ranges from ∼-0.3 eV at a pO_2 of 1.5×10^{-4} mbar up to ∼-0.7 eV at a pO_2 of 5 mbar. The overall shift of the 1 at% doped n-$SrTiO_3$ sample is lower, ranging from ∼-0.2 eV up to ∼-0.6 eV in the same pO_2-limits. The shift of the 5 at% doped n-$SrTiO_3$ sample ranges from ∼-0.2 eV at 0.05 mbar O_2 up to ∼-0.4 eV at a pO_2 of 5 mbar. Note that the overall binding energy shift observed in the Sr3d core level is lower in comparison to the O1s and Ti2p core levels. This effect might be due to measurement uncertainties and the

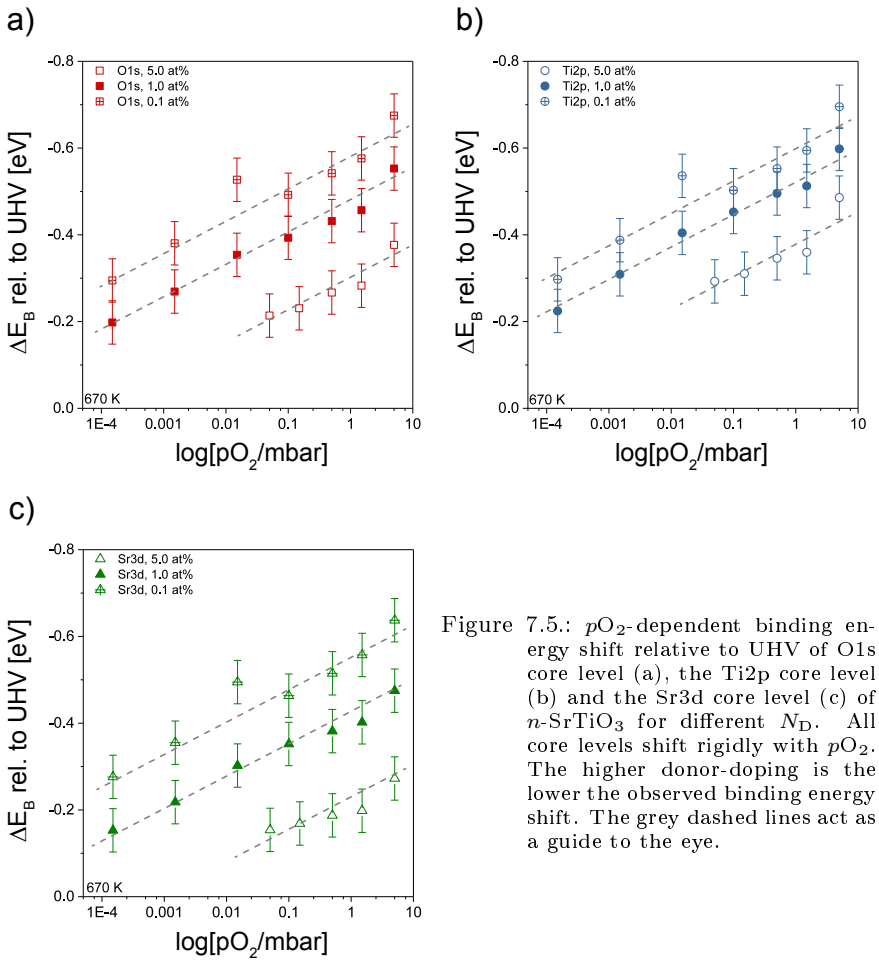

Figure 7.5.: pO_2-dependent binding energy shift relative to UHV of O1s core level (a), the Ti2p core level (b) and the Sr3d core level (c) of n-$SrTiO_3$ for different N_D. All core levels shift rigidly with pO_2. The higher donor-doping is the lower the observed binding energy shift. The grey dashed lines act as a guide to the eye.

resulting evaluation corresponding to the rise of the second strontium oxide component in the Sr3d core level, cf. section 9.1. With increasing doping concentration the overall binding energy shift relative to UHV decreases. This evolution indicates a more pronounced effect with a lower doping concentration, but as will be shown below this indication is misleading.

Figure 7.6 shows the pO_2-dependent binding energy shifts (ΔE_B) relative to

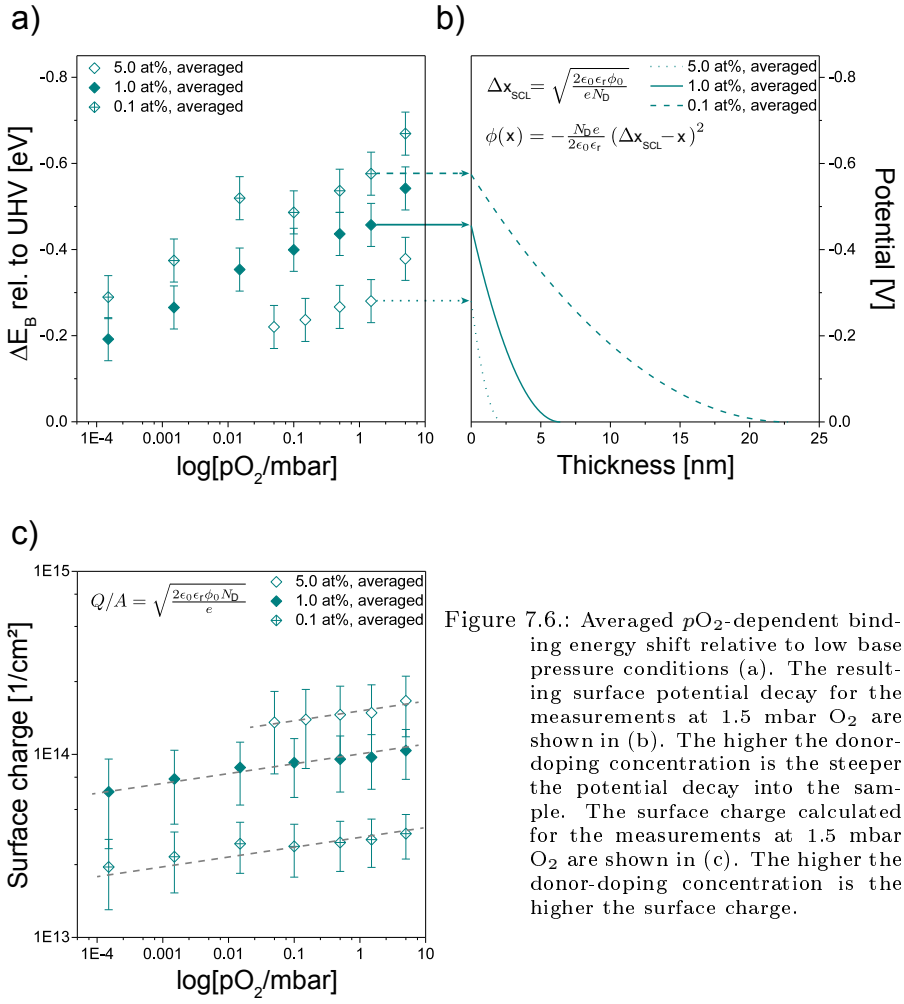

Figure 7.6.: Averaged pO_2-dependent binding energy shift relative to low base pressure conditions (a). The resulting surface potential decay for the measurements at 1.5 mbar O_2 are shown in (b). The higher the donor-doping concentration is the steeper the potential decay into the sample. The surface charge calculated for the measurements at 1.5 mbar O_2 are shown in (c). The higher the donor-doping concentration is the higher the surface charge.

low base pressure conditions averaged over the three characteristic core levels (a), the resulting surface potential decay (b) and the negative surface charge (c) for measurements at 1.5 mbar O_2. In the following the averaged binding energy shift relative to low base pressure observed at 1.5 mbar O_2 will be used as the surface potential ϕ_0. Utilizing eqs. 6.1 and 6.3 the shape of the surface space charge layer at different N_D is resolved as the course of the surface potential drop into the sample. Here a relative permittivity of ϵ_r ~122 determined from the empirical equation 6.2 was used. Under the assumption of full ionization, the concentrations of donor dopants and thereby the carrier concentrations were estimated to $N_D(0.1\ \text{at\%}) \approx 1.5 \times 10^{19}$ cm^{-3}, $N_D(1.0\ \text{at\%}) \approx 1.5 \times 10^{20}$ cm^{-3} and $N_D(5.0\text{at\%}) \approx 7.5 \times 10^{20}$ cm^{-3} for the different donor-doping concentrations. As shown above the average binding energy shift decreases rigidly with increasing doping concentration.

The course of the potential decay into the sample changes significantly with N_D. Using the binding energy shift at 1.5 mbar O_2 as the surface potential, the space charge layer width is calculated to $\Delta x_{SCL}(0.1\ \text{at\%}) \approx 22.7$ nm, $\Delta x_{SCL}(1.0\ \text{at\%}) \approx 6.4$ nm and $\Delta x_{SCL}(5.0\ \text{at\%}) \approx 2.2$ nm. It decreases substantially with increasing doping concentration. Consequently, the steepness of the initial slope of the potential decay increases with increasing N_D. The initial slope of the potential decay is proportional to the electric field at the surface of the n-$SrTiO_3$ samples.[65] The surface electric fields were determined analytically to $E(0.1\ \text{at\%}) \sim 0.5$ MV/cm, to $E(1.0\ \text{at\%}) \sim 1.2$ MV/cm and $E(5.0\ \text{at\%}) \sim 2.5$ MV/cm for n-$SrTiO_3$ samples with 0.1 at%, 1.0 at% and 5.0 at% donor-doping concentration, respectively. With increasing N_D the surface electric fields increase significantly. The negative surface charges were calculated using equation 6.5, see figure 7.6 (c). The overall surface charge increases with increasing doping concentration. It scales with the square root of the donor-doping concentration. For the 0.1 at% n-$SrTiO_3$ sample it ranges from 2.4×10^{13} e/cm^2 up to 3.7×10^{13} e/cm^2 for pO_2 of 1.5×10^{-4} mbar and 5 mbar, respectively. For the 1.0 at% n-$SrTiO_3$ sample the surface charge extends from 6.2×10^{13} e/cm^2 up to 1.0×10^{14} e/cm^2 for the same pO_2. For the 5.0 at% n-$SrTiO_3$ sample the surface charge ranges from 1.5×10^{14} e/cm^2 up to 2.0×10^{14} e/cm^2 at pO_2 of 0.05 mbar and 5 mbar, respectively. Table 7.1 sums up the results determined from AP-XPS measurements with different donor-doping

Table 7.1.: Summary of the doping concentration-dependent results. Note that the calculated space charge layer widths and generated surface charges are regarded as a lower limit.

Donor-doping level [at%]	0.1	1.0	5.0
ΔE_B rel. to UHV at 1.5 mbar O_2 [eV]	-0.58	-0.46	-0.28
Doping conc. N_D [10^{20} cm^{-3}]	0.15	1.5	7.5
Space charge layer width Δx_{SCL} [nm]	22.7	6.4	2.2
Electric field [MV/cm]	0.5	1.2	2.5
Neg. surface charge [10^{13} e/cm^2]	3.4	9.6	16.9

concentrations.

The generated negative surface charge increases with both increasing pO_2 and increasing doping concentration. This is in good agreement with the dopant concentration dependent broadening of the spectra and the flattening of the intensity valley between the $Sr3d_{3/2}$ and the $Sr3d_{5/2}$ peak shown in figure 7.3. The pO_2-dependence of the surface space charges is similar for all doping concentrations, indicating again an identical underlying surface process. Even though the sample with the highest N_D undergoes the smallest binding energy shift, the underlying surface effect is the strongest manifesting in the highest surface electric field and the highest generated surface charge.

Regardless of the nature of the underlying process its impact on the surface of n-$SrTiO_3$ is substantial even with N_D as low as 0.1 at% and becomes even more significant with increasing donor-doping concentrations. At a certain pO_2 changing N_D allows to directly control the generated surface charge and thus the corresponding electron depletion at the surface of n-$SrTiO_3$. By controlling the electron concentration, representing the majority carrier in the system, it is possible to manipulate the properties of the surface space charge layer, its width, shape and the surface electric field.

7.2. Surface space charge layer at different temperatures

Besides pO_2 and N_D another thermodynamic parameter possibly impacting the surface space charge layer is the temperature. As can be seen in eqs. 6.2 and 6.5, in addition to the temperature and pO_2dependence of an underlying surface redox process, the generated surface charge as well as the shape of the potential decay of the surface charge and especially its width depends directly on the temperature-dependent relative permittivity ϵ_r. Figure 7.7 shows the oxygen 1s (O1s), the titanium 2p (Ti2p) and strontium 3d (Sr3d) core level spectra as well as the valence band region of a 1.0 at% donor-doped n-$SrTiO_3$ sample measured at a low base pressure of 10^{-8} mbar (a) and at 1.5 mbar O_2 (b) at different temperatures. The dashed vertical circles and lines indicate the position of the apparent binding energy measured at the highest temperature.

The apparent binding energy positions measured for all characteristic core level as well as for the valance band maximum are generally higher in UHV conditions in comparison to 1.5 mbar O_2. In the low base pressure, the apparent binding energy positions do not shift monotonously with temperature and are stable within measurement accuracy. In contrast, at 1.5 mbar O_2 with decreasing temperature the apparent binding energy values of all characteristic core levels shift slightly towards higher values. Consequently, there seems to be an impact of the temperature on the underlying surface redox process taking place under oxidizing conditions. In order to examine if there is an unambiguous change in the chemical composition of

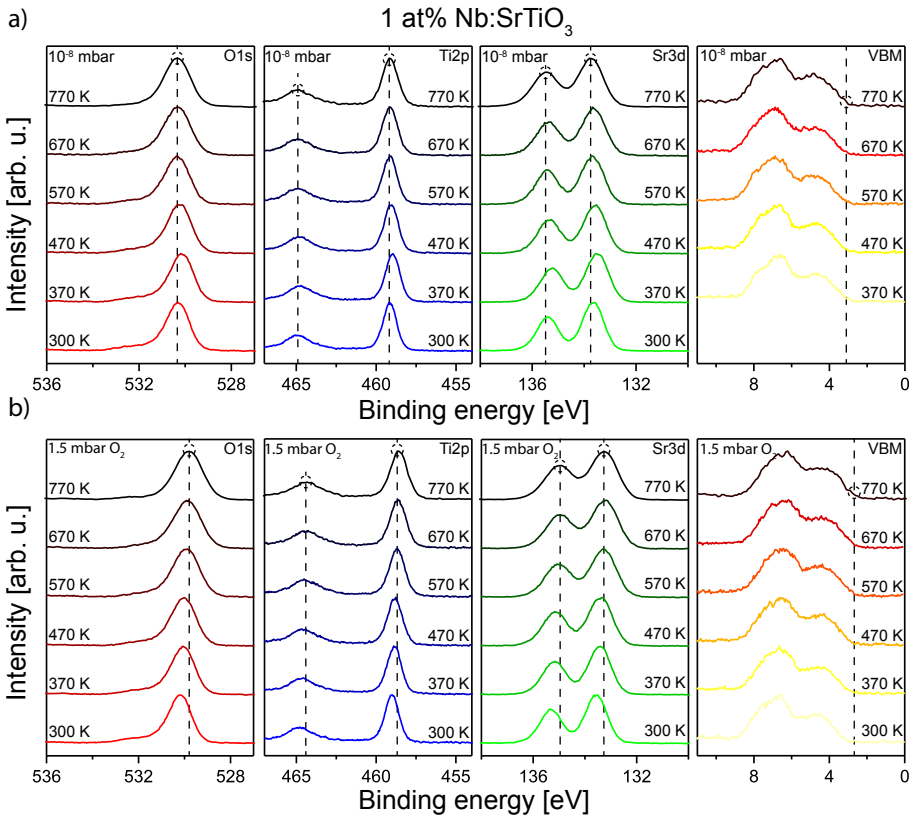

Figure 7.7.: Temperature-dependent core level spectra of the O1s, Ti2p and Sr3d core levels and the valence band region of a 1 at% donor-doped $SrTiO_3$ sample measured at a low base pressure of 10^{-8} mbar (a) and at 1.5 mbar O_2 (b). The dashed vertical lines and circles indicate the position of the apparent characteristic binding energies measured at the highest temperature.

the surface that allows to draw a conclusion on the surface process, the shape of all characteristic core levels needs to be investigated. Figure 7.8 shows the superposition of the O1s (a, d), the Ti2p (b, e) and the Sr3d (c, f) core level spectra measured at different temperatures at a low base pressure and a high pO_2 of 1.5 mbar, respectively.

The spectra of both core levels demonstrate a broadening with increasing temperature. This broadening is more pronounced at 1.5 mbar O_2. As explained in sec. 6.1, such a broadening can be due to a space charge layer at the n-$SrTiO_3$ sur-

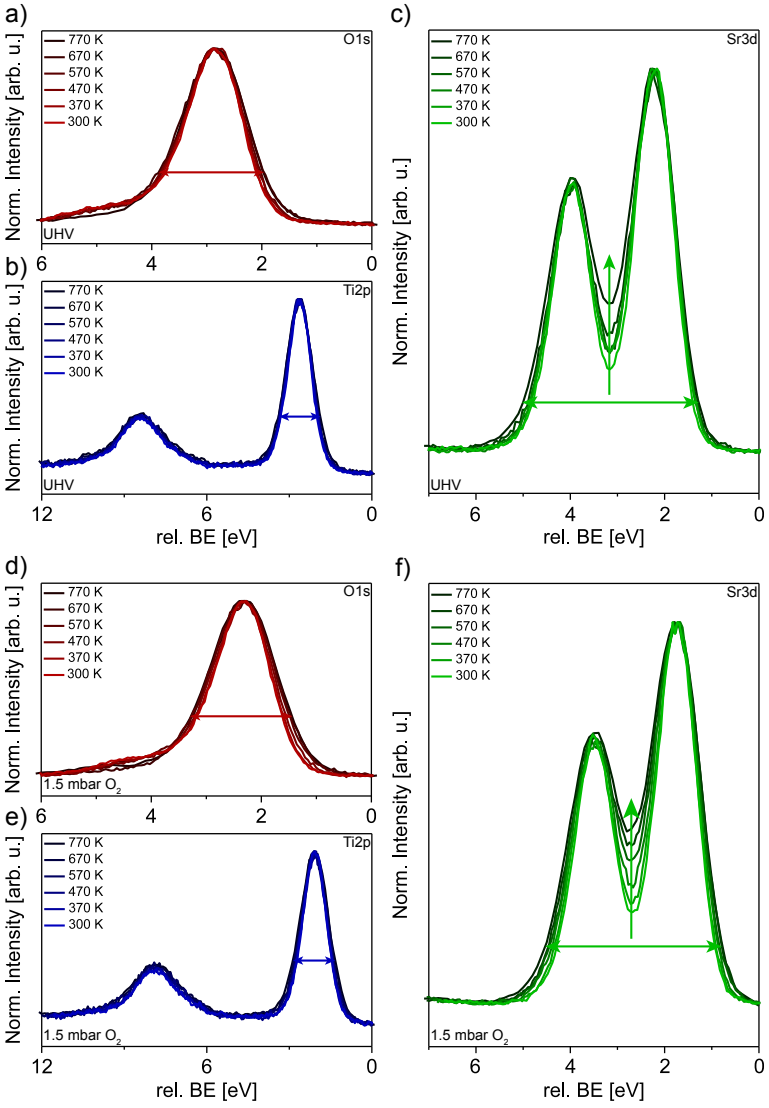

Figure 7.8.: Superposition of the O1s (a, d), Ti2p (b, e) and the Sr3d (c, f) core level spectra measured at different adjusted temperatures and at a low base pressure and a pO_2 of 1.5 mbar O_2, respectively.

face. Hence, the enhanced broadening at high pO_2 points towards a more pronounced space charge layer in high oxygen partial pressures. This is consistent with all prior results that all indicate a surface space charge layer in high pO_2. Nevertheless, the slight broadening in UHV conditions also suggests a space charge layer which is consistent with what has been found by the synchrotron-based AP-XPS experiments at different probing depths. In addition, the intensity valley between the $Sr3d_{3/2}$ peak and the $Sr3d_{5/2}$ peak which has been described above flattens with increasing temperature in both the low base pressure regime and in 1.5 mbar O_2. Again, the impact of varying temperatures is more pronounced at high pO_2, leading to a enhanced flattening of the intensity valley at 1.5 mbar O_2. As will be discussed in detail in section 9.1 this effect is due to the precipitation of a stron-

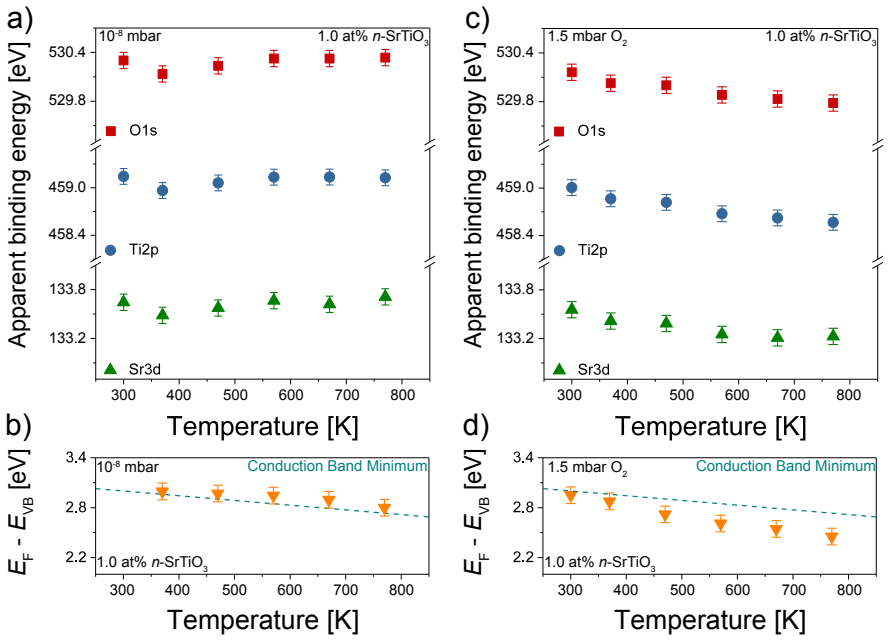

Figure 7.9.: Apparent binding energy positions of the O1s, the Ti2p and the Sr3d core level and the energy difference between the Fermi energy and the valence band maximum as well as the estimated temperature-dependent conduction band minimum in UHV conditions (a, b) and at 1.5 mbar O_2 (c, d) measured at different temperatures. The binding energies in UHV conditions do not shift steadily while in 1.5 mbar O_2 the binding energy position of all core levels and the valence band maximum is shifted towards lower values with increasing temperature. The higher the temperature is the higher the binding energy shift relative to UHV conditions.

tium oxide secondary component at the surface of n-$SrTiO_3$ which decreases with decreasing temperature. Due to the measurement accuracy the slight flattening of the valence band which has been described above (see section 6.2) is not visible here and hence has been neglected for the detailed analysis.

To further analyze the temperature dependence of the binding energy shift, figure 7.9 shows the apparent binding energy positions of all characteristic core levels and the energy difference between the Fermi energy and the valence band maximum as well as the estimated temperature dependent conduction band minimum[37, 38] at a base pressure of 10^{-8} mbar (a, b) and 1.5 mbar O_2 (c, d). All values were determined using *KolXPD* software and the fitting procedures described above in section 6.1 and 6.2.

As already indicated above, the apparent binding energy positions in UHV conditions are higher than in a high pO_2 of 1.5 mbar (a,c). In the low base pressure regime, the apparent binding energy positions of all characteristic core level and the valence band maximum do not change significantly with temperature (a,b). For all temperatures the measured valance band maximum and hence the Fermi energy is located slightly above the conduction band edge with its error bars reaching its extrapolated values. For classical semiconductor with full ionization of shallow donor dopants a Fermi energy slightly below the conduction band edge is expected, cf. section 2.1. Consequently, within the measurement accuracy these results are consistent with what is expected for donor-doped semiconductors.[37, 38] In the high pO_2 regime at 1.5 mbar O_2 all binding energy positions as well as the valance band maximum are shifted towards lower values with increasing temperature. Here the

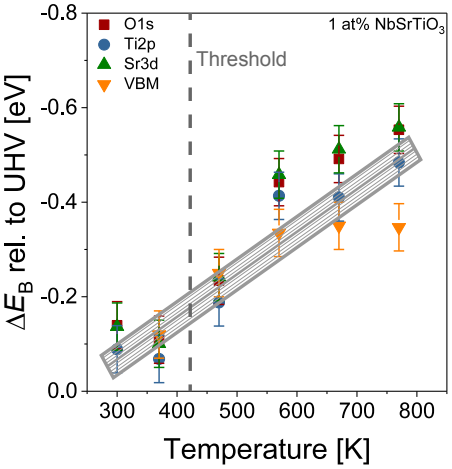

Figure 7.10.: ΔE_B relative to UHV of the O1s, the Ti2p and the Sr3d core level and the valence band maximum. The grey lines act as a guide to the eye.

valence band maximum is significantly shifted away from the conduction band edge extrapolated at different temperatures. As already shown above, these findings indicate a strong electron depletion underneath the surface and hence the formation of a surface space charge layer, cf. sec. 6.1.

Figure 7.10 sums up the binding energy shifts relative to low base pressure conditions of the O1s, the Ti2p and the Sr3d core levels and the valence band maximum. The binding energy shift of all core levels and the valence band maximum increases rigidly with temperature from ∼-0.1 eV at room temperature up

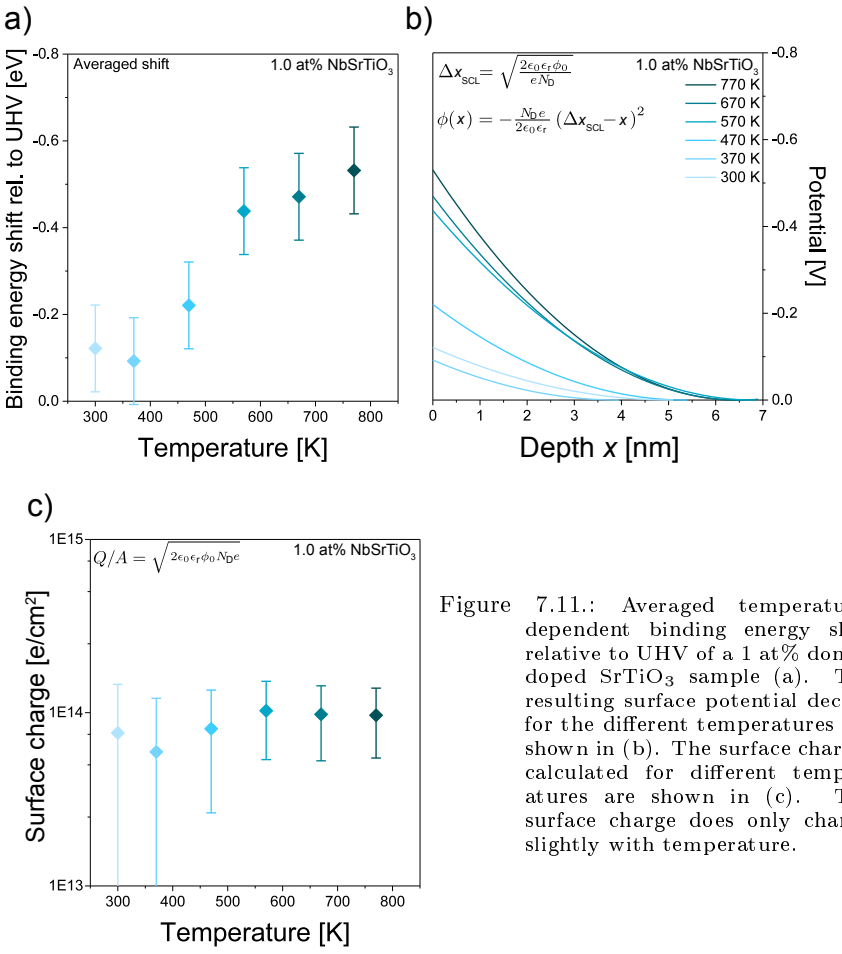

Figure 7.11.: Averaged temperature-dependent binding energy shift relative to UHV of a 1 at% donor-doped $SrTiO_3$ sample (a). The resulting surface potential decays for the different temperatures are shown in (b). The surface charges calculated for different temperatures are shown in (c). The surface charge does only change slightly with temperature.

to ∼-0.55 eV at 770 K. At small temperatures below 370 K the Fermi energy is located slightly below the conduction band edge. At intermediate temperatures of 470 K the Fermi energy is shifted ∼-0.2 eV deeper into the band gap. At high temperature above 570 K the Fermi energy is shifted even deeper into the band gap by ∼0.25 eV. So, with increasing temperature the band bending becomes stronger reaching its maximum at temperatures above 570 K. These results point towards an underlying surface process that is temperature activated at threshold temperatures below 470 K and increased at higher temperatures. Such a behavior is typical for redox processes involving the activation of ionic sublattices.

As described above the binding energy shift stems from a negative charge generated at the surface of the n-$SrTiO_3$ samples, which dominates the electrical surface properties. To further analyze the temperature dependence of the electrical surface properties figure 7.11 shows the temperature dependence of the averaged binding energy shifts in a 1 at% n-$SrTiO_3$ sample relative to UHV at a pO_2 of 1.5 mbar (a), the resulting course of the surface potential decays into the sample (b) and the generated negative surface charges (c). For the calculations the pO_2-dependent averaged binding energy shift was used as the surface potential ϕ_0. The temperature-dependent averaged binding energy shift can be divided into three regimes, the low temperature regime ranging from 370 K down to room temperature, the intermediate regime at 470 K and the high temperature regime ranging from 570 K up to 770 K. In the low temperature regime both the binding energy shift at room temperature and at 370 K is close to the measurement accuracy of the used setup. Hence, the observed values as well as the resulting calculations should be treated with caution. In the intermediate temperature regime a shift of -0.22 eV unambiguously indicates a surface effect. Hence, the underlying surface process is activated at temperatures as low as 470 K. As will be shown in section 9.3, the surface process is linked directly to the defect chemistry of n-$SrTiO_3$ making this result remarkable since in general the defect chemistry of n-$SrTiO_3$ involving the strontium sublattice is believed to be only active at much higher temperatures. In the high temperature regime an even stronger binding energy shift of up to -0.53 eV demonstrates a significant reaction of the n-$SrTiO_3$ surface on the changing atmo-

Table 7.2.: Summary of the temperature-dependent rel. permittivity ϵ_r used for the calculations of the surface potential decay, the resulting space charge layer widths Δx_{SCL}, the surface electric field and the correspond negative surface charge.

Temperature [K]	300	370	470	570	670	770
Ave. binding energy shift [eV]	- 0.12	- 0.09	- 0.22	- 0.44	- 0.47	- 0.53
Rel. permittivity ϵ_r	288	229	177	144	122	105
Δx_{SCL} [nm]	5.0	3.9	5.4	6.8	6.5	6.4
Electric filed [MV/cm]	0.6	0.3	0.8	1.2	1.4	1.6
Neg. surf. charge [$10^{13}\times$e/cm^2]	7.6	5.9	8.1	10.0	9.8	9.7

sphere.

For the calculation of the potential decay and the space charge layer width the temperature-dependent relative permittivity is determined by equation 6.2. The donor-doping concentration used for calculations is $N_D = 1.5\times10^{20}$ cm^{-3}. With decreasing temperature the shape of the potential decay is slightly flattened. In the low temperature regime the space charge layer width is in the range of ∼5.0 nm and ∼3.9 nm. In the intermediate regime it is increased to ∼5.4 nm. In the high temperature regime the space charge layer width is increased even further to values between ∼6.4 nm to ∼6.8 nm. The surface electric fields change accordingly, ranging from between ∼0.3 MV/cm and ∼0.6 MV/cm in the low temperature regime over ∼0.8 MV/cm in the intermediate regime up to values between ∼1.6 MV/cm and ∼1.2 MV/cm in the high temperature regime. The generated negative surface charge is calculated using equation 6.5. In the low temperature regime it is in the range between $\sim5.9\times10^{13}$ e/cm^2 and $\sim7.6\times10^{13}$ e/cm^2. In intermediate temperatures it is slightly increased to $\sim8.1\times10^{13}$ e/cm^2, while in the high temperature regime it is $\sim1.0\times10^{14}$ e/cm^2. Note that the values calculated for the low temperature regime might be exposed to larger errors due to the accuracy of the measurement setup. Table 7.2 sums up the averaged binding energy shifts, the relative permittivity ϵ_r values calculated for the different temperatures, the resulting space charge layer widths Δx_{SCL}, the surface electric fields and the generated negative surface charge.

By changing the temperature in certain regimes it is possible to initiate a surface process and directly control the properties of an emerging surface space charge layer by the corresponding surface charge. Below 370 K the surface space charge layer cannot be confirmed unambiguously and the underlying surface process seems to be inactive on the timescale of the experiments performed. With increasing temperature the surface process is accelerated and the generated surface charge increases. It reaches a maximum at temperatures between 570 K and 770 K. In this high temperature regime the temperature dependence of the average binding energy shift, the shape of the potential decay into the sample, the space charge layer width and the electric field depend only on the temperature dependence of the relative permittivity ϵ_r, cf. section 6.1.

7.3. Comparison of the doping concentration and temperature-dependence

In order to compare the donor-doping concentration dependence with the temperature dependence, figure 7.12 shows the averaged binding energy shifts between a low base pressure of 10^{-8} mbar and 1.5 mbar O_2 (a) and the generated surface charge (b) of donor-doped n-$SrTiO_3$ samples with different doping concentration of 0.1 at%, 1.0 at% and 5.0 at% measured at different temperatures.

The overall binding energy shift relative to low base pressure conditions de-

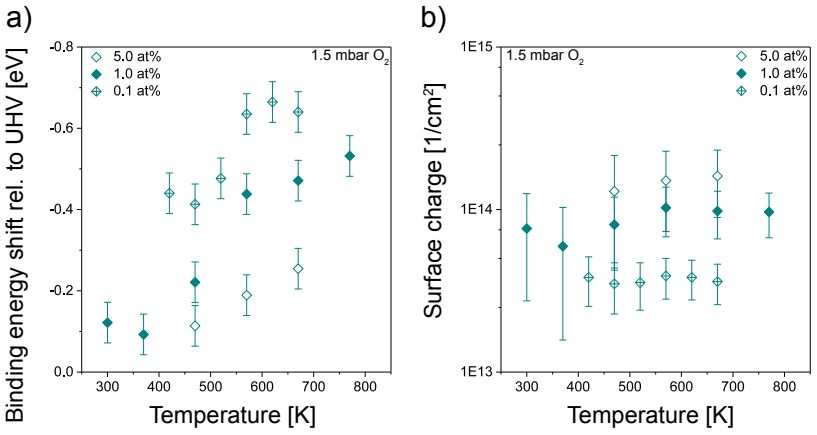

Figure 7.12.: Averaged temperature-dependent binding energy shifts between a base pressure of 10^{-8} mbar and 1.5 mbar O_2 of donor-doped $SrTiO_3$ samples with different doping concentrations (a). With increasing temperature the relative binding energy shift increases for all doping concentrations, while it decreases with increasing doping concentrations. The resulting temperature-dependent calculated surface charges of donor-doped $SrTiO_3$ samples with different doping concentrations are shown in (b). The surface charge show only slight changes with temperature, but is strongly affected by the doping concentration.

pends strongly on N_D and slightly on the temperature. With increasing doping concentration the binding energy shift decreases. This evolution is present at all temperatures. With increasing temperature, the relative binding energy shift increases. The strongest binding energy shift is observed in the high temperature regime above 570 K. It slightly decreases in the intermediate temperature regime between 420 K and 520 K (0.1 at% n-$SrTiO_3$) and becomes the lowest in the low temperature regime below 370 K. This trend holds for all N_D, but is attenuated with increasing N_D. In comparison, the impact of changes of the doping concentration is more pronounced than changes in temperature, i.e. changing N_D from 0.1 at% to 5.0 at% the binding energy shift relative to UHV at 670 K decreases from -0.64 eV to -0.25 eV while increasing the temperature from 470 K to 670 K the binding energy shift of a 1.0 at% n-$SrTiO_3$ sample only changes from -0.22 eV to -0.47 eV. The resulting generated negative surface charge also exhibits a strong dependence on the doping concentration. Regardless of the temperature, with increasing N_D the negative surface charge is increased. In contrast, it only decreases slightly with decreasing temperatures.

Table 7.3 sums up the results of the doping concentration- and temperature-dependent measurements at temperatures above 470 K. The surface charge as the dominating parameter of the space charge layer is proportional to the square

Table 7.3.: Summary of the doping concentration- and temperature-dependent results observed for temperatures above 470 K.

	BE shift rel. to UHV [eV]			Surface charge [10^{13}×e/cm^2]		
Temp.[K]	0.1 at%	1.0 at%	5.0 at%	0.1 at%	1.0 at%	5.0 at%
670	-0.64	-0.47	-0.25	3.6	9.8	16.1
570	-0.64	-0.44	-0.19	3.9	10.3	15.1
470	-0.41	-0.22	-0.11	3.5	8.0	13.0

root of N_D and the relative permittivity ϵ_r ($Q/A \sim \sqrt{N_D \epsilon_r}$), cf. equation 6.5. The temperature-dependence of the binding energy shift relative to UHV and the resulting generated surface charge only depends on the temperature-dependence of the relative permittivity ϵ_r which is antiproportional to the temperature T ($\epsilon_r = \frac{78400}{T-28}$). Consequently, in comparison to the doping concentration dependence the temperature-dependence of the relative permittivity and hence the generated negative surface charge is weaker. Even though the donor-doping concentration has a much stronger impact on the generated surface charge, the properties of the corresponding surface space charge layer can be controlled by varying doping concentration and temperature. Note that the temperature dependence of the underlying surface redox process might be much stronger than the temperature dependence of ϵ_r which hence might be negligible in the overall picture.

Summary

In this chapter the thermodynamical control of the surface space charge layer in n-$SrTiO_3$ was investigated by comparing the impact of changing the donor-doping concentration and the temperature. In the first section, it was demonstrated that even in n-$SrTiO_3$ with a donor-doping-concentration as small as 0.1 at% a pO_2-dependent negative surface charge and a corresponding space charge layer are generated in oxidizing conditions. The amount of the surface charge as well as the properties of the space charge layer depend strongly on the donor-doping concentration N_D. With increasing N_D the surface charge and the surface electric field increase while the space charge layer width and the shift relative to low base pressure conditions decrease.

In the second section it was shown that, the negative surface charge and the corresponding space charge layer are generated at a temperature as low as 470 K. This low threshold temperature is remarkable since for a surface process involving the strontium sublattice, cf. sec. 9.1.[37, 38] With increasing temperature up to 670 K the surface charge, the surface electric field, the space charge layer width and the binding energy shift relative to low base pressure conditions are increased

slightly. This trend is directly linked to the temperature dependence of the relative permittivity ϵ_r.

In the third section, the effect of the donor-doping concentration and the temperature dependence was compared. Both N_D and temperature allow to control the surface charge and the properties of the corresponding space charge layer. The impact of the doping concentration, however, is much stronger than the one of the temperature. This is due to the dependence of the space charge layer on the generated surface charge, which is directly proportional to the square root of N_D and and antiproportional to the square root of the temperature ($Q/A \sim \sqrt{N_D/T}$).

So far, the generation of a negative surface charge and a corresponding space charge layer in n-$SrTiO_3$ in oxidizing and UHV conditions has been shown for different doping concentrations and temperatures. This space charge layer goes along with an electron depletion layer underneath the surface and hence impacts the electrical surface properties. The next chapter will investigate how changing the negative surface charge controls the electrical surface properties and *in-plane* transport behavior.

8. Control of electronic properties in n-$SrTiO_3$ thin films

Small changes in the surface chemistry and composition of n-$SrTiO_3$ are expected to have a large impact on the electrical transport through thin films. In chapter 6 and 7 it was shown that a surface space charge layer and a corresponding electron depletion layer is generated at n-$SrTiO_3$ surfaces in oxidizing conditions, which intuitively results in an increased surface resistance, cf. ch. 5. To further probe the significance of changes in the ambient atmosphere on the electrical properties of n-$SrTiO_3$ thin films, electrochemical conductivity relaxation (ECR) experiments were carried out. The pO_2-dependent sheet resistance R_s of a 32 nm thick 0.5 wt% n-$SrTiO_3$ thin film grown on an undoped $SrTiO_3$ substrate was investigated. At this layer thickness, the electrical properties of the thin film are already governed by the surface space charge layer.

The first section of this chapter focuses solely on the evolution of the sheet resistance at different pO_2, while in the second section the temperature dependence

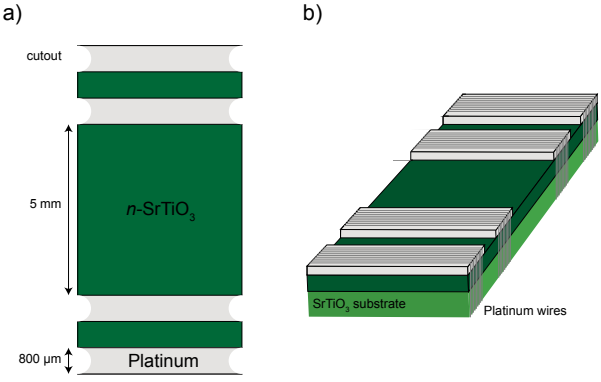

Figure 8.1.: Schematic illustration of the samples used for the electrochemical conductivity relaxation experiments. The thin films were contacted by four sputtered platinum pads which form a central square of 5 mm×5 mm. The cutouts at the edges of the platinum pads allowed for a secure contact with platinum wires connecting the samples to the measurement setup.

will be examined. The third section discusses a model to fit the transient course of the pO_2-dependent conductivity which considers a surface transfer reaction in combination with a bulk diffusion process. In the fourth section the results of the electrical measurements will be compared with what has been concluded from the spectroscopic measurements so far.

For all electrochemical conductivity relaxation measurements similar samples were used. Figure 8.1 shows a schematic illustration of the used sample stack. 32 nm 1.0 at% n-$SrTiO_3$ thin films were grown on top of undoped $SrTiO_3$ substrates with a size of 10 mm×5 mm. Four platinum contacts were sputtered on top of the thin film creating a central square of 5 mm×5 mm. Such a measurement geometry allows for comparison of the results to other electrical measurement techniques which rely on the van der Pauw geometry, cf. sec. 5.2.[103] The outer contacts were used to induce a current into the thin film while the inner contacts were used to measure the induced voltage, cf. sec. 3.4. In addition, all measurements took place in pO_2 ranging from 0.005 mbar up to 1 mbar which is comparable to the ones that were used for the *in-situ* AP-XPS experiments (chps. 6, 7). Using comparable ambient pO_2, the occurring electrical effects can be linked to the changes in the chemical composition at the surface observed above. The pO_2 was adjusted using mixtures of argon gas with a purity of 6.0 and a premixed gas consisting of 0.1 % O_2 in Ar (*Air Products and Chemicals, PRAXAIR*). The transition between two gas atmospheres was realized almost instantaneously by premixing the gas mixtures with varying oxygen content in two different flow channels and switching between them by a 4-port valve. This way it is ensured that the switching of the ambient atmosphere can be regarded as instantaneous with respect to the timescale of the conductivity relaxation.

8.1. Electrochemical conductivity relaxation at different pO_2

In order to investigate the sheet resistance of a n-$SrTiO_3$ thin film, the pO_2-dependent sheet resistance of the underlying undoped $SrTiO_3$ substrate needs to be significantly higher than the one of the thin film. To rule out a significant influence of the underlying $SrTiO_3$ substrate on the thin film experiments, the sheet resistance of an undoped $SrTiO_3$ substrate is investigated at different temperatures and oxygen partial pressures. Figure 8.2 shows a typical evolution of the sheet resistance (R_s) of a $SrTiO_3$ substrate measured as a reference at 770 K and changing pO_2 (a) and the equilibrium R_s at different temperatures typically achieved after 12 h equilibration at a low pO_2 of 0.005 mbar O_2 and a high pO_2 of 1 mbar O_2 (b).

Changing the ambient pO_2 stimulates a prompt response of the sheet resistance. With increasing the pO_2 from 0.005 mbar O_2 to 1 mbar O_2 (orange) R_s of the undoped-$SrTiO_3$ substrate decreases from ∼960 kΩ to ∼480 kΩ. When decreasing the pO_2 again to 0.005 mbar O_2 (green), R_s is increased again to ∼960 kΩ. This

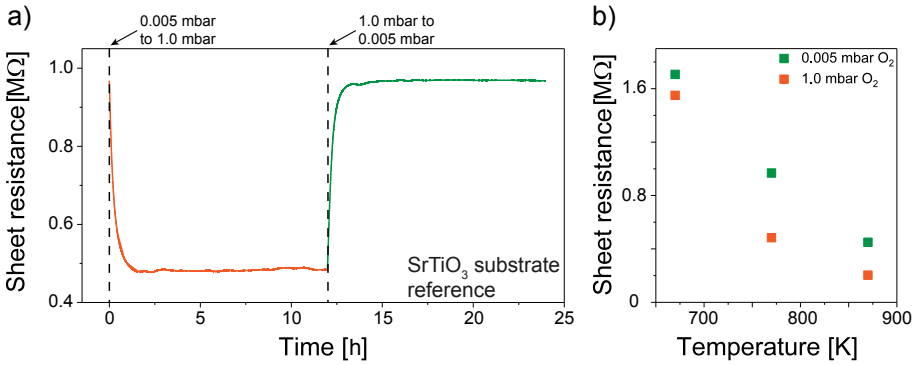

Figure 8.2.: Evolution of the sheet resistance R_s of a $SrTiO_3$ substrate measured as a reference at 770 K (a) and changing pO_2. An increasing pO_2 decreases R_s while a decreasing pO_2 increases R_s. The temperature-dependent equilibrium state R_s for different pO_2 is shown in (b). As expected for undoped $SrTiO_3$ substrates with increasing temperature the sheet resistance decreases.

trend is present at temperatures between 670 K and 870 K. At high temperatures of 870 K R_s ranges from ∼200 kΩ to ∼400 kΩ at 1.0 mbar O_2 and 0.005 mbar O_2, respectively. When decreasing the temperature to 670 K, the sheet resistance of the undoped $SrTiO_3$ substrate rises to ∼1500 kΩ at 1.0 mbar O_2 and ∼1700 kΩ at 0.005 mbar O_2. This evolution is consistent with the increasing p-type conductivity in undoped $SrTiO_3$ in the high pO_2-regime at high temperatures.[37, 148] In order to minimize the impact of the underlying substrate on the sheet resistance measurements of the n-$SrTiO_3$ thin films expected to deliver resistance values of some tens of kΩ, all electrochemical conductivity relaxation experiments have been performed at temperatures of 670 K and below.

Figure 8.3 shows a typical evolution of the sheet resistance of a 32 nm thick 1.0 at% n-$SrTiO_3$ thin film measured at 670 K and varying pO_2 (a) and the corresponding equilibrium R_s determined after 12 h equilibration (b). Changing the ambient pO_2 at elevated temperatures immediately drives a reaction of the sheet resistance. An increase of the pO_2 results in an increase of R_s from ∼78.3 kΩ to ∼83.9 kΩ while a subsequent decrease of the pO_2 results in a decrease of R_s back to ∼78.3 kΩ. This sheet resistance regime is more than one order of magnitude lower than the one determined for the undoped $SrTiO_3$ substrate. In addition, the trend of an increasing R_s with increasing pO_2 is opposite to the experiments on undoped $SrTiO_3$ substrates. Consequently, the observed impact on the sheet resistance is clearly attributed to the n-$SrTiO_3$ thin film and hence in the following the impact of the undoped $SrTiO_3$ substrate is neglected.

The equilibrated R_s displayed in figure 8.3 (b) illustrate the pO_2-dependence of the electron transport in more detail. The sheet resistance increases continuously with increasing pO_2. Considering the carrier concentration to be responsible for the

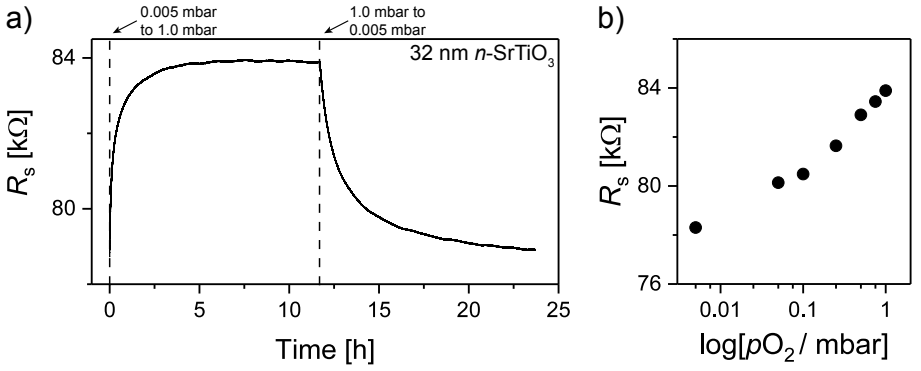

Figure 8.3.: Evolution of the sheet resistance R_s of a 32 nm thick 1.0 at% n-$SrTiO_3$ thin film measured at 670 K and changing pO_2 (a). The equilibrium R_s at different pO_2 is shown in (b). An increasing pO_2 increases R_s while reducing the pO_2 to low background pressures decreases the sheet resistance. Switching of the ambient atmosphere with respect to the timescale of the conductivity relaxation can be regarded as instantaneous. The figure was published in ref. [121].

loss in conductivity this trend indicates a monotonously increasing effect of surface electron depletion with pO_2. By increasing the pO_2 by three orders of magnitude R_s increases by 5.6 kΩ corresponding to a change of 6.7 % in sheet resistance as compared to lower pO_2. This impact is consistent with the electron depletion detected above in chapters 5, 6 and 7 and can be seen directly in the sheet carrier concentration (n_s), which is inversely proportional to R_s by

$$n_s = (eR_s\mu(\mathrm{T}))^{-1} \quad , \tag{8.1}$$

where $\mu(T)$ denotes the temperature-dependent electron mobility. As summarized in section 5.2, $\mu(T)$ was measured at elevated temperatures directly in high temperature Hall measurements and determined to $\mu(670\ \mathrm{K}) = 0.45\ \mathrm{cm}^2/\mathrm{Vs}$, now yielding the evolution of the average sheet carrier density in the n-$SrTiO_3$ thin film upon a change in pO_2.

Figure 8.4 illustrates a typical pO_2-dependent development of n_s (a) and the corresponding equilibrium n_s after 12 h equilibration at 670 K (b). Changing the ambient atmosphere at elevated temperatures thus drives an instantaneous response of the sheet carrier concentration. With increasing pO_2, n_s is decreased from $\sim 1.76\times10^{-14}$ cm^{-2} at 0.005 mbar O_2 to $\sim 1.63\times10^{-14}$ cm^{-2} at 1.0 mbar O_2. The trend of n_s correlates directly to the formation of the surface space charge layer in oxidizing conditions compensating a negative surface charge. The higher the ambient pO_2 the higher the generated negative surface charge, thus leading to a lower remaining carrier concentration in the thin film.

In order to investigate the kinetics of the relaxation process the transient course

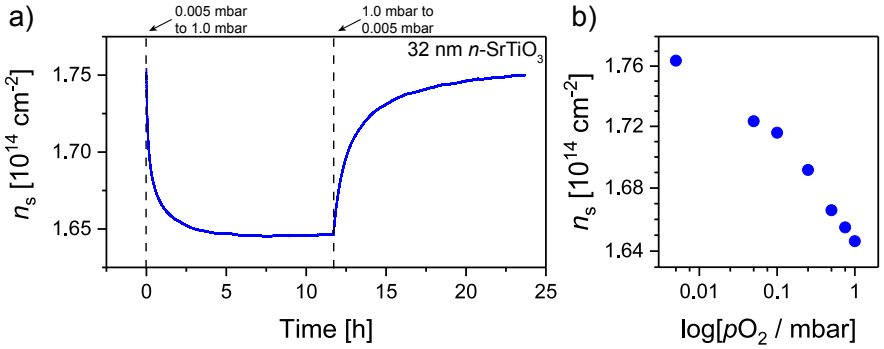

Figure 8.4.: Evolution of the sheet carrier concentration n_s of a 32 nm thick 1.0 at% n-$SrTiO_3$ thin film measured at 670 K and changing pO_2 (a). The equilibrium n_s derived at the different pO_2 is shown in (b). An increasing pO_2 decreases n_s while reducing the pO_2 to low background pressures increases the sheet carrier concentration. Switching of the ambient atmosphere with respect to the timescale of the conductivity relaxation can be regarded as instantaneous. The figure was published in ref. [121].

of the conductivity after an oxidizing and a reducing jump will be used. It allows for a qualitative statement on the reaction rate as well as on the total number of processes involved in the measured data.[149, 150] The conductivity is calculated as the reciprocal of the sheet resistance R_s

$$\sigma = 1/R_s t \qquad \left[\frac{\mathrm{S}}{\mathrm{cm}}\right], \tag{8.2}$$

where σ denotes the conductivity and t the film thickness. In order to compare the course of the conductivity between the oxidizing and the reducing jump experiments, the normalized conductivity is determined by

$$\bar{\sigma}(t) = \frac{\sigma(t) - \sigma_0}{\sigma_\infty - \sigma_0} \quad , \tag{8.3}$$

where $\bar{\sigma}(t)$ denotes the normalized conductivity, σ_0 the conductivity at t=0 and σ_∞ the conductivity at the end of the measurement. Figure 8.5 shows the transient normalized conductivity curves of a 32 nm n-$SrTiO_3$ thin film reacting to an oxidizing (blue, 0.005 mbar O_2 to 1.0 mbar O_2) and a reducing jump (green, 1.0 mbar O_2 to 0.005 mbar O_2) measured at 670 K (a) as well as the semi-logarithmic plot of the same curves (b). The dotted lines act as a guide to the eye.

It is clearly visible that the reaction to the reducing jump is significantly slower than the response to the oxidizing jump. After the oxidizing jump, the conductivity reaches its equilibrium state substantially faster than after the reducing jump, cf. fig. 8.5 (a). In addition, as can be seen from the two distinguishable slopes in the

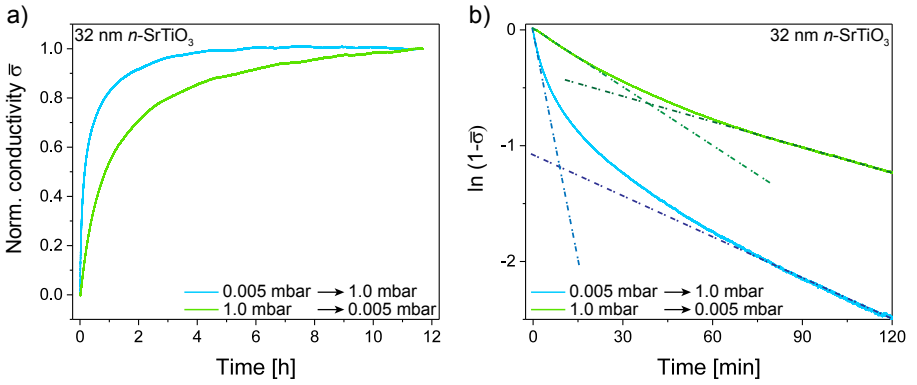

Figure 8.5.: Normalized conductivity curves of a 32 nm n-$SrTiO_3$ thin film reacting to an oxidizing (blue, 0.005 mbar O_2 to 1.0 mbar O_2) and reducing (green, 1.0 mbar O_2 to 0.005 mbar O_2) jump measured at 670 K (a). Semi-logarithmic plot of the same curves (b). The dotted blue and green lines give a guide to the eye demonstrating more than one process to be present during the relaxation.

semi-logarithmic plot, in both the oxidizing and reducing experiments there are two distinct reactions contributing to the underlying surface process, a fast and a slow one as indicated by the two distinct slopes in fig. 8.5 (b). As will be explained below, these distinct reactions can not be observed in the AP-XPS measurements. Hence, the slower process might be located deeper in the sample pointing towards the involvement of cation diffusion in the surface redox process, cf. sec. 8.4. Note that the slopes observed in the measurement results after the oxidizing jump are significantly steeper than after the reducing jump. This effect substantiates the lowered response rate after the reducing jump and indicates a slower reverse process. As will be discussed below, the lowered response rate might be due to underlying surface process involving an equilibrium reaction based on the defect chemistry of n-$SrTiO_3$ and associated to the strontium sublattice.

Surface charge calculation

In order to quantitatively evaluate the changes in the electrical surface properties, the surface charge Q/A was calculated from the sheet resistance measurements. Figure 8.6 shows a schematic illustration of the calculation. The expected total number of electrons in the 1 at% n-$SrTiO_3$ thin film is given by the donor-doping concentration N_D under the assumption of full ionization and the film thickness ($n_s = N_D \times t = 1.5{\times}10^{20}$ cm^{-3} $\times$ $32{\times}10^{-7}$ cm $= 4.8{\times}10^{14}$ cm^{-2}). The number of free electrons potentially contributing is thus described by the rectangle and derived by multiplying N_D with the film thickness. The black curve illustrates the

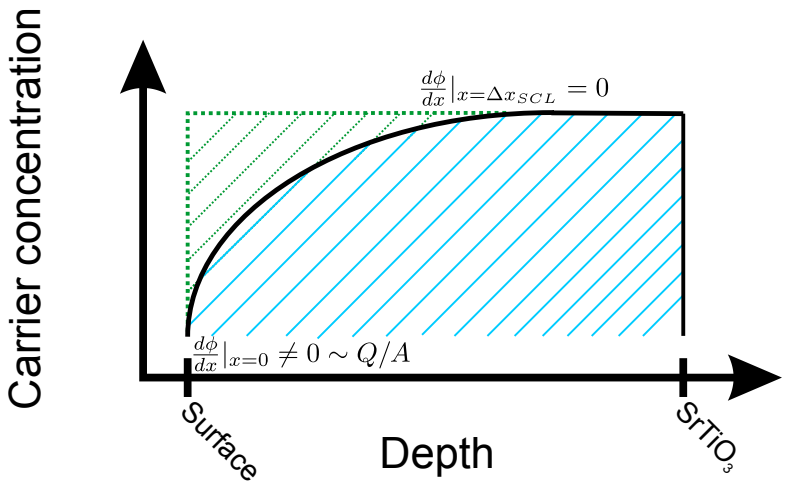

Figure 8.6.: Schematic illustration of the surface charge calculation from electrical transport measurements.

observed surface space charge layer assuming a classical parabolic approximation. The number of free electrons that still take part in the electrical transport considering a surface space charge layer is measured as the sheet carrier concentration n_s and illustrated by the light blue area. Consequently, the green area corresponds to the number of missing electrons which are trapped as they are trapped as charge at the surface. Assuming that all missing electrons are being compensated by the negative charge accumulation at the surface, the surface charge is calculated by subtracting the measured sheet carrier concentration n_s from the total number of free electrons in the 1.0 at% n-$SrTiO_3$ thin film,

$$Q/A = (N_D \cdot \ d - n_s)e \quad , \tag{8.4}$$

where Q/A denotes the negative surface charge in e/cm^2 and d denotes the thin film thickness.
Using the determined negative surface charge the resulting screening length of the surface space charge layer is derived from by combining equation 6.3 and 6.5,

$$\Delta x_{SCL} = \frac{Q/A}{eN_D} \quad , \tag{8.5}$$

where Δx_{SCL} denotes the surface space charge layer thickness in m. In addition, the corresponding electric field at the surface of the n-$SrTiO_3$ thin film is given

by

$$E_{\mathrm{surf}} = \frac{Q/A}{\epsilon_0 \epsilon_{\mathrm{r}}} \quad , \tag{8.6}$$

where E_{surf} denotes the surface electric field in MV/cm, ϵ_0 the vacuum permittivity and ϵ_{r} the temperature-dependent relative permittivity.

Figure 8.7 shows the calculated pO_2-dependent surface charges (a), the resulting screening lengths (b) and the corresponding surface electric fields (c) for a 32 nm thick 1.0 at% n-$SrTiO_3$ thin film determined at 670 K. At a pO_2 as low as 0.005 mbar O_2, the generated negative surface charge is already as high as $3.05{\times}10^{14}$ e/cm^2 resulting in an estimated space charge layer thickness of 20.3 nm and a corresponding surface electric field of 4.5 MVcm^{-1}. So, even in the lowest pO_2 adjusted within this thesis using 0.3 % O_2/Ar, the influence of the under-

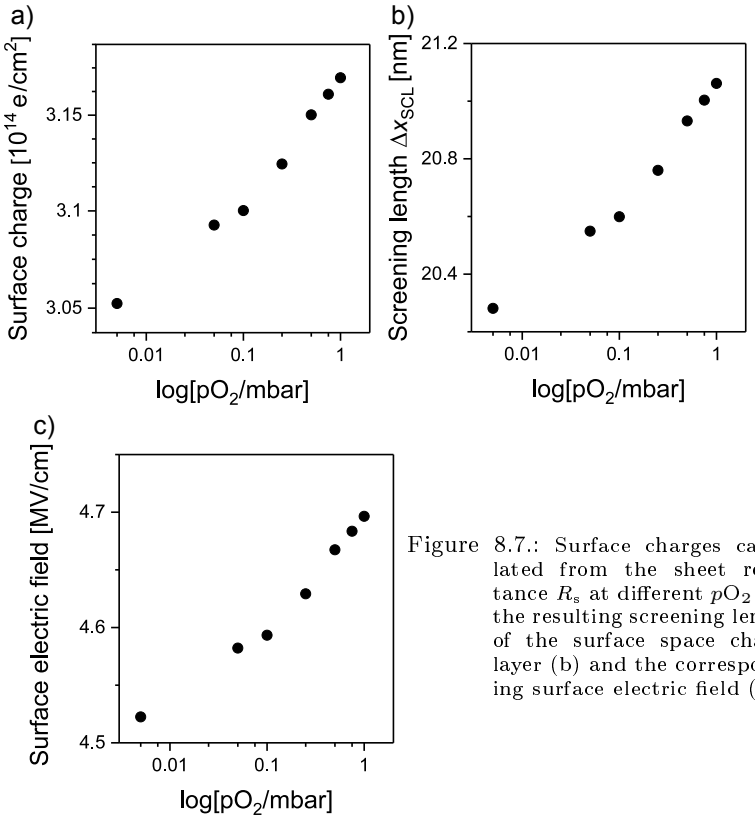

Figure 8.7.: Surface charges calculated from the sheet resistance R_{s} at different pO_2 (a), the resulting screening length of the surface space charge layer (b) and the corresponding surface electric field (c).

lying surface process on the electrical surface properties is significant. With increasing pO_2, the generated negative charge, the resulting screening length as well as the electric field of at the surface of the n-$SrTiO_3$ thin film increase substantially. At a pO_2 of 1.0 mbar O_2 the generated surface charge was determined to 3.17×10^{14} e/cm^2, developing a screening length of 21.1 nm and a surface electric field of 4.7 MVcm^{-1}. By increasing the pO_2 by three orders of magnitude the negative surface charge is increased by 0.12×10^{14} e/cm^2, the screening length is extended by 0.8 nm and the surface electric field has increased by 0.18 MVcm^{-1} representing changes of $\sim$4%. These evolution are consistent with a growing surface space charge formation with increasing pO_2 shown above, cf. chps. 6 and 7. Table 8.1 summarizes the results of the electrical transport measurements of a 32 nm n-$SrTiO_3$ thin film.

Regardless of the pO_2, the screening length of the space charge layer is in the range of the film thickness d, which might explain the absent conductivity in thin films at film thicknesses of up to 30 nm discussed in section 5.2. Note that all calculations are based on the assumption that all missing electrons are compensated by the generated negative surface charge. All other effects that might trap electrons, like impurities, contamination, ad-atoms or dislocations, lead to an overestimation of the generated surface charge and the resulting space charge layer width.[37, 129–131] In addition, the calculations of the surface charge and the surface electric field depend on the temperature dependence of the electron mobility, the thin film thickness, the donor doping concentration and the field dependence of the relative permittivity ϵ_r. Hence, slight deviations in either of these values also lead to variations in the calculated surface charges and electric fields. Consequently, all the pO_2-dependent surface charges, screening lengths and surface electric fields calculated from electrical transport measurements are treated as an upper limit.
Small changes in the ambient atmosphere lead to significant changes in the electrical properties of n-$SrTiO_3$ thin films. By increasing the pO_2 a negative charge is generated at the surface of n-$SrTiO_3$ thin films. This negative surface charge is compensated by electron depletion and hence a surface space charge layer, which is equivalent with a reduction of free carriers in the n-$SrTiO_3$ thin film and thereby leads to substantial changes of the sheet resistance R_s.

Table 8.1.: Summary of the electrical transport measurements on a 32 nm 1.0 at% n-$SrTiO_3$ thin film and the resulting parameters of the surface space charge layer.

pO_2 [mbar]	0.005	0.05	0.1	0.25	0.5	0.75	1.0
Sheet resistance R_s [kΩ]	78.3	80.1	80.5	81.6	82.9	83.4	83.9
Sheet carrier conc. n_s [10^{14} cm^{-2}]	1.76	1.72	1.71	1.69	1.67	1.66	1.65
Neg. surface charge [10^{14} cm^{-2}]	3.05	3.09	3.10	3.12	3.15	3.16	3.17
Screening length Δx_{SCL} [nm]	20.3	20.5	20.6	20.7	20.9	21.0	21.1
Surface electric field [MVcm^{-1}]	4.52	4.58	4.59	4.63	4.67	4.68	4.70

8.2. Temperature-dependent sheet resistance

Chemical redox reactions typically involve the impact of the temperature either as an activation energy or as a constraint, e.g. the incorporation of oxygen is expected to be accelerated at increased temperature, while the adsorption of oxygen molecules is expected to diminish at increased temperature. Consequently, one would expect opposite temperature dependence of these two effects. In order to in-

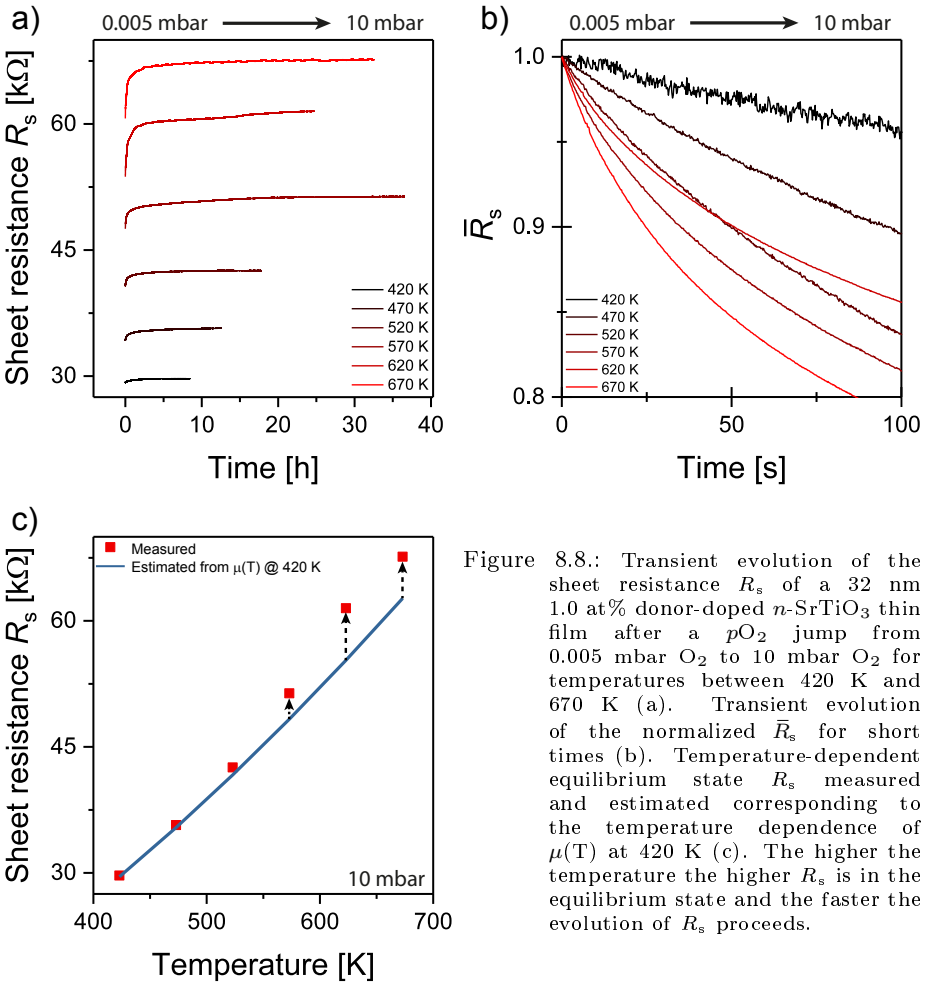

Figure 8.8.: Transient evolution of the sheet resistance R_s of a 32 nm 1.0 at% donor-doped n-$SrTiO_3$ thin film after a pO_2 jump from 0.005 mbar O_2 to 10 mbar O_2 for temperatures between 420 K and 670 K (a). Transient evolution of the normalized $\bar{R}_s$ for short times (b). Temperature-dependent equilibrium state R_s measured and estimated corresponding to the temperature dependence of μ(T) at 420 K (c). The higher the temperature the higher R_s is in the equilibrium state and the faster the evolution of R_s proceeds.

vestigate the character of the surface process in more detail, the transient course of the electrical surface properties is examined at different pO_2. Figure 8.8 shows the evolution of the sheet resistance R_s of a 32 nm 1 at.% donor-doped n-$SrTiO_3$ thin film after a pO_2 jump from 0.005 mbar O_2 to 10 mbar O_2 for temperatures between 420 K and 670 K (a), the evolution of the normalized sheet resistance $\bar{R}_s$ for short times (b), and the measured equilibrium state R_s at different temperatures in comparison to R_s calculated corresponding to the temperature dependence of the mobility μ(T) (c). Here, in order to ensure comparability, the literature value of the electron mobility μ is used.[37, 38] As has been shown above, changing the ambient atmosphere results in a systematical alteration of R_s of a n-$SrTiO_3$ thin film. With increasing pO_2, the sheet resistance increases down to a threshold temperature as low as 420 K. In addition, the normalized $\bar{R}_s$ for short times in figure 8.8 (b) also displays a temperature dependence. With increasing temperature, the starting curvature of the time-dependent course of R_s increases significantly, indicating an acceleration of the underlying process with temperature. This trend illustrates a faster reaction at higher temperatures. As already seen above in the results of the lab-based AP-XPS measurements at different temperatures these results consistently point towards a temperature activated underlying surface process with a threshold temperature in the range of 420 K, cf. sec. 7.2. Intuitively, such a behavior points towards a redox processes involving the activation of ionic sublattices.[37] Furthermore, as will be shown in section 9.3, the curvature of the course of normalized $\bar{R}_s$ allows a conclusion to be drawn about the number of partial processes involved in the surface reaction.

Furthermore, with increasing temperature R_s also increases more significantly. In classical semiconductors, this is due to the temperature dependence of the electron mobility μ(T). The electron mobility of n-$SrTiO_3$ has been determined empirically to $\mu = 3.95{\times}10^4{\cdot}\mathrm{T}^{-1.62}\left[\frac{\mathrm{cm}^2}{\mathrm{Vs}}\right]$.[37] In order to compare the temperature dependence of the electron mobility in n-$SrTiO_3$ to the temperature dependence of the measured equilibrium state R_s of the n-$SrTiO_3$ thin film, R_s has been calculated at different temperatures. Equation 8.7 shows the estimation of the sheet resistance R_s at different temperatuers for classical semiconductors [65]

$$R_s = (\mathrm{e}\ n_s\ \mu(\mathrm{T}))^{-1} \quad , \tag{8.7}$$

where μ(T) denotes the electron mobility at different temperatures. Under the assumption of n_s being constant over all temperatures, R_s(T) can be calculated. With increasing temperature the calculated sheet resistance increases, cf fig. 8.8 (c, blue). The increase of the measured R_s(red), however, is stronger than predicted for classical semiconductors. Hence, this reflects another manifestation of the additional process that increases the sheet resistance of n-$SrTiO_3$ thin films which adds up to the classical temperature dependence of the electron mobility μ resulting from the variable n_s as discussed above.

As described in section 8.1, using the sheet resistance R_s it is possible to determine the parameters which dominate the electrical surface properties. Figure 8.9

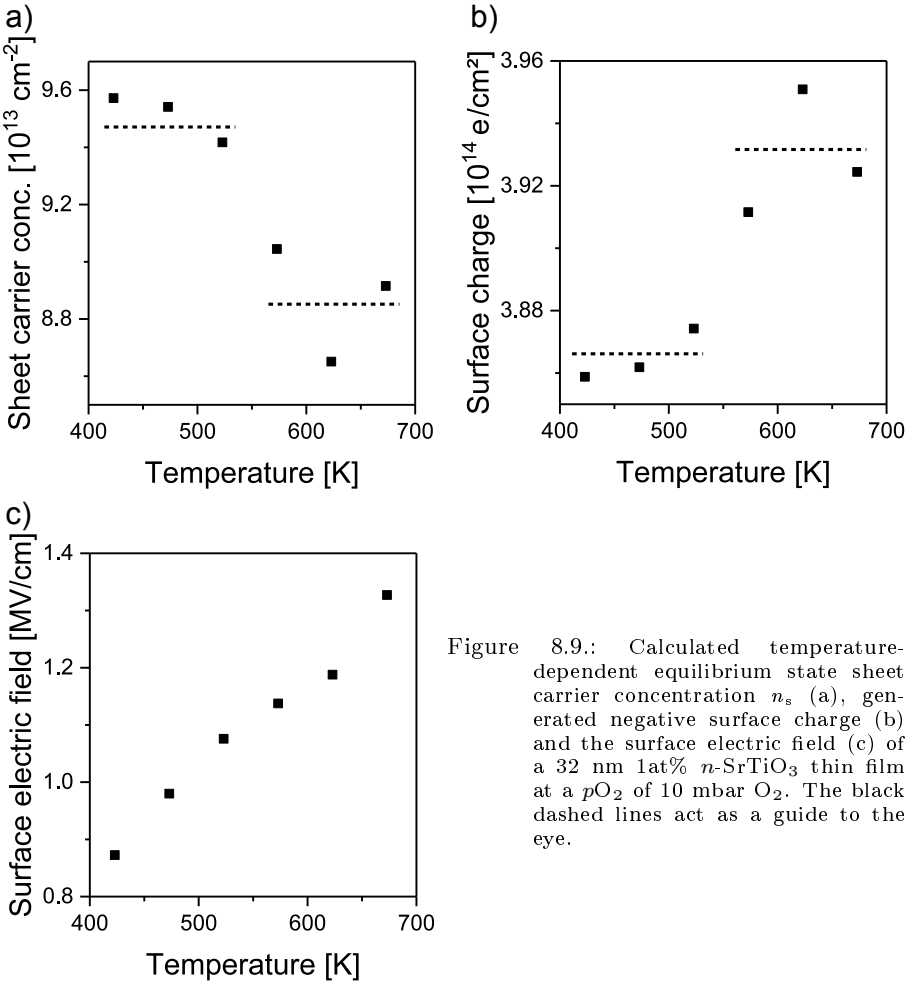

Figure 8.9.: Calculated temperature-dependent equilibrium state sheet carrier concentration n_s (a), generated negative surface charge (b) and the surface electric field (c) of a 32 nm 1at% n-$SrTiO_3$ thin film at a pO_2 of 10 mbar O_2. The black dashed lines act as a guide to the eye.

shows the equilibrium state sheet carrier concentration n_s (a), the generated negative surface charge (b) and the corresponding surface electric field (c) determined from the measured sheet resistance R_s as a function of temperature. The dashed black lines act as a guide to the eye. With increasing temperature the sheet carrier concentration n_s is reduced. As explained above, this reduction corresponds directly to an increase of the negative generated surface charge that needs to be compensated by electron depletion. At temperatures below 520 K, n_s and consequently the negative surface charge are just changed slightly from 9.57×10^{13} e/cm^2 to

9.42×10^{13} e/cm^2 and from 3.86×10^{14} e/cm^2 to 3.87×10^{14} e/cm^2, respectively. At temperatures above 520 K n_s is decreased significantly from 9.42×10^{13} e/cm^{-2} to 8.92×10^{13} e/cm^2 while the negative surface charge is increased from 3.87×10^{14} e/cm^2 to 3.92×10^{14} e/cm^2. The overall change of the sheet carrier concentration and the negative surface charge from low to high temperatures is in the range of $\sim$1.5 %. Nevertheless, even such small changes lead to significant alterations in the electrical surface properties of n-$SrTiO_3$ thin films, cf. section 8.1. Note that, the results determined at 620 K do not fit the observed trend entirely, which can already be suspected in the time-dependent R_s measurements. In contrast to the other temperatures the evolution at 620 K does not show an almost flat increase to the equilibrium state for longer times but undergoes a second rise at around 14 hours. This increase might be due to experimental difficulties, namely long-term instabilities in the adjusted pO_2, cf. section 9.3 and appendix A. These long-term instabilities made the utilization of additional premixed gas compositions like Ar/H_2 for strongly reducing conditions in further measurements inappropriate using the illustrated measurement setup. Nevertheless, it will be interesting to investigate the impact of reducing conditions on the electrical surface properties in future experiments utilizing an updated measurement setup.

In contrast to the results observed for the sheet carrier concentration and the surface charge, the pO_2 dependence of the surface electric field does not show different regimes with increasing temperature, cf. fig. 8.9 (c). It increases monotonously from 0.87 MV/cm at 420 K to 1.33 MV/cm at 670 K, representing a change of 65 %. These results are consistent with the measured total temperature dependence of R_s shown above. The divergence in the course of the temperature dependence might be due to the weaker impact of the temperature dependence of the relative permittivity ϵ_r on the surface electric field calculation in comparison to the impact of the temperature dependence of the electron mobility μ on the calculation of the sheet carrier concentration.

8.3. Numerical fitting of the transient sheet resistance

Utilizing numerical simulations it is possible to draw conclusion on the surface processes dominating the transient course of the pO_2-dependent sheet resistance. As shown in figure 8.5 (b), the semi-logarithmic plot of the normalized conductivity points towards the impact of two distinct reactions to be involved in the surface redox process, a fast and a slow one. Moreover, the comparison of the transient AP-XPS and ECR measurements indicates the fast process to be located at the surface, while the slow one induces additional oxidation in depths not accessible by spectroscopy, cf. sec. 8.4.

A numerical fitting routine of the transient sheet resistance that considers both a surface transfer reaction and bulk diffusion in three sample dimensions was implemented by Katharina Skaja (PGI-7, FZ Jülich). The numerical simulation routine is described in detail in ref. [77]. The assumption of a surface transfer process in

combination with bulk diffusion is in good agreement with the observed results. In contrast to the implemented fitting routine, however, the low n-$SrTiO_3$ thin film thickness of 32 nm used within the ECR experiments in comparison to the much wider sample surface area (5 μm×5μm) allows for the modeling of the diffusion in just one dimension perpendicular to the surface. Consequently, the implemented fitting routine is adjusted to a model introduced by *v. d. Otter et al.* which considers surface transfer and diffusion in just one dimension, perpendicular to the sample surface, cf. sec. 2.5.[79] One assumption made by *v. d. Otter et al.* is the process to be an ideal step response. This assumption is reasonable for the executed experiments considering the flushtime of the experimental reactor is in the range of seconds and is hence negligible in comparison to the overall relaxation time in the order of several hours.

Considering an unknown concentration of impurities, contamination, ad-atoms and dislocations, the exact number of charge carriers, namely electrons, is not accessible by determining the conductivity. Therefore, only the relative changes of the conductivity will be analyzed within this thesis, by the normalized conductivity. Within the model explained in detail in section 2.5, it is calculated (eqs. 2.11, 2.12 and 2.14) to

$$\bar{\sigma}_{\mathrm{step}} = \frac{\sigma_{\mathrm{step}}(t) - \sigma_0}{\sigma_\infty - \sigma_0} = 1 - \sum_{n=1}^{\infty} \frac{2L_\alpha^2}{\alpha_n^2(\alpha_n^2 + L_\alpha^2 + L_\alpha)} \exp\left(-\frac{t}{\tau_n}\right) \quad \text{, with} \tag{8.8}$$

$$\tau_n = \frac{a^2}{D \cdot \alpha_n^2} \quad ; \quad L_\alpha = \frac{aK_{\mathrm{tr}}}{D} = \alpha_n \tan(\alpha_n) \quad , \tag{8.9}$$

where $\bar{\sigma}_{\mathrm{step}}$ denotes the normalized conductivity of the ideal step response, $\sigma_{\mathrm{step}}(t)$ the measured normalized conductivity at a given time t, σ_0 the conductivity at t=0, σ_∞ the conductivity at t=∞, L_α a calculation parameter, α_n the eigenvalues of the sheet diffusion problem, τ_n the time constant, a half the film thickness, D the diffusion coefficient and K_{tr} the surface transfer coefficient. As described in section 2.5, this equation cannot be solved analytically due to the infinite number of α_n for each combination of K_{tr} and D. Within this thesis only the first ten eigenvalues α_n were utilized for the simulation of K_{tr} and D, since higher n do not contribute significantly to resulting conductivity relaxation curve.[77, 81]

In order to adjust the calculated to the measured values a squared error was used

$$\Delta = |\bar{\sigma}_{\mathrm{step,calculated}}(t) - \bar{\sigma}_{\mathrm{step,measured}}(t)|^2 \quad , \tag{8.10}$$

where Δ denotes the deviation of the calculated value from the measured value of the conductivity.

Figure 8.10 shows the normalized conductivity of a 32 nm n-$SrTiO_3$ thin film after a pO_2 jump from 1.0 mbar to 0.005 mbar at a temperature of 520 K and the corresponding fit (a) as well as the false color map of the logarithm of the squared error matrix for the evaluation of the surface transfer coefficient and the diffusion

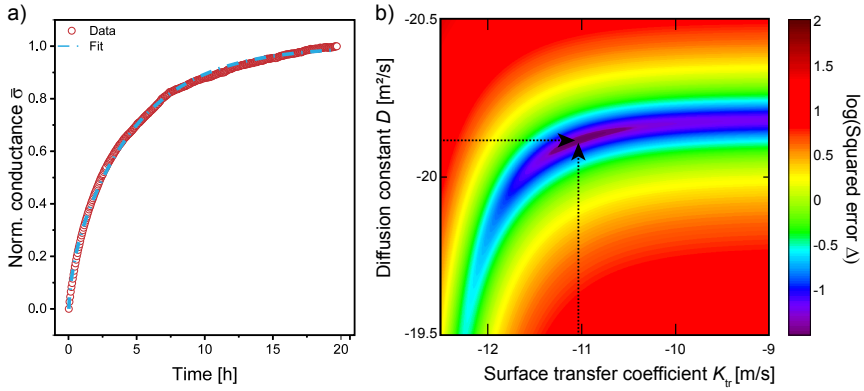

Figure 8.10.: Normalized conductivity of a 32 nm n-$SrTiO_3$ thin film measured after a pO_2 jump from 1.0 mbar to 0.005 mbar at a temperature of 520 K and the corresponding fit (a). False color map of the logarithm of the squared error matrix (color scale) for the evaluation of the surface transfer coefficient K_{tr} (x-axis) and the diffusion coefficient D (y-axis) is depicted in (b).

coefficient (b).

The fit resulting from the applied model matches the course of the determined conductivity reasonably well. Thus, the implemented one dimensional model combining a surface transfer process and a bulk diffusion process is able to describe the observed pO_2-dependent evolution of the conductivity. This result is substantiated by the false color map. It illustrates a clear minimum of the squared error in the transition (curvature) between the surface transfer coefficient and the diffusion coefficient (dark purple), fig. 8.10 (b). The surface transfer coefficient is fitted to K_{tr}=9.5×10^{-12} m/s while the diffusion coefficient is determined to D=6.4×10^{-21} m^2/s. The resulting characteristic length L_c determined from equation 2.15 to 0.67 nm. Utilizing the fitted diffusion coefficient a diffusion length of ∼21.5 nm in 20 hours is calculated. Thus, the ratio of the characteristic length L_c and the diffusion length is ∼30. At this value none of the two processes is dominant. Consequently, it is reasonable to draw conclusions from the fitting procedure on specific values of both K_{tr} and D.[77, 79]

The surface transfer coefficient is attributed to the pO_2-dependent formation of a charged species at the n-$SrTiO_3$ surface. In addition, the diffusion coefficient is attributed to the diffusion of the charged species formed at the surface into the sample. These findings substantiate the formation of a surface space charge layer ranging into the sample proposed in chapters 6 and 7. Moreover, the resulting D might correspond to the oxidation process taking place at sample depths not accessible by spectroscopic experiments as will be discussed below, cf. sec. 8.4.

A detailed discussion if the determined reaction rates are considered reasonable in terms of the surface redox process is given in section 9.3.

8.4. Comparison of AP-XPS and ECR results

All electrochemical conductivity relaxation experiments took place in pO_2 ranging from 0.005 mbar up to 1 mbar which is comparable to the ones that were used for the *in-situ* AP-XPS experiments, cf. chapters 6 and 7. Note that the lowest adjusted pO_2 during AP-XPS (10^{-8} mbar) is more reducing than the one adjusted during ECR experiments (0.005 mbar). Using comparable ambient pO_2 the occurring electrical effects are linked to the generated space charge layer at the surface of n-$SrTiO_3$. Figure 8.11 illustrates the comparison of the generated negative surface charge (a), the resulting screening length of the surface space charge layer (b) and the corresponding surface electric field (c) as function of the pO_2 determined by AP-XPS (green) and electrochemical relaxation conductivity measurements (red). The dotted lines indicate the pO_2-dependent evolution, while the shaded area marks the possible values given by the determined upper and lower limit.

As has been shown above a negative surface charge dominates the electrical surface properties of n-$SrTiO_3$ thin films and single crystals. Both spectroscopic and electrical transport measurements, two independent experimental techniques, which evaluate two independent measurement values, revealed a negative surface charge that is in the same order of magnitude of $\sim 10^{14}$ e/cm^2. In addition, the results show an analogous pO_2-dependent evolution indicating the same underlying surface redox-process to be active in both measurements.

Moreover, these findings are consistent with the identical pO_2-dependent evolution of the resulting screening lengths of the corresponding surface potentials and the matching surface electric fields, which are in the range of $\sim$5 nm to $\sim$20 nm and $\sim$1 MVcm^{-1} to $\sim$5 MVcm^{-1} at low and high pO_2 conditions, respectively. Hence, all results may be linked to the same underlying surface redox process. Consequently, the values of the surface charge, the screening length and the surface electric field derived at a given temperature and pO_2 should ideally be equal. Nevertheless, the conclusion of an identical underlying process is reasonable due to the assumptions applied during the determination of the specific surface charge values. On the one hand, as explained in section 6.1 the negative surface charge concluded from AP-XPS experiments is considered a lower limit, due to the underestimation of the apparent binding energy shift. On the other hand, the negative surface charge determined from electrochemical conductivity relaxation experiments is considered an upper limit, due to the neglection of any other electron trapping defects in the n-$SrTiO_3$ thin film, the temperature dependence of the electron mobility, variations in the thin film thickness and the inherent donor doping concentration, cf. section 8.1. In this way, by specifying a lower and an upper limit the results open up a range of possible values for the generated negative surface charge and all resulting space charge layer screening lengths and corresponding surface electric fields linked to the same underlying surface redox process.

To give a ballpark estimation, assuming a parabolic potential[65] and using a value of $\epsilon_r(670\ \mathrm{K}) = 122$[37, 38], a surface potential ϕ_0 in the range of $\sim$4 V is calculated from the negative surface charge determined by ECR experiments at

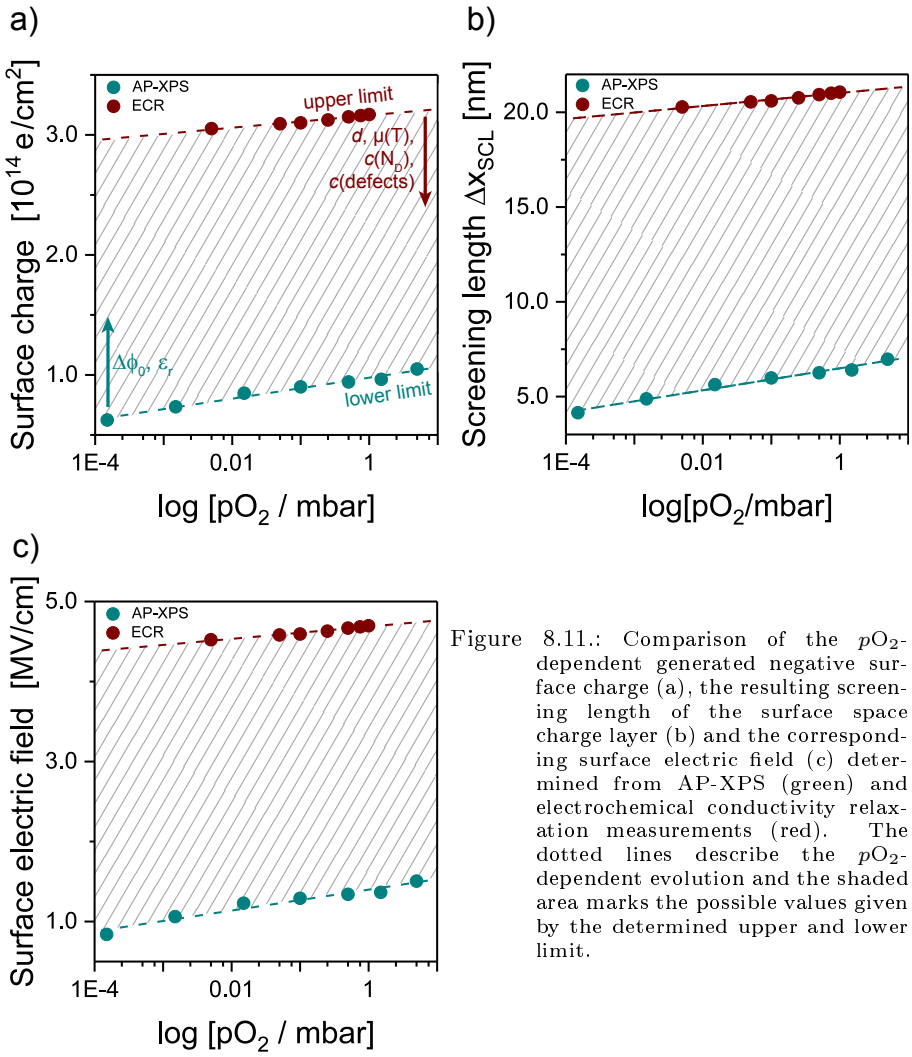

Figure 8.11.: Comparison of the pO_2-dependent generated negative surface charge (a), the resulting screening length of the surface space charge layer (b) and the corresponding surface electric field (c) determined from AP-XPS (green) and electrochemical conductivity relaxation measurements (red). The dotted lines describe the pO_2-dependent evolution and the shaded area marks the possible values given by the determined upper and lower limit.

1 mbar O_2. Such a surface potential would indicate a shift of the Fermi energy by 4 eV which would be larger than the band gap, pointing towards that the parabolic approximation breaks down, cf. sec. 9.3. In addition, the negative surface charge determined by AP-XPS at a temperature of 670 K, a pO_2 of 1.5 mbar O_2 and an electron mobility of $\mu(670\ \mathrm{K}) = 0.45\ \mathrm{cm}^2/\mathrm{Vs}$ correlates to a sheet carrier concen-

tration of 3.9×10^{14} cm^{-2} and a corresponding sheet resistance of 36 kΩ. For all samples the measured R_s was always significantly higher. This deviation might be due to the fact that even in low pO_2 a significant amount of negative charge is present at the n-$SrTiO_3$ surface, since AP-XPS measurements demonstrated the existence of a surface space charge layer, which counteracts the assumption of the flatband case used for the calculation. Hence, the presence of a negative surface charge at low base pressure conditions of 10^{-8} mbar and the corresponding space charge layer may explain the higher resistance observed in ECR experiments.

Note that for both these ballpark estimations a classical semiconductor approach with a negative surface charge located solely at the surface, a purely parabolic course of the surface potential drop as well as a constant relative permittivity are assumed. The negative surface charge here, however, is generated by a surface chemical process, cf. section 9.3, pointing towards that either prerequisite assumption is not correct. As theoretical simulations revealed, the diffusion of ions into the sample might change the distribution of the negative surface charge, break down the parabolic course of the potential or even vary the local relative permittivity.[151]

This conclusion is substantiated by the comparison of the relevant time scale of the electrical and spectroscopic measurements. The overall resistance change occurs on a time scale of several hours (up to 12 h), while 82 % of the resistance changes takes place within the first hour, coinciding with the time required to adjust and stabilize the atmospheric conditions in the AP-XPS experiments, cf. chs. 6,7. In the AP-XPS experiments no transient changes in spectral change or position was observed on a longer time scale, indicating that the underlying surface reaction is responsible for the majority of the resistance relaxation. The remaining change in resistance potentially occurs in addition to this space charge effect and is not tracked by AP-XPS. This may hint towards an additional oxidation process taking place deeper in the sample. Intuitively, such an oxidation process is most likely related to cation vacancy diffusion. Cation vacancies, however, can not be detected by spectroscopic measurements, but can only be detected as slight deviations of the lattice site cation concentration, cf. sec. 9.3. Therefore, the determined surface charges may not be reasonably compared directly between the different experimental techniques, but define a reasonable range of possible values that is given by the assumption of the upper and the lower limit.

Combining the results of spectroscopic and electrical measurements demonstrate that changing the ambient atmosphere, the oxygen partial pressure and the temperature, allows a control of the electrical surface properties and the electrical transport within a n-$SrTiO_3$ thin film. By generating a negative surface charge the surface band bending is altered yielding in an electron depletion.

Summary

In this chapter the impact of the pO_2-dependent surface space charge layer on the electrical surface and transport properties of n-$SrTiO_3$ thin films was investi-

gated by electrical conductivity relaxation experiments. In the first section, it was shown, that at elevated temperatures even slight alterations of the ambient pO_2 result in significant changes of the sheet resistance. These changes are attributed to an increasing negative surface charge that is accompanied by electron depletion underneath the surface. This decrease of the sheet carrier concentration is consistent with the surface space charge layer that has been described above by AP-XPS. Thus, by just slightly altering the ambient pO_2 the electrical surface properties can be controlled.

In the second section it was illustrated, that the increase of the sheet resistance R_s is more sensitive to the applied temperature than expected. In addition, the reaction rate of the surface process is shown to increase with increasing temperature. Both these findings point towards a temperature activated surface redox process.

In the third section of this chapter a fitting procedure is discussed that attributes the pO_2-dependent transient conductivity to a model combining a surface transfer process with bulk diffusion in one dimension. The model simulates the measured evolution reasonably well and results in specific values for both the surface transfer coefficient K_{tr} and the diffusion coefficient D.

In the fourth section it was demonstrated, that the pO_2-dependent generated negative surface charge and the corresponding surface electric field determined by two independent measurement techniques are in the same order of magnitude. The pO_2-dependent evolution is similar. The results of the AP-XPS measurements act as a lower limit, while the results of the ECR measurements give an upper limit specifying a range of plausible values for the negative charge generated at the surface of n-$SrTiO_3$ samples.

So far it was confirmed, that a pO_2-dependent surface charge controls the electrical surface properties of n-$SrTiO_3$ at elevated temperatures. The next chapter will clarify the chemical process responsible for the changes at the n-$SrTiO_3$ surface and illustrate how it affects the properties upon oxidizing annealing of single crystals.

9. Discussion

The previous chapters illustrated the impact of pO_2, temperature and donor-doping concentrations on the electrical and chemical properties generating a negative surface charge at the surface of n-$SrTiO_3$ single crystals, interfaces and thin films. These properties may be affected by multiple surface reactions that form the observed charge and thus need to be considered. Considering all former experimental results resolved from impedance spectroscopy, IV-curves, Hall measurements, lab- and synchrotron-based AP-XPS and electrochemical conductivity relaxation measurements in a comprehensive manner, this chapter will consistently explain the influence of the surface redox chemistry on the electrical surface properties of n-$SrTiO_3$ thin films and single crystals. The first section focuses on the specification of surface redox processes that are well-known to dominate the surface properties of single crystals, heterojunctions and thin films. It will be examined whether or not the described redox processes are consistent with the observed results. In the second section, two complex surface redox processes that are consistent with the majority of the results, namely strontium oxide (SrO) precipitation and the adsorption of oxygen molecules withdrawing electrons from the surface, are compared directly. It will be discussed how synchrotron-based AP-XPS demonstrates the strontium sublattice to be dominantly involved in the underlying surface redox process. Consequently, the precipitation of SrO at the n-$SrTiO_3$ surface, corresponding to the formation of charged strontium vacancies (V''_{Sr}) and accompanied by nanoscopic morphological changes is clarified as the underlying surface redox process. In the third section the influence of this process on the spectroscopic and electrical surface properties of n-$SrTiO_3$ is discussed.

9.1. Surface redox processes at the n-$SrTiO_3$ surface

There are various parameters that affect different experimental techniques while investigating doped and undoped $SrTiO_3$ at varying oxygen partial pressure. Figure 9.1 shows schematic illustrations of the possible effects that might be causing the negative surface charge observed in the individual experimental techniques that will be discussed in detail in the following.

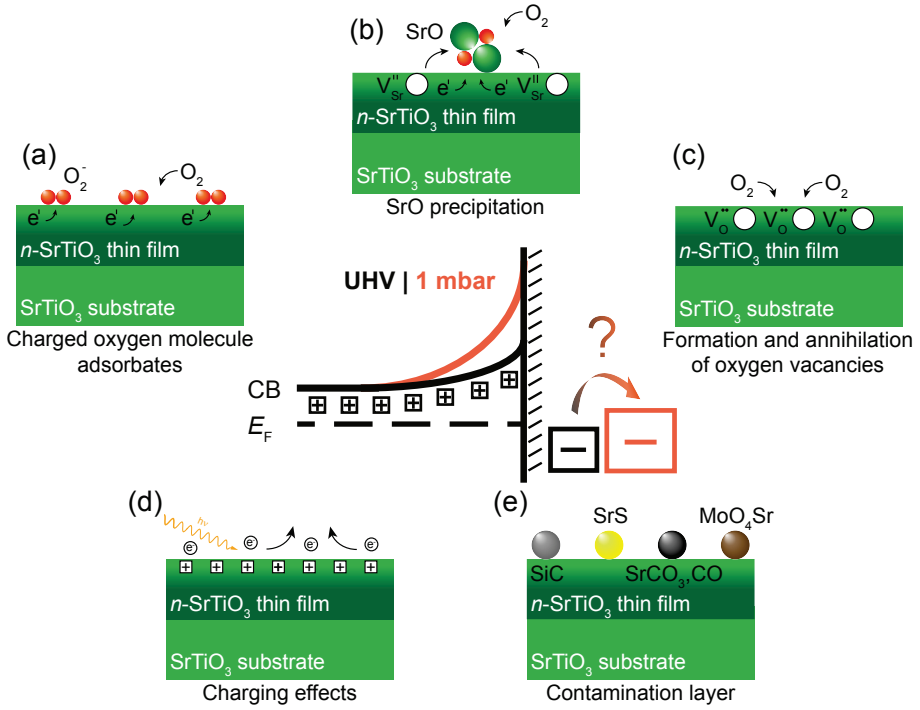

Figure 9.1.: Schematic illustrations of effects that might cause the negative surface charge observed in the different experimental techniques.

One effect that is well-known in literature and that depends directly on the pO_2 is the formation and annihilation of oxygen vacancies, cf. fig. 9.1 (c). In addition, in spectroscopic experiments the applied X-ray beam can induce surface charging in insulating samples. This is due to the low conductivity preventing the system to compensate for the electrons extracted by the X-ray beam (fig. 9.1 (d)), cf. sec. 3.5. Moreover, some effects have been demonstrated on n-$SrTiO_3$ surfaces but their pO_2 dependence is not clarified yet, such as the formation of a contamination layer or an intrinsic surface pinning potential such as dangling bonds, cf. fig. 9.1 (e). Furthermore, complex surface redox reactions can be driven by varying the thermodynamic biases such as the precipitation of SrO which is accompanied by the formation of V''_{Sr} (fig. 9.1 (b)) and the adsorption of oxygen molecules trapping a surface electron (fig. 9.1 (a)). All these influencing parameters will be discussed in the following and it will be examined whether or not they consistently explain the pO_2-dependent formation of the negative surface charge observed in the experiments.

Formation and annihilation of oxygen vacancies

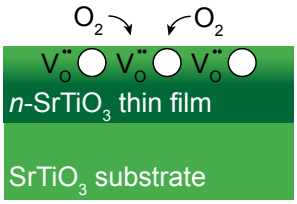

Formation and annihilation of oxygen vacancies

One major influencing parameter that needs to be considered in terms of $SrTiO_3$, especially in variable oxygen partial pressures, is the pO_2-dependent formation and annihilation of oxygen vacancies. On the one hand, there are phenomena related directly to oxygen vacancies in undoped $SrTiO_3$ such as resistive switching, where by changing the oxygen vacancy concentration the resistance can be altered between an insulating and a metallic state.[11, 152–154] These effects are detectable by spectroscopic experiments by a changing concentration of Ti^{3+} ions which can be identified from a shoulder on the right side of the Ti2p spectra.[124] Note that Ti^{3+} ions are also produced by the donor doping. Hence, in order to be able to actually observe oxygen vacancies in donor doped $SrTiO_3$ by spectroscopic experiments a vancancy concentration significantly exceeding the doping concentration is crucial. On the other hand, the presence and accumulation of oxygen vacancies at the surface of $SrTiO_3$ is also known to influence experimental methods that at first sight do not seem sensitive to variable oxygen vacancy concentration, cf. by varying the local work function.[123] In the very low pO_2 regime, the charge carrier concentration is dominated by the concentration of oxygen vacancies in the so-called intrinsic regime. With increasing pO_2, the oxygen vacancy concentration decreases constantly. The defect chemistry of donor-doped $SrTiO_3$, however, predicts the impact of oxygen vacancies to be reduced reduced dramatically due to charge carrier concentration being dominated by the donor doping concentration, cf. sec. 2.4.

Spinelli et. al. performed annealing experiments on $SrTiO_3$ single crystals with different donor-doping concentrations and evaluated the carrier concentration by Hall measurements in van der Pauw geometry. Thereby, they were able to determine the oxygen vacancy concentration at varying thermodynamical biases corresponding to what is used throughout this thesis. As a result, the expected concentration of donor-type oxygen vacancies at the temperatures and oxygen partial pressures employed within this work (470 K to 770 K, 10^{-8} mbar to 5.0 mbar O_2) is in the range of 10^{18} cm^{-3} and below.[37, 58] This value is significantly lower than all donor-doping concentrations utilized within this thesis. Therefore, a varying oxygen vacancy concentration alone is not expected to provide sufficient charge for substantial changes of the surface space charge region in doped $SrTiO_3$.

These considerations are corroborated by the results of the lab-based AP-XPS measurements. As is seen from figure 6.9 there is no implication for any Ti^{3+} states during the lab- and synchrotron-based AP-XPS measurements. Intuitively the oxygen vacancy concentration should be higher at low base pressure conditions, but neither in UHV nor in high pO_2 conditions, a significant peak or shoulder related to Ti^{3+} is detectable, indicating a Ti^{3+} concentration below the detection limit.

Thus, even the free electrons corresponding to the donor doping concentration can not be observed.

These findings are substantiated by the superposition of the Ti2p peaks measured at different conditions and probing depths where only a slight broadening of the peak is detectable, cf. fig. 6.15. As was already shown in section 6.1, this broadening is due to the space charge layer at the surface of n-$SrTiO_3$. Thus, both defect chemical predictions as well as experimental results demonstrated in literature and within this thesis lead to the conclusion that the pO_2-dependent formation and annihilation of oxygen vacancies is not the cause of the observed negative surface charge. This is also rule true considering the acucmulation of oxygen vacancies at the $SrTiO_3$ surface.[155, 156] Consequently, any influence of oxygen vacancies will therefore be neglected in the following.

Charging effects in spectroscopic experiments

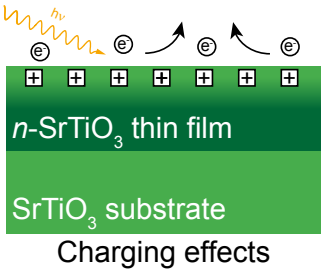

In spectroscopic measurements the X-ray beam can cause charging effects on insulating sample surface, cf. sec. 3.5. Such a beam related surface charge typically results in a shift of the binding energy towards higher values.[118] By extracting electrons from the surface without compensating them from the bulk of the material a positive surface charge is formed corresponding to a positive surface potential. The positive surface potential decreases the kinetic energy of the emitted electrons and the referencing of the measured binding energy by the experimental setup′s Fermi level is no longer valid. As shown above, n-$SrTiO_3$ is more conducting in the low base pressure regime than in oxidizing atmospheres as demonstrated by ECR experiments, cf. sec 8.1. Thus, with increasing oxygen partial pressure the X-ray beam related charging should be increased due to the lower conductivity of the sample shifting the apparent binding energy towards higher values. In contrast, all spectroscopic experiments on n-$SrTiO_3$ samples show the opposite behavior. With increasing pO_2, the binding energies of all core levels and the valence band maximum shifts towards lower values, regardless of the measurement setup, the applied temperature or the donor doping concentration of the investigated sample, cf. chps. 6 and 7.

Moreover, to even more safely exclude charging, additional reference measurements were performed on an Au electrode deposited on the sample with an additional titanium interlayer. The interlayer ensured an ohmic contact and thereby Fermi coupling of the thin film to the analyzer, cf. fig. 6.10. In contrast to the measurements on the characteristic core levels of $SrTiO_3$ (cf. chps. 6 and 7), there is neither any pO_2-dependent binding energy shift nor any peak broadening visible in the Au4f spectra. Consequently, both considerations as well as the experimental

results demonstrate that X-ray beam related charging effects are not the dominating processes in terms of the observed pO_2-dependence in lab- and synchrotron-based AP-XPS and are therefore neglected.

Contamination layer, intrinsic pinning potential, and surface reconstruction

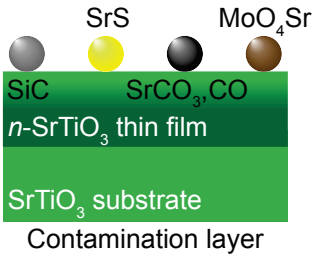

A surface charge may be provided by the presence of an unintentional contamination layer absorbed on the surface trapping charge carriers.[25, 68] Contamination on n-$SrTiO_3$ surfaces typically involve the presence of carbon in form of carbon monoxide (CO) and strontium carbonate ($SrCO_3$) introduced by the residual gas atmosphere in UHV or by *ex-situ* sample transport.[157] Moreover, most spectroscopic setups are used for the investigation of various samples and hence, contamination that might be left over in the measurement system attached to the chamber walls such as silicon and sulfur need to be considered. Another source of contamination is introduced by the measurement chamber itself mostly consisting of alloyed steel. At high temperatures and high pO_2, some of the alloys tend to be released from the chamber walls and adsorbed at the sample surface such as molybdenum. Thus, in order to investigate the influence of contamination on the negative surface charge the characteristic core level spectra of carbon (C1s, a), molybdenum (Mo3d, b), sulfur (S2s, b) and silicon (Si2s, c) were investigated in detail by AP-XPS, cf. figs. 6.2 (a) and 6.8.

As discussed in section 6.1, the C1s core level is present at the initial measurements at room temperature and in UHV conditions. With increasing temperature, the carbon contamination is reduced and with increasing pO_2 up to 0.15 mbar it completely vanishes. The systematic and reversible character of the surface space charge formation as well as the disappearance of any observable carbon peak intensity makes a merely contaminants-based scenario unlikely. In addition, regardless of the applied pO_2 neither molybdenum nor sulfur nor silicon contamination are detected at elevated temperatures, indicating a surface contamination below the detection limit. Consequently, a dominating impact of unintentional contamination layers on the negative surface charge is excluded.

Another possible impact was described by *Ohtomo et al.* who observed a surface electron depletion in La-doped $SrTiO_3$ thin films at temperatures below 300 K. They related it to an intrinsic surface pinning potential of about 0.7 V formed by positively charged surface defects attracting oxygen and thereby binding free electrons in the bulk.[39] The trapping of free bulk electrons results in a shift of the Fermi-energy at the surface. The surface defects were attributed to oxygen defects

at the surface as well as to dangling bonds.[119, 158, 159] An intrinsic surface potential, however, would not show the pO_2-dependence of the negative surface charge and the corresponding apparent binding energies in general and the Sr3d core level in particular observed in sections 6 and 7 and can hence not describe the observed results comprehensively.

Furthermore, surface reconstructions and anti-domain boundaries were reported to be pO_2-dependent and also directly connected to apparent surface band bending.[160–163] These dependence already point towards nanoscopic morphological changes being involved in the underlying surface process. In the following two more complex surface redox processes that involve pO_2-dependent morphological changes will be introduced and discussed.

Strontium oxide precipitation and strontium vacancy formation

Another redox process that may dominate the space charge formation at the n-$SrTiO_3$ surface at elevated temperatures is the pO_2-dependent precipitation of SrO accompanied by the formation of V''_{Sr}.[37, 38, 70–72] *Marchewka et al.* revealed the existence of an electron depletion layer in Pt/Fe:$SrTiO_3$/Nb:$SrTiO_3$ structures extending into the Nb-doped bottom electrode. They correlated this depletion to acceptor-type defects and suggested the presence of strontium vacancies (V''_{Sr}) at the Fe:$SrTiO_3$/Nb:$SrTiO_3$ interface.[52] These findings are complemented by *Meyer et al.* who recently proposed a high temperature surface oxidation model that associates electron depletion in the near surface region of n-$SrTiO_3$ in oxidizing conditions with the incorporation of negatively charged surface V''_{Sr}. Based on the defect chemistry of n-$SrTiO_3$ they evaluate the V''_{Sr} concentration, which is the dominating cation defect in oxidizing conditions, to even exceed the donor dopant concentration in the near surface region.[38]

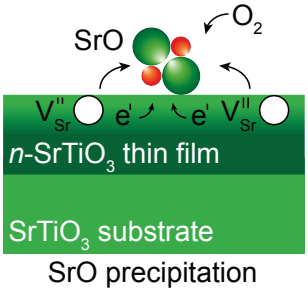

The defect chemistry of donor-doped bulk $SrTiO_3$ that involves the activation of the strontium sublattice is generally accepted for elevated temperatures above 1200 K, cf. sec. 2.4.[37] At lower temperatures, however, it might not be possible to equilibrate either of the ionic sublattices (oxyge, strontium, titanium) in the entire sample due to sluggish ionic movement.[23, 38] At temperatures between 420 K and 770 K, as utilized within this thesis, the bulk diffusion coefficient of V''_{Sr} is determined to values between 1.3×10^{-38} cm^2/s and 2.4×10^{-23} cm^2/s, respectively.[37, 38] Hence, the formation and movement of V''_{Sr} at temperatures as low as applied during the AP-XPS and ECR measurements is remarkably. Nevertheless, in the case of the localization at the surface there is no need for an ionic movement over

large distances. This would freeze-in the defect concentrations, resulting in an effective charge separation at the surface. Consequently, the observed negative surface charge may be consistent with the formation of V''_{Sr} at the surface even at temperatures as low as 420 K.

In terms of AP-XPS the precipitation of SrO at the n-$SrTiO_3$ surface will result in the formation of a secondary component doublet in the Sr3d core level which is shifted by 0.8 eV towards higher values.[72] With increasing pO_2, the secondary component doublet increases. Moreover, due to the SrO precipitation being located at the surface, with decreasing probing depth the secondary component doublet increases. This trend leads to a flattening of the valley between $Sr3d_{3/2}$ and $Sr3d_{5/2}$ peaks with decreasing probing depth. The accompanied formation of strontium vacancies is not detectable directly, but only by the link between the Sr3d lattice component and SrO secondary component as defined by the area ratio. Furthermore, theoretically the O1s should also exhibit an additional component corresponding to the changed strontium oxide binding state. Even though an additional oxygen component was found in all spectroscopic experiments, due the data accuracy and the superposition with the unsaturated oxygen surface lattice peak this additional component could not be observed.[137] All other core level peaks display a slight broadening due to the evolution of the surface space charge layer and the corresponding potential drop into the sample. Note that this broadening is asymmetric but due to the measurement accuracy this effect might not be measurable, cf. sec. 6.1.

Adsorption of oxygen molecules

Another possible redox process that would be able to dominate the negative surface charge and has thus to be considered is the adsorption of oxygen molecules at the n-$SrTiO_3$ surface. With increasing pO_2, an increasing concentration of oxygen molecules chemisorbs at the surface. Due to the high electronegativity of oxygen in comparison to the $SrTiO_3$ lattice an electron is transferred from the n-$SrTiO_3$ surface to the oxygen molecule potentially generating the observed negative surface charge.[164] In this way, a Taguchi-type space charge layer is formed.[29]

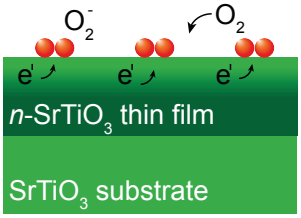

Charged oxygen molecule adsorbates

Setvin et al. showed the existence of oxygen molecules forming superoxides at TiO_2 surfaces at temperatures below 300 K.[50, 51] Similarly, the existence of charged oxygen adsorbate species are proposed on perovskite type oxide surfaces comparable to $SrTiO_3$ ($(La,Sr)MnO_{3-\delta}$) with finite concentrations up to temperatures of 1000 K.[75, 165, 166] Thus, even though their concentration supposedly

decreases with increasing temperature, it is reasonable to consider that the negative surface charge observed within this thesis might consistently be explained by the adsorption of charged oxygen molecules.

In terms of AP-XPS the adsorption of charged oxygen molecules onto the n-$SrTiO_3$ surface should result in an additional component in the O1s core level spectra. It is difficult to unambiguously interpret such an additional component peak due to the measurement accuracy and the superposition with the unsaturated O1s surface lattice component. All other characteristic core levels exhibit a slight broadening due to the surface space charge layer and the corresponding potential drop into the sample. In the Sr3d core level such a continuous broadening leads to a flattening of the intensity valley between the $Sr3d_{3/2}$ and $Sr3d_{5/2}$ peaks with increasing probing depth. Consequently, a conclusive way to demonstrate the chemisorption of charged oxygen molecules onto the n-$SrTiO_3$ surface is the broadening of all characteristic core levels without an additional SrO surface component in the Sr3d core level.

At this point, it is difficult to decide which surface redox process is dominating the electrical properties of n-$SrTiO_3$, the formation of intrinsic ionic surface defects, namely V''_{Sr}, or the chemisorbtion of charged oxygen molecules withdrawing free electrons from the n-$SrTiO_3$ surface. Both redox processes would be able to from a negative surface charge and cause the observed space charge layer. In order to distinguish between the two processes in the following the pO_2- and probing depth-dependence of the Sr3d core level will be employed in detail, giving further insight into the underlying mechanism.

9.2. SrO precipitation vs. oxygen adsorption

Analyzing the results of AP-XPS and ECR measurements it is remarkable that both independent experimental techniques indicate a surface redox process that is active at temperatures above 420 K, cf. secs. 7.2 and 8.2. With increasing sample temperature the thermal energy of the system is increased while the electron mobility decreases due to enhanced phonon-scattering. Comparing the two chemical reactions initiating the suggested surface redox processes such a temperature activation points towards the precipitation of SrO rather than towards the adsorption of oxygen molecules. Intuitively, with increasing temperature an acceleration of the chemical reaction extracting strontium from the lattice is more comprehensible than an increased adsorption rate of oxygen molecules due to increased thermal energy of the system. Nevertheless, this is just another indication but not yet an unambiguous proof for neither of the two proposed models. In order to distinguish between the process an *in-situ* evaluation of the chemical composition of the sample surface is inevitable.

AP-XPS provides a unique tool for the *in-situ* study of electronic and chemical

processes in different oxygen gas atmospheres.[120, 145] By fitting the measured core level spectra it is possible to determine the chemical composition in general as well as the specific chemical binding states. Hence, by utilizing AP-XPS a distinction between the two underlying surface redox processes introduced above is achievable. For this purpose, the Sr3d core level is of special interest due to the presence or absence of a SrO secondary component doublet as well as its development being the physical fingerprint of either of the suggested mechanisms.

The Sr core level spectra shows an altered intensity valley between the $Sr3d_{3/2}$ and $Sr3d_{5/2}$ peaks for both pO_2-dependence and probing depth dependence, cf. secs. 6.1 and 6.2, respectively. These changes in spectral shape may directly result from a SrO[72, 128] or strontium hydroxide ($Sr(OH)_2$)[21] surface phase. Similar intensity changes in the Sr core level, however, have also been assigned to a changed potential profile in the surface space charge layer[21, 133] and hence could be consistent with the chemisorption of oxygen molecules withdrawing free electrons from the n-$SrTiO_3$ surface.

Evaluation of the AP-XPS results at varying pO_2

In order to compare the two surface redox processes different fitting procedures corresponding to their specific characteristics have to be utilized. Figure 9.2 shows the Sr3d core level spectra of a 1.0 at% n-$SrTiO_3$ sample measured with lab-based AP-XPS resulting in a fixed probing depth at low base pressure conditions and high pO_2 at 620 K (cf. sec. 6.1). The different fitting procedures and the residuals correspond to strontium oxide precipitation (a) and the chemisorption of charged oxygen molecules (b), respectively. For both fitting procedures a Shirley background subtraction and two Voigt doublets representing the $SrTiO_3$ lattice component and an additional higher binding energy SrO surface component shifted by 0.8 eV , are used. Both doublets have the same Lorentzian width (natural line width), peak splittings and area ratio, but different Gaussian widths (experimental broadening). The SrO surface component is mandatory in both fitting procedures since its intensity consists of the intensity of the SrO termination layer and the intensity of the precipitated SrO.[26, 44, 72, 167] Consequently, it is present even if there are no SrO precipitates at the surface.

The main difference between the two fitting procedures is the pO_2 dependence of the Gaussian widths of the two Voigt doublets. For the SrO precipitation fitting procedure the Gaussian width of both doublets corresponding to the $SrTiO_3$ lattice component and the SrO surface component is kept constant between the UHV conditions and 1.5 mbar O_2. In contrast, for the fitting procedure corresponding to the chemisorption of oxygen molecules the Gaussian width is variable due to the influence of the pO_2-dependent space charge layer, cf. sec. 6.1.

Both fitting procedures result in reasonable fits of the measured curves. In case of the SrO precipitation fitting procedure (a) the contribution of the secondary component peak increases with increasing pO_2. This trend indicates the strontium

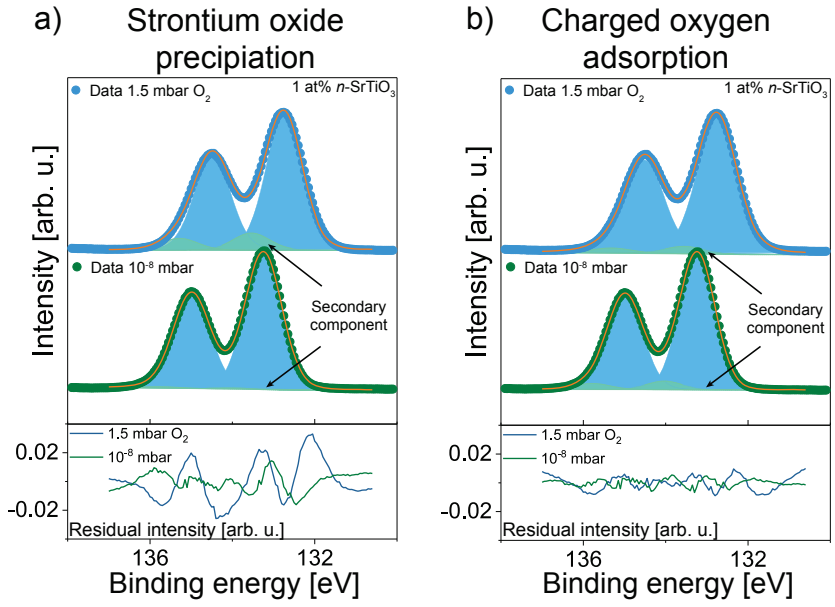

Figure 9.2.: Comparison two fitting procedures and the resulting residual functions of the Sr3d core level peaks measured in both UHV conditions and at 1.5 mbar O_2 corresponding to the SrO precipitation (a) and the chemical adsorption of charged oxygen molecules (b).

sublattice to be involved in the formation of the negative surface charge. In oxidizing conditions the amount of precipitated SrO rises and the concentration of corresponding negatively charged strontium vacancies results in the observed generation of a negative surface charge. In case of the chemisorption of charged oxygen molecules fitting procedure (b) the contribution of the SrO secondary component does not change significantly. This pO_2 independence of the Sr3d peak indicates the absence of chemical changes within the strontium sublattice. The secondary component doublet would be given solely by the SrO termination layer. Hence, this fitting procedure might indicate the strontium sublattice not participating in the formation of the generated surface charge, which would consequently be formed by the chemisorption of charged oxygen molecules. As can be seen from the residual functions both fitting procedures reproduce the measured experimental data almost equally adequate. Hence, both surface redox processes describe the changes in the peak shapes in the pO_2-dependent results determined by lab-based AP-XPS at fixed probing depths equally well and the distinction is not decisive.

Note that the challenges in drawing precise conclusions from the pO_2-dependent AP-XPS results might also be due to the data accuracy. The signal-to-noise ra-

tio depends strongly on the absolute pressure in the measurement chamber, thus increasing the detection limit for determining chemical changes at higher pO_2. In order to decisively clarify which of the two surface processes is actually present, in the following the results of the synchrotron-based AP-XPS measurements with varying probing depth will be evaluated. These experiments allowed for both a potentially higher energy resolution and the evaluation of the core level spectra at different probing depths.

Evaluation of the AP-XPS results at varying probing depths

As described in section 6.2 all core level spectra of a 1.0 at% n-$SrTiO_3$ sample measured at 670 K in low and high pO_2 conditions show a probing-depth dependent broadening. Figure 9.3 reproduces the superposition of the Sr3d core level spectra at different probing depths at a low base pressure (a) and a high pO_2 of 1.3 mbar (b) at 670 K, cf. fig. 6.17.

The superposition of the Sr3d core level spectra reveals two probing depth-dependent effects. Firstly, the spectra show a non-monotonous evolution of the core level shape with decreasing probing depth at high binding energies. From the highest to the second highest probing depth the width of the measured core level decreases slightly. In accordance to the results of the O1s core level spectra, this discrepancy might be due to the interplay of two contrary effects caused by the presence of the surface space charge layer and an additional surface component, cf. sec. 6.2. For all other probing depths, however, the core level width increases continuously with decreasing probing depth. Secondly, the intensity valley between

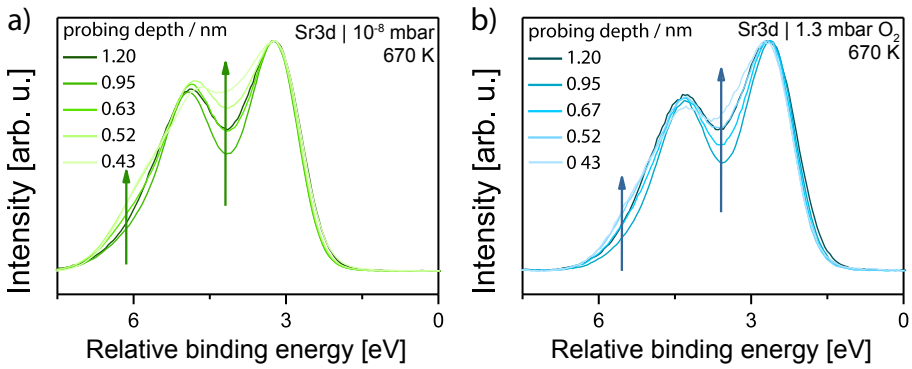

Figure 9.3.: The normalized superposition of the Sr3d core level spectra measured in a low base pressure of 10^{-8} mbar (a) and at a high pO_2 of 1.3 mbar (b) at 670 K and different probing depths after a Shirley background subtraction. This figure is published in ref. [115].

the $Sr3d_{3/2}$ peak and the $Sr3d_{5/2}$ peak, with the exception of the highest probing depth, is continuously flattened with decreasing probing depth.

As explained in section 9.1, both these trends unambiguously demonstrate pO_2-dependent chemical changes in the strontium sublattice at the n-$SrTiO_3$ surface. With decreasing probing depth the influence of the SrO secondary component intensity on the shape of the measured Sr3d core level is increased significantly resulting in the observed broadening of the Sr3d core level shape and the intensity flattening between the $Sr3d_{3/2}$ peak and the $Sr3d_{5/2}$ peak. As the amount of strontium atoms in the near surface region is considered constant due to sluggish diffusion. Due to the pO_2-dependent redox process the concentration of V''_{Sr} located directly at the n-$SrTiO_3$ surface increases according to the concentration of precipitated SrO. At the same time, the concentration of lattice strontium decreases accordingly leaving behind an increasing concentration of V''_{Sr}. Consequently, the observed negative surface charge is formed by the presence of doubly negatively charged V''_{Sr} at the n-$SrTiO_3$ surface and not by the chemisorption of oxygen molecules.

In order to quantify the impact of the strontium sublattice on the AP-XPS measurements at different probing depths, figure 9.4 reproduces the results of the fitting procedure of the Sr3d core level spectra at different information depths applied in section 6.2. As a result of the varied oxygen atmosphere, the peak positions obtained in a low base pressure and at high pO_2 are offset by ~0.55 eV. In addition, a probing depth-dependent evolution of the SrO surface component is observed at a low base pressure and in high pO_2. Moreover, with decreasing probing depth

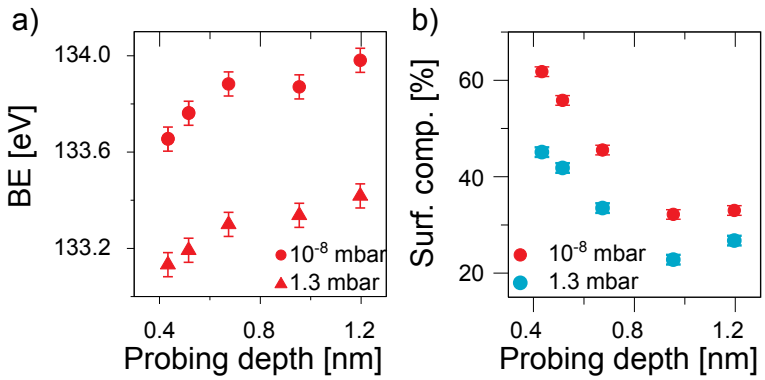

Figure 9.4.: The probing depth-dependent binding energy positions of the $Sr3d_{5/2}$ low binding energy component peaks are shown in (a). The relative contribution of the surface component (turquoise) estimated by the area of the high binding energy doublet in comparison to the peak area is shown in (b). With a decreasing probing depth, the binding energy shifts towards lower values while the share of the high binding energy component phase is increased for both measurements at low base pressures and high pO_2.

the SrO surface component increases strongly, indicating a distinct SrO coverage of the n-$SrTiO_3$ surface in both low base pressure and high pO_2 conditions. The overall contribution determined by the area ratio of the high binding energy doublet in comparison to the total areal intensity of the Sr3d core level increases with decreasing probing depth from 33 % to 62 % at a low base pressure and from 27 % to 45 % at 1.3 mbar O_2, respectively. In agreement with literature, this finding at first sight indicates a higher contribution of the surface component in lower base pressure, which would contradict the introduced SrO precipitation model.[38, 44, 52, 72, 115] Nevertheless, as will be explained in detail below the observations here can be understood by a chemical response limited to the very surface region of the n-$SrTiO_3$ sample which is accompanied by nanoscopic morphology changes.

9.3. Clarification of the chemical surface redox process

Figure 9.5 shows a schematic illustration of the pO_2-dependent surface redox process controlling the electrical surface properties of n-$SrTiO_3$ by SrO precipitation in the case of low base pressure (a) and high pO_2 (b) and how it effects the electrical surface properties (c). The precipitation is consistently described by the equilibrium redox reaction in Kroger-Vink notation[38, 76]

$$\frac{1}{2}O_2(g) + Sr_{Sr}^{x} + 2e^{-} \rightleftharpoons V_{Sr}^{''} + (SrO)_{s.p.} \quad , \tag{9.1}$$

where $O_2(g)$ denotes oxygen molecules in the gas phase, Sr_{Sr}^{x} a charge-neutral strontium ion at a strontium lattice position, e^{-} a negatively charged electron, $V_{Sr}^{''}$ a double negatively charged strontium vacancy and $(SrO)_{s.p.}$ a strontium oxide compound in the secondary phase, cf. sec. 2.4.

Considering the proposed chemical surface reaction, at low base pressures, it is reasonable to assume a thin film surface that is partially SrO terminated, cf. fig. 9.5 (a). This tendency of the thin film growth process to produce strontium oxide terminated surfaces is due to the incomplete growth of unit cells, slight non-stoichiometric growth of the n-$SrTiO_3$ thin films or due to an incomplete polishing process of the single crystalline substrate.[88, 128] This initial SrO coverage is part of the $SrTiO_3$ lattice of the thin film and thus not accompanied by strontium vacancies at the surface. Consequently, this type of SrO coverage is not accompanied by a negative surface charge but still contributes to the spectroscopic SrO secondary component in the Sr3d core level spectra. With increasing pO_2 at elevated temperatures the equilibrium of the surface redox reaction is moved to the right side, cf. eq. 9.1. Thus an increasing amount of Sr from the $SrTiO_3$ lattice precipitates with oxygen from the surrounding gas atmosphere to SrO at the n-$SrTiO_3$ surface, cf. fig. 9.5 (b) leaving behind a double negatively charged strontium vacancy in the

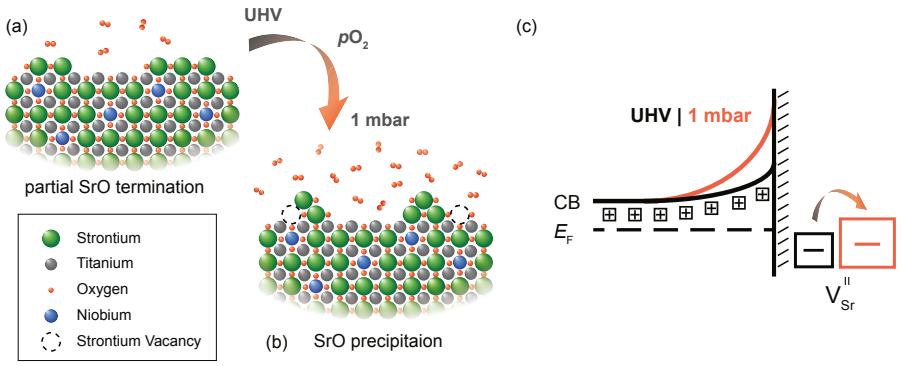

Figure 9.5.: Schematic illustration of the possible atmospheric dependence of the strontium oxide precipitation at the surface of n-$SrTiO_3$ at 670 K at low base pressure (a) and high pO_2 (b). The impact on the electric properties is shown in (c). This figure is published in ref. [115].

$SrTiO_3$ lattice.

Due to the low temperatures, the cation vacancy diffusion into the crystal lattice is ideally very sluggish and the described reaction focuses primarily on the n-$SrTiO_3$ surface.[37] Consequently, a charge equilibration across the entire sample is prohibited leading to an effective charge separation which is not present at high temperatures.[38] The localized V_{Sr}'' at the n-$SrTiO_3$ surface generate a negative surface charge that is compensated by an electron depletion underneath the surface. Accordingly, an upwards band bending is introduced at the n-$SrTiO_3$ surface that is characterized by a surface potential ϕ_0 with a decay length Δx_{SCL}, hence defining the observed surface space charge layer, cf. fig. 9.5 (c). In this way a chemical control of the electrical surface properties of n-$SrTiO_3$ is achieved by the precipitation of SrO which is accompanied by the formation of V_{Sr}''.

Impact of SrO precipitation on the surface properties of n-$SrTiO_3$

Probing depth-dependent AP-XPS measurements revealed SrO precipitation accompanied by the formation of V_{Sr}'' to be present at the n-$SrTiO_3$ surface at elevated temperatures and different oxygen partial pressures. In the following, the impact of the clarified model on the spectroscopic and electrical characterization by AP-XPS and ECR as well as on impedance spectroscopy and IV-curves will be reconsidered. Moreover, to investigate the impact on the transient sheet resistance measurements the proposed simulation model will be discussed with respect to the identified surface redox process, cf. sec. 8.3.

Morphology-dependent Sr3d doublet intensities

An intuitive way to form strontium oxide at the n-$SrTiO_3$ surface is the stacking of strontium atoms from the surface-termination on top of each other while incorporating oxygen from the ambient atmosphere. This process is energetically favored as it minimizes the surface energy of the SrO precipitates, which have been shown to produce a strong tendency for SrO to nucleate in the form of islands and not monolayers.[44, 72, 128, 168–173] A further ripening of the SrO islands through coalescence is suppressed at temperatures below 770 K disabling the SrO movement on the n-$SrTiO_3$ surface. In this way, a transformation of the former SrO termination layer embedded into the $SrTiO_3$ lattice to more extended precipitates yields the formation of rock-salt-type SrO structures at the surface leaving behind double negatively charged strontium vacancies as sketched in figure 9.5 (b). The described island nucleation of precipitated SrO explains the higher overall contribution of the SrO doublet to the Sr3d core level spectra at low base pressure, cf. fig. 9.4. Figure 9.6 shows a schematic illustration of the total intensity dependence of the SrO high binding energy component on the pO_2-dependent stacking of SrO unit cells.

The total intensity of the SrO secondary high binding energy doublet consists of the intensity of the initial SrO lattice termination layer and the intensity of the stacked SrO.[44, 72, 167, 174] By evaluation of the Sr3d core level spectra, however, it is not possible to distinguish if the initial surface state is given solely by SrO ter-

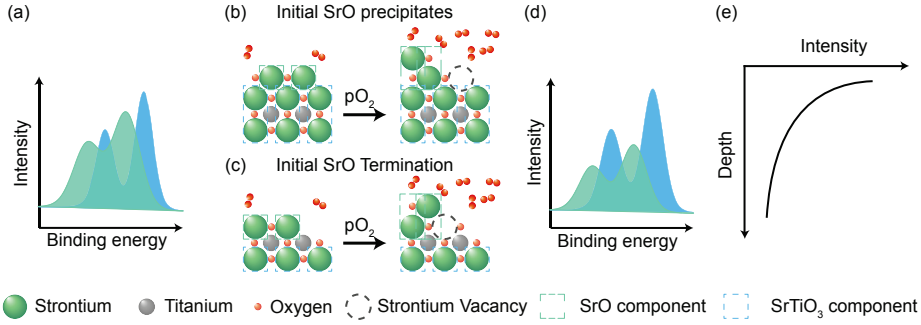

Figure 9.6.: Schematic illustration of the total intensity dependence of the SrO high binding energy component on the pO_2-dependent stacking of SrO unit cells for initial SrO precipitates (b) and a solely SrO termination (c). The light blue rectangles indicate the atomic contribution to the total intensity of the SrO high binding energy component, while the light turquoise rectangles show the atomic contribution to the $SrTiO_3$ low binding energy component. Schematic illustration of the resulting contribution of the $SrTiO_3$ and the SrO phase in reducing conditions (a) and oxidizing conditions (d). The exponential decrease of the depth dependent intensity contribution is shown in (e). This fiugre is published in the supplemental information of ref. [115].

mination directly after growth or by an additional SrO precipitation layer stacked on top of a SrO termination. By increasing the pO_2, the total amount of SrO unit cells stacked on top of the initial SrO termination increases while the total amount of Sr atoms measured in the AP-XPS probing depth is constant due to the sluggish cation movement at the applied temperatures.[37] Thus, as schematically shown in figure 9.6 (b,c), the stacking process reduces the effective area of the SrO coverage that is hit directly by the X-ray beam, see turquoise rectangles. A buried SrO unit cell, however, contributes less to the total intensity of the Sr3d core level spectra due to the exponential attenuation of the emitted electrons, cf. fig. 9.6 (e) and sec. 3.5. Consequently, the total intensity of the SrO high binding energy component at oxidizing conditions is reduced due to increased stacking of SrO unit cells, regardless of the initial surface coverage by SrO precipitates or SrO termination, cf. fig. 9.6 (a,d).

Strontium vacancy concentration at the n-$SrTiO_3$ surface

Utilizing the pO_2-dependent surface charge determined by AP-XPS and ECR in chapters 6, 7 and 8 respectively, the V''_{Sr} concentration needed to create the observed surface space charge layer can be calculated. A single V''_{Sr} is double negatively charged. Hence, to realize the estimated surface charges a V''_{Sr} surface concentration is needed that is equivalent to half of the estimated surface charge. The V''_{Sr} surface concentration correlated to the spectroscopic experiments performed on 1.0 at% n-$SrTiO_3$ samples at 670 K are calculated to $\sim 3\times10^{13}$ cm^{-2} and $\sim 5\times10^{13}$ cm^{-2} at 1.5×10^{-4} mbar O_2 and 1.5 mbar O_2, respectively. In comparison, the V''_{Sr} surface concentration corresponding to the electrical characterization of 1.0 at% n-$SrTiO_3$ samples at 670 K are determined to $\sim 1.5\times10^{14}$ cm^{-2} and $\sim 1.6\times10^{14}$ cm^{-2} for 0.005 mbar and 1.0 mbar O_2, respectively. Comparing these concentrations to the concentration of strontium atoms needed for a full monolayer (6.25×10^{14} cm^{-2}) concludes an additional SrO surface coverage of 5 % and 8 % calculated from AP-XPS measurements for 1.5×10^{-4} mbar O_2 and 1.5 mbar O_2, respectively and 24 % and 25 % determined from electrical characterization measurements for 0.005 mbar O_2 and 1.0 mbar O_2. In good agreement with the determined surface charges, the V''_{Sr} surface coverages estimated for the two independent measurement techniques are in the same order of magnitude and can both be considered reasonable in comparison to SrO surface coverages found directly after growth.[88, 128] As explained in more detail in section 8.4, due to different error estimations these values correspond to a lower limit (AP-XPS) and an upper limit (ECR). In addition, these results show that V''_{Sr} are present at all conditions and cannot be removed even in nominally reducing conditions. However, even rather subtle alterations of the V''_{Sr} concentration by just a few % lead to significant changes in the electronic n-$SrTiO_3$ surface properties, namely band bending, decreasing sheet carrier concentration and increasing sheet resistance.

Transient evolution of the pO_2-dependent conductivity

In section 8.3 a fitting procedure is introduced that attributes the transient course of the pO_2-dependent conductivity to a combination of a surface transfer reaction and a bulk diffusion process. The surface transfer coefficient and the diffusion coefficient were fitted to K_{tr}=9.5×10^{-12} m/s and D=6.4×10^{-21} m^2/s, respectively, cf. fig. 8.10 (b).

In accordance to the proposed model, the surface transfer reaction is attributed to the precipitation of SrO and the accompanied formation of strontium vacancies while the subsequent bulk diffusion process is attributed to the diffusion of strontium vacancies into the n-$SrTiO_3$ thin film. Thus, the surface transfer coefficient (K_{tr}=9.5×10^{-12} m/s) refers to the precipitation rate of SrO at the n-$SrTiO_3$ surface (K_{SrO}) while the diffusion coefficient D=6.4×10^{-21} m^2/s is correlated to the diffusion coefficient of strontium vacancies ($D_{V_{Sr}''}$) in n-$SrTiO_3$ at a given pO_2 and temperature.

A precipitation rate and hence an oxygen incorporation rate of K_{SrO}=9.5×10^{-12} m/s is considerably fast in comparison to other surface reactions like the incorporation of oxygen into the $SrTiO_3$ lattice of k_s ∼10^{-27} m/s as extrapolated from the description of *Merkle and Maier.*[75] Thus, the values determined here are remarkably as compared to what is known from $SrTiO_3$ bulk behavior and might be due to the impact of the pO_2-dependent surface redox process.

In literature, the self-diffusion coefficient V_{Sr}'' in n-$SrTiO_3$ is determined empirically at high temperatures to

$$5 \times 10^{-9} \times \exp(-\frac{2.8\text{eV}}{k_B T}) \qquad \left[\frac{\text{m}^2}{\text{s}}\right], \tag{9.2}$$

where k_B denotes the Boltzmann constant in eV/K.[37, 38] Extrapolating this equation down to 520 K results in a V_{Sr}'' self-diffusion coefficient of 3.6×10^{-36} m^2/s. The extrapolated value of the V_{Sr}'' self diffusion coefficient is significantly lower than what is determined by the used fitting procedure. This estimation is consistent with the defect chemistry of n-$SrTiO_3$ involving an activation of the strontium sublattice which is believed to be active only at higher temperatures. As has been shown directly by AP-XPS and ECR experiments, however, the strontium sublattice is active at temperatures as low as 420 K, cf. secs. 7.2 and 8.2. Hence, the extrapolated value might not be accurate due to the fact that the possible impact range of the strontium sublattice activation can not be clarified.

The substantial increase of the V_{Sr}'' diffusion rate in comparison to the literature value might be caused by two different effects. Firstly, the literature value does not include the impact of a space charge layer and thus an electric field accelerating the diffusion of V_{Sr}'' from the surface into the sample. As illustrated in ref. [38] high electric fields in the space charge region can enhance the diffusion of V_{Sr}'' by about a factor of 100. Secondly, the temperatures at which the self diffusion coefficient was determined are significantly higher than the temperatures applied in the shown

experiments.

Thirdly, the self-diffusion coefficient was determined at high temperatures and long diffusion lengths in bulk materials which might not reasonable be extrapolated towards very short diffusion lengths in the nm-regime. Thus, the extrapolation of the self-diffusion coefficient to lower temperatures and shorter length scales might cause additional strong deviations and the fitted value is considered reasonable.

The fitting results based on he one dimensional model implemented by *v. d. Otter et. al.* do not contradict the proposed SrO precipitation model as the underlying surface redox process. Nevertheless, in order to harmonize the precipitation of SrO with the fitting of the transient sheet resistance further experiments have to be performed in more stable conditions to explain the remaining open questions.

Strontium vacancy-dependent transport barrier

All results obtained experimentally by impedance spectroscopy and IV-curves demonstrated a dependence of the interfacial transport barrier in Pt/n-$SrTiO_3$ heterojunctions on the specific annealing procedure applied to the n-$SrTiO_3$ single crystals prior to the platinum contact evaporation. After oxidation, a substantial increase of the contact resistance (R_{SC}) is found by both experimental techniques while the contact capacitance (C_{SC}) did not change significantly, cf. sec. 5.1.

In comparison to the thermodynamical conditions present in the AP-XPS experiments, the annealing procedures applied prior to the electrical characterization of the Pt/n-$SrTiO_3$ interface Schottky contact higher temperatures (1320 K to 1420 K) and oxidizing pO_2 (ambient pressure) and reducing conditions (4 % H_2/Ar) were used. In accordance to the defect chemistry of n-$SrTiO_3$, the precipitation of SrO is more pronounced at higher temperatures and higher oxygen partial pressures.[37, 38] Hence, even though the applied conditions are not fully identical, it is reasonable to assume SrO precipitation and the accompanied formation of V''_{Sr} to be active during the annealing procedures.

DFT-simulation of a Pt/n-$SrTiO_3$ heterojunction

To probe the influence of a V''_{Sr} on the Pt/n-$SrTiO_3$ Schottky contact properties on the atomic scale quantum mechanical simulations based on *ab initio* density functional theory (DFT) combined with the non-equilibrium Green's function (NEGF) formalism are employed, that provide local density of states (LDOS) for each atomic layer across the heterojunction.[66] All the simulations were prepared and conducted by Carsten Funck, IWE II, RWTH Aachen University. Details on the supercell structure used for the calculations can be found in appendix B and ref. [66].

Two different systems are generated: one pristine heterojunction of Pt and n-$SrTiO_3$ without any distortion of the lattice and one with a distortion by a V''_{Sr} in

the near surface region, reflecting the ionic constitution of n-$SrTiO_3$ treated under reducing and oxidizing conditions, respectively. Figure 9.7 shows the DFT + NEGF simulations of the Pt/n-$SrTiO_3$ contact. The atomic model is displayed in (a), and the local density of states for calculations without (b) and with a V''_{Sr} in the near contact region (c). The red circle in (a) marks the strontium atom that is removed for the calculation. The purple and black color indicate regimes of large and low LDOS.

DFT-simulation of a Pt/n-$SrTiO_3$ heterojunction results

The basic characteristic of the two simulated systems is similar. For the platinum electrode (d = 4 nm to 6 nm), the purple regime indicates a high density of electronic states at the Fermi level (ϵ_F, (b, c)) as expected for a metal electrode. For the n-$SrTiO_3$ side of the heterojunction (d = 0 nm to 4 nm), the black area

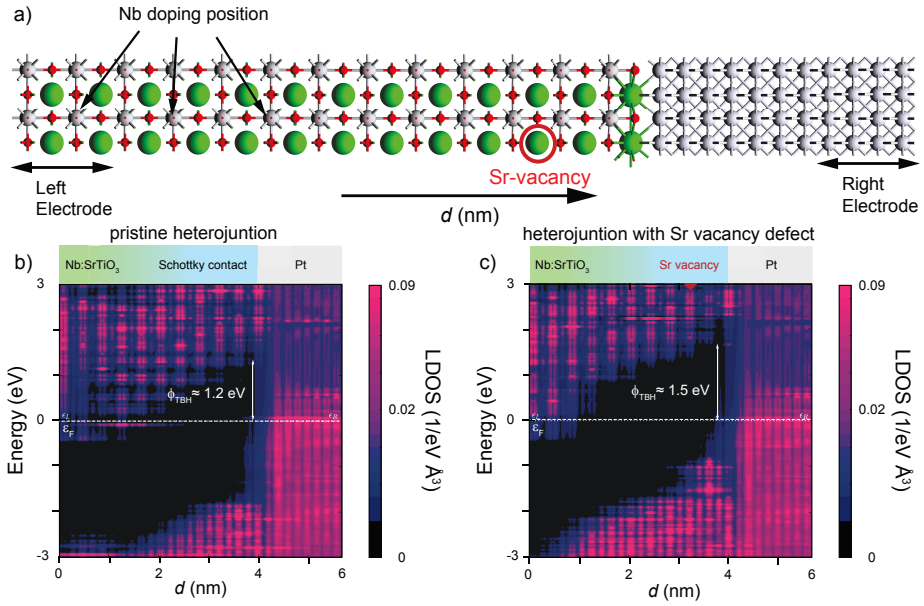

Figure 9.7.: DFT + NEGF simulations of a n-$SrTiO_3$ platinum contact. The atomic model is shown in (a). The local density of states is plotted for calculations without (b) and with (c) a strontium vacancy in the near contact region. The purple regime indicates a high concentration of electronic states while the black regime indicates a low concentration of electronic states. All the simulations were prepared and conducted by Carsten Funck, IWE II RWTH Aachen University. The figure is published in ref. [127]

illustrates a low local density of states corresponding to the band gap, while the purple regimes describe the valence and conduction band, respectively. At the edges of the simulated atomic model, away from the interface ($d \sim 0$), ϵ_F is located in the conduction band, as expected for a donor-doped semiconductor system. In the central Schottky contact region (d = 1 nm to 4 nm) the concentration of electronic states at the Fermi level vanishes completely, as the conduction band is moved up in terms of energy. This upwards band bending corresponds to a Schottky-type electron depletion region at the Pt/n-$SrTiO_3$ interface. Consequently, the Fermi energy is shifted deeper into the band gap forming a transport barrier for the electronic transport through the heterojunction.

There are two main differences between the pristine and the distorted system. Firstly, the apparent transport barrier height (Φ_{TBH}) increases significantly from 1.2 eV in the pristine system (b) to 1.5 eV in the distorted system (c). Secondly, the overall shape of the barrier is slightly broadened which corresponds to an increased screening length of the transport barrier. This is consistent with the presence of the additional negative charge introduced by the doubly negatively charged strontium vacancy within the Pt/n-$SrTiO_3$ heterojunction. Both findings, a significant increase of Φ_{TBH} as well as the slight broadening of the space charge layer are observed independent of the actual position of the V''_{Sr}. The specific shape of the transport barrier, however, changes with a varying V''_{Sr} position in the calculation. In order to correlate these theoretical results to the experimental results found by impedance spectroscopy and IV-curves the electrical transport mechanisms through the barrier need to be considered, cf. chp. 5. *Wang et al.* reported previously that regardless of the transport mechanism (direct tunneling, Fowler-Nordheim tunneling, thermionic emission, hopping transport) the contact resistance R_{SC} depends exponentially on the apparent transport barrier Φ_{TBH}.[67] Hence, a 0.3 eV-change in the transport barrier height would change the contact resistance by a factor of $\exp\left(\frac{e\Delta\Phi_{TBH}}{k_B}\right) \approx 10^5$. This estimation explains the changes in the contact resistance observed by impedance spectroscopy and $I(V)$-characterization, which revealed a 2-3 orders of magnitude change. The remaining over-estimation obtained from DFT calculations is a result of the high concentration of donor ($\sim$6.8 at%) and Sr vacancy defects ($\sim$2.2 at%) assumed in the calculation in order to limit the cell size and thus computational costs. Furthermore, the particular form of the barrier will depend on the exact positions of dopants and defects, locally resulting in higher/lower barriers, which is averaged in the macroscopic measurements.

In contrast, assuming a classical capacitor the contact capacitance C_{SC} depends only inversely proportional on the barrier width, converting into a much weaker square-root dependence on the barrier height,[65]

$$C_{SC} = \epsilon_0 \epsilon_r \frac{A}{d_{SC}} \propto \frac{1}{\sqrt{\Phi_{TBH}}} \quad , \tag{9.3}$$

where ϵ_0 denotes the vacuum permittivity, ϵ_r the relative permittivity, A the contact area and d_{SC} the transport barrier width, cf. sec. 2.2. As an estimate, the calculated barrier heights translate into a relative change in the capacitance by a

factor of $\sqrt{1.5/1.2} \approx 1.1$, appearing as an unchanged value given the general scatter of the data shown in figure 5.5.

Hence, a V''_{Sr} in the near contact region increases the transport barrier of the pristine heterojunction by 0.3 eV and thereby increases R_{SC} exponentially. The width of the transport barrier, however, is only changed slightly with a V''_{Sr} in the near contact region resulting in a primarily unaffected C_{SC}. Thus, the theoretical simulations are consistent with the results of the impedance spectroscopy and IV-curves which both demonstrated a strong increase of the transport barrier while the contact capacitance did not change as significantly. Consequently, the results of the impedance spectroscopy and IV-curves are consistent with the incorporation of strontium vacancies during annealing in oxidizing conditions and hence with the clarified surface redox process.

In terms of possible applications, the incorporation of V''_{Sr} as localized negative charges in the near surface region might be used to tailor transport barrier heights in Pt/n-$SrTiO_3$ heterojunctions. For the functionality of such devices, this translates into the opportunity to tailor band alignments by controlling the intrinsic cationic disorder.[175, 176] It would be possible to produce heterojunctions with specifically tailored transport properties like strongly rectifying behavior or with more symmetric IV-characteristics or even to affect the photocatalytic response due to the effective charge separation.[20] In terms of the application of n-$SrTiO_3$ as substrate material for resistive switching devices tailored interface band alignments might allow to vary the initial state of the device to strongly affect the electroforming process or the subsequent cycling of the cells, where the redistribution of oxygen vacancies into the electron depletion are at the heterojunction is thought to be responsible for the resistive switching effect.[12, 25]

Summary

In this chapter the chemical process at the n-$SrTiO_3$ surface that controls the pO_2-dependent electrical properties has been discussed comprehensively. Consistent with the defect chemistry, in oxidizing conditions strontium atoms from the $SrTiO_3$ lattice react with oxygen from the atmosphere to strontium oxide precipitates which grow in form of islands at the n-$SrTiO_3$ surface. As a result, doubly negatively charged strontium vacancies are formed at the surface of the $SrTiO_3$ lattice dominating the electrical properties. The illustrated surface redox process is consistent with all results observed within this thesis.

The spectroscopic results of pO_2-dependent as well as probing depth-dependent apparent binding energies are due to the formation of a negative surface charge and a corresponding shift of the Fermi energy, initially close to the conduction band in reducing atmospheres, deeper into the band gap. Moreover, the chemical changes at the n-$SrTiO_3$ surface results in alterations in the shape of the characteristic core levels. Especially the evolution of the valley between the $Sr3d_{3/2}$ and the $Sr3d_{5/2}$

peak is most important. Due to the pO_2-dependent formation of a strontium oxide secondary surface component the activation of the strontium sublattice at the surface at considerably low temperatures is unambiguously revealed.

The electrical results depending on both annealing pre-treatments as well as the applied pO_2 are demonstrated to be consistent with the generated negative surface charge formed by V''_{Sr} and the corresponding space charge layer. In *n*-$SrTiO_3$ single crystals DFT-calculations illustrated an increased V''_{Sr} concentration in the near *n*-$SrTiO_3$ surface region leads to an annealing-dependent transport barrier, cf. sec. 9.3. In addition, the negative surface charge observed directly after growth in oxidizing conditions by the film thickness-dependent carrier concentration is compensated by electron depletion in the surface region. Thus depletion corresponds to the formation of a surface space charge layer. Moreover, the *in-situ* pO_2-dependent sheet resistance is caused by the pO_2-dependent formation of V''_{Sr} at the *n*-$SrTiO_3$ surface reducing the amount of carriers that contribute to the conductivity in the thin film.

10. Conclusion and Outlook

The scope of this thesis has been to investigate the impact of the surface chemistry (pO_2, T) on the electrical properties of donor-doped $SrTiO_3$ surfaces and demonstrate the differences to expected bulk behavior. For this purpose this thesis has utilized a variety of different measurements techniques ranging from morphological imaging methods and electrical experiments to advanced *in-situ* spectroscopic measurements was utilized to identify and interpret the occurring pO_2-dependent properties. Based on the defect chemistry of n-$SrTiO_3$ and in agreement with the experimental observations and results, the thesis finds that there is a surface redox process chemically controlling the electrical surface properties.

As the underlying surface redox process, this thesis identifies the precipitation of strontium oxide in oxidizing conditions forming clusters at the n-$SrTiO_3$ surface and leaving behind negatively charged strontium vacancies. Subtle changes of the strontium sublattice consistently explain all spectroscopic and electrical results which are summarized in fig. 10.1 (a). The existence of such a redox process is remarkable. Up to now, the defect chemistry of n-$SrTiO_3$ single crystals proposed the strontium sublattice, and especially the cation diffusion, to be active only at much higher temperatures. At lower temperatures, due to the inhibited cation diffusion into the sample, the rearrangement of the strontium sublattice was considered to be restricted to the n-$SrTiO_3$ surface. In fact, this restriction is presumed to be fundamental for the electrical charge separation revealed in this thesis for forming a surface space charge layer. In this way, classical rules of bulk defect chemistry were expanded to the surface allowing for accelerated ionic dynamics and thus chemical control of the electrical surface properties of n-$SrTiO_3$ by its redox chemistry.

Contrary to the prevailing assumptions, in this thesis, *in-situ* AP-XPS has demonstrated the activation of the strontium sublattice at temperatures between 470 K and 770 K as well as the fully reversible generation and annihilation of a pO_2-dependent negative surface charge and a corresponding surface potential. With increasing pO_2, a growing secondary component has been identified in the spectroscopic results of the strontium 3d core level clarifying SrO to precipitate at the n-$SrTiO_3$ surface in oxidizing conditions, cf. fig. 10.1 (a). As the origin of the illustrated negative surface charge, this thesis has singled out the doubly negatively charged strontium vacancies formed during the precipitation process.

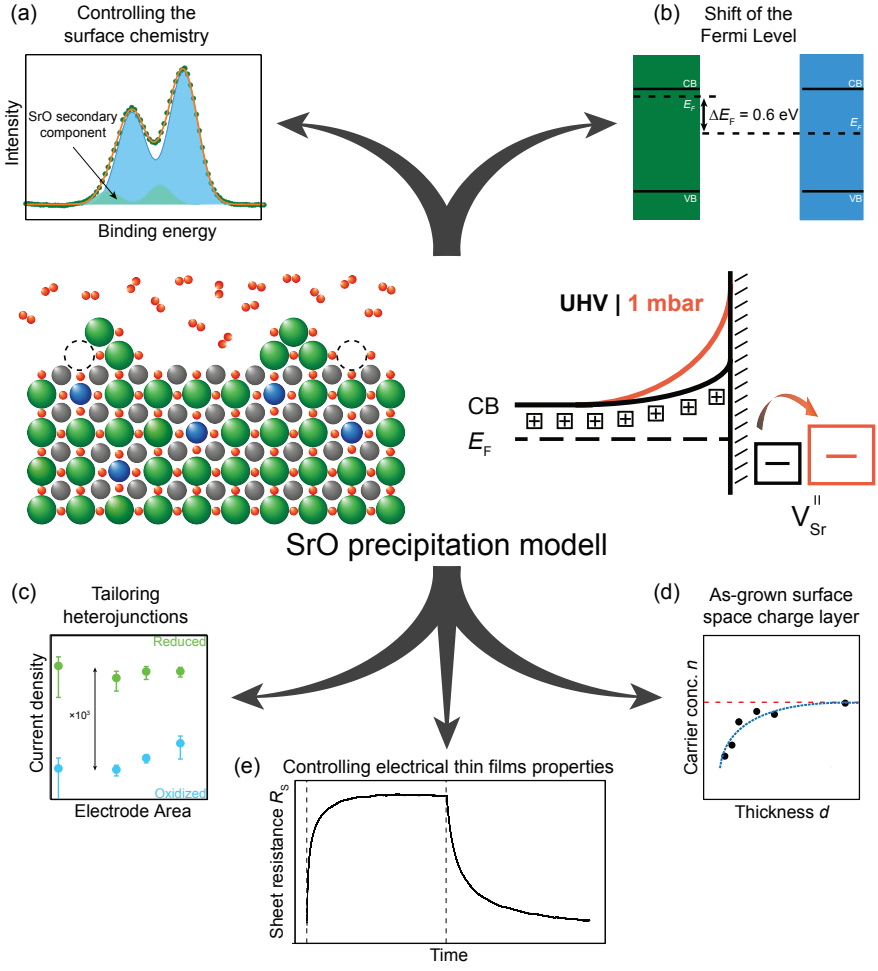

Figure 10.1.: Schematic illustration of the SrO precipitation process accompanied by the formation of $V_{Sr}^{''}$ that is controlling the electrical surface properties of n-$SrTiO_3$. Representative spectroscopic results illustrating a SrO secondary surface component and hence the activation of the strontium sublattice (a). Schematic illustration of the impact of the surface potential on the position of the Fermi energy in the band gap (b). Transport barrier of Pt/n-$SrTiO_3$ heterojunctions after reducing and oxidizing annealing treatments (e). Thickness dependence of the carrier concentration in n-$SrTiO_3$ thin films directly after growth (d). pO_2-dependent sheet resistance of a n-$SrTiO_3$ thin film (e).

This thesis has identified the corresponding surface potential to be due to a shift of the Fermi energy deeper into the band gap which occurred as the n-$SrTiO_3$ surface was oxidized, cf. fig. 10.1 (b). The potential was found to decrease into the n-$SrTiO_3$ sample resulting in band bending and hence the presence of a surface space charge layer. In this surface space charge layer electrons were depleted compensating the generated negative ionic surface charge. In addition to a varied pO_2, it was also possible to tune the characteristic properties of the space charge layer and especially its width by external parameters like the donor doping concentration and the applied temperature.

Remarkably, regardless of the applied temperature, it was not possible to completely remove the negative surface charge dominating the electrical surface properties even at low, nominally reducing, ultra high vacuum base pressures. Thus, this thesis shows that in basic conditions of most UHV experimental setups which are widely believed to preserve the properties of transition metal oxide samples, the samples' surface chemistry can in fact impact or even dominate the electrical properties of donor-doped oxides by oxygenation.

The precipitation of SrO at the n-$SrTiO_3$ surface dominated the electrical properties of Pt/n-$SrTiO_3$ heterojunctions as demonstrated by impedance spectroscopy and $I(V)$-curves, cf. fig. 10.1 (c). By applying specific oxidizing and reducing annealing treatments to the n-$SrTiO_3$ single crystals prior to the heterojunction fabrication the transport barrier between the metal top electrode and the oxide single crystal was adjusted to values between 1.5 eV and 1.2 eV, respectively. As was shown by theoretical DFT simulations this tailoring of the heterojunction's transport barrier was due to the presence of strontium vacancies in the near contact region after oxidizing annealing treatments.

Furthermore, the electrical properties of n-$SrTiO_3$ thin films were consistently controlled by SrO precipitation. Hall measurements illustrated the impact of a surface space charge layer directly after growth by a thickness-dependent charge carrier concentration, cf. fig. 10.1 (d). Thus, typical oxidizing growth conditions of donor-doped transition metal oxides can dominate the electrical surface properties. Moreover, electrochemical conductivity relaxation experiments demonstrated the *in-situ* control the n-$SrTiO_3$ *in-plane* properties by precisely controlling the applied pO_2, cf. fig. 10.1 (e). In agreement with the spectroscopic results, this trend was attributed to a pO_2-dependent negative surface charge dominating the charge carrier concentration in the thin film contributing to electrical conductivity. The negative surface charges determined from spectroscopic and electrical characterization were in the same order of magnitude and due to specific experimental constraints defined a lower and an upper limit for the absolute value, respectively.

The results of this thesis offer fundamentally new insights regarding the electrical surface properties of n-$SrTiO_3$ and their dependence on different thermodynamical biases by expanding classic bulk defect chemistry to the very surface. The defect chemistry of surfaces can vary significantly from the well-known bulk behav-

ior. Especially the dynamics which limit the defect formation in the bulk at low temperatures may be much faster and more pronounced in the first monolayers. The findings are of significant and direct scientific interest in particular for investigations into n-$SrTiO_3$ thin film surfaces and into heterojunctions and interfaces involving n-$SrTiO_3$. In addition, the thesis' findings are of relevance for a wide variety of other perovskite transition metal oxide thin film applications in which n-$SrTiO_3$ single crystals are used as quasi-metallic degenerate n-type semiconductor substrates. The electrical and spectroscopic results demonstrate the surface properties to be dominated by the surface chemistry and the applied thermodynamic biases, and hence to be more complex than previously assumed. Consequently, the growth as well as the measurement conditions need to be selected and adjusted carefully when addressing donor-doped transition metal oxides.

Furthermore, the findings in this thesis open up a new field of possible direct functionalities of n-type transition metal oxides. Annealing treatments are fairly simple processes to tailor the functional properties of heterojunctions with tunable transport barriers possibly resulting in novel resistive switching devices. Moreover, controlling the electrical properties of thin films by their surface chemistry could lead to the development of innovative gas sensing applications able to realize more sensitive characteristics than state of the art type sensors.

A. Pressure instabilities during ECR experiments

Within this thesis electrochemical conductivity relaxation experiments are used to to draw conclusions on pO_2-dependent processes dominating the electrical properties at the n-$SrTiO_3$ surfaces, cf. ch. 8. Hereby the pO_2 in the measurement reactor is changed between two specific values while measuring *in-plane* sheet resistance, cf. sec. 3.4. In order to to allow for a time-dependent fitting of the course of the conductivity it is important to ensure a jump between to equilibrium states. Therefore, the pO_2 needs to be controlled precisely.

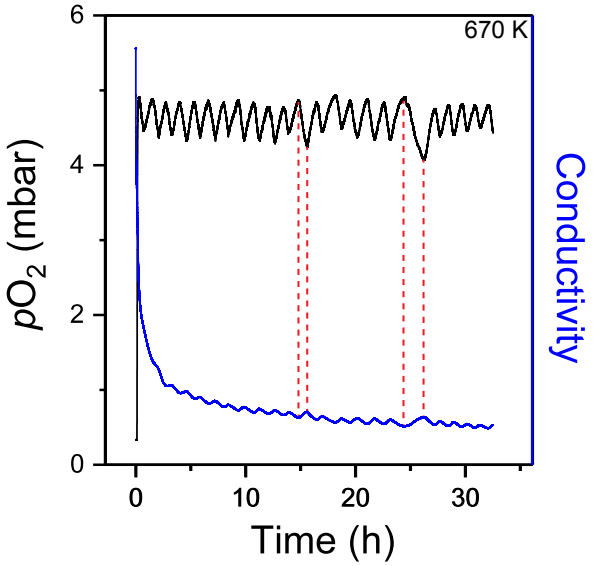

Figure A.1.: Exemplary oscillations of the pO_2 (black) and the corresponding conductivity (blue) during long-term electrochemical conductivity relaxation experiments at 670 K.

During the measurements within this thesis, however, the pO_2 showed non-negligible oscillations. Figure A.1 shows the exemplary course of the pO_2 and the corresponding conductivity measured over time at a temperature of 670 K.

The observed pO_2 exhibit a clear oscillation with a frequency of about 1.5 h and an amplitude of about 0.5 mbar O_2. The determined *in-plane* conductivity demonstrates the oscillations with the same frequency. With increasing/decreasing pO_2 the conductivity decreases/increases. These results are consistent with the pO_2-dependent surface charges and the corresponding surface space charge layer observed by AP-XPS and Hall measurements. As a consequence, no equilibrium pO_2 and thus no equilibrium conductivity is adjusted over time. Thus, these oscillations limit the opportunity of fitting the time-dependent course of the conductivity with suitable surface process models.

After excluding the measurement electronics, electronic cross talk with other setups, the used gas quality and external stimuli such as vibrations, the surrounding atmosphere in the laboratory and magnetic fields as the cause of the pO_2 oscillations, the measurement uncertainty most likely originates from the used mass flow controllers. The flows necessary to adjust a pO_2 comparable to the AP-XPS experiments were at the lower limit of the mass flow controller. At this limit the internal PID-controller might result in the observed high fluctuations. In order to overcome these oscillations Ar/O_2 premix gases with high flow rates were utilized within this thesis.

B. Description of the supercell applied for DFT calculations

The supercell has a dimension of 2x2 unit cells in x-y dimension and a length of eleven unit cells of $SrTiO_3$ and three unit cells of platinum. The structure is completed by the integration of Nb-dopants on titanium lattice sites (c.f. fig. 9.7 (a)). All structures have been relaxed up to a force less than 0.05 eV/Å. Using the DFT+NEGF formalism implemented in ATK 2017.12 semi-periodical boundary conditions are applied in perpendicular direction to the Schottky interface and a k-point sampling of 3x3x(100) for the electrodes and the periodic directions of the central region.[177–179] For the DFT simulation a local basis set with pseudo-potentials and the *Perdew-Burke-Emzerhof* (PBE) exchange potential are applied.[180–182] To overcome the bandgap problem and to fit the bandgap of the isolated $SrTiO_3$ slab a Hubbard $U = 6$ eV has been applied to the Sr, Nb, Ti d-orbitals and the O p-orbitals. Note that this may induce a vague error to the quantitative transport barrier height but will not impact the trends qualitatively investigated here.

List of Figures

1.1. Schematic illustration of the scope of this thesis. 2

2.1. $SrTiO_3$crystal strucutre and DOS. 5
2.2. Schematic illustration of the electric transport across a Schottky barrier with a height Φ_{TBH}. 8
2.3. Schematic illustration of the pO_2-dependent defect concentrations in donor-doped $SrTiO_3$ with an active and frozen Schottky equilibrium. 12
2.4. Schematic illustration of the pO_2-dependent conductivity in ECR experiments. 14

3.1. Schematic illustration of the experimental annealing furnace setup and a depiction of the platinum sample basket. 18
3.2. Schematic illustration of the construction of a PLD chamber equipped with a RHEED system. 19
3.3. Schematic illustration of the mode of operation of of a Reflection High Energy Electron Diffraction setup. 21
3.4. Schematic illustration of the mode of operation of a magnetron sputtering process. 22
3.5. Schematic illustration of a typical impedance spectroscopy result and the corresponding equivalent circuit. 26
3.6. Schematic illustration of the electrochemical conductivity relaxation measurement setup. 28
3.7. Schematic illustration of the relaxation process of the electrical conductivity after a spontaneous jump of the surrounding pO_2. 29
3.8. Schematic illustration of the mode of operation of an X-ray photoelectron spectroscopy setup. 30
3.9. XPS spectra of $SrTiO_3$ single crystals with n-type and p-type doping. 31
3.10. Schematic illustration of the ambient-pressure X-ray photoelectron spectroscopy measurement setup. 32

4.1. Representative AFM topography images of Nb:$SrTiO_3$ single crystals after preliminary annealing procedures. 34
4.2. Schematic illustration of the limitation of donor-doped $SrTiO_3$ single crystals in terms of the characterization of the electrical surface properties. 35

4.3. Representative AFM topography of undoped $SrTiO_3$ single crystal substrates as-received and after the initial annealing procedure. . . 36
4.4. Representative RHEED oscillations of a 20 nm thick 0.5 wt.% Nb:$SrTiO_3$ thin film grown stoichiometrically on an undoped $SrTiO_3$ substrate. . . 37
4.5. Representative topography images of an annealed $SrTiO_3$ substrate and a 32 nm Nb:$SrTiO_3$ thin film after growth. 38
4.6. Representative (002) Bragg peak of a 200 nm stoichiometric 0.5 wt.% Nb:$SrTiO_3$ thin film homoepitaxially grown on an undoped $SrTiO_3$ substrate. 39
4.7. Representative SIMS intensities of a 200 nm thick Nb:$SrTiO_3$ thin film grown on an undoped $SrTiO_3$ substrate. 40
4.8. Low temperature Hall measurements of a 200 nm thick 0.5 wt.% Nb:$SrTiO_3$ thin film grown on an undoped $SrTiO_3$ substrate. . . . 41

5.1. Schematic illustration of the single crystal sampled stack used during C-AFM experiments, the *through-plane* electrical measurements and the utilized equivalent circuit model. 44
5.2. Local conductivity atomic force microscopy measurements after *in-situ* different annealing procedures of a n-$SrTiO_3$ single crystal. . . 45
5.3. Representative impedance spectroscopy of an n-$SrTiO_3$ single crystal with 30 nm sputtered platinum top electrodes. 47
5.4. Representative impedance spectroscopy of an n-$SrTiO_3$ single crystal with 30 nm evaporated platinum top electrodes. 48
5.5. Electrode area-dependent surface contact resistance and contact capacitance of n-$SrTiO_3$ single crystals as received and after reducing and oxidizing annealing treatments. 49
5.6. Electrode area-dependent $I(V)$-curves measured on n-$SrTiO_3$/platinum contact after different annealing procedures. 51
5.7. Electrode area-dependent current densities through a n-$SrTiO_3$/platinum contact after different annealing treatments. 52
5.8. Schematic illustration of the n-$SrTiO_3$ thin film sample stack used during Hall measurements. 53
5.9. Carrier concentration obtained for 1.0 wt% n-$SrTiO_3$ thin films with different layer thickness and a schematic illustration of the impact of a surface space charge layer on *in-plane* Hall measurements with varying film thicknesses. 54
5.10. Temperature-dependent Hall mobility measured by high temperature Hall measurements of a 200 nm thick 1.0 wt% n-$SrTiO_3$ film. . . . 55

6.1. Schematic illustration of the sample stack as well as the near ambient pressure X-ray photoelectron spectroscopy measurement setup. . . 58
6.2. Representative core level spectra of O1s and C1s, Ti2p and Sr3d, as well as the valence band region of a 32 nm thick n-$SrTiO_3$ film measured at different pO_2. 59

6.3. Superposition of the O1s, Ti2p and the Sr3d core level spectra measured at different adjusted pO_2. 60
6.4. Comparison of the O1s and Sr3d core level of a 32 nm 1 at% n-$SrTiO_3$ thin film and a 1 at% n-$SrTiO_3$ single crystal. 62
6.5. Typical examples of the fitting procedures for the O1s, Ti2p and the Sr3d core level and the valence band maximum. 63
6.6. Position of the characteristic binding energy of n-$SrTiO_3$ core levels, the energy difference between the Fermi energy and the valence band maximum as well as the conduction band minimum and the binding energy shift relative to measurements in low base pressure conditions. 64
6.7. Schematic illustration of the relative positions of the Fermi energy at a low base pressure and 5 mbar pO_2 at 770 K. 65
6.8. Core level spectra of typical surface contamination of n-$SrTiO_3$ surfaces. 67
6.9. Superposition of the Ti2p peaks measured at different pO_2. 68
6.10. Representative sample stack and Au4f core level spectra taken on Ti/Au reference electrodes deposited on a 1.0 at% n-$SrTiO_3$ sample at a temperature of 670 K and different pO_2. 69
6.11. Decay of the surface potential into n-$SrTiO_3$ sample in different pO_2 and the schematic illustration of the negative surface charge compensation by electron depletion underneath the surface. 70
6.12. The impact of the pO_2-dependent surface space charge layer over the entire probing depth and a schematic illustration of the consequences of the potential profile on the XPS measurements. 72
6.13. Schematic illustration of the layer stack used for *in-situ* AP-XPS experiments enabling the application of thermodynamic biases during the measurements. 73
6.14. Synchrotron-based AP-XPS measurements of the O1s, Ti2p, Sr3p, Sr3d core levels and the valance band region using different probing depths. 75
6.15. Ti2p core level spectra and their normalized superposition. 76
6.16. O1s core level spectra and their normalized superposition. 77
6.17. Sr3d core level spectra and their normalized superposition. 78
6.18. Valence band spectra and their normalized superposition. 79
6.19. Probing depth dependent apparent binding energy positions of the O1s, Ti2p, Sr3p and Sr3d core levels. 81
6.20. Evolution of the Sr3d spectra at different probing depths. 82

7.1. Schematic illustration of the sample stacks for the n-$SrTiO_3$ thin films and single crystals. 85
7.2. Core level spectra of O1s, Ti2p and Sr3d of n-$SrTiO_3$ samples with 0.1 at%, 1.0 at% and 5.0 at% donor-doping and different pO_2. . . . 87
7.3. The O1s core level, the Ti2p core level and the Sr3d core level of n-$SrTiO_3$ samples superimposed for different doping concentrations. 88

7.4. pO_2-dependent apparent binding energy position of the characteristic core levels of n-$SrTiO_3$ with different doping concentrations. . . . 89
7.5. pO_2-dependent binding energy shift relative to UHV of O1s core level, the Ti2p core level and the Sr3d core level of n-$SrTiO_3$ for different N_D. . . . 90
7.6. Averaged pO_2-dependent binding energy shift relative to low base pressure conditions and the resulting surface potential decay for the measurements at 1.5 mbar O_2. . . . 91
7.7. Temperature-dependent core level spectra of the O1s, Ti2p and Sr3d core levels and the valence band region of a 1 at% donor-doped $SrTiO_3$ sample. . . . 94
7.8. Superposition of the O1s, Ti2p and the Sr3d core level spectra measured at different adjusted temperatures and pO_2. . . . 95
7.9. Apparent binding energy positions of the O1s, the Ti2p and the Sr3d core level and the energy difference between the Fermi energy and the valence band maximum as well as the estimated temperature-dependent conduction band minimum. . . . 96
7.10. ΔE_B relative to UHV of the O1s, the Ti2p and the Sr3d core level and the valence band maximum. . . . 97
7.11. Averaged temperature-dependent binding energy shift relative to UHV of a 1 at% donor-doped $SrTiO_3$ sample and the resulting surface potential decays for the different temperatures. . . . 98
7.12. Averaged temperature-dependent binding energy shifts between a base pressure of 10^{-8} mbar and 1.5 mbar O_2 of donor-doped $SrTiO_3$ samples with different doping concentrations. . . . 101

8.1. Schematic illustration of the samples used for the electrochemical conductivity relaxation experiments. . . . 105
8.2. Evolution of the sheet resistance R_s of a $SrTiO_3$ substrate measured as a reference at 770 K and changing pO_2. . . . 107
8.3. Evolution of the sheet resistance R_s of a 32 nm thick 1.0 at% n-$SrTiO_3$ thin film measured at 670 K and changing pO_2 and the equilibrium R_s at different pO_2. . . . 108
8.4. Evolution of the sheet carrier concentration n_s of a 32 nm thick 1.0 at% n-$SrTiO_3$ thin film measured at 670 K and changing pO_2 and the equilibrium n_s derived at the different pO_2. . . . 109
8.5. Normalized conductivity curves of a 32 nm n-$SrTiO_3$ thin film reacting to an oxidizing and reducing pO_2 jump. . . . 110
8.6. Schematic illustration of the surface charge calculation from electrical transport measurements. . . . 111
8.7. Surface charges calculated from the sheet resistance R_s at different pO_2, the resulting screening length of the surface space charge layer and the corresponding surface electric field. . . . 112
8.8. Transient evolution of the sheet resistance R_s of a 32 nm 1.0 at% donor-doped n-$SrTiO_3$ thin film after a pO_2 jump. . . . 114

8.9. Calculated temperature-dependent equilibrium state sheet carrier concentration n_s, generated negative surface charge and the surface electric field of a 32 nm 1at% n-$SrTiO_3$ thin film. 116
8.10. Normalized conductivity of a 32 nm n-$SrTiO_3$ thin film measured after a pO_2 jump, the corresponding fit and the false color map of the logarithm of the squared error matrix. 119
8.11. Comparison of the pO_2-dependent generated negative surface charge, the resulting screening length of the surface space charge layer and the corresponding surface electric field determined from AP-XPS and electrochemical conductivity relaxation measurements. 121

9.1. Schematic illustrations of effects that might cause the negative surface charge observed in the different experimental techniques. . . . 126
9.2. Comparison two fitting procedures and the resulting residual functions of the Sr3d core level peaks measured in different pO_2 corresponding to the SrO precipitation and the chemical adsorption of charged oxygen molecules. 134
9.3. The normalized superposition of the Sr3d core level spectra measured at different pO_2 and different probing depths. 135
9.4. The probing depth-dependent binding energy positions of the $Sr3d_{5/2}$ low binding energy component peaks and the relative contribution of the surface component. 136
9.5. Schematic illustration of the possible atmospheric dependence of the strontium oxide precipitation at the surface of n-$SrTiO_3$. 138
9.6. Morphology-dependent Sr3d doublet intensities. 139
9.7. DFT + NEGF simulations of a n-$SrTiO_3$ platinum contact. 143

10.1. Schematic illustration of the SrO precipitation process and its impact on the surface properties of n-$SrTiO_3$. 148

A.1. Pressure instabilities during ECR experiments. XI

List of Tables

7.1. Summary of the doping concentration-dependent results. 92
7.2. Summary of the temperature-dependent rel. permittivity ϵ_r used for the calculations of the surface potential decay, the resulting space charge layer widths Δx_{SCL}, the surface electric field and the correspond negative surface charge. 99
7.3. Summary of the doping concentration- and temperature-dependent results observed for temperatures above 470 K. 102

8.1. Summary of the electrical transport measurements on a 32 nm 1.0 at% n-$SrTiO_3$ thin film and the resulting parameters of the surface space charge layer. 113

Bibliography

1. Singhal, S. Advances in solid oxide fuel cell technology. *Solid State Ionics* **135,** 305–313. ISSN: 0167-2738. https://www.sciencedirect.com/science/article/pii/S0167273800004525 (2000).
2. Tang, C. W. & VanSlyke, S. A. Organic electroluminescent diodes. *Applied Physics Letters* **51,** 913–915. ISSN: 0003-6951. http://aip.scitation.org/doi/10.1063/1.98799 (1987).
3. Chopra, K., Major, S. & Pandya, D. Transparent conductors - A status review. *Thin Solid Films* **102,** 1–46. ISSN: 0040-6090. https://www.sciencedirect.com/science/article/pii/0040609083902560 (1983).
4. Mannhart, J & Schlom, D. G. Oxide interfaces–an opportunity for electronics. *Science (New York, N.Y.)* **327,** 1607–11. ISSN: 1095-9203. http://www.ncbi.nlm.nih.gov/pubmed/20339065 (2010).
5. Kawasaki, M *et al.* Atomic Control of the $SrTiO_3$ Crystal Surface. *Science (New York, N.Y.)* **266,** 1540–2. ISSN: 0036-8075. http://www.ncbi.nlm.nih.gov/pubmed/17841713 (1994).
6. Rao, C. Transition metal oxides. *Annu. Rev. Phys. Chern.* **40,** 291–326 (1989).
7. Christen, H. M. & Eres, G. Recent advances in pulsed-laser deposition of complex oxides. *Journal of Physics: Condensed Matter* **20,** 264005. ISSN: 0953-8984. http://stacks.iop.org/0953-8984/20/i=26/a=264005?key=crossref.690294ed090895ca4528063f564315a1 (2008).
8. Schlom, D. G. & Mannhart, J. Interface takes charge over Si. *Nature Materials* **10,** 168–169. ISSN: 1476-1122. http://www.nature.com/articles/nmat2965 (2011).
9. Anderson, P. W. More is different. *Science (New York, N.Y.)* **177,** 393–6. ISSN: 0036-8075. http://www.ncbi.nlm.nih.gov/pubmed/17796623 (1972).
10. Waser, R. & Aono, M. Nanoionics-based resistive switching memories. *Nature Materials* **6,** 833–840. ISSN: 1476-1122. http://www.nature.com/articles/nmat2023 (2007).
11. Waser, R., Dittmann, R., Staikov, G. & Szot, K. Redox-Based Resistive Switching Memories - Nanoionic Mechanisms, Prospects, and Challenges. *Advanced Materials* **21,** 2632–2663. ISSN: 09359648. http://doi.wiley.com/10.1002/adma.200900375 (2009).

12. Baeumer, C. *et al.* Verification of redox-processes as switching and retention failure mechanisms in Nb:$SrTiO_3$ metal devices. *Nanoscale* **8,** 13967–13975. ISSN: 2040-3364. http://xlink.rsc.org/?DOI=C6NR00824K (2016).

13. Dittmann, R. *et al.* Scaling Potential of Local Redox Processes in Memristive $SrTiO_3$ Thin-Film Devices. *Proceedings of the IEEE* **100,** 1979–1990. ISSN: 0018-9219. http://ieeexplore.ieee.org/document/6189371/ (2012).

14. Ohtomo, A. & Hwang, H. Y. A high-mobility electron gas at the $LaAlO_3/SrTiO_3$ heterointerface. *Nature* **427,** 423–426. ISSN: 0028-0836. http://www.nature.com/articles/nature02308 (2004).

15. Gunkel, F. *et al.* Transport limits in defect-engineered $LaAlO_3/SrTiO_3$ bilayers. *Nanoscale* **7,** 1013–1022. ISSN: 2040-3364. http://xlink.rsc.org/?DOI=C4NR06272H (2015).

16. Liu, Z. Q. *et al.* Origin of the Two-Dimensional Electron Gas at $LaAlO_3/SrTiO_3$ Interfaces: The Role of Oxygen Vacancies and Electronic Reconstruction. *Physical Review X* **3,** 021010. ISSN: 2160-3308. https://link.aps.org/doi/10.1103/PhysRevX.3.021010 (2013).

17. Hodes, G. Applied physics. Perovskite-based solar cells. *Science (New York, N.Y.)* **342,** 317–8. ISSN: 1095-9203. http://www.ncbi.nlm.nih.gov/pubmed/24136955 (2013).

18. Huang, Y.-H., Dass, R. I., Xing, Z.-L. & Goodenough, J. B. Double perovskites as anode materials for solid-oxide fuel cells. *Science (New York, N.Y.)* **312,** 254–7. ISSN: 1095-9203. http://www.ncbi.nlm.nih.gov/pubmed/16614219 (2006).

19. Chroneos, A., Yildiz, B., Tarancón, A., Parfitt, D. & Kilner, J. A. Oxygen diffusion in solid oxide fuel cell cathode and electrolyte materials: mechanistic insights from atomistic simulations. *Energy & Environmental Science* **4,** 2774. ISSN: 1754-5692. http://xlink.rsc.org/?DOI=c0ee00717j (2011).

20. Hikita, Y. *et al.* Band Edge Engineering of Oxide Photoanodes for Photoelectrochemical Water Splitting: Integration of Subsurface Dipoles with Atomic-Scale Control. *Advanced Energy Materials* **6,** 1502154. ISSN: 16146832. http://doi.wiley.com/10.1002/aenm.201502154 (2016).

21. Chambers, S. A., Du, Y., Comes, R. B., Spurgeon, S. R. & Sushko, P. V. The effects of core-level broadening in determining band alignment at the epitaxial $SrTiO_3$ (001)/ *p*-Ge(001) heterojunction. *Applied Physics Letters* **110,** 082104. ISSN: 0003-6951. http://aip.scitation.org/doi/10.1063/1.4977422 (2017).

22. Kornblum, L., Morales-Acosta, M. D., Jin, E. N., Ahn, C. H. & Walker, F. J. Transport at the Epitaxial Interface between Germanium and Functional Oxides. *Advanced Materials Interfaces* **2,** 1500193. ISSN: 21967350. http://doi.wiley.com/10.1002/admi.201500193 (2015).

23. Gunkel, F. *et al.* Space charges and defect concentration profiles at complex oxide interfaces. *Physical Review B* **93,** 245431. ISSN: 2469-9950. https://link.aps.org/doi/10.1103/PhysRevB.93.245431 (2016).

24. Swartz, A. G. *et al.* Polaronic behavior in a weak-coupling superconductor. *Proceedings of the National Academy of Sciences of the United States of America* **115,** 1475–1480. ISSN: 1091-6490. http://www.ncbi.nlm.nih.gov/pubmed/29382769http://www.pubmedcentral.nih.gov/articlerender.fcgi?artid=PMC5816158 (2018).

25. Mikheev, E., Hwang, J., Kajdos, A. P., Hauser, A. J. & Stemmer, S. Tailoring resistive switching in $Pt/SrTiO_3$ junctions by stoichiometry control. *Scientific Reports* **5,** 11079. ISSN: 2045-2322. http://www.nature.com/articles/srep11079 (2015).

26. Rodenbücher, C. *et al.* Inhomogeneity of donor doping in $SrTiO_3$ substrates studied by fluorescence-lifetime imaging microscopy. *Applied Physics Letters* **103,** 162904. ISSN: 0003-6951. http://aip.scitation.org/doi/10.1063/1.4825367 (2013).

27. Schultz, A. M., Brown, T. D. & Ohodnicki, P. R. Optical and Chemi-Resistive Sensing in Extreme Environments: La-Doped $SrTiO_3$ Films for Hydrogen Sensing at High Temperatures. *The Journal of Physical Chemistry C* **119,** 6211–6220. ISSN: 1932-7447. http://pubs.acs.org/doi/10.1021/jp512391f (2015).

28. Kumar, R., Akhtar Imam, S. & R. Khan, M. A critical review of Taguchi gas sensors for the detection of VOC's. **1,** 177–183 (2009).

29. Seiyama, T., Kato, A., Fujiishi, K. & Nagatani, M. A New Detector for Gaseous Components Using Semiconductive Thin Films. *Analytical Chemistry* **34,** 1502–1503. ISSN: 0003-2700. http://pubs.acs.org/doi/abs/10.1021/ac60191a001 (1962).

30. Meyer, R. & Waser, R. Resistive donor-doped $SrTiO_3$ sensors: I, basic model for a fast sensor response. *Sensors and Actuators B: Chemical* **101,** 335–345. ISSN: 09254005. http://linkinghub.elsevier.com/retrieve/pii/S0925400504001534 (2004).

31. Ge, J.-F. *et al.* Superconductivity above 100 K in single-layer FeSe films on doped $SrTiO_3$. *Nature Materials* **14,** 285–289. ISSN: 1476-1122. http://www.nature.com/articles/nmat4153 (2015).

32. Garcia, V. *et al.* Giant tunnel electroresistance for non-destructive readout of ferroelectric states. *Nature* **460,** 81–84. ISSN: 0028-0836. http://www.nature.com/articles/nature08128 (2009).

33. Chanthbouala, A. *et al.* Solid-state memories based on ferroelectric tunnel junctions. *Nature Nanotechnology* **7,** 101–104. ISSN: 1748-3387. http://www.nature.com/articles/nnano.2011.213 (2012).

34. Wen, Z., Wu, D. & Li, A. Memristive behaviors in Pt/$BaTiO_3$/Nb:$SrTiO_3$ ferroelectric tunnel junctions. *Applied Physics Letters* **105,** 052910. ISSN: 0003-6951. http://aip.scitation.org/doi/10.1063/1.4892846 (2014).

35. May, K. J. *et al.* Thickness-Dependent Photoelectrochemical Water Splitting on Ultrathin $LaFeO_3$ Films Grown on Nb:$SrTiO_3$. *The Journal of Physical Chemistry Letters* **6,** 977–985. ISSN: 1948-7185. http://pubs.acs.org/doi/10.1021/acs.jpclett.5b00169 (2015).

36. Muenstermann, R., Menke, T., Dittmann, R. & Waser, R. Coexistence of Filamentary and Homogeneous Resistive Switching in Fe-Doped $SrTiO_3$ Thin-Film Memristive Devices. *Advanced Materials* **22,** 4819–4822. ISSN: 09359648. http://doi.wiley.com/10.1002/adma.201001872 (2010).

37. Moos, R. & Hardtl, K. H. Defect Chemistry of Donor-Doped and Undoped Strontium Titanate Ceramics between 1000° and 1400°C. *Journal of the American Ceramic Society* **80,** 2549–2562. ISSN: 00027820. http://doi.wiley.com/10.1111/j.1151-2916.1997.tb03157.x (2005).

38. Meyer, R., Zurhelle, A. F., De Souza, R. A., Waser, R. & Gunkel, F. Dynamics of the metal-insulator transition of donor-doped $SrTiO_3$. *Physical Review B* **94,** 115408. ISSN: 2469-9950. https://link.aps.org/doi/10.1103/PhysRevB.94.115408 (2016).

39. Ohtomo, A. & Hwang, H. Y. Surface depletion in doped $SrTiO_3$ thin films. *Applied Physics Letters* **84,** 1716–1718. ISSN: 0003-6951. http://aip.scitation.org/doi/10.1063/1.1668329 (2004).

40. Kozuka, Y., Hikita, Y., Bell, C. & Hwang, H. Y. Dramatic mobility enhancements in doped $SrTiO_3$ thin films by defect management. *Applied Physics Letters* **97,** 012107. ISSN: 0003-6951. http://aip.scitation.org/doi/10.1063/1.3457994 (2010).

41. Verma, A., Kajdos, A. P., Cain, T. A., Stemmer, S. & Jena, D. Intrinsic Mobility Limiting Mechanisms in Lanthanum-Doped Strontium Titanate. *Physical Review Letters* **112,** 216601. ISSN: 0031-9007. https://link.aps.org/doi/10.1103/PhysRevLett.112.216601 (2014).

42. Son, J. *et al.* Epitaxial $SrTiO_3$ films with electron mobilities exceeding 30,000 cm2 V-1 s-1. *Nature Materials* **9,** 482–484. ISSN: 1476-1122. http://www.nature.com/articles/nmat2750 (2010).

43. Inoue, H. *et al.* Tunable coupling of two-dimensional superconductors in bilayer $SrTiO_3$ heterostructures. *Physical Review B* **88,** 241104. ISSN: 1098-0121. https://link.aps.org/doi/10.1103/PhysRevB.88.241104 (2013).

44. Cai, Z., Kubicek, M., Fleig, J. & Yildiz, B. Chemical Heterogeneities on La 0.6 Sr 0.4 CoO 3-δ Thin Films-Correlations to Cathode Surface Activity and Stability. *Chemistry of Materials* **24,** 1116–1127. ISSN: 0897-4756. http://pubs.acs.org/doi/10.1021/cm203501u (2012).

45. De Souza, R. A., Gunkel, F., Hoffmann-Eifert, S. & Dittmann, R. Finite-size versus interface-proximity effects in thin-film epitaxial $SrTiO_3$. *Physical Review B* **89,** 241401. ISSN: 1098-0121. https://link.aps.org/doi/10.1103/PhysRevB.89.241401 (2014).

46. Sanna, S. *et al.* Enhancement of Ionic Conductivity in Sm-Doped Ceria/Yttria-Stabilized Zirconia Heteroepitaxial Structures. *Small* **6,** 1863–1867. ISSN: 16136810. http://doi.wiley.com/10.1002/smll.200902348 (2010).

47. Sanna, S. *et al.* Enhancement of the chemical stability in confined δ-Bi_2O_3. *Nature Materials* **14,** 500–504. ISSN: 1476-1122. http://www.nature.com/articles/nmat4266 (2015).

48. Gunkel, F. *et al.* Influence of charge compensation mechanisms on the sheet electron density at conducting $LaAlO_3/SrTiO_3$-interfaces. *Applied Physics Letters* **100,** 052103. ISSN: 0003-6951. http://aip.scitation.org/doi/10.1063/1.3679139 (2012).

49. Gunkel, F. *et al.* Thermodynamic Ground States of Complex Oxide Heterointerfaces. *ACS Applied Materials & Interfaces* **9,** 1086–1092. ISSN: 1944-8244. http://pubs.acs.org/doi/10.1021/acsami.6b12706 (2017).

50. Setvín, M. *et al.* Reaction of O_2 with Subsurface Oxygen Vacancies on TiO_2 Anatase (101). *Science* **341,** 988–991. ISSN: 0036-8075. http://www.sciencemag.org/cgi/doi/10.1126/science.1239879 (2013).

51. Setvín, M. *et al.* Surface preparation of TiO_2 anatase (101): Pitfalls and how to avoid them. *Surface Science* **626,** 61–67. ISSN: 00396028. http://linkinghub.elsevier.com/retrieve/pii/S0039602814000958 (2014).

52. Marchewka, A. *et al.* Determination of the electrostatic potential distribution in Pt/Fe:$SrTiO_3$/Nb:$SrTiO_3$ thin-film structures by electron holography. *Scientific Reports* **4,** 6975. ISSN: 2045-2322. http://www.nature.com/articles/srep06975 (2015).

53. De Groot, F. M. F. *et al.* Oxygen 1s X-ray absorption of tetravalent titanium oxides: A comparison with single-particle calculations. *Physical Review B* **48,** 2074–2080. ISSN: 0163-1829. https://link.aps.org/doi/10.1103/PhysRevB.48.2074 (1993).

54. Kröger, F. A. & Nachtrieb, N. H. The Chemistry of Imperfect Crystals. *Physics Today* **17,** 66–69. ISSN: 0031-9228. http://physicstoday.scitation.org/doi/10.1063/1.3051186 (1964).

55. Rothschild, A., Menesklou, W., Tuller, H. L. & Ivers-Tiffée, E. Electronic Structure, Defect Chemistry, and Transport Properties of $SrTi_{1-x}FexO_{3-y}$ Solid Solutions (2006).

56. Eglitis, R. & Kotomin, E. Ab initio calculations of Nb doped $SrTiO_3$. *Physica B: Condensed Matter* **405,** 3164–3166. ISSN: 09214526. http://linkinghub.elsevier.com/retrieve/pii/S0921452610003959 (2010).

57. Hashimoto, S., Kindermann, L., Poulsen, F. & Mogensen, M. A study on the structural and electrical properties of lanthanum-doped strontium titanate prepared in air. *Journal of Alloys and Compounds* **397,** 245–249. ISSN: 0925-8388. https://www.sciencedirect.com/science/article/pii/S0925838805000964 (2005).

58. Spinelli, A., Torija, M. A., Liu, C., Jan, C. & Leighton, C. Electronic transport in doped $SrTiO_3$: Conduction mechanisms and potential applications. *Physical Review B* **81,** 155110. ISSN: 1098-0121. https://link.aps.org/doi/10.1103/PhysRevB.81.155110 (2010).

59. Van der Berg, R. A., Blom, P. W. M., Cillessen, J. F. M. & Wolf, R. M. Field dependent permittivity in metal-semiconducting $SrTiO_3$ Schottky diodes. *Applied Physics Letters* **66,** 697–699. ISSN: 0003-6951. http://aip.scitation.org/doi/10.1063/1.114103 (1995).

60. Mikheev, E. *et al.* Limitations to the room temperature mobility of two- and three-dimensional electron liquids in $SrTiO_3$. *Applied Physics Letters* **106,** 062102. ISSN: 0003-6951. http://aip.scitation.org/doi/10.1063/1.4907888 (2015).

61. Hao, X., Wang, Z., Schmid, M., Diebold, U. & Franchini, C. Coexistence of trapped and free excess electrons in $SrTiO_3$. *Physical Review B* **91,** 085204. ISSN: 1098-0121. https://link.aps.org/doi/10.1103/PhysRevB.91.085204 (2015).

62. Shang, D. S. *et al.* Electronic transport and colossal electroresistance in $SrTiO_3$:Nb-based Schottky junctions. *Applied Physics Letters* **94,** 052105. ISSN: 0003-6951. http://aip.scitation.org/doi/10.1063/1.3077615 (2009).

63. Park, C., Seo, Y., Jung, J. & Kim, D.-W. Electrode-dependent electrical properties of metal/Nb-doped $SrTiO_3$ junctions. *Journal of Applied Physics* **103,** 054106. ISSN: 0021-8979. http://aip.scitation.org/doi/10.1063/1.2872707 (2008).

64. Lee, M.-J. *et al.* A fast, high-endurance and scalable non-volatile memory device made from asymmetric Ta_2O_{5-x}/TaO_{2-x} bilayer structures. *Nature Materials* **10,** 625–630. ISSN: 1476-1122. http://www.nature.com/articles/nmat3070 (2011).

65. Sze, S. M. & Ng, K. K. *Physics of semiconductor devices* ISBN: 0470068302 (Wiley-Interscience, 2007).

66. Funck, C. *et al.* A Theoretical and Experimental View on the Temperature Dependence of the Electronic Conduction through a Schottky Barrier in a Resistively Switching $SrTiO_3$ -Based Memory Cell. *Advanced Electronic Materials* **4,** 1800062. ISSN: 2199160X. http://doi.wiley.com/10.1002/aelm.201800062 (2018).

67. Wang, W., Lee, T. & Reed, M. A. Mechanism of electron conduction in self-assembled alkanethiol monolayer devices. *Physical Review B* **68,** 035416. ISSN: 0163-1829. https://link.aps.org/doi/10.1103/PhysRevB.68.035416 (2003).

68. Mikheev, E., Hoskins, B. D., Strukov, D. B. & Stemmer, S. Resistive switching and its suppression in Pt/Nb:$SrTiO_3$ junctions. *Nature Communications* **5,** 3990. ISSN: 2041-1723. http://www.nature.com/articles/ncomms4990 (2014).

69. Wang, Z. *et al.* Vacancy clusters at domain boundaries and band bending at the $SrTiO_3$ (110) surface. *Physical Review B* **90,** 035436. ISSN: 1098-0121. https://link.aps.org/doi/10.1103/PhysRevB.90.035436 (2014).

70. Meyer, R., Waser, R., Helmbold, J. & Borchardt, G. Observation of Vacancy Defect Migration in the Cation Sublattice of Complex Oxides by O^{18} Tracer Experiments. *Physical Review Letters* **90,** 105901. ISSN: 0031-9007. https://link.aps.org/doi/10.1103/PhysRevLett.90.105901 (2003).

71. Wei, H. *et al.* Study of SrO segregation on $SrTiO_3$ (100) surfaces. *Journal of the European Ceramic Society* **21,** 1677–1680. ISSN: 09552219. http://linkinghub.elsevier.com/retrieve/pii/S0955221901000917 (2001).

72. Szot, K. *et al.* Formation of micro-crystals on the (100) surface of $SrTiO_3$ at elevated temperatures. *Surface Science* **460,** 112–128. ISSN: 00396028. http://linkinghub.elsevier.com/retrieve/pii/S0039602800005227 (2000).

73. Smyth, D. M. *The defect chemistry of metal oxides* 294. ISBN: 0195110145 (Oxford University Press, 2000).

74. Gunkel, F. *The role of defects at functional interfaces between polar and non-polar perovskite oxides* PhD thesis (2013).

75. Merkle, R. & Maier, J. How Is Oxygen Incorporated into Oxides? A Comprehensive Kinetic Study of a Simple Solid-State Reaction with $SrTiO_3$ as a Model Material. *Angewandte Chemie International Edition* **47,** 3874–3894. ISSN: 14337851. http://doi.wiley.com/10.1002/anie.200700987 (2008).

76. Kröger, F. & Vink, H. Relations between the Concentrations of Imperfections in Crystalline Solids. *Solid State Physics* **3,** 307–435. ISSN: 0081-1947. https://www.sciencedirect.com/science/article/pii/S0081194708601356 (1956).

77. Skaja, K. *Redox processes and ionic transport in resistive switching binary metal oxides* PhD thesis (2017). ISBN: 9783958062368.

78. Fick, A. Ueber Diffusion. *Annalen der Physik und Chemie* **170,** 59–86. ISSN: 00033804. http://doi.wiley.com/10.1002/andp.18551700105 (1855).

79. Den Otter, M. W., Bouwmeester, H. J. M., Boukamp, B. A. & Verweij, H. Reactor Flush Time Correction in Relaxation Experiments. *Journal of The Electrochemical Society* **148,** J1. ISSN: 00134651. http://jes.ecsdl.org/cgi/doi/10.1149/1.1337604 (2001).

80. Crank, J. *The mathematics of diffusion* ISBN: 0198533446 (Oxford University Press, 1979).

81. Den Otter, M., van der Haar, L. & Bouwmeester, H. Numerical evaluation of eigenvalues of the sheet diffusion problem in the surface/diffusion mixed regime. *Solid State Ionics* **134,** 259–264. ISSN: 0167-2738. https://www.sciencedirect.com/science/article/pii/S0167273800006846 (2000).

82. Yasuda, I. & Hikita, T. Precise Determination of the Chemical Diffusion Coefficient of Calcium-Doped Lanthanum Chromites by Means of Electrical Conductivity Relaxation. *Journal of The Electrochemical Society* **141,** 1268. ISSN: 00134651. http://jes.ecsdl.org/cgi/doi/10.1149/1.2054908 (1994).

83. Rijnders, A. J. H. M. *The initial growth of complex oxides: study and manipulation* PhD thesis (University of Twente, 2001).

84. Dittmann, R. Stoichiometry in epitaxial oxide thin films. *Epitaxial Growth of Complex Metal Oxides,* 231–261. https://www.sciencedirect.com/science/article/pii/B9781782422457000099 (2015).

85. Hensling, F. V. E. *Influence of UV Radiation during Pulsed Laser Deposition on the Electrical Properties of $SrTiO_3$* Master Thesis (RWTH Aachen, 2015).

86. Wicklein, S. *et al.* Pulsed laser ablation of complex oxides: The role of congruent ablation and preferential scattering for the film stoichiometry. *Applied Physics Letters* **101,** 131601. ISSN: 0003-6951. http://aip.scitation.org/doi/10.1063/1.4754112 (2012).

87. Xu, C *et al.* Impact of the interplay between nonstoichiometry and kinetic energy of the plume species on the growth mode of $SrTiO_3$ thin films. *Journal of Physics D: Applied Physics* **47,** 034009. ISSN: 0022-3727. http://stacks.iop.org/0022-3727/47/i=3/a=034009?key=crossref.847e28183a57dc19412df60e51af298e (2014).

88. Xu, C. *et al.* Disentanglement of growth dynamic and thermodynamic effects in $LaAlO_3/SrTiO_3$ heterostructures. *Scientific Reports* **6,** 22410. ISSN: 2045-2322. http://www.nature.com/articles/srep22410 (2016).

89. Raab, N. *Fabrication of $SrTiO_3$ thin films with tailored defect structure for future non-volatile memories* PhD thesis (RWTH Aachen, 2017).

90. Wicklein, S. *Defect engineering of $SrTiO_3$ thin films for resistive switching applications* PhD thesis (2013).

91. Keeble, D. J. *et al.* Nonstoichiometry accommodation in $SrTiO_3$ thin films studied by positron annihilation and electron microscopy. *Physical Review B* **87,** 195409. ISSN: 1098-0121. https://link.aps.org/doi/10.1103/PhysRevB.87.195409 (2013).

92. Ohnishi, T., Lippmaa, M., Yamamoto, T., Meguro, S. & Koinuma, H. Improved stoichiometry and misfit control in perovskite thin film formation at a critical fluence by pulsed laser deposition. *Applied Physics Letters* **87,** 241919. ISSN: 0003-6951. http://aip.scitation.org/doi/10.1063/1.2146069 (2005).

93. Gunkel, F. *et al.* Stoichiometry dependence and thermal stability of conducting $NdGaO_3/SrTiO_3$ heterointerfaces. *Applied Physics Letters* **102,** 071601. ISSN: 0003-6951. http://aip.scitation.org/doi/10.1063/1.4792509 (2013).

94. Eason, R. *Pulsed laser deposition of thin films: applications-led growth of funtional materials* (John Wiley & Sons, Ltd, 2007).

95. Ichimiya, A, Cohen, P. & Cohen, P. *Reflection high-energy electron diffraction* (Cambridge University Press, 2004).

96. Harsha, K. *Principles of vapor deposition of thin films* (Elsevier Science, 2005).

97. Kelly, P., Vacuum, R. A. & 2000, U. Magnetron sputtering: a review of recent developments and applications. *Elsevier* (2000).

98. Depla, D. & Mahieu, S. *Reactive Sputter Deposition* ISBN: 978-3-540-76662-9 (Springer Berlin Heidelberg, 2008).

99. Voigtländer, B. *Scanning Probe Microscopy* (Springer Berlin Heidelberg, 2015).

100. Bragg, W. H. & Bragg, W. L. The Reflection of X-rays by Crystals. *Proceedings of the Royal Society A: Mathematical, Physical and Engineering Sciences* **88,** 428–438. ISSN: 1364-5021. http://rspa.royalsocietypublishing.org/cgi/doi/10.1098/rspa.1913.0040 (1913).

101. Miller, W. *A Treatise on Crystallography* (J. & J. J. Deighton, 1839).

102. Guinier, A. *X-ray diffraction in crystals, imperfect crystals, and amorphous bodies* (DOVER PUBN INC, 1994).

103. Van der Pauw, L. A method of measuring specific resistivity and Hall effect of discs of arbitrary shape. *Philips Research Reports* (1958).

104. E. H. Hall. On a New Action of the Magnet on Electric Currents. *American Journal of Mathematics* **2,** 287–292 (1879).

105. Lake Shore Cryotronics. in *Model 8404 Manual* March 2014 (2014).

106. Von Klitzing, K. The quantized Hall effect. *Reviews of Modern Physics* **58,** 519–531. ISSN: 0034-6861. https://link.aps.org/doi/10.1103/RevModPhys.58.519 (1986).

107. Barsoukov, E & Macdonald, J. *Impedance spectroscopy: theory, experiment, and applications* (Wiley, 2018).

108. Macdonald, J. R. Impedance spectroscopy. *Annals of Biomedical Engineering* **20,** 289–305. ISSN: 0090-6964. http://link.springer.com/10.1007/BF02368532 (1992).

109. Baeumer, C. *Spectroscopic characterization of local valence change processes n resitively switching complex oxides* PhD thesis (RWTH Aachen, 2016).

110. Hamann, E., Manger, H. & Steinke, L. *Lambda-Sensor with Y_2O_3-Stabilized ZrO_2 Ceramic for Application in Automotive Emission Control Systems* 1977.

111. Hüfner, S. *Photoelectron spectroscopy: principles and applications* (Springer Berlin Heidelberg, 2013).

112. Siegbahn, K. Electron spectroscopy for atoms, molecules, and condensed matter. *Reviews of Modern Physics* **54,** 709–728. ISSN: 0034-6861. https://link.aps.org/doi/10.1103/RevModPhys.54.709 (1982).

113. Andrä, M. *et al.* Chemical control of the electrical surface properties in donor-doped transition metal oxides. *Physical Review Materials* **3,** 044604. ISSN: 2475-9953. https://link.aps.org/doi/10.1103/PhysRevMaterials.3.044604 (2019).

114. Hertz, H. Ueber einen Einfluss des ultravioletten Lichtes auf die electrische Entladung. *Annalen der Physik und Chemie* **267,** 983–1000. ISSN: 00033804. http://doi.wiley.com/10.1002/andp.18872670827 (1887).

115. Andrä, M. *et al.* Chemical control of the electrical surface properties in donor-doped transition metal oxides. *Physical Review Materials* **3,** 044604. ISSN: 2475-9953. https://link.aps.org/doi/10.1103/PhysRevMaterials.3.044604 (2019).

116. Watts, J. & Wolstenholme, J. *The Electron Spectrum: Qualitative and Quantitative Interpretation* (John Wiley & Sons, Ltd, 2005).

117. Tanuma, S., Powell, C. J. & Penn, D. R. Calculations of electron inelastic mean free paths. IX. Data for 41 elemental solids over the 50 eV to 30 keV range. *Surface and Interface Analysis* **43,** 689–713. ISSN: 01422421. http://doi.wiley.com/10.1002/sia.3522 (2011).

118. Cros, A. Charging effects in X-ray photoelectron spectroscopy. *Journal of Electron Spectroscopy and Related Phenomena* **59,** 1–14. ISSN: 03682048. http://linkinghub.elsevier.com/retrieve/pii/036820489285008U (1992).

119. Higuchi, T. *et al.* Electronic structure of *p*-type $SrTiO_3$ by photoemission spectroscopy. *Physical Review B* **57,** 6978–6983. ISSN: 0163-1829. https://link.aps.org/doi/10.1103/PhysRevB.57.6978 (1998).

120. Ogletree, D. F. *et al.* A differentially pumped electrostatic lens system for photoemission studies in the millibar range. *Review of Scientific Instruments* **73,** 3872–3877. ISSN: 0034-6748. http://aip.scitation.org/doi/10.1063/1.1512336 (2002).

121. Andrä, M. *et al.* Oxygen partial pressure dependence of surface space charge formation in donor-doped $SrTiO_3$. *APL Materials* **5,** 056106. ISSN: 2166532X (2017).

122. Rodenbücher, C. *et al.* Homogeneity and variation of donor doping in Verneuil-grown Nb:$SrTiO_3$ single crystals. *Scientific Reports* **6,** 32250. ISSN: 2045-2322. http://www.nature.com/articles/srep32250 (2016).

123. Andrä, M. *et al.* The influence of the local oxygen vacancy concentration on the piezoresponse of strontium titanate thin films. *Nanoscale* **7,** 14351–14357. ISSN: 2040-3364. http://xlink.rsc.org/?DOI=C5NR03643G (2015).

124. Bäumer, C. & Dittmann, R. Redox-based memristive metal-oxide devices. *Metal Oxide-Based Thin Film Structures,* 489–522. https://www.sciencedirect.com/science/article/pii/B9780128111666000200?via%3Dihub (2018).

125. Orazem, M. E. & Tribollet, B. *Electrochemical Impedance Spectroscopy* ISBN: 9780470381588 (John Wiley & Sons, Inc., 2008).

126. Lasia, A. in *Modern Aspects of Electrochemistry* 143–248 (Kluwer Academic Publishers, 2002).

127. M. Andrä, C. Funck, N. Raab, R. Dittmann, R. Waser, S. Menzel, F. G. Effect of cationic interface defects on the contact resistance of Pt/Nb:$SrTiO_3$ heterojunctions. *Under Review* (2018).

128. Baeumer, C. *et al.* Surface Termination Conversion during $SrTiO_3$ Thin Film Growth Revealed by X-ray Photoelectron Spectroscopy. *Scientific Reports* **5,** 11829. ISSN: 2045-2322. http://www.nature.com/articles/srep11829 (2015).

129. Blennow, P., Hagen, A., Hansen, K. K., Wallenberg, L. R. & Mogensen, M. Defect and electrical transport properties of Nb-doped $SrTiO_3$. *Solid State Ionics* **179,** 2047–2058. ISSN: 0167-2738. https://www.sciencedirect.com/science/article/pii/S016727380800516X (2008).

130. Kovalevsky, A. V. *et al.* Designing strontium titanate-based thermoelectrics: insight into defect chemistry mechanisms. *Journal of Materials Chemistry A* **5,** 3909–3922. ISSN: 2050-7488. http://xlink.rsc.org/?DOI=C6TA09860F (2017).

131. Adepalli, K. K., Yang, J., Maier, J., Tuller, H. L. & Yildiz, B. Tunable Oxygen Diffusion and Electronic Conduction in $SrTiO_3$ by Dislocation-Induced Space Charge Fields. *Advanced Functional Materials* **27,** 1700243. ISSN: 1616301X. http://doi.wiley.com/10.1002/adfm.201700243 (2017).

132. Haasch, R. T., Breckenfeld, E. & Martin, L. W. Single Crystal Perovskites Analyzed Using X-ray Photoelectron Spectroscopy: 1. $SrTiO_3$ (001). *Surface Science Spectra* **21,** 87–94. ISSN: 1055-5269. http://avs.scitation.org/doi/10.1116/11.20140901 (2014).

133. Lichterman, M. F., Richter, M. H., Brunschwig, B. S., Lewis, N. S. & Lewerenz, H.-J. Operando X-ray photoelectron spectroscopic investigations of the electrochemical double layer at Ir/KOH(aq) interfaces. *Journal of Electron Spectroscopy and Related Phenomena* **221,** 99–105. ISSN: 03682048. http://linkinghub.elsevier.com/retrieve/pii/S0368204816301736 (2017).

134. Rogers, J. W. *et al.* Identification of a superoxide in superconducting $La_2CuO_{4+\delta}$ by X-ray photoelectron spectroscopy. *Physical Review B* **38,** 5021–5024. ISSN: 0163-1829. https://link.aps.org/doi/10.1103/PhysRevB.38.5021 (1988).

135. Ohsawa, T., Shimizu, R., Iwaya, K., Shiraki, S. & Hitosugi, T. Negligible Sr segregation on $SrTiO_3$(001)-(13×13)-R33.7° reconstructed surfaces. *Applied Physics Letters* **108,** 161603. ISSN: 0003-6951. http://aip.scitation.org/doi/10.1063/1.4947441 (2016).

136. Dudy, L. *et al.* In Situ Control of Separate Electronic Phases on $SrTiO_3$ Surfaces by Oxygen Dosing. *Advanced Materials* **28,** 7443–7449. ISSN: 09359648. http://doi.wiley.com/10.1002/adma.201600046 (2016).

137. Stoerzinger, K. A. *et al.* Water Reactivity on the $LaCoO_3$ (001) Surface: An Ambient Pressure X-ray Photoelectron Spectroscopy Study. *The Journal of Physical Chemistry C* **118,** 19733–19741. ISSN: 1932-7447. http://pubs.acs.org/doi/10.1021/jp502970r (2014).

138. Oku, M., Matsuta, H., Wagatsuma, K., Waseda, Y. & Kohiki, S. Removal of inelastic scattering part from Ti2p XPS spectrum of TiO_2 by deconvolution method using O1s as response function. *Journal of Electron Spectroscopy and Related Phenomena* **105,** 211–218. ISSN: 03682048. http://linkinghub.elsevier.com/retrieve/pii/S0368204899000675 (1999).

139. Chambers, S. A., Droubay, T., Kaspar, T. C. & Gutowski, M. Experimental determination of valence band maxima for $SrTiO_3$, TiO_2, and SrO and the associated valence band offsets with Si(001). *Journal of Vacuum Science & Technology B: Microelectronics and Nanometer Structures* **22,** 2205. ISSN: 0734211X. http://scitation.aip.org/content/avs/journal/jvstb/22/4/10.1116/1.1768525 (2004).

140. Johansson, G., Hedman, J., Berndtsson, A., Klasson, M. & Nilsson, R. Calibration of electron spectra. *Journal of Electron Spectroscopy and Related Phenomena* **2,** 295–317. ISSN: 0368-2048. https://www.sciencedirect.com/science/article/pii/0368204873800222 (1973).

141. Nefedov, V., Salyn, Y., Leonhardt, G. & Scheibe, R. A comparison of different spectrometers and charge corrections used in X-ray photoelectron spectroscopy. *Journal of Electron Spectroscopy and Related Phenomena* **10,** 121–124. ISSN: 0368-2048. https://www.sciencedirect.com/science/article/pii/036820487785010X (1977).

142. Kraut, E. A., Grant, R. W., Waldrop, J. R. & Kowalczyk, S. P. Precise Determination of the Valence-Band Edge in X-Ray Photoemission Spectra: Application to Measurement of Semiconductor Interface Potentials. *Physical Review Letters* **44,** 1620–1623. ISSN: 0031-9007. https://link.aps.org/doi/10.1103/PhysRevLett.44.1620 (1980).

143. Nenning, A. *et al.* Ambient Pressure XPS Study of Mixed Conducting Perovskite-Type SOFC Cathode and Anode Materials under Well-Defined Electrochemical Polarization. *The Journal of Physical Chemistry C* **120,** 1461–1471. ISSN: 1932-7447. http://pubs.acs.org/doi/10.1021/acs.jpcc.5b08596 (2016).

144. Shavorskiy, A. *et al.* Direct Mapping of Band Positions in Doped and Undoped Hematite during Photoelectrochemical Water Splitting. *The Journal of Physical Chemistry Letters* **8,** 5579–5586. ISSN: 1948-7185. http://pubs.acs.org/doi/10.1021/acs.jpclett.7b02548 (2017).

145. Frank Ogletree, D., Bluhm, H., Hebenstreit, E. D. & Salmeron, M. Photoelectron spectroscopy under ambient pressure and temperature conditions. *Nuclear Instruments and Methods in Physics Research Section A: Accelerators, Spectrometers, Detectors and Associated Equipment* **601,** 151–160. ISSN: 0168-9002. https://www.sciencedirect.com/science/article/pii/S0168900208020214 (2009).

146. Tanuma, S., Powell, C. J. & Penn, D. R. Calculations of electron inelastic mean free paths. V. Data for 14 organic compounds over the 50-2000 eV range. *Surface and Interface Analysis* **21,** 165–176. ISSN: 0142-2421. http://doi.wiley.com/10.1002/sia.740210302 (1994).

147. De Groot, F. M. F. *et al.* Oxygen 1s X-ray absorption of tetravalent titanium oxides: A comparison with single-particle calculations. *Physical Review B* **48,** 2074–2080. ISSN: 0163-1829. https://link.aps.org/doi/10.1103/PhysRevB.48.2074 (1993).

148. Denk, I., Münch, W. & Maier, J. Partial Conductivities in $SrTiO_3$: Bulk Polarization Experiments, Oxygen Concentration Cell Measurements, and Defect-Chemical Modeling. *Journal of the American Ceramic Society* **78,** 3265–3272. ISSN: 15512916. http://doi.wiley.com/10.1111/j.1151-2916.1995.tb07963.x (1995).

149. Ko, C., Karthikeyan, A. & Ramanathan, S. Studies on oxygen chemical surface exchange and electrical conduction in thin film nanostructured titania at high temperatures and varying oxygen pressure. *The Journal of Chemical Physics* **134,** 014704. ISSN: 0021-9606. http://aip.scitation.org/doi/10.1063/1.3524341 (2011).

150. Kerman, K., Ko, C. & Ramanathan, S. Orientation dependent oxygen exchange kinetics on single crystal $SrTiO_3$ surfaces. *Physical Chemistry Chemical Physics* **14,** 11953. ISSN: 1463-9076. http://xlink.rsc.org/?DOI=c2cp41918a (2012).

151. Van der Berg, R. A., Blom, P. W. M., Cillessen, J. F. M. & Wolf, R. M. Field dependent permittivity in metal-semiconducting $SrTiO_3$ Schottky diodes. *Applied Physics Letters* **66,** 697–699. ISSN: 0003-6951. http://aip.scitation.org/doi/10.1063/1.114103 (1995).

152. Sawa, A. Resistive switching in transition metal oxides. *Materials Today* **11,** 28–36. ISSN: 1369-7021. https://www.sciencedirect.com/science/article/pii/S1369702108701196 (2008).

153. Hensling, F., Heisig, T., Raab, N., Baeumer, C. & Dittmann, R. Tailoring the switching performance of resistive switching $SrTiO_3$ devices by SrO interface engineering. *Solid State Ionics* **325,** 247–250. ISSN: 0167-2738. https://www.sciencedirect.com/science/article/pii/S0167273818305812 (2018).

154. Raab, N., Bäumer, C. & Dittmann, R. Impact of the cation-stoichiometry on the resistive switching and data retention of $SrTiO_3$ thin films. *AIP Advances* **5,** 047150. ISSN: 2158-3226. http://aip.scitation.org/doi/10.1063/1.4919697 (2015).

155. De Souza, R. A., Metlenko, V., Park, D. & Weirich, T. E. Behavior of oxygen vacancies in single-crystal $SrTiO_3$: Equilibrium distribution and diffusion kinetics. *Physical Review B* **85,** 174109. ISSN: 1098-0121. https://link.aps.org/doi/10.1103/PhysRevB.85.174109 (2012).

156. Lewin, M. *et al.* Nanospectroscopy of Infrared Phonon Resonance Enables Local Quantification of Electronic Properties in Doped SrTiOOrientation dependent oxygen exchange kinetics on single crystal $SrTiO_3$ surfaces Ceramics. *Advanced Functional Materials* **28,** 1802834. ISSN: 1616301X. http://doi.wiley.com/10.1002/adfm.201802834 (2018).

157. Hensling, F., Baeumer, C., Marc-André Rose, Gunkel, F. & Dittmann, R. $SrTiO_3$ termination control: A method to tailor the oxygen exchange kinetics. *Under Review* (2019).

158. Reihl, B. *et al.* Electronic structure of strontium titanate. *Physical Review B* **30,** 803–806. ISSN: 0163-1829. https://link.aps.org/doi/10.1103/PhysRevB.30.803 (1984).

159. Dingle, R., Störmer, H. L., Gossard, A. C. & Wiegmann, W. Electron mobilities in modulation-doped semiconductor heterojunction superlattices. *Applied Physics Letters* **33,** 665–667. ISSN: 0003-6951. http://aip.scitation.org/doi/10.1063/1.90457 (1978).

160. Wang, Z. *et al.* Transition from Reconstruction toward Thin Film on the (110) Surface of Strontium Titanate. *Nano Letters* **16,** 2407–2412. ISSN: 1530-6984. http://pubs.acs.org/doi/10.1021/acs.nanolett.5b05211 (2016).

161. Marshall, M. S. J., Becerra-Toledo, A. E., Marks, L. D. & Castell, M. R. Surface and Defect Structure of Oxide Nanowires on $SrTiO_3$. *Physical Review Letters* **107,** 086102. ISSN: 0031-9007. https://link.aps.org/doi/10.1103/PhysRevLett.107.086102 (2011).

162. Becerra-Toledo, A. E., Marshall, M. S. J., Castell, M. R. & Marks, L. D. c(4 × 2) and related structural units on the $SrTiO_3$ (001) surface: Scanning tunneling microscopy, density functional theory, and atomic structure. *The Journal of Chemical Physics* **136,** 214701. ISSN: 0021-9606 (2012).

163. Gerhold, S., Wang, Z., Schmid, M. & Diebold, U. Stoichiometry-driven switching between surface reconstructions on $SrTiO_3$ (001). *Surface Science* **621,** L1–L4. ISSN: 0039-6028 (2014).

164. Bielanski, A & Haber, J. *Oxygen in catalysis* (CRC Press, 1990).

165. Mastrikov, Y. A., Merkle, R., Heifets, E., Kotomin, E. A. & Maier, J. Pathways for Oxygen Incorporation in Mixed Conducting Perovskites: A DFT-Based Mechanistic Analysis for (La, Sr)$MnO_{3-\delta}$. *The Journal of Physical Chemistry C* **114,** 3017–3027. ISSN: 1932-7447. `http://pubs.acs.org/doi/10.1021/jp909401g` (2010).

166. Merkle, R. & Maier, J. Oxygen incorporation into Fe-doped $SrTiO_3$: Mechanistic interpretation of the surface reaction. *Physical Chemistry Chemical Physics* **4,** 4140–4148. ISSN: 14639076. `http://xlink.rsc.org/?DOI=b204032h` (2002).

167. Hara, T., Ishiguro, T. & Shinozaki, K. Annealing Effects on Sensitivity of Atomic-Layer-Deposited $SrTiO_3$-Based Oxygen Sensors. *Japanese Journal of Applied Physics* **49,** 09MA15. ISSN: 0021-4922. `http://stacks.iop.org/1347-4065/49/09MA15` (2010).

168. Rahmati, B. *et al.* Oxidation of reduced polycrystalline Nb-doped $SrTiO_3$: Characterization of surface islands. *Surface Science* **595,** 115–126. ISSN: 0039-6028. `https://www.sciencedirect.com/science/article/pii/S0039602805008988` (2005).

169. Nie, Y. F. *et al.* Atomically precise interfaces from non-stoichiometric deposition. *Nature Communications* **5,** 4530. ISSN: 2041-1723. `http://www.nature.com/articles/ncomms5530` (2014).

170. Lee, J. H. *et al.* Dynamic layer rearrangement during growth of layered oxide films by molecular beam epitaxy. *Nature Materials* **13,** 879–883. ISSN: 1476-1122. `http://www.nature.com/articles/nmat4039` (2014).

171. Chen, Y. *et al.* Segregated Chemistry and Structure on (001) and (100) Surfaces of $(La_{1-x}\ Sr_x)_2\ CoO_4$ Override the Crystal Anisotropy in Oxygen Exchange Kinetics. *Chemistry of Materials* **27,** 5436–5450. ISSN: 0897-4756. `http://pubs.acs.org/doi/10.1021/acs.chemmater.5b02292` (2015).

172. Druce, J. *et al.* Surface termination and subsurface restructuring of perovskite-based solid oxide electrode materials. *Energy Environ. Sci.* **7,** 3593–3599. ISSN: 1754-5692. `http://xlink.rsc.org/?DOI=C4EE01497A` (2014).

173. Dulli, H., Dowben, P. A., Liou, S.-H. & Plummer, E. W. Surface segregation and restructuring of colossal-magnetoresistant manganese perovskites La 0.65 Sr 0.35 MnO_3. *Physical Review B* **62,** R14629–R14632. ISSN: 0163-1829. https://link.aps.org/doi/10.1103/PhysRevB.62.R14629 (2000).

174. Rodenbücher, C., Wicklein, S., Waser, R. & Szot, K. Insulator-to-metal transition of $SrTiO_3$:Nb single crystal surfaces induced by Ar^+ bombardment. *Applied Physics Letters* **102,** 101603. ISSN: 0003-6951. http://aip.scitation.org/doi/10.1063/1.4795611 (2013).

175. Kan, D. & Shimakawa, Y. Transient behavior in Pt/Nb-doped $SrTiO_3$ Schottky junctions. *Applied Physics Letters* **103,** 142910. ISSN: 0003-6951. http://aip.scitation.org/doi/10.1063/1.4824169 (2013).

176. Tachikawa, T., Minohara, M., Hikita, Y., Bell, C. & Hwang, H. Y. Tuning Band Alignment Using Interface Dipoles at the Pt/Anatase TiO_2 Interface. *Advanced Materials* **27,** 7458–7461. ISSN: 09359648. http://doi.wiley.com/10.1002/adma.201503339 (2015).

177. Stradi, D., Martinez, U., Blom, A., Brandbyge, M. & Stokbro, K. General atomistic approach for modeling metal-semiconductor interfaces using density functional theory and nonequilibrium Green's function. *Physical Review B* **93,** 155302. ISSN: 2469-9950. https://link.aps.org/doi/10.1103/PhysRevB.93.155302 (2016).

178. Brandbyge, M., Mozos, J.-L., Ordejón, P., Taylor, J. & Stokbro, K. Density-functional method for nonequilibrium electron transport. *Physical Review B* **65,** 165401. ISSN: 0163-1829. https://link.aps.org/doi/10.1103/PhysRevB.65.165401 (2002).

179. Soler, J. M. *et al.* The SIESTA method for ab initio order- N materials simulation. *Journal of Physics: Condensed Matter* **14,** 2745–2779. ISSN: 0953-8984. http://stacks.iop.org/0953-8984/14/i=11/a=302?key=crossref.8ed2406c09184bcd143191af26e9f492 (2002).

180. Troullier, N. & Martins, J. L. Efficient pseudopotentials for plane-wave calculations. *Physical Review B* **43,** 1993–2006. ISSN: 0163-1829. https://link.aps.org/doi/10.1103/PhysRevB.43.1993 (1991).

181. Hamann, D. R. Generalized norm-conserving pseudopotentials. *Physical Review B* **40,** 2980–2987. ISSN: 0163-1829 (1989).

182. Perdew, J. P., Burke, K. & Ernzerhof, M. Generalized Gradient Approximation Made Simple. *Physical Review Letters* **77,** 3865–3868. ISSN: 0031-9007. https://link.aps.org/doi/10.1103/PhysRevLett.77.3865 (1996).

Acknowledgements

This doctoral thesis would not have been possible without the professional and non-professional contribution and assistance of many people. I would like to thank all the colleagues and everyone who supported me during this work:

First of all, I would like to thank Prof. Waser who gave me the opportunity to work in his institute. Throughout the entire thesis the fruitful discussion encouraged me to think out of the box.

My special thanks goes to Prof. Mayer for agreeing to act as reviewer of this doctoral thesis.

Furthermore, I want to thank Felix Gunkel for the supervision of this thesis and the support during international beamtimes. In uncounted discussions he helped me develop in all the various aspects of scientific work, writing, and orientation in the wide field surface physics.

I also want to thank David Mueller for introducing me into the often distracting field of XPS spectra analysis and surface chemistry. His great experimental expertise, dedication and eye for details helped me circumnavigate various stumbling blocks.

Moreover, I want to thank Prof. Regina Dittmann for supporting me during the development of the PLD thin film growth process. Her fruitful remarks from a different point of view lifted this thesis to another level.

During my entire time in Jülich at the PGI-7 starting with my master thesis and finishing with this doctoral thesis, so many colleagues were involved in my scientific development while making every day work life enjoyable. I want to thank my various office mates Nicolas Raab, Chencheng Xu, Felix Hensling, Thomas Heisig, Thorsten Meiners, Phillip Müller, Jacqueline Börgers, Marc-André Rose and Venkata Raveendra Nallagatla for supporting me no matter if measurement results are up for discussion, a brilliant idea is needed or the cluster is leaking and making even the longest days entertaining. Special thanks also go to Katharina Skaja for always supporting me in the sometimes nerve-jangling field of physical theory and

spectroscopy and for introducing me to the most reliable tool ever made. I also want to thank Christoph Bäumer for his almost infinite understanding of whatever topic is brought up for discussion.

This thesis would not have been possible without the help of many international colleagues and collaborations. I want to thank Prof. Vladimír Matolin, Filip Dvořák, Mykhailo Vorokhta and Břetislav Šmíd from the Department of Surface and Plasma Science of the Charles University in Prague, Hendrik Bluhm from the Chemical Science Division of the Lawrence Berkeley National Laboratory and Slavomír Nemšák from the Peter Grünberg Institute of the Forschungszentrum Jülich for their support during various beamtimes. Moreover, I want to thank Carsten Funck and Stephan Menzel of the IWE II of the RWTH Aachen for providing me with DFT calculations.

I also want to thank Georg Pickartz and Jochen Friedrich for technical support in the cluster lab. Special thanks go to René Borowski for providing me with structured top electrodes and making me laugh no matter what happened. In addition, I would like to thank Marcel Gerst for IT-support and Maria Garcia and Luise Snyders for support with administration.

Of course the time of such a thesis is not only about work, but also about growing together as a team and evolving as a person. My special thanks to Nicolas Raab for providing shelter for long computer weekends, to René Ebeling for not always winning in board games, to Felix Hensling for helping me finding my place in Bonn and introducing me to my new favorite place to watch football and to Chrsitoph Bäumer for hosting various superbowl nights. I also want to thank Daniel Hartnick, Daniel Schröder and Robert August for providing me diversion after exhausting days. Special thanks go to Marius Piel, Robert Rechmann and Simon von Bülow for reminding me of the world outside the scientific ivory tower.

Finally, a special thanks to all my friends who helped me to face all the hard work with a smile. I want to thank my family who made this all possible with their support through my entire studies. The biggest thanks to Anna for all the courage you gave me when I was down, the patience you had when I was upset and just being my partner no matter what.

Bonn, December 10, 2019

Band / Volume 46
Growth and characterization of crystalline rare-earth based thin oxide fims for the application as gate dielectric in nanotechnology
A. B. Schäfer (2015), xiii, 157 pp
ISBN: 978-3-95806-111-8

Band / Volume 47
TEM/STEM Investigations of Phase Change Materials for Non-volatile Memory Applications
M. Bornhöfft (2017), viii, 135 pp
ISBN: 978-3-95806-221-4

Band / Volume 48
Investigation of ternary nitride semiconductor alloys by scanning tunneling microscopy
V. Portz (2017), 140 pp
ISBN: 978-3-95806-232-0

Band / Volume 49
Redox processes and ionic transport in resistive switching binary metal oxides
K. Skaja (2017), VII, 203 pp
ISBN: 978-3-95806-236-8

Band / Volume 50
Investigation of switching mechanism in Ta_2O_5 -based ReRAM devices
K. Wonjoo (2017), iii, 138 pp
ISBN: 978-3-95806-261-0

Band / Volume 51
Development of ReRAM-based Devices for Logic- and Computation-in-Memory Applications
T. Breuer (2017), x, 179 pp
ISBN: 978-3-95806-270-2

Band / Volume 52
Resistive switching memory devices from atomic layer deposited binary and ternary oxide thin films
N. Aslam (2017), X, 172 pp
ISBN: 978-3-95806-274-0

Band / Volume 53
Operando X-ray photoemission electron microscopy (XPEEM) investigations of resistive switching metal-insulator-metal devices
C. J. Schmitz (2017), IX, 153 pp
ISBN: 978-3-95806-283-2

Band / Volume 54
Optimization of powder and ceramic processing, electrical characterization and defect chemistry in the system $Yb_xCa_{1-x}MnO_3$
M. Rahmani (2018), XIV, 164 pp
ISBN: 978-3-95806-323-5

Band / Volume 55
Organic-Metal Hybrid Interfaces at the Mesoscopic Scale
G. Zamborlini (2018), xi, 133 pp
ISBN: 978-3-95806-328-0

Band / Volume 56
Configurable frequency synthesizer for large scale physics experiments
N. Parkalian (2019), xxi, 114 pp
ISBN: 978-3-95806-393-8

Band / Volume 57
Resistive switching phenomena in stacks of binary transition metal oxides grown by atomic layer deposition
H. Zhang (2019), ix, 196 pp
ISBN: 978-3-95806-399-0

Band / Volume 58
Element-Selective Investigation of Femtosecond Spin Dynamics in Ni_xPd_{1-x} Magnetic Alloys using Extreme Ultraviolet Radiation
S. Gang (2019), 93, xx pp
ISBN: 978-3-95806-411-9

Band / Volume 59
Defect engineering in oxide thin films
F. V. E. Hensling (2019), 10, 164 pp
ISBN: 978-3-95806-424-9

Band / Volume 60
Chemical control of the electrical surface properties of *n*-doped transition metal oxides
M. Andrä (2019), X, 150, XXXVIII pp
ISBN: 978-3-95806-448-5

Information
Band / Volume 60
ISBN 978-3-95806-448-5

Mitglied der Helmholtz-Gemeinschaft

JÜLICH
Forschungszentrum